Predicting the Formation Pathways and Morphologies of Oxygenated Carbonaceous Nanoparticle Precursors in Premixed Flames

by

Vernon Tyler Dillstrom

A dissertation submitted in partial fulfillment
of the requirements for the degree of
Doctor of Philosophy
(Mechanical Engineering)
in the University of Michigan
2017

Doctoral Committee:

Professor Angela Violi, Chair
Professor John R. Barker
Professor H. Scott Fogler
Professor Margaret Wooldridge

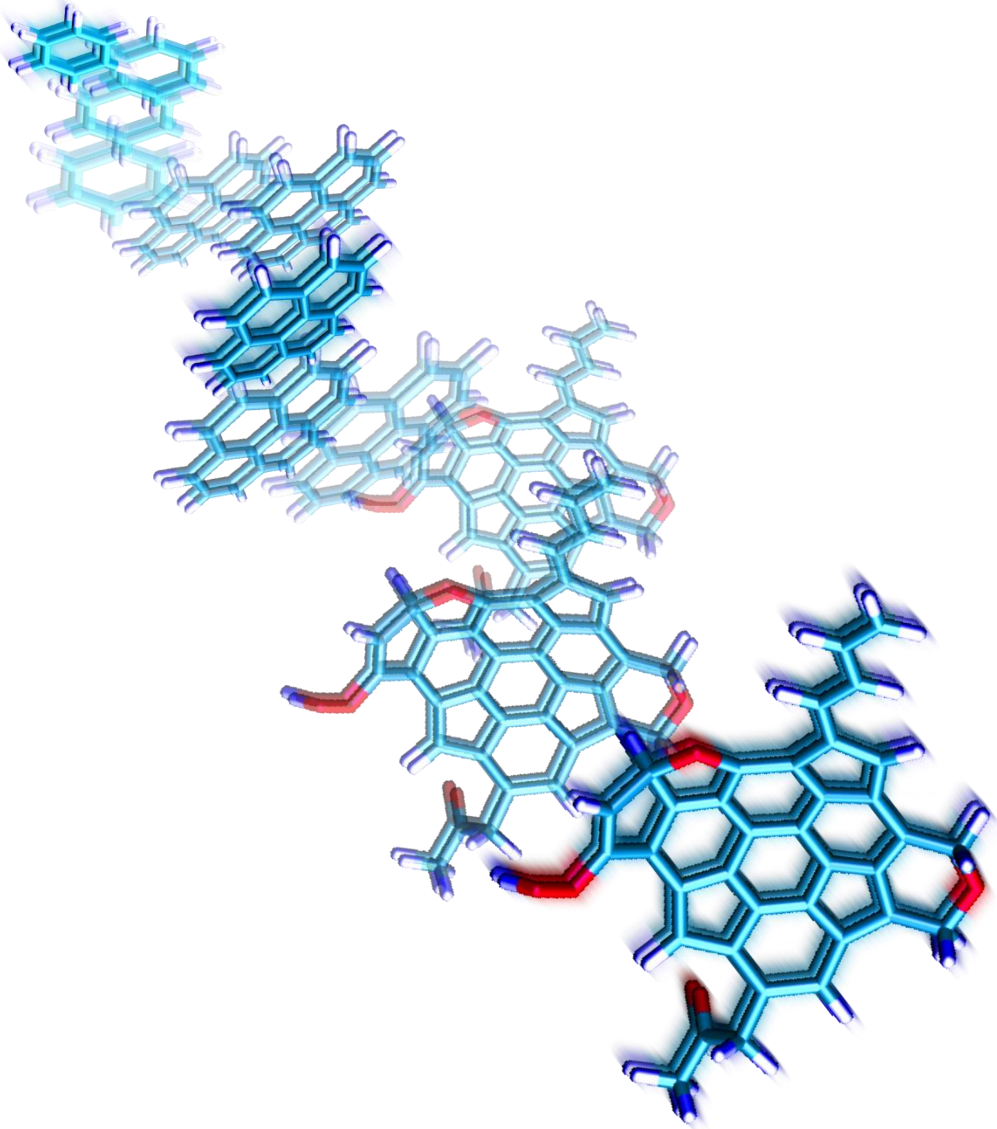

© Vernon Tyler Dillstrom 2017
All Rights Reserved

vtdillst@umich.edu
ORCID iD 0000-0001-9176-0483

Para Diana.

Mi vida sería severamente disminuida

sin tu amor y aliento.

Estoy eternamente agradecido.

Acknowledgments

The research represented in this dissertation is the result of several years of scholarship which would not have been possible without the guidance of my advisor, Professor Angela Violi. Nothing would have been accomplished without her expertise and zest for discovery that inspired and motivated me daily. I have learned as much about scientific discovery as I have the topic of this dissertation thanks to her advice and support; for that I am greatly indebted.

I owe a sincere thank you to my thesis committee, Professors John Barker, Scott Fogler, and Margaret Wooldridge for graciously donating their time and expertise to the execution of this dissertation.

To all the friends I have gained in the Violi Group, thank you for making our collaborations invigorating and our conversations exciting. The lessons and knowledge learned in my time here are a result of stimulating discussions we have had.

To the friends that have suffered me for years, I am grateful for our camaraderie and the joy we have shared. Life is nothing if not a collection of moments to share.

Finally, my most heartfelt thanks and love to my family, especially my wife, Diana, for investing in me more than I invest in myself. This accomplishment would not have been possible without you. Your love and support mean the world to me.

Table of Contents

Dedication .... **ii**

Acknowledgments .... **iii**

List of Figures .... **viii**

List of Tables .... **xxii**

Abstract .... **xxvi**

Chapter 1 Introduction **1**

- 1.1 Particle Formation Process 2
- 1.2 Particle Inception 3
  - 1.2.1 Modeling Particle Inception and Growth 5
- 1.3 Formation and Growth of Aromatic Precursors 7
  - 1.3.1 Kinetic Growth Pathways 8
  - 1.3.2 Kinetic Reaction Rate Constants 14
  - 1.3.3 Deterministic Modeling of PAH Formation and Growth 16
  - 1.3.4 Stochastic Modeling of PAH Formation and Growth 21
- 1.4 Composition of Particle Precursors 24
  - 1.4.1 Oxygenated Precursors 26
  - 1.4.2 Influence of Oxygenated Fuels on Particle Precursors 27

1.5 Summary and Scope 29

Chapter 2 Methodology 38

2.1 Developing Oxygenation Pathways 41

2.1.1 Reaction Rate Constant Development 43

2.2 Designing a Synergistic Growth Mechanism 48

2.3 Reaction Sites Description 51

2.4 SNAPS team 55

2.5 Summary 55

2.5.1 Contributions 56

Chapter 3 Exploring the Effect of Oxygenation Pathways on PAH Growth in a Benzene-Air Flame 78

3.1 Simulation Design 78

3.2 Results and Discussion 79

3.2.1 PAH Production in Simulations 80

3.2.2 Effect of Seed on Growth Rate 82

3.2.3 Oxygenation Pathways Increase Precursor Growth 84

3.2.4 Effect of Oxygenation Pathways on Mass Spectra 88

3.3 Summary and Conclusions 92

3.3.1 Contributions and Collaborations 93

Chapter 4 The Formation of Oxygenated Compounds in a Premixed Ethylene-Oxygen Flame 100

4.1 Simulation Design 100

4.1.1 Experimental Setup 101

4.2 Results and Discussion 102

4.2.1 Electronic Structure Calculations 103

4.2.2 Evolution of OPAHs 105

4.2.3 Enol Intermediates 106

4.2.4 Furanic Structures 106

4.2.4.1 Furan Formation Pathway 108

4.2.4.2 Furan Formation Kinetics 110

4.2.5 Impact of SNAPS Predicted Particles 111

4.2.6 Structural Predictions of Pyrene and its Isomers 113

4.2.7 Radical-Radical Recombination 115

4.3 Summary and Conclusions 116

4.3.1 Contributions and Collaborations 117

Chapter 5 Effect of Oxygenated Fuels on PAH Growth and Particle Formation in Ethylene Flames 127

5.1 Simulation Design 128

5.1.1 Primary Flame System 129

5.1.2 Secondary Flame System 130

5.2 Results and Discussion 131

5.2.1 Gas-phase Modeling 131

5.2.1.1 Primary Flame System 131

5.2.1.2 Secondary Flame System 133

5.2.2 Fuel Effects on Growth Rate of Particle Precursors 134

5.2.3 Characteristics of Precursors in the Flames 137

5.3 Summary and Conclusions 140

5.3.1 Contributions and Collaborations 142

Chapter 6 Conclusions and Recommendations for Future Work 149

Appendix 156

Bibliography 172

List of Figures

Figure 1.1: Schematic of particulate formation in flames – from fuel and oxidizer to small gas-phase molecules through PAH growth to large particulates and then oxidized products. The flame is a premixed flame where fuel and air flow from the bottom. As the flow of the gas proceed up through the flame the highlighted classes of species are likely to be found in that order with respect to flame height. Molecules and particles not shown to scale. Image concept adapted from reference [39]. 32

Figure 1.2: Potential representation of a nascent ordered nanoparticle. The particle is held together by Van der Waals forces and is formed when PAH dimers, trimers, and tetramers agglomerate which generates clusters of physically bound stable PAHs. 33

Figure 1.3: Potential representation of a nascent disordered nanoparticle. The particle contains aliphatic side-chains and several oxygenated functional groups including enols, furans, and peroxyls. The particle contains aliphatically-linked PAHs. The structures are randomly ordered and formed by processes that are not thermodynamically controlled. 33

Figure 1.4: Representative “sandwich-style” (parallel planar PAHs whose centers of mass are in close proximity to each other) pyrene-pyrene dimerization: two pyrene monomers that are in near enough proximity to form a physical bond via Van der Waals attractive forces. One of the most common descriptions of particle inception includes the formation of dimers like this. Dimerization of pyrene is often assumed to initiate particle inception despite the abundance of evidence that suggests that such a dimer is not stable or does not have a significant lifetime at flame temperatures. 33

Figure 1.5: Pictorial of the formation of an oxygenated polycyclic aromatic hydrocarbon (OPAH) in a combustion environment. The evolution of particles and their precursors occurs in both time and space dependent on the bulk flow of the gas-phase environment. 34

Figure 1.6: Chemical formation schemes for the formation of naphthalene: (a) Bittner-Howard, (b) hydrogen-abstraction-C_2H_2-addition (HACA). 35

Figure 1.7: Hydrogen and ring migration pathways proposed by Frenklach et al. [130] 35

Figure 1.8: The Diels-Adler growth scheme proposed by Siegmann and Sattler that does not involve radical species. 36

Figure 1.9: The resonantly stabilized radical (RSR) growth scheme proposed by Colket and Seery: (a) propargyl addition to benzyl yields naphthalene, (b) a growth scheme up to anthracene from toluene and benzyl. Ring closure reaction require hydrogen elimination. 36

Figure 1.10: Ring fusing reactions presented by Marinov et al. in which naphthalene and phenanthrene are created via reactions between cyclopentadienyl and indenyl radicals. 36

Figure 1.11: Definition of a free edge site and a zig-zag site on a PAH. In SNAPS the carbon sites are distinguished as unique from each other for certain reaction types, e.g. ring closures. 37

Figure 2.1: A schematic of the SNAPS algorithm. If a reaction is rejected, step two is repeated and the cycle continued. 69

Figure 2.2: Flow chart schematic of the design process of the new oxygenated hydrocarbon kinetic mechanism used in SNAPS modeling of PAH growth in premixed flames for this work. 70

Figure 2.3: Examples of key oxygenation reactions in SNAPS mechanism. Specific reactions chosen to represent each type of class of reactions are because they are the most dominant reactions in their respective class. 71

Figure 2.4: Oxygenated functional groups that are generated in SNAPS trajectories via the oxygenation and oxidation pathways. 72

Figure 2.5: The blue highlights are the definition of a reaction site for bimolecular hydroxyl addition to a radical aromatic carbon. They reaction site only considers the exact composition and structure of the six highlighted carbon atoms (and their attached hydrogen neighbors), thus the two distinct species on the left undergo the same reaction event. This eliminates the need to specifically define all species – of which there are hundreds of thousands when considering all potential species larger than benzene. 72

Figure 2.6: 92 bimolecular reaction rate coefficients as evaluated at 1750K sorted in descending order. 80% of the reaction rate coefficients are within 2 orders of magnitude of each other. There is one outlier (far left) on the far side and the slowest 10% of rate coefficients are several orders slower than the median ($1.69*10^{12}$ $cm^3*s^{-1}*mol^{-1}$) and average ($4.08*10^{15}$ $cm^3*s^{-1}*mol^{-1}$). Red bars are novel oxygenation pathways. Blue bars are hydrocarbon reactions. The sets of pathways work synergistically to create a more comprehensive chemical evolution mechanism. 73

Figure 2.7: 48 Unimolecular reaction rate coefficients as evaluated at 1750K sorted in descending order. Because the rate coefficients of the lower half of the reactions steadily and continuously decrease, the average of the coefficients ($2.39*10^{11}$ s^{-1}) is skewed such that the lower 75% of reactions are slower than the average. The median reaction rate coefficient is $2.19*10^9$ s^{-1}. Red bars are novel oxygenation pathways. Blue bars are hydrocarbon reactions. The sets of pathways work synergistically to create a more comprehensive chemical evolution mechanism. 73

Figure 2.8: Example subset of a potential reaction pathway diagram. A trajectory where indene (center) is the seed molecule could evolve along the given route shown or any number of other routes not depicted. All reactions and pathways are reversible. 74

Figure 2.9: Comparing the hydrocarbon-only pathways to the combined oxygenation and hydrocarbon pathways. Here the pathways from naphthalene (2 rings) to a 3 ring structure with no chains. In the set of pathways (b) there are only a small set of pathways that go from naphthalene to a 3 ringed structure, and there are only 4 possible structures that contain 3 rings. In the set of pathways (a) oxygenation pathways that work synergistically with hydrocarbon growth pathways lead to many multiples of potential growth pathways from naphthalene to a 3 ringed structure. Additionally there are 10 conformations of a structure with one oxygenated ring in addition to the same 4 carbon-only 3 ringed structures present in the set of pathways (a). Oxidation pathways present in the oxygen growth mechanism provide quick avenues from oxygenated rings to carbon-only rings. This provides a mechanism to eliminate embedded oxygen atoms from the PAH and nanoparticles structures. Note: not all pathways and bimolecular additions present in the SNAPS mechanism are shown in the diagram for the purpose of clarity. Because oxygenation reactions work in parallel and in coordination with hydrocarbon reactions including all pathways has a multiplier effect on the number of number of pathways when oxygen chemistry is included in the SNAPS mechanism. 75

Figure 2.10: The blue highlights are the definition of a reaction site for which a 5 membered ring could form on a zig-zag site. They reaction site only considers the exact composition and structure of the 5 highlighted carbon atoms (and their attached hydrogen neighbors), thus the two distinct species on the left undergo the same reaction event. This eliminates the need to specifically define all species – of which there are hundreds of thousands when considering all potential species larger than benzene. 76

Figure 2.11: Reaction site definitions for the key reaction types in the mechanism. Dark blue circles are reaction sites for all reactions which lead to hydrogen abstraction from a saturated aromatic carbon. Light blue circles are reaction sites for all reactions which lead to hydrogen abstraction from a saturated aliphatic carbon. The top examples are representative of carbons which are a member of a ring of 5 carbons comprising a zig-zag site. The right examples are representative of generic aliphatic carbons. The light green circles are reaction sites for all reactions which are vulnerable to ring opening reactions. The top example would be the opening of a five-member carbon ring on a zig-zag site. The bottom example would be the opening of a pyran (5 carbons, 1 oxygen atom) ring. The light red circles are reaction sites for all reactions which lead to the bimolecular addition of a gas-phase species to a radical site on the molecule. The top example would be addition to an aliphatic carbon. The bottom example would be addition to an oxyradical. The light chain highlighted in light maroon on the right is an example of a reaction site that could undergo ring closure. The highlighted six carbons in that structure and composition are able to form a six-member aromatic ring on the edge of the molecule. 76

Figure 3.1: Flow process showing the order and decision points of experimental choice and simulations required in the design of this study, as well as subsequent studies. 94

Figure 3.2: Ratios of particular species throughout the height of the flame from [248]. The experiment measured these species; shown here is the ratio of species: (a) acenaphthylene to indene, (b) acenaphthylene to naphthalene, and (c) phenanthrene to anthracene. Compared are the experiment (blue), a deterministic simulation in CHEMKIN (red), SNAPS while using a mechanism with no oxygen chemistry (green), and SNAPS while using the more comprehensive oxygen/hydrocarbon mechanism (purple). 95

Figure 3.3: Profiles of the average masses of the ensembles of trajectories versus the height of the flame obtained using a mechanism that comprises hydrocarbon and oxygenation pathways. The larger pyrene seed allows for more potential growth pathways early in the flame when the environment is radical-rich and thus the rate of growth is appreciably faster than when using the smaller benzene or toluene seeds. The inset molecules are representative of typical SNAPS-generated PAHs at 8 mm with a mass roughly equivalent to the average mass of the ensemble at 8 mm. The top molecule has a mass of 654 amu (average mass for pyrene-seed trajectories is 655 amu at 8mm). The lower molecule has a mass of 403 amu (average mass for benzene-seed trajectories is 395 amu at 8 mm)...................... 96

Figure 3.4: Average SNAPS ensemble masses profiles over the height of the flame. The inclusion of oxygenation pathways allows for a greater number of growth options and thus a faster rate of growth, hence the much higher plateau mass (about 400 amu) than when oxygenation is not allowed in the SNAPS mechanism (200 amu plateau). A slight deviation is observed greater than 2 mm when the oxygenation is accounted for; very little difference is observed when the oxygenation is not accounted for because the restricted number of pathways confines toluene and benzene to identical growth pathways after 2 mm. The inset molecules are representative of typical SNAPS-generated PAHs at 8 mm with a mass roughly equivalent to the average mass of the ensemble at 8 mm. The top molecule has a mass of 403 amu (average mass for benzene-seed trajectories with oxygenation pathways is 395 amu at 8mm). The lower molecule has a mass of 202 amu (average mass for benzene and toluene-seed trajectories without oxygenation pathways is 189 amu at 8 mm). 97

Figure 3.5: Computed mass spectra using a benzene seed with two varying mechanisms: (a) without accounting for the oxygenation of PAHs and (b) while accounting for the oxygenation pathways. SNAPS ensembles consist of 3000 trajectories to achieve statistical significance. The spectrum created with oxygen chemistry included in the SNAPS code shows that the oxygenation pathways work with the HACA pathways to broaden the range of potential species to all masses. 98

Figure 3.6: Computational mass spectra developed with SNAPS using a toluene seed with two varying mechanisms: (a) without accounting for the oxygenation of PAHs and (b) while accounting for the oxygenation pathways. SNAPS ensembles consist of 3000 trajectories to achieve statistical significance. The spectrum created with oxygen chemistry included in the SNAPS code is much noisier with no dominant peaks because the oxygenated PAHs do not fall into the ± 12 amu pattern that purely hydrocarbon PAHs do. 98

Figure 3.7: (a) Computed mass spectrum using a mixture of initial seed molecules, benzene:toluene:pyrene of 0.945:0.045:0.01. The ratios of the relative mole fraction concentrations of benzene:toluene:pyrene are 0.037:0.0018:0.00039 at the beginning of the flame where SNAPS simulation commence. The computational mass spectra are a combination of 4000 trajectories with oxygenation reactions and 6000 trajectories without oxygenation reactions. (b) Experimental mass spectrum of benzene–air laminar premixed flame [248]. SNAPS correctly predicts the dominant masses (202, 226, 252, 276, 300 amu) as well as predicting the spectrum of less abundant masses that make up the noisy bedding of the spectrum. Both sets of growth pathways work in parallel to yield an ensemble of partially oxygenated PAHs that represent the spectrum in the flame. 99

Figure 4.1: Simulated concentration profiles of key species from the premixed laminar ethylene flame. Four distinct deterministic mechanisms were utilized in identical simulations using CHEMKIN [155]: Appel et al. [95], Miller et al. [32], Raj et al. [158], and Richter et al. [260]. Of the four, all were relatively similar for the entire set of species. Miller et al. is the least like the other three. Of the set, the mechanism from Appel et al. most closely captured the average of the species concentrations and profiles. 120

Figure 4.2: Most probable reaction sequence leading to formation of a furan group. (Left to Right) H-abstraction followed by OH addition to the radical free edge site on an aromatic ring; H-abstraction from the OH group, followed by acetylene addition, forming an ether group; H-elimination during ring closure to form a furan group. The left side of the molecule has been left attached to an indeterminate PAH backbone to illustrate an arbitrary molecular size. 121

Figure 4.3: Potential-energy diagram for the formation of benzofuran. The energies are in kilocalories per mole and are referenced to the reactant species. The ring-closing reaction is exothermic, and the closed-ring structure is thus favored over the phenoxy + acetylene reactants as well as the open-ring structure (first intermediate). In SNAPS the first reaction (TS1) is distinct from the second reaction (TS2 and TS3). The first reaction is a unimolecular acetylene addition to an oxyradical and the second reaction is a unimolecular ring closure to form a furan ring (steps TS2 and TS3 are treated as one reaction in SNAPS because the second intermediate structure would only go to the product or the first intermediate due to the unique nature of the over coordination and loss of aromaticity of the structure). The energy barriers of the ring closure reaction steps are low compared with the average temperature fluctuations in flames. For example, at 1,500 K, TS2 is $3k_BT$ and TS3 is$-1k_BT$ with respect to the first intermediate species. 122

Figure 4.4: Enols predicted by the SNAPS simulations. Enols predicted to be important to the OC chemistry at small DFFOs in premixed combustion are (A) 94 u (phenol), (B) 108 u (C7H8O), (C) 118 u (C8H6O), (D) 168 u (C12H8O), and (E) 192 u (C14H8O). 123

Figure 4.5: Frequently predicted oxygen-containing structures of selected masses low in a premixed flame. Red atoms, oxygen; gray, carbon; white, hydrogen. (A and B) Ether and ether/ketene, 160 u. (C) Furan, 168 u. (D and E) Ether and furan, 194 u. (F) Ether, 220 u. 123

Figure 4.6: Predicted H and OH mole fractions at low flame heights in the Ar-diluted premixed flame using the Appel–Bockhorn–Frenklach deterministic mechanism [95]. The ratio between the H and OH mole fractions is also shown. The vertical dashed lines are the edges of the region where the majority of the oxygenation occurs, according to the SNAPS simulations. 123

Figure 4.7: Experimental AMS spectra from a premixed flame as measured by Michelsen and coworkers [241]. Mass spectra are shown for particles extracted from selected heights in the flame; that is, DFFOs of (A) 3.5, (B) 5.0, and (C) 7.5 mm. Red peaks contain signal from oxygenated species. The arrows indicate the peaks at 160, 194, and 220 u for comparison with Figure 4.4 where one can see the main predicted structures at a DFFO of ~3.5 mm. 124

Figure 4.8: Relative concentrations of the most abundant species with mass 202 u (left) and 226 u (right) at a DFFO of 3.4 mm computed by SNAPS. These species account for 98% of all 202-u species and 97% of all 226-u species at 3.4 mm. 125

Figure 4.9: SNAPS results showing the five most common pairs of radicals that combine to make structures at 266 u and 278 u at a DFFO of 3.4 mm in the premixed flame. These reactions account for 72% of all combined structures at 266 u and 89% of all combined structures at 278 u. 126

Figure 5.1: Red solid lines represent the pure ethylene flame and blue dashed lines represent the ethanol doped flames. (a) Temperature profile obtained from the Salamanca et al. [234] (b) Axial velocity of the flames as modeled in with the CHEMKIN PREMIX [155], [247] software. (c) Residence time of the gases in the flames. The residence time is shown to highlight that particles have almost equal residence times in the flames to grow, thus differences in SNAPS simulations is not due to residence time. 143

Figure 5.2: Species profiles of the pure ethylene (solid red lines) and ethanol doped (dashed blue lines) flames from [234] simulated in CHEMKIN [155], [247]. (a) O_2, (b) C_2H_2, (c) H_2, (d) H, (e) OH, (f) O, (g) O_2 0-2mm only, (h) OH 0-2mm only, (i) O 0-2mm only. The latter three are presented for qualitative clarity at HAB less than 2 mm. 144

Figure 5.3: Species profiles of the pure ethylene (solid red lines) and ethanol doped (dashed blue lines) flames from [234] simulated in CHEMKIN [155], [247]. (a) benzene, (b) toluene, (c) indene, (d) naphthalene, (e) acenaphthylene. The ethanol doped flame has consistently higher concentrations of small aromatics than the pure ethylene flame. 145

Figure 5.4: Species profiles of the pure ethylene (solid red lines) and ethanol doped (dashed blue lines) flames from Wu et al. [235] simulated in CHEMKIN [155], [247]. (a) C_2H_2, (b) benzene, (c) toluene, (d) naphthalene, (e) acenaphthylene. The pure ethylene flame has consistently higher concentrations of acetylene and small aromatics than the ethanol doped flame.. 145

Figure 5.5: Small (left) and large (right) PAH profiles of the pure ethylene (experiment: red star symbols, gas-phase model: solid red lines) and ethanol doped (experiment: blue square symbols, gas-phase model: dashed blue lines) flames from Wu et al. [235] and simulated in CHEMKIN. The pure ethylene flame has consistently higher concentrations of small and large PAHs. The model captures that as well as the general shape of the profiles (slight concavity around five mm in the small PAH profiles and near linearity in the large PAH profiles). As defined in reference [235], the profiles are normalized by the final concentration of the pure flame. That is, the models are normalized by the concentration at 20 mm in the pure flame, and the sets of experimental data are normalized by the concentration at 20 mm in the pure flame. 146

Figure 5.6: Average mass of an ensemble of HMAMs generated using SNAPS in the pure flame (circles) and doped flame (squares). Closed and open symbols represent simulations with the oxygen/hydrocarbon and the reduced (hydrocarbon only, no oxygenation pathways) growth mechanism, respectively. Each line is obtained by averaging 11000 trajectories (oxygen/hydrocarbon mechanism) or 1000 trajectories (HC only). The 99% confidence interval for the ensemble mean was calculated for all data points. The largest range for each ensemble is: ±6.1 u (pure flame with full mechanism), ±3.9 u (doped flame with full mechanism), ±12.9 u (pure flame with partial mechanism), and ±16.6 u (doped flame with partial mechanism). 146

Figure 5.7: Ensemble average C/H (a) and C/O (b) ratios of the HMAMs predicted by SNAPS for the pure ethylene (solid red lines) and ethanol doped (dashed blue lines) flames from [234]. At each height every HMAM trajectory is sampled and a molecule-specific C/H and C/O ratio is calculated; the ratios are then averaged to create the plotted profiles. The sampled heights for both methods were 0.1, 0.2, 0.5, 1, 3, 6, 8, 10, 12, and 14 mm HAB. 147

Figure 5.8: Ensemble average ratios of net oxygenation to net carbonation in the pure ethylene (solid red lines) and ethanol doped (dashed blue lines) flames of [234]. Reported are both the cumulative ratios (a) as well as the non-cumulative ratios (b left y-axis) overlaid with the relative O_2 concentrations of the flames (b right y-axis). The medium dashed bright red line represents the O_2 profile of the pure ethylene flame and the dotted bright blue line represents the O_2 profile of the ethanol doped flame. Net oxygenation accounts for the difference in reactions that add oxygen atoms to the HMAM and those that remove or abstract oxygen atoms (including the number of oxygen atoms involved in the reaction). Similarly, for net carbonation, but with carbon atoms. The cumulative ratios (a) involve accounting for all reactions in all SNAPS trajectories up to that height in the flame. The non-cumulative ratios involve accounting for all reactions in all SNAPS trajectories only in the range of the sampled height, i.e. from midway between the previously sampled height and the current sample height to midway between the currently sampled height and the next height to be sampled. The sampled heights for both methods were 0.1, 0.2, 0.5, 1, 3, 6, 8, 10, 12, and 14 mm HAB. The calculation heights are intentionally more compacted from 0 to 2 mm because the HMAMs were shown to undergo a much faster rate of growth in that region. It is noteworthy that both flames show their highest oxygen addition to carbon addition ratios at 0.2 mm (second height represented) and the ratios quickly become smaller with flame height. This parallels the rate of growth of HMAMs as functions of height of the flame; in particular that the fastest rate of growth was between 0.1 and 0.5 mm.. 147

List of Tables

Table 2.1: The main classes of reaction pathways that the oxygenation kinetic growth mechanism comprises. 58

Table 2.2: Example reactions from each major class of oxygenation pathways in the SNAPS mechanism. (g) signifies a gas-phase molecule interacting with a HMAM, C_{ar} represents an aromatic carbon on the HMAM, C_{al} represents and aliphatic carbon on the HMAM, C with no subscript represents either type of carbon on the HMAM, X(Y) implies that atom(s) Y is bonded to atom X on the HMAM, $^+$ signifies that the rate was calculated from the forward rate using standard thermodynamic properties to calculate the equilibrium constant, and * implies a radical or active site. Units for pre-exponential factor A are s^{-1} for unimolecular reactions and $cm^3*s^{-1}*mol^{-1}$ for bimolecular reactions, units for Activation Energy (Ea) are $kcal*mol^{-1}$.. 58

Table 2.3: The set of equations used to calculate the reverse rate constant given the forward constant, temperature, and NASA polynomials for each species in the reaction. This method was used several times at varying temperatures to calculate several reverse rates and then modified Arrhenius parameters were fit to the rates to derive parameters used in the SNAPS mechanism for reach reverse reaction.

Note that coefficients $\{a_1 \ldots a_7\}$ are the appropriate coefficients from the NASA polynomial table for that particular species for the temperature at which the enthalpy and entropy are being evaluated. 59

Table 2.4: List of all new oxygenation reactions in the mechanism. A listing of all reactions demonstrating how the oxygenation pathways are weaved into hydrocarbon pathways is give in Table A.1. Reactions are organized by class (color). The classes of reactions (in order top to bottom): light red are hydrogen removal/abstraction reactions; dark red are hydrogen addition reactions; dark orange are hydrogen transfer reactions; dark blue are fragment addition reactions; light blue are fragment removal/abstraction reactions; light green are ring closure reactions; dark green are ring opening reactions; tan are isomerization reactions; dark tan are oxidation reactions. Within each class (color) the reactions are ordered in descending reaction rate coefficient as evaluated at 1750 K (1750 K chosen to represent a median combustion temperature for a broad range of flame types/conditions). Notations for the "Reaction Description" column: (g) represents gas-phase molecule interacting with HMAM, C_{ar} represents and aromatic carbon on the HMAM, C_{al} represents and aliphatic carbon on the HMAM, C with no subscript represents either type of carbon on the HMAM, X(Y) implies that atom(s) Y is bonded to atom X on the HMAM. Units for the pre-exponential factor ("A" column) are s^{-1} for unimolecular reactions and $cm^3*s^{-1}*mol^{-1}$ for bimolecular reactions. Units for the activation energy ("Ea" column) are kcal/mol. PW stands for present work, Eq is used to signify that the rate constant was calculated in this work using thermodynamic properties to obtain the equilibrium constant.. 59

Table 2.5: Pictorials of reaction types. Dashed lines on the molecules off of atoms signify that anything can be attached to those atoms. For example, ---CH signifies that they key group is a saturated carbon atom bonded to any other atom (which in turn may or may not be bonded to other atoms). Where there is an “X” in the pictorial, the “X” can represent any of the species listed underneath the pictorial. 62

Table 2.6: SNAPS developer descriptions.. 67

Table 4.1: Analysis of mass peaks. Columns 5 and 6 are my predictions based on analysis of SNAPS simulations. The first four columns are the verifications as measured by the XPS experiment.. 119

Table A.6.1: List of all reactions in the new SNAPS mechanism corresponding to Table 2.4. All reactions are listed in descending order of rate coefficient evaluated at 1750 K within each class. Oxygenation reactions and hydrocarbon reactions are highly interconnected. Units for the pre-exponential factor (“A” column) are s^{-1} for unimolecular reactions and $cm^3*s^{-1}*mol^{-1}$ for bimolecular reactions. Units for the activation energy (“Ea” column) are kcal/mol.. 156

Table A.6.2: Pictorials of al reaction types in the new SNAPS mechanism corresponding to Table 2.5. Dashed lines on the molecules off of atoms signify that anything can be attached to those atoms. For example, ---CH signifies that they key group is a saturated carbon atom bonded to any other atom (which in turn may or may not be bonded to other atoms). Where there is an “X” in the pictorial, the “X” can represent any of the species listed underneath the pictorial. 162

Abstract

Organic nanoparticles are an inevitable by-product of combustion phenomena that have deleterious health and environmental effects. They are carcinogenic because they damage biological cells due to their small size and their presence in the atmosphere contributes to global warming. We would be better able to effectively manage the harmful effects of these nanoparticles if we better understood their formation mechanisms and chemical compositions at an atomic level. The complexities of the reaction chemistry involved along with the difficulties of experimental techniques to capture the atomic level details of nanoparticles and their chemical precursor molecules during flame synthesis, has led to a gap in the understanding of their formation pathways and molecular structures. This work presents a novel chemical kinetic reaction scheme and utilizes a computational approach to model laboratory-scale flames in order to elucidate the compositions and morphologies of organic nanoparticle precursors. Organic nanoparticles formed during combustion have long been assumed to comprise only hydrogen and carbon atoms, however, recent work has noted the presence of oxygen atoms. Using the first model to account for oxygenation of aromatic precursors, this work demonstrates that oxygen chemistry is key to understanding the formation pathways and morphologies of nanoparticles and their chemical precursors. Kinetic oxygenation pathways capture the influence of alcohol-doped-fuel on particle formation in premixed flames by identifying the fuel's effect on precursor growth.

Stochastic simulations reveal an abundance of previously unconsidered oxygenated aromatic species to be present in premixed aromatic- and aliphatic-fuel flames. Key morphologies of oxygenated precursor species predicted by the model were confirmed in experiments, including a significant presence of furanic compounds. Similarly, simulations led to experiments that confirmed model predictions that large oxygenated aromatic molecules are important participants in particle formation. The model developed in this work demonstrates for the first time that inclusion of oxygenation pathways is necessary and vital in order to represent the chemical kinetic growth of nanoparticle precursors in premixed flames. The recognition of the previously unexpected importance of oxygenated aromatic precursors and their influence on nanoparticle formation in flames constitutes a notable advancement in the field of combustion-generated nanoparticle chemistry. The impact of the present findings are considerable to the efforts to investigate combustion generated particle formation with the aim to reduce their deleterious health and environmental effects.

Chapter 1

Introduction

Carbonaceous nanoparticles (CNPs) are everywhere in our lives; they are formed as a result of common manufacturing processes [1], are prevalent in ink pigments, are key components of solar cells cathodes [2], and, most importantly, are produced globally at a rate of 100 tons per day as a byproduct of hydrocarbon combustion phenomena [3]; in fact, combustion is the main process through which particles are emitted in the atmosphere. Ascertaining and understanding the underlying causes of the production of nanoparticles is important because they have deleterious impacts on human health when inhaled in sufficient quantities [4]–[8]. They are toxic partly because their small size affords them an ability to interact with cells in the human body [9]–[11]; their morphology significantly influences the nature of the interaction with cells – partially determining the level of toxicity [12]–[15].

Additionally, carbonaceous particles have serious negative impacts on the environment. They are a contributing factor to changes in global weather patterns [16]–[18] since the aerosol nature of carbonaceous particles results in unique physical and chemical properties that lead to solar absorption and contributes to global warming effects [19], [20]. The fundamentals of the formation pathways of CNPs, their composition, and their morphologies are not fully understood despite the value that information would provide towards ameliorating their negative effects on human health and the environment. Thus the mechanisms that lead to the production of CNPs during combustion need to be more thoroughly investigated and clearly defined to elucidate some of the uncertainties.

1.1 Particle Formation Process

It was initially proposed by Jensen [21] and synthesized by Haynes and Wagner [22], [23] that particle formation in high temperature combustion environments broadly proceeds in three stages: 1) formation of 1- and 2-ring aromatics, 2) growth from the small aromatics to larger aromatic precursor molecules, and 3) particle inception – the process of transitioning from gas-phase to particle phase, in which molecules accumulate into a single solid phase object suspended in a fluid such as air, as depicted in Figure 1.1. The supporting evidence for the general process has been reviewed several times since 1981 [22]–[30] and over the decades, a general consensus has formed that supports this process [23], [25], [26]. Most recently, Wang reviewed the particle formation process and concluded that the breadth of laboratory-scale flames demonstrated the validity of the three stage process for particle formation during combustion [26].

The chemical kinetic formation pathways of single ring aromatics have been discussed extensively partly because of their importance to particle formation during combustion [26]. In particular, studies by Fahr and Stein [31] and Miller and

Klippenstein [32]–[35] showed that propargyl combination forms a number of vibrationally excited complexes which form benzene through collisional stabilization at high temperatures and atmospheric pressures. Several reviews have concluded that the two dominant formation pathways in high temperature diffusion and premixed flames are the combination of C_4 and C_2 aliphatic species that close to form benzene or phenyl radicals or the self-reaction of propargyl radicals which close to form benzene [26], [29], [36], [37].

Though particle inception was initially proposed to occur via acetylene polymerization [38], ionic species combination [24], or dimerization of polycyclic aromatic hydrocarbon (PAH) molecules [23], the latter is the focus of the community now because of the plethora of such molecules observed in many types of flames [25], [26], [29], [39]. The methods of particle inception are discussed in section 1.2. There is now general consensus that gas-phase PAHs are the key particle precursors, but their kinetics are not as well defined [23], [25], [26], [38], [40]–[45]; section 1.3 discusses the chemical pathways of PAH evolution, rate constants for the pathways, experimental evidence, and modeling of PAH formation and growth in flames.

1.2 Particle Inception

Particle inception mechanisms are complex, involve both chemical and physical growth mechanisms [25], and may have a significant impact on the size and morphology of mature particles as measured in experiments [46]. Little is known about inception mechanisms because experiments expose limited aspects of the overall process due to varying conditions and rapidity in which particle inception occurs.

While many experiments have measured particles with diameters from 1.5 nm to 5 nm [47]–[59] and provided valuable insights about particle size distributions such as bimodality in flames [52], [57], they provide limited insights as to the chemical composition, molecular structure, or mechanism of inception of the particles. However, as discussed by Michelsen [39], the collection of experiments [47], [60]–[67] suggests two important concepts: 1) there is significant evidence that nascent particulates have both aromatic and aliphatic characteristics [68]–[72] and contain oxygen [68], [69], [72]–[83], and 2) there are two types of particulates – ordered and disordered. Ordered particulates tend to be greater than 3 nm in diameter [26], [47], [66], [84]–[88] and comprise aromatic content stacked and held together [56], [58], [67], [88]–[90] by van der Waals forces [67]. Figure 1.2 shows a representation of an ordered particle consisting of a set of pericondensed planar aromatic molecules stacked together in an orderly fashion. Disordered particulates tend to be less than 3 nm in diameter [47], [60]–[63], [65], [66] and comprise randomly ordered aromatic-aliphatic structures [60], [61], [65], [67]. Figure 1.3 represents this type of nascent particle; the structure is not ordered and consists of a seemingly random set of aromatic molecules that have either physically bonded or chemically bonded. The chemical composition and morphology of the constituents of the particle are difficult to ascertain.

The process of nanoparticle formation starts with the decomposition and oxidation of the fuel [24], [91]–[93]. The chemical initiation of combustion generates small radical species, e.g. hydrogen, oxygen, hydroxyl, propargyl, and acetylene. The radicals contribute to the formation of single ring aromatics and PAHs which, despite the lack of detailed knowledge about their chemical composition and morphologies, are known to be key precursors to nanoparticles [24]–[26], [29], [93], [94]. These larger polycyclic aromatic species eventually undergo a process to create solid-phase particulates known as nucleation (or inception) [39]. Therefore, knowledge of the composition and morphologies of the larger PAHs is integral to understanding the particle formation process. These small particles then aggregate to form larger particles such as soot which then continue to grow via chemical and physical reactions.

The process of creating particulates stretches across both large time scales and large size scales. In this process the main knowledge gaps are regarding the composition of PAHs and how they initiate particle inception. This process is complex, fast, has significant influence on particle size distributions, and is difficult to elucidate because of the experimental challenges of measuring these transitory phases of the process. As such, it has been necessary to develop models to describe the process from gas-phase aromatics to particles.

1.2.1 Modeling Particle Inception and Growth

The dominant theory for describing particle inception in models revolves around PAH-PAH dimerization as depicted in Figure 1.4 that will create molecules large enough to initiate particle inception. Many have assumed for the sake of simplicity that pyrene-pyrene dimerization is the starting point for particle inception [95]–[98] despite the fact that some studies have suggested that pyrene-pyrene dimerization is unlikely to occur frequently at flame temperatures due to their relatively small size [99]–[103]. There is considerable debate about the molecular size required for two PAH molecules to be physically bound long enough to constitute particle nucleation. Miller [101] suggested that only PAHs larger than a mass of 800 amu need be considered for potential sticking in a dimerization reaction. However, Schuetz and Frenklach [104] found that pyrene dimers are stabilized by internal rotational and vibrational motion and thus have a long enough lifetime to enable further growth. Similarly it has been suggested that the binding energies of dimers with small masses can survive at flame temperatures [105]. However, recent experimental evidence [102] and computational calculations [99], [100], [103] demonstrated that pyrene dimers are not feasible and thus not a likely source of particle inception in flames. According to these studies, it is apparent that monomers would need to be larger than pyrene (by mass) in order to form stable dimers at flame temperatures.

Despite the evidence to the contrary, however, existing models for particle growth depend on the simplistic inception concepts and thus have many limitations. Many models, for example, assume particle inception occurs solely via irreversible dimerization of simple monomers [25], [28], [95]–[98], [106]. For example, Kraft and coworkers considered dimerization of pyrene as the method for particle inception in their stochastic particle growth model [46], [107], [108]. After the irreversible dimerization process, the 32 carbon particle then continues growth in the particle phase. However, this model is based on unrealistic assumptions – as discussed by Violi and others [99]–[103] – that all pyrene dimerization is not only feasible, but the dominant particle inception mechanism. Kraft later developed the PAH-PP model [109], [110], and though it expands its definition beyond pyrene, it still only considers planar pericondensed PAHs as precursors to particle formation. Similarly, though the recent Reversible PAH Clustering (RPC) model from Thomson and coworkers [111], [112] has made advancements by accounting for the inherent reversibility of such nucleation events, the model is still limited to pericondensed hydrocarbon species. However, precursor species comprise a much more complex and intricate set of molecules than simple pericondensed PAHs [113]. Therefore, it is necessary to investigate their chemical pathways in order to ascertain detailed knowledge of the composition and morphology of the precursor species.

1.3 Formation and Growth of Aromatic Precursors

Though it is well established that aromatic gas-phase species are involved in the particle nucleation process, there is less certainty about the structure, chemical composition, size of the particle precursor species, and the kinetic pathways that form them. The species are known to be at least partially aromatic in nature and evolve from single ring aromatic species to polycyclic structures [22], [23], [25], [29], as depicted in Figure 1.5. The chemistry of single ring aromatics formation is well established, but their evolution to polycyclic aromatic structures is not fully understood [25], [26], [114]. There are several proposed sets of kinetic pathways that describe the evolution of particle precursor species in combustion conditions.

1.3.1 Kinetic Growth Pathways

There are several proposed growth schemes for prescribing the manner in which particle precursor molecules kinetically evolve in combustion environments. Bittner and Howard [115] noted that in a low pressure laminar fuel-rich benzene-oxygen flame the concentration of high molecular weight aromatics is controlled by mole fractions of the low weight molecular aromatics such as benzene and toluene. They proposed three reaction schemes that might account for the evolution of phenyl radical to two-, three-, and four-ring PAHs. One such scheme is a three step process: 1) addition of acetylene to the radical carbon of phenyl, 2) a second bimolecular reaction where acetylene is added to the vinyl radical group, and 3) a unimolecular ring closure forming naphthalene, as depicted in Figure 1.6a. They showed that the enthalpies of reaction favor the formation of the stabilized naphthalene over decomposition back to phenyl and acetylene reactants. Another proposed reaction scheme involves the addition of vinylacetylene to a phenyl radical followed by a unimolecular ring closure reaction forming naphthalene. The enthalpies of reaction also favor the formation of the stabilized naphthalene over the phenyl and vinylacetylene reactants. The latter scheme yields a greater thermodynamic gain in enthalpy than the former, but the authors noted that the former scheme may account for more PAH formation than the latter because of the much greater abundance of acetylene in the flame. An additional scheme described pathways that created 3- and 4-ring aromatics from the chemical growth of naphthalene via methyl and acetylene addition. Methyl addition to naphthalene followed by hydrogen elimination and acetylene addition to the resulting methylene group would lead to 3-ring PAHs. A repetition of these steps could form 4-ring PAHs such as pyrene.

A few years later Frenklach and coworkers introduced the hydrogen-abstraction-C_2H_2-addition (HACA) growth scheme based on their experimental studies of the pyrolysis of acetylene, 1,3-butadiene, benzene, and ethylene in shock tubes [116], [117]. They concluded that the pathway proposed by Bittner and Howard – in which acetylene addition to phenyl is followed by acetylene addition to the vinyl radical chain and then ring closure – contributed only a minor portion of PAH growth to that pathway. Instead the more significant pathway proceeded as: 1) addition of acetylene to phenyl radical just like in the Bittner and Howard scheme, 2) ejection of H converting vinyl radical group to ethynyl group, 3) abstraction of a hydrogen atom on the neighboring ring carbon to the ethynyl chain, 4) addition of acetylene to the radical ring carbon, and 5) unimolecular ring closure to form naphthalene, as depicted in Figure 1.6b. This reaction pathway was three orders of magnitude faster than the pathway introduced by Bittner and Howard in the given conditions because the hydrogen abstraction rates were relatively fast in the H radical rich environment. The authors proposed that these pathways would continue in the same manner such that two-ring aromatics would grow larger and form stabilized three- and four-ring structures (phenanthrene and pyrene, respectively). Additionally, they proposed that the acetylene additions could occur on zig-zag sites and be proceeded by unimolecular ring closure to form five-member rings [116]. Results from atmospheric and higher pressure (up to 3.1 bar) shock tube pyrolysis experiments of 10 binary hydrocarbon mixtures (hydrogen-, allene-, and vinylacetylene-acetylene and acetylene-, allene-, vinylacetylene-, and 1,3-butadiene-benzene) suggested that the main factor affecting PAH production in the mixtures was the rate of acetylene-addition reactions to aromatics [118]. For example, the aromatic fuel mixtures had increased PAH production because the global rate of acetylene-addition to phenyl radicals increased. Subsequent studies in acetylene-oxygen shock tube experiments noted that the significant single-to-multiple-ring aromatic pathways were unchanged [119] in an oxidative environment. The fuel oxidation chemistry altered the initial decomposition of the fuel but did not alter the dominant PAH formation pathways. Frenklach, Warnatz, and Wang subsequently showed that the growth mechanism extends to low pressure premixed acetylene-oxygen and ethylene-oxygen flames [120]–[122] and that the addition of chlorine to hydrocarbon mixtures could increase PAH production because chlorine atoms increase the rate of hydrogen abstraction from aromatic carbon atoms [123], [124]. The concluding thoughts from Frenklach and coworkers were that: (a) the HACA scheme consisting of one irreversible step and two reversible steps is largely responsible for the formation and growth of particle precursors in pyrolysis and oxidation environments, and (b) at low temperatures the hydrogen abstraction reactions are rate limiting and at high temperatures the acetylene addition kinetics are rate limiting [40], [125]–[128]. As Dean noted, however, the kinetic rate coefficients for radical additions employed in the HACA scheme are several orders of magnitude greater than those usually observed for similar reactions [129]; while Wang and Frenklach later concluded that even if the rate constants were higher than expected, HACA pathways alone were not sufficient to explain all PAH growth [127], [130].

Thus, Frenklach and coworkers proposed additional growth pathways (that were complementary to the tenets of hydrogen abstraction and acetylene addition at the core of the HACA mechanism) in which hydrogen migration reactions and ring opening reactions played a key role [130], [131]. As depicted in Figure 1.7, the three pathways are induced or assisted by hydrogen atom migration reactions which quantum calculations of potential energies and transition state theory evaluation of reaction rates showed to be reasonable at combustion temperatures. The basics of the pathways involve hydrogen migration which facilitates opening of five-member rings and subsequent ring closure reactions to form six-member rings. A result of the reactions is increasing the amount of six-member rings on the edge of the PAH at the expense of five-member rings. This enables further growth via the HACA scheme which does not provide pathways for acetylene addition to five-member rings. Monte Carlo simulations to model aromatic-edge growth using the five→six member transformation pathways demonstrated that the rate limiting step is the β-scission of five-member rings after hydrogen migration [132]. The results of the simulations implied that five-member rings are constantly being formed on the graphene-like edge of PAHs, but they do not accumulate because they are converted to six-member rings. Further calculations of the energies of structures with edge five-member rings demonstrated that species where five-member rings were converted to six-member rings are relatively thermodynamically stable below 2500 K and can serve as nucleating sites for continued edge growth [133], [134].

Siegmann and Sattler proposed an alternative PAH growth pathway in laminar methane diffusion flames to explain the presence of compact pericondensed PAHs [135]. The growth scheme (depicted in Figure 1.8) does not involve any radical species but does involve acetylene addition closing bay sites on PAHs (a Diels-Alder adduct) followed by H_2 ejection to create a pericondensed structure with one additional ring to the reactant PAH. The authors introduced the growth mechanism as a way to account for the production of compact PAHs up to 788 amu ($C_{64}H_{20}$) in the methane flame. However, Mebel and coworkers noted in extensive *ab initio* studies that this growth scheme cannot compete with the HACA and ring migration schemes even at high temperatures due to the high reaction barriers and consequently low reaction rate constants [136].

Colket and Seery determined that the HACA mechanism alone was not fast enough to model the production of PAHs during the high temperature, high pressure pyrolysis of toluene in a shock tube [137]. They proposed additional PAH formation reactions involving odd-carbon species and resonantly stabilized benzyl radicals – the primary toluene radical – which proceeds as: 1) the combination of benzyl and propargyl radicals followed by rapid ring closure and H_2 loss that leads to naphthalene formation (Figure 1.9a), and 2) benzyl addition to toluene followed by a series of ring opening and closure reactions that leads to the formation of anthracene (Figure 1.9b). These proposed pathways were significant to 2- and 3-ring PAH production during toluene pyrolysis because of the great abundance of benzyl, which was the primary species created during toluene decomposition in the experimental conditions. In conditions without such an abundance of toluene and benzyl, the pathways are not necessarily as significant to the production of PAHs.

Marinov and coworkers studied PAHs in atmospheric pressure laminar premixed, rich, sooting, n-butane-, ethylene-, methane-, and ethane-oxygen flames and concluded that the rate constants for the previously proposed HACA pathways calculated from first principles by Wang and Frenklach [126] were not fast enough to account for the abundance of high-mass aromatics they observed [138]–[140]. Similar to the recommendations of Colket and Seery, Marinov and coworkers proposed pathways for the formation of polycyclic aromatics that involve the combination of radical species.

The authors noted that self-combination of cyclopentadienyl radicals through a series of ring openings and ring closures leading to the formation of naphthalene ($C_5H_5 + C_5H_5 \rightarrow C_{10}H_8 + 2H$ depicted in Figure 1.10a) accounted for the generation of polycyclic aromatics in great enough quantity to account for the amount of large aromatics generated in the flames. Quantum chemical calculations carried out to determine the thermochemical properties of the intermediates and transition states of the reaction pathway showed the feasibility of cyclopentadienyl combination is due to the low reaction barriers and mobility of hydrogen atoms in the cyclopentadienyl moiety [141]. This fused-ring PAH formation scheme was extended to phenanthrene formation via combination of indenyl and cyclopentadienyl radicals ($C_9H_7 + C_5H_5 \rightarrow C_{14}H_{10} + 2H$ in Figure 1.10b) because the HACA mechanism of sequential acetylene addition to naphthalene did not produce significant amounts of phenanthrene in the flames. However, the authors noted that combination of larger PAHs containing a shared C_5 side structure was not likely to be a significant growth pathway because of the high energy barrier associated with destroying the aromaticity in both reactant molecules necessary to form a larger fused-ring structure.

This survey yielded a considerable number of proposed kinetic growth pathways for PAHs in flames. However, the pathways are considered only as solutions to specific PAH structures observed in specific experiments rather than as part of larger set of kinetics. Each study focused on the ascertaining or hypothesizing about the dominant growth pathways that yield the formation of particular PAH species, while neglecting to consider how the pathway participates amongst others.

1.3.2 Kinetic Reaction Rate Constants

Wang and Frenklach [126], [127] employed Rice–Ramsperger–Kassel–Marcus (RRKM) rate theory calculations in the first attempt to assign rate constants to HACA reactions based specifically on the phenyl-C_2H + C_2H_2 reaction relevant to the growth scheme. The rate constant was comparable to other radical-radical reactions for smaller hydrocarbons in flames. However, the reaction pathway analysis neglected to consider a complex set of pathways also available to the reactant and intermediate species. Thus, Kislov, Mebel, and coworkers performed extensive density functional *ab initio* calculations in an effort to elucidate the potential energy surfaces of two-ring PAHs and develop reaction rate constants for relevant HACA reactions [142]–[144]. Their first significant contribution was to demonstrate that acetylene-addition reactions have relatively low barriers and high exothermicity at high temperatures, in support of HACA pathways [145]. Bittner-Howard and HACA pathways for naphthalene and phenanthrene formation were shown to have appreciably lower barriers and higher reaction rate constants than corresponding Diels-Adler pathways [136] at high temperatures. Experiments in which crossed molecular beams are used to ascertain product species in a high temperature chemical reactor supported the branching ratios given by the calculations, namely that naphthalene was formed at a 70% probability for the phenyl-C_2H_2 + C_2H_2 reaction complex.

Furthermore, Mebel and Kislov showed that ring fusing of cyclopentadienyl radicals is a favorable at temperatures below 1000K to form naphthalene, but does not compete with HACA pathways at higher temperatures [144]. Experiments by Popov [146] and *ab initio* and RRKM/ master equation (ME) calculations by Cavallotti and coworkers

[147]–[149] have provided similar results; though there is an effective route for naphthalene formation from cyclopentadienyl self-combination, the reaction is more likely to favor indene formation than naphthalene formation at higher flame temperatures. Indene formation was also shown to be favored in the event of propargyl and propylene addition to phenyl radicals in 1200-2000K conditions [143], [150]. However, Mebel and Klippenstein demonstrated that the conversion of indene to naphthalene was feasible above 1500K in environments with high methyl radical concentration [151].

Recently, RRKM/ME calculations from Kislov, Mebel, and Klippenstein revealed three noteworthy concepts: 1) in contrast to the generally accepted view assumed with the HACA mechanism, naphthalene + acetylene produces mostly cyclopentafused three-ring PAHs instead of PAHs with six-member rings only in the 1000-2000K temperature range [152], 2) there is likely to be a strong pressure dependence for HACA reactions below 2000K [153], and 3) early ab initio and RRKM efforts to calculate reaction rate constants for HACA pathways, e.g. Wang and Frenklach [126], yield rate constants that are orders of magnitude different from what current calculations yield [154]. Specifically, the authors warn against using low pressure flame studies to validate PAH mechanisms for broader ranges of pressure and caution against relying on decades-old rate calculations because current quantum methodologies are more accurate. Accurate and reliable rate constants prove useful to model PAH growth in flames as a complement to experiment. Simulations can only be as reliable as the kinetic pathways and their rates that describe the expected formation and growth of PAHs.

1.3.3 Deterministic Modeling of PAH Formation and Growth

Computational models of aromatic formation and growth of polycyclic aromatic content complement experiments and provide predictive and descriptive capabilities beyond those provided by experiments. The most common method to model chemical evolution of PAHs in flames is deterministic simulation of gas-phase chemical kinetics. This method involves modeling the interconnecting system of gas-phase species as a set of coupled ordinary differential equations. The initial, intermediate, and product species are required to be known as well as the chemical connectivity among all the species. The deterministic mechanism is developed by compiling all the relevant chemical reactions for each species and the associated reaction rate constants, which serve as the differential equations to be solved in parallel. Deterministic mechanisms are often utilized in combustion simulators, e.g. CHEMKIN [155], that solve the set of differential equations in discreet time steps to simulate the chemical evolution of gas-phase species in combustion environments. Deterministic mechanisms for PAH growth require describing the chemical evolution pathways of each structure present in the model, which is increasingly difficult to do when defining PAHs because of the sheer number of potential reaction pathways and morphologies. However, several such mechanisms have been developed that describe, in part, the kinetic pathways of PAH evolution.

Wang and Frenklach [122], [127] integrated the HACA pathways into a deterministic kinetic mechanism and simulated the chemistry of laminar premixed low pressure acetylene-oxygen flames [120], [156] and atmospheric pressure ethylene-air flames [157]. In the mechanism HACA pathways prescribe all PAH growth starting from benzene up to pyrene, which is the largest simulated gas-phase PAH produced in the flames – pyrene is assumed to be the species which initiates nucleation of particles. Reaction rate constants describing fuel decomposition and benzene formation are taken from those introduced by Westmoreland et al [156]. While the mass growth of PAHs up to pyrene was reasonably well described in the 90 torr acetylene flame by HACA reactions, PAHs in the atmospheric flames were less well described. The authors note the importance of thermochemical information (reverse reaction rate constants are not explicitly prescribed but calculated using the equilibrium constant) but do not suggest why PAHs are predicted well only in one low pressure flame. Appel et al. updated the mechanism by including hydrogen and ring migration pathways in addition to HACA pathways; they modeled the chemical growth in nine premixed laminar acetylene, ethylene, and ethane flames [95]. Over the range of flames modeled, there is reasonable (within a factor of 10) matching of the concentrations of two- to four-ring aromatics. However, artificial temperature adjustments were required, which suggests that some PAH growth pathways were unaccounted for.

Chung and coworkers performed several investigations regarding PAH formation in counterflow diffusion flames with mixtures of aliphatic fuels (methane, ethane, ethylene, propane, and propene) and concluded that HACA pathways alone are insufficient in describing PAH production and that odd-carbon chemistry may play a significant role [158]–[161]. To that end, Chung and coworkers developed a kinetic mechanism that utilizes HACA pathways and the odd-carbon pathways of Colket and Seery for formation of PAHs up to coronene. In a set of counterflow diffusion flames with varying fuels (methane, ethane, ethylene, propane, n-heptane, iso-octane, and toluene) the mechanism matched concentration profiles of naphthalene, phenanthrene, and pyrene within a factor of ten.

Pitsch and coworkers [162] developed a deterministic mechanism that included PAH growth up to a five-ring aromatic structure via 4 growth schemes: 1) HACA [125], [136], 2) vinylacetylene addition to aromatic radicals [163], 3) odd-carbon growth via propargyl addition to substituted aromatics [34], [35], [138]–[140], [164], and 4) ring fusing of cyclopentadienyl radicals to form naphthalene and cyclopentadienyl + indene to form phenanthrene [164]. The mechanism was used to model laminar premixed (n-heptane and iso-octane) and diffusion (acetylene and n-heptane) flames with an emphasis on validating the concentration profiles of acetylene, allene, propyne, and benzene. The growth schemes for PAHs are more exhaustive than previous deterministic mechanisms, yet the authors do not report comparisons of the model to experiments for polycyclic species. Even though PAHs with more than three rings are generated only with HACA pathways, it would be interesting if the competition amongst growth pathways affects the production of naphthalene, which all four growth schemes could generate.

Westbrook and coworkers developed a deterministic mechanism to describe the chemistry of up to four-ring PAHs in laminar premixed atmospheric ethylene- and n-butane-oxygen flames that utilized cyclopentadienyl ring fusing pathways and propargyl addition pathways [138]–[140]. Simulations of the n-butane flame under-predicted the amount of two- to four-ring PAHs at low heights above the burner. Additionally, the model predicted a lower concentration of pyrene than anthracene but the experiments demonstrated the opposite trend. Simulations of the ethylene flame also did not capture the concentration profiles of two- to four-ring aromatics within a factor of five consistently with respect to distance from the burner. The mechanism under-predicted the amount of indene, naphthalene, and phenanthrene by a factor of 10-20 at low heights above burner. The mechanism captured the concentrations of benzene, styrene, and ethylbenzene much more accurately, hinting that the set of PAH growth pathways needed to be broadened.

Slavinskaya and Frank developed a mechanism to describe the formation of PAHs up to five rings in methane and ethane flames utilizing odd-carbon chemistry of mono-substituted aromatics and propargyl addition to form two-ring structures [165]. The formation of three- to five-ring structures was described through the HACA sequence. Indene and naphthalene were captured within a factor of 10 while larger PAHs were captured within a factor of five in the methane flame. The authors noted the lack of reliable thermo kinetic data for larger aromatic structures inhibits the construction of a mechanism with a low level of uncertainty. Thomson and coworkers [166], [167] extended the mechanism to include hydrogen and ring migration and cyclopentadienyl combination for modeling laminar ethylene [168] and ethane [169] diffusion flames from Senkan. The mechanism captured the concentration of phenanthrene, pyrene, and benzo(a)pyrene within a factor of five, which is considerably better than the mechanism from Appel et al. [95] which relies only on HACA pathways and under-predicted the same species by three orders of magnitude as well as the mechanism from Marinov et al. [140] which relies on ring fusing reactions for polyaromatic formation and under-predicted by a similar amount.

Violi, D’Anna, and coworkers developed a kinetic mechanism to describe the formation of PAHs up to three rings in premixed acetylene and ethylene flames [170],

[171]. The mechanism utilizes resonantly stabilized radical (RSR) pathways, namely, cyclopentadienyl combination and propargyl addition to benzyl to form two-ring aromatics and cyclopentadienyl plus indene combination as well as propargyl addition to form three-ring PAHs [137], [139], [172]. The authors found that in very fuel rich environments, the corresponding HACA model predicts similar formation rates of two- and three-ring aromatics, but in slightly fuel rich (equivalence ration of 1.5) conditions the HACA model predicts significantly slower PAH formation rates than their RSR model and under-predicts aromatic concentrations by more than an order of magnitude. This indicates that HACA pathways may control formation of polycyclic aromatics in very oxygen-poor environments and RSR pathways may control formation of polycyclic aromatics in oxidative environments [173], [174].

This survey of deterministic kinetic mechanisms describing the formation and growth of pericondensed aromatics up to five rings reveals that no one set of pathways accounts for PAH formation. Fuel, temperature, and environmental conditions have varying effects on different pathways. Furthermore, the deterministic mechanisms focused on the formation of aromatics with only a few rings because it is intractable and improbable to explicitly specify every potential reaction as PAHs grow in size and variability. For example, HACA pathways are extendable only to very specific larger PAHs (pericondensed entirely aromatic structures) and it is still unyieldingly complex due to the number of species possible for say, five or more rings. It is apparent, however, that all the chemical pathways utilized in various deterministic mechanisms are relevant to PAH growth in flames. Yet, it is necessary to also include other pathways that describe the formation of non-pericondensed structures with aliphatic content chains, and other atomic constituents in order to appropriately capture the breadth of gas-phase aromatic content in flames.

1.3.4 Stochastic Modeling of PAH Formation and Growth

The effectiveness of using deterministic methods to model PAH kinetics is limited because it requires that we develop a list of reactions that describe the potential kinetic pathways for all species that may be present in the environment. Usually mechanisms are compiled by relying on chemical intuition and experience, but it is increasingly difficult to be confident in the mechanisms as the complexity of the system increases because it is increasingly difficult to explicitly specify all of the pathways. PAH growth is a large and complex kinetic system because of the vast set of unique isomers and the exponentially expanding number of species that are generated as molecule size increases. To counter these drawbacks, Violi and coworkers developed a code to model PAH growth in high temperature environments that does not rely on deterministic kinetic mechanisms.

Violi and coworkers developed a unique code to model PAH growth named the fully integrated kinetic Monte Carlo/Molecular Dynamics (KMC/MD) which utilized both simulation procedures to capture the molecular level configuration of evolving precursors during large time scales [175], [176]. This code was updated and renamed atomistic model for particle inception (AMPI) and utilized to model particle growth in premixed aliphatic and aromatic flames [177]–[179].

Molecular dynamics (MD) techniques were employed to resolve the actual temporal dynamic resolution of a precursor molecule. Kinetic Monte Carlo (kMC) techniques developed by Gillespie [180], [181] were employed to account for the infeasibility of molecular dynamics to be employed for the milliseconds timescale of particle formation in flames. A simulation is not a collection of molecules that evolve simultaneously but rather tracking the evolution of a single target molecule. In a simulation, an aromatic seed molecule is placed in a gas-phase environment typical during combustion scenarios (as input, the local gas-phase species concentrations and temperature are defined). A list of possible kMC events, i.e. kinetic reactions, is provided as user input to the code. A kinetic reaction is not a specific reaction between two defined species like in a deterministic model. Instead, the target molecule is defined as comprising a series of sites. A site, e.g. an aromatic carbon atom, is available to a set of reaction types, e.g. hydrogen abstraction. A reaction is selected from the list and the site on the target molecule is modified according to the reaction type, e.g. carbon become radical after loss of hydrogen. For each kMC step the event (kinetic reaction) is randomly chosen according to a probability defined by the rate constant assigned to each reaction, i.e. the probability a reaction is selected is equal to its rate relative to the sum of the rates of all possible reactions. The MD module of the code serves to equilibrate the structure modified during the kMC step. The code alternates between kMC and MD steps and defines the time step size for each cycle in proportion to the sum of rates.

A code called the Stochastic Nanoparticle Simulator (SNAPS) was developed by Violi that is based on the established kMC philosophy of AMPI but does not utilize the separate MD module for structural equilibration [182]. Rather, an open source cheminformatics toolbox, Open Babel [183], was utilized to relax the structural conformations with much less computational cost than the MD module used in AMPI. Similar to AMPI, SNAPS requires as inputs a list of elementary chemical reaction types and a set of environmental conditions such as pressure, temperature, and relative concentrations of a select set of gas-phase compounds. Like AMPI, SNAPS utilizes kMC algorithms [184], [180], [181], [185] because of their computational efficiency and ability to model multi-scale phenomena, the latter of which allows the code to simultaneously resolve picosecond kinetic reactions and millisecond transport phenomena in the flame. SNAPS focused on elementary chemical reactions for particle precursors as seed molecules evolve temporally given time-dependent environmental conditions. Recent studies demonstrated the efficacy of SNAPS to model PAH growth in premixed flames and exhibited the software’s ability to describe the formation of a wide variety of precursor species [182], [186].

Kraft and coworkers developed the kinetic Monte Carlo-aromatic site model (KMC-ARS) in which HACA pathways are utilized to grow planar pericondensed PAHs using similar kMC techniques presented with AMPI [187], [188]. KMC-ARS focuses on defining reaction sites on the surface of PAHs – zig-zag, armchair, bay, free-edge (see Figure 1.11 for site descriptions) – and implementing reactions specific to each site type that result in adding pericondensed rings to the surface of the PAH. The code only accounts for the creation of five- and six-member aromatic rings. A subsequent update of KMC-ARS included so-called ring capping reactions in which five-member rings are formed on zig-zag sites that can induce curvature in the structure [189], a reaction Kislov and Mebel showed to be favorable at 1000-2000K temperatures [152]. Despite recent updates, there still exists a lack of reactions in the modeling codes that explore more complex kinetic growth pathways; the set of precursor species is more involved than pericondensed PAHs.

SNAPS shows the most promise as a code to model the formation and growth of PAHs due to its adaptability and ability to be expanded and modified. Furthermore, as new kinetic pathways are introduced or kinetic rates updated, the code can be altered to accept the updated information. Additionally, only SNAPS is able to accommodate simulations as one desires more accurate and reliable modeling of complex PAH systems comprising structures with a wide range of sizes up to thousands of amu. SNAPS has shown the unique ability to predict a great variety of morphological aspects of PAHs and capture their atomic level fidelity.

1.4 Composition of Particle Precursors

Despite the focus on pericondensed PAHs since the introduction of Bittner-Howard and HACA pathways, results from recent experiments suggest that the set of precursor species are likely not all, or even mostly, pericondensed structures. For example, hydrogen:carbon (H:C) ratios for measured particles [190], [191] and PAHs [192]–[194] fall outside the H:C band in which the those structures reside. Homann and coworkers noticed the H:C ratios of large PAHs (250 to 600 amu) measured in low pressure benzene-oxygen premixed flame were higher than expected for those composed of condensed six-member rings [192]; they attributed the H:C ratios to H-rich PAHs resulting from aliphatic content. Separate studies led by Wang, Homann, and Michelsen yielded evidence that point toward the presence of aliphatic content embedded in PAH structures [70], [76], [193], [195], [196]. Together these strongly suggest that gas-phase particle precursors are not simply pericondensed aromatic structures, but rather a mix of aliphatic, aromatic, and unknown content. Computational studies have also contributed to the idea that the set of precursors are not composed exclusively of pericondensed six-member rings, instead suggesting an abundance of five-member rings and aliphatic side-chains [75], [100], [182], [186], [196], [197]. Furthermore, recent evidence suggests the presence of oxygenated content in particles and their precursors. Studies have observed the presence of oxygenated content embedded in small nascent nanoparticles [72], [77], [78] and in precursors PAHs [68], [198].

Oxygenated hydrocarbons produced during combustion can have a wide range of detrimental effects on human health, air quality, and regional and global climate. Oxygenated PAHs (OPAHs) are frequently found in the exhaust plumes of manufacturing processes, in nearby environment of combustion sources, and have been found in relatively high concentrations the atmosphere over various rural and metropolitan areas [199]–[205]. They come from a number of combustion sources [206] and are more mobile in the environment than PAHs due to their polarity, thus they are more likely to spread and dissolve into ground water [207], [208]. OPAHs are toxic, whether ingested or inhaled, and thus pose a considerable threat to human health [209]–[213], and they are considered to be among the key compounds in toxicity of particulate matter [214]. Of particular interest are furans, which are organic compounds that contain five-member rings with four carbon atoms and one oxygen atom. Furans are a high priority carcinogenic substance [209], [215] produced during biomass burning [216]–

[219] and combustion [220], [221]. Furan and its substituted structures have been shown to be kinetically linked [222], [223]. Furans released during combustion are often partitioned into particles and are found in ash from peat [219] and wood [217] burning and in secondary organic aerosols from hydrocarbon oxidation [224], [225]. Despite the presence of OPAHs, and specifically furans, formed during combustion, their presence in gas-phase precursors [68], [198], and their potential role in particle formation [72], [77], [78], there is no significant research into the role of oxygen in the growth mechanisms of particle precursors.

1.4.1 Oxygenated Precursors

Previous studies have shown that small PAHs in premixed and diffusion flames contain oxygenated content [68], [198] and that oxygenated species can be embedded in particles formed during flame synthesis [69], [76], [77], [79]–[83]. Functional groups that have been identified include alcohols/enols, furans, aldehydes, carbonyls, and ethers. Wang and coworkers detected oxygenated content in PAHs between 200 and 600 amu in jet fuel coflow diffusion flames [68]. Similarly, they found that there is an appreciable amount of ether and carbonyl content in small particles sampled in premixed ethylene-oxygen flames with varying maximum flame temperature [76], suggesting oxygen pathways are important to nanoparticles formation over a broad temperature range. X-ray photoelectron spectroscopy techniques have been used to detect oxygen content in nascent particles created during operation of internal combustion engines [79]–[81]. Oxygen atoms bound to organic species on the particle surface have been shown to greatly affect particle hygroscopicity [77] and the ability of particles to adsorb atmospheric water vapor and act as cloud-condensation or ice nuclei in the atmosphere. Particles emitted from combustors, such as diesel engines, are generally hydrophobic, and enhancements in hygroscopic particle emissions could have substantial indirect climate effects via their influence on cloud formation [19]. The effect of particulate emissions on cloud-nucleation is a major uncertainty in climate predictions [226]–[228].

Despite the recent evidence demonstrating the presence of oxygenated content in particles and their precursor molecules, there is not much in the way of modeling oxygenated PAHs. For example, of all the deterministic mechanisms that attempt to describe PAH growth, the current stochastic codes that model PAH growth [175]–[179], [182], [187]–[189], [229] or particle formation [46], [107]–[112], none account for the potential involvement of oxygen in the process with the exception of an updated version of AMPI by Chung and Violi [230]. The latter addresses the oxidation of large particles via ring reducing reactions; oxygen interaction results in abstraction of ring carbons and reduction of the size of particles. There are no pathways that create oxygenated functional groups like ethers and carbonyls observed in some experiments. Therefore, there is a need for an approach that accounts for oxygenation during the chemical growth process of particle precursors.

1.4.2 Influence of Oxygenated Fuels on Particle Precursors

Use of oxygenated components in fuel tends to reduce particulates in premixed flames by altering the flame temperatures and the combustion chemistry [19]. It has been observed in many laboratory scale experiments [231]–[235] that doping hydrocarbon flames with ethanol decreases the amount or size of particulates produced. The reasoning behind this seems to be tied to the decreased production of prototypical gas-phase particle precursors, namely single-ring aromatics (e.g. benzene) and small hydrocarbon building blocks (e.g. acetylene) because it is generally acknowledged that the creation of single-ring aromatic species is one of the rate limiting steps in PAH, and subsequently particulate, formation [26], [236]. Where oxygenate doping increased particulate production, it was proposed to be because the oxygen promoted methyl production which in turn promotes propargyl formation which in turn promotes benzene formation via propargyl self-combination reactions [31], [32], [36], [231]. What had not been specifically considered is that the differences in gas-phase environment are important for another reason: oxygenated particle precursors may spur or retard their chemical growth. Recent work has shown some evidence that oxygen concentrations can impact the volume of particulates and soot formed [237], that oxygenated fuels can alter the amount of particulate production [238], the chemical composition of nanoparticles [78], [239], and that PAHs ranging from one to several hundred atomic mass units (amu) are likely oxygenated in laminar premixed and counter-flow diffusion flames [240]–[243].

Several experiments have observed that adding excess oxygen to the flame system leads to an increase in particulates and soot [244]–[246]. The explanations offered in those works do not consider how oxygen itself could drive chemical growth, but rather they focus on how the excess oxygen leads to an increase in gas-phase acetylene or propargyl, which in turn could lead to greater particle production. However, there is a need to explore the effect of oxygenation and how that might spur further chemical growth of particle precursors, and in turn spur the formation of particles. This dissertation explores for the first time the kinetic pathways in which OPAHs are generated in flames and how they influence the production of particles.

1.5 Summary and Scope

Characterizing the growth, composition, and morphology of PAHs is an integral component of understanding particle formation. The present study investigates chemical growth pathways of particle precursors and provides evidence for the integral role that oxygen chemistry plays in the evolution of PAHs and the formation of particles in premixed flames. Specifically, despite the presence of OPAHs and their potential influence on particle formation, the environment, and human health, very little is known about their formation mechanisms. This dissertation work utilizes computational techniques to characterize the formation, chemical growth, and composition of OPAHs working towards elucidating the key processes involved in the evolution of particle precursors in premixed flames. It represents an important step toward elucidating the morphologies and kinetic growth pathways of OPAHs in addition to ascertaining the effects oxygenated fuels have on particle precursors and particle formation.

The first aim of this dissertation work was to develop kinetic pathways for particle precursor molecules that account for oxygen chemistry and to design a novel kinetic growth mechanism for particle precursors that includes the oxygen chemistry and conventional hydrocarbon chemistry. The mechanism comprises an intricate set of pathways incorporating previously proposed reaction schemes as well as those newly proposed in this work; the pathways are described by 70 elementary oxygenation and oxidation reactions. Where appropriate, reaction constants from analogous reactions were assigned to newly proposed oxygenation reactions. Eight important reaction rate constants for key pathways were calculated using first principle quantum and chemical kinetics methodologies. Rate constants for forward and reverse reactions were assigned independently; 16 reaction rate constants were calculated using thermodynamic properties and rate constant equilibriums.

The second aim was to modify the code base of a stochastic simulator to accommodate the newly designed mechanism and validate the model against deterministic models and experiments. The simulations conducted matched experimental data, e.g. mass spectra and chemical composition as determined from mass spectrometry, as well as deterministic simulations of small PAH profiles in premixed flames. Validation in a sooting benzene flame revealed that the newly designed oxygenation pathways play a dominant role in to the formation of large particle precursors; the results matched measured mass spectra profiles. Similarly, oxygenation pathways work synergistically with traditional hydrocarbon and HACA pathways; the pathways are intertwined and operate in parallel.

The third aim involved simulating kinetic evolution of PAHs in premixed ethylene and acetylene flames in an effort to predict the oxygenated compounds in the flame and help ascertain if they are present in particulates captured and analyzed *ex situ*. Simulations predict, for the first time, an abundance of OPAHs with oxygen embedded in the molecules and reveal their dominant kinetic formation pathways. Several oxygenated functional groups, including enols and ethers, are identified as being abundant in smaller molecules ranging from approximately 100 amu to 300 amu and serving as stepping stones to larger OPAHs up to 1000 amu that can contribute to particle formation.

The final aim focused on investing the effects of oxygenated fuels on particle production in premixed flames. Oxygenation pathways prove to be the key to differentiating between PAH growth in ethylene flames with and without ethanol doped fuel. Thus, only with the new reaction mechanism can simulations capture variance in rates of particle precursor formation which lead to variance in particle formation rate and particle sizes produced in the flames.

The major species predicted by simulations contrast with the commonly held assumptions of PAH growth; across aliphatic and aromatic flames and a broad range of C/O ratios, there is a significant presence of oxygenated compounds. Furthermore, the present work supports a prominent role of the HACA growth scheme while demonstrating the breadth of additional pathways involved in PAH evolution and highlighting the importance of oxygen chemistry on the evolution of particle precursors and impact on particle formation. This dissertation highlights previously unconsidered chemistry of PAHs and further informs the understanding of their growth and influence on particles in premixed flames, in particular that oxygen chemistry might play a significant role in the formation and growth of PAHs in flames. This work synthesized theoretical, computational, and experimental methods to motivate future investigations concerning the evolution of key molecular precursors and nanoparticle formation in combustion.

Figures

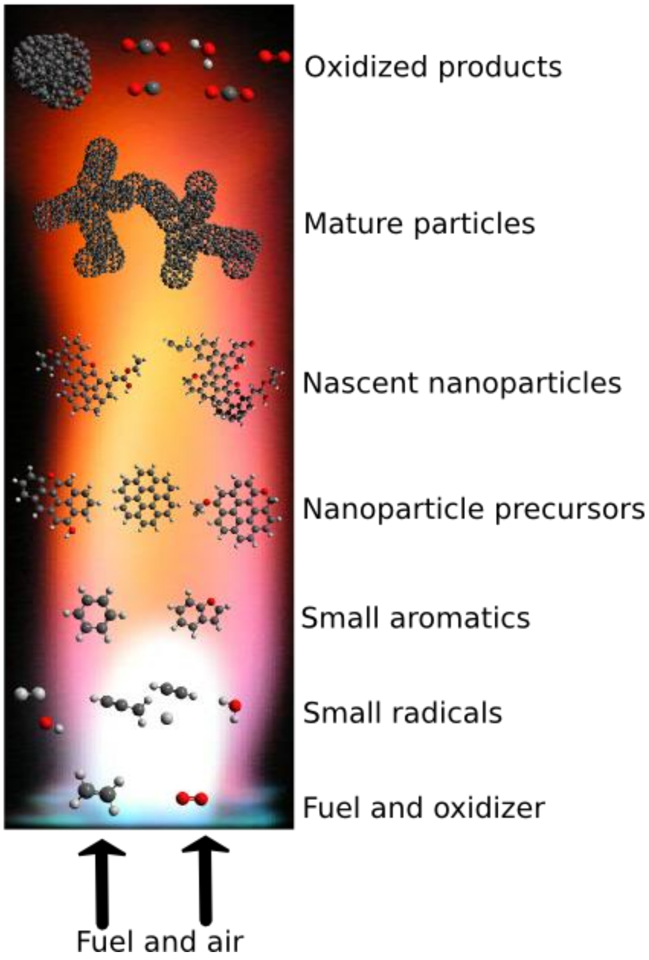
Oxidized products
Mature particles
Nascent nanoparticles
Nanoparticle precursors
Small aromatics
Small radicals
Fuel and oxidizer
Fuel and air

Figure 1.1: Schematic of particulate formation in flames – from fuel and oxidizer to small gas-phase molecules through PAH growth to large particulates and then oxidized products. The flame is a premixed flame where fuel and air flow from the bottom. As the flow of the gas proceed up through the flame the highlighted classes of species are likely to be found in that order with respect to flame height. Molecules and particles not shown to scale. Image concept adapted from reference [39].

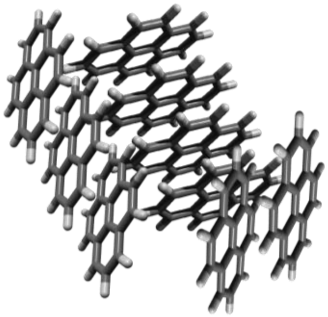

Figure 1.2: Potential representation of a nascent ordered nanoparticle. The particle is held together by Van der Waals forces and is formed when PAH dimers, trimers, and tetramers agglomerate which generates clusters of physically bound stable PAHs.

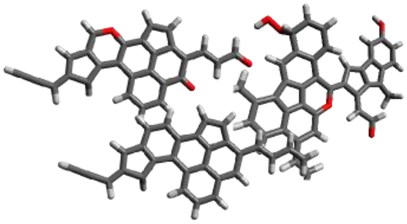

Figure 1.3: Potential representation of a nascent disordered nanoparticle. The particle contains aliphatic side-chains and several oxygenated functional groups including enols, furans, and peroxyls. The particle contains aliphatically-linked PAHs. The structures are randomly ordered and formed by processes that are not thermodynamically controlled.

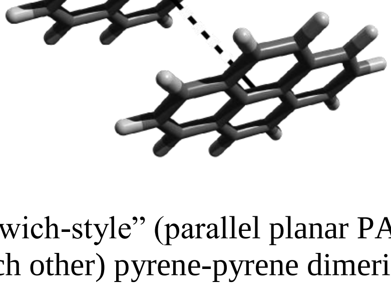

Figure 1.4: Representative “sandwich-style” (parallel planar PAHs whose centers of mass are in close proximity to each other) pyrene-pyrene dimerization: two pyrene monomers that are in near enough proximity to form a physical bond via Van der Waals attractive forces. One of the most common descriptions of particle inception includes the

formation of dimers like this. Dimerization of pyrene is often assumed to initiate particle inception despite the abundance of evidence that suggests that such a dimer is not stable or does not have a significant lifetime at flame temperatures.

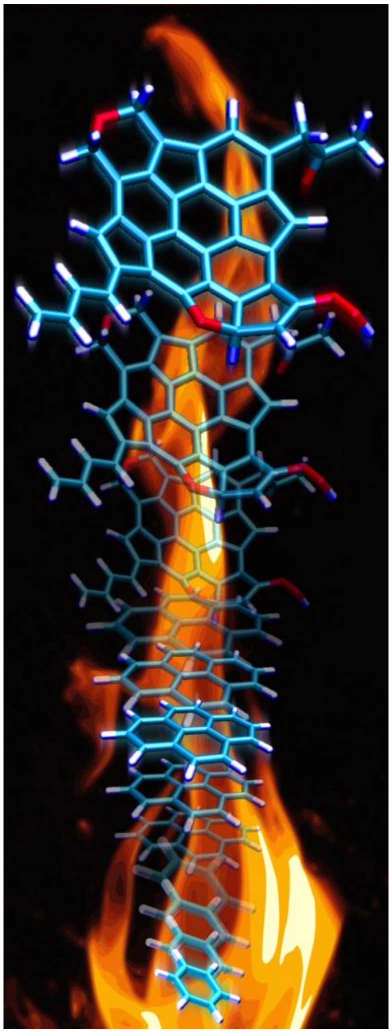

Figure 1.5: Pictorial of the formation of an oxygenated polycyclic aromatic hydrocarbon (OPAH) in a combustion environment. The evolution of particles and their precursors occurs in both time and space dependent on the bulk flow of the gas-phase environment.

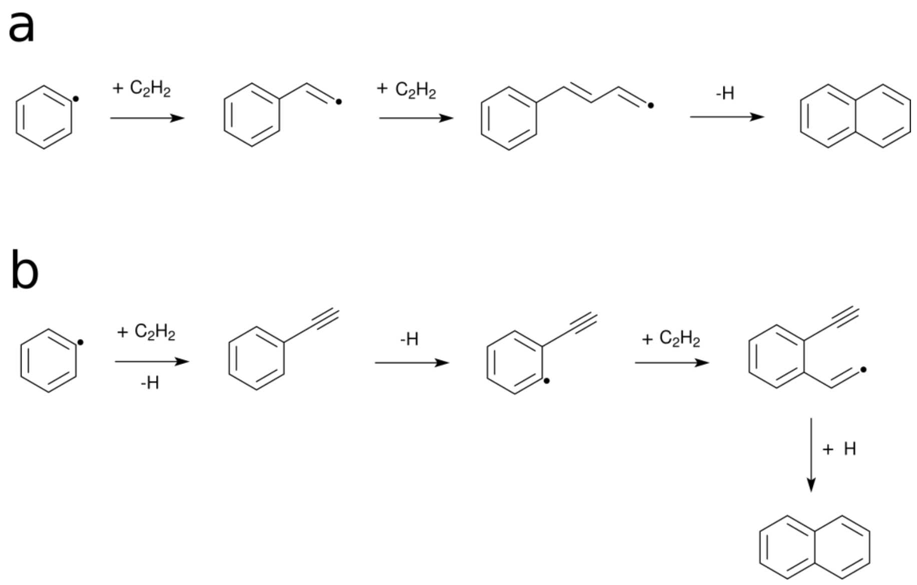
a
+ C2H2
+ C2H2
-H
b
+ C2H2
-H
-H
+ C2H2
+ H

Figure 1.6: Chemical formation schemes for the formation of naphthalene: (a) Bittner-Howard, (b) hydrogen-abstraction-C_2H_2-addition (HACA).

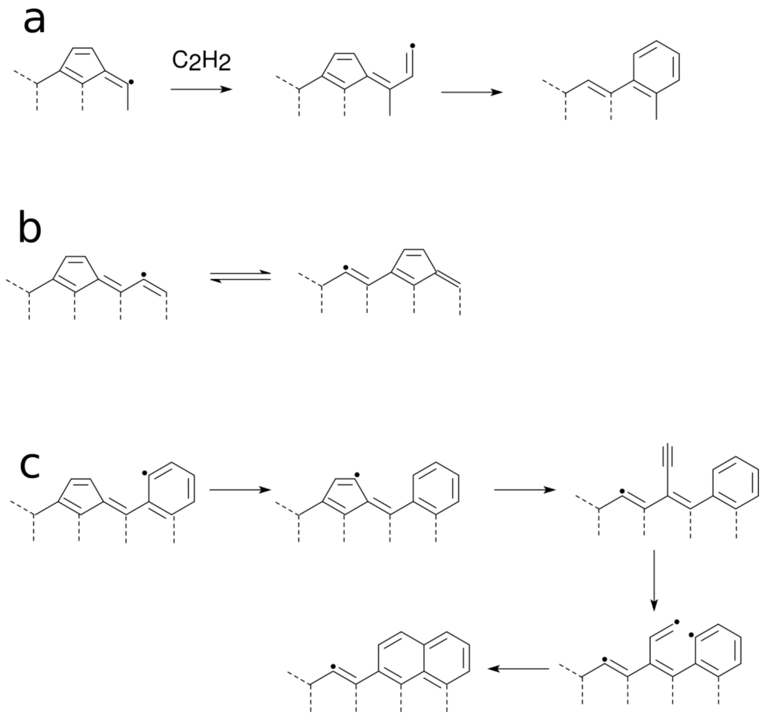

Figure 1.7: Hydrogen and ring migration pathways proposed by Frenklach et al. [130]

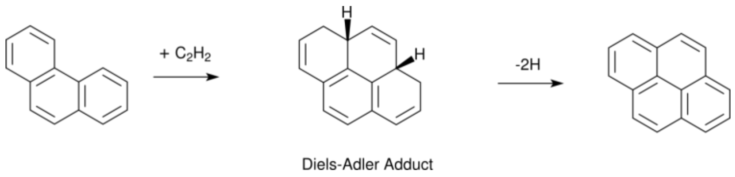

Figure 1.8: The Diels-Adler growth scheme proposed by Siegmann and Sattler that does not involve radical species.

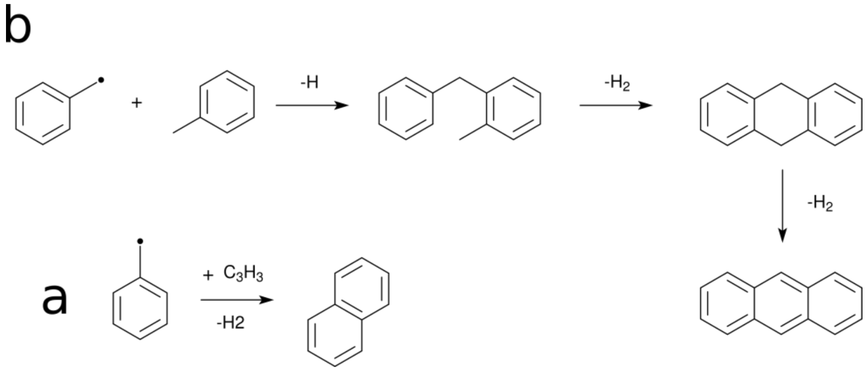

Figure 1.9: The resonantly stabilized radical (RSR) growth scheme proposed by Colket and Seery: (a) propargyl addition to benzyl yields naphthalene, (b) a growth scheme up to anthracene from toluene and benzyl. Ring closure reaction require hydrogen elimination.

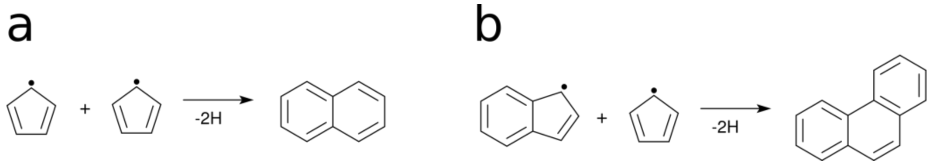

Figure 1.10: Ring fusing reactions presented by Marinov et al. in which naphthalene and phenanthrene are created via reactions between cyclopentadienyl and indenyl radicals.

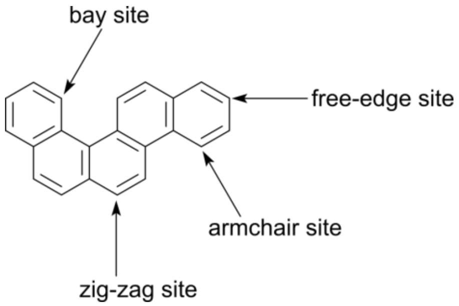
bay site
free-edge site
armchair site
zig-zag site

Figure 1.11: Definition of a free edge site and a zig-zag site on a PAH. In SNAPS the carbon sites are distinguished as unique from each other for certain reaction types, e.g. ring closures.

Chapter 2

Methodology

SNAPS [182] was greatly extended and improved in this work to expand its ability to model particle precursor growth and improve its predictive capabilities. SNAPS requires as inputs a set of chemical reactions, the growth/oxidation mechanism, a set of environmental conditions such as pressure, temperature, and concentrations of a select set of gas-phase compounds (obtained from modeling the flame as a laminar premixed flame in the CHEMKIN and PREMIX software suite [155], [247] using a deterministic kinetic mechanism), and a user-defined ‘seed’ molecule from which to initiate molecular evolution; SNAPS then simulates a single possible sequence of consecutive chemical reactions for that initial seed molecule. A single stochastic trajectory represents the potential chronological order of chemical reactions – or events in kMC algorithm terms – that the seed molecule could undergo while in the defined environment. Thus, a large ensemble of trajectories is needed in order to represent the statistically probable nature of particles in the flame. CHEMKIN is a deterministic differential equation solver used to solve complex gas-phase transport and kinetics problems. PREMIX is a code first developed by Reaction Design in 2000 for computing temperature and species profiles in steady-state premixed laminar flames; it models finite-rate chemical kinetics and multicomponent molecular transport of the flame. Together with the integration solver of CHEMKIN, the PREMIX module processes the chemical kinetics, and transport properties of the simulated flame in discrete time steps.

The SNAPS algorithm iteratively computes each successive chemical kinetic event with no 'memory' of what the previous states of the target particle were with a four step approach, as depicted in Figure 2.1: 1) build the list of available reactions (events) that can occur with an associated probability (rate) of it happening based on the conformation of the particle, the available reaction sites (section 2.3 contains descriptions of reactions sites) and the gas-phase environment; 2) select the reaction at random

i= r(rxn i)j=1nr(rxn j) , (1)

$$P(rxn\ i) = \frac{r(rxn\ i)}{\sum_{j=1}^{n} r(rxn\ j)}, \tag{1}$$

where reaction i is part of the set of reactions j to n, the denominator of the right side of the equation is k_{tot}, and n – the number of reactions possible at the given time step according to the available reaction sites – is less than or equal to total number of reactions in the mechanism; 3) test whether to accept or reject the choice by minimizing the structure and comparing the energy to the previous energy of the particle – if the reaction is rejected due to a large change in energy (indicating a reaction was implemented that forced the particle into an unrealistic conformation) then step 2 is repeated; 4) apply the changes to the particle, advance the time according to equation$\delta tkMC$= $\frac{-\ln(rand)}{k_{tot}}$,

(2)

$$\delta t_{kMC} = \frac{-\ln(rand)}{k_{tot}}, \tag{2}$$

where δt_{kMC} is the time advancement in seconds and *rand* is a random number in the range (0,1], then check if the simulation should be terminated because the total time is greater than the specified simulation end time. An ensemble of dozens of thousands of individual trajectory simulations nearly describes the macroscopic evolution of particle precursors because, in the limit of an infinite number of trajectories the results are equivalent to a deterministic solution.

Initially, the SNAPS growth mechanism consisted solely of elementary reactions that described the interaction of PAHs and gas-phase hydrocarbon molecules including growth through addition of methyl, acetylene, ethylene, ethyl, and propargyl. The HACA reaction mechanism [122] played the dominant role as reported in previous simulations [182], [186]. In addition, experimental mass spectra measured in diffusion [56], [58] and premixed [190], [192], [248], [249] flames exhibit dominant peaks separated by 12 or 24 amu (the mass of one or two carbons, respectively). Though the set of hydrocarbon reactions composing the mechanism was adequate to describe growth in specific atomic increments, it was not comprehensive. Recent work has suggested the presence of oxygen atoms in the chemical composition of PAHs and nanoparticles [77], [78], [230]. To include oxygen in SNAPS for the first time in this work required developing a kinetic growth scheme to include the addition of oxygenated groups via interactions with, amongst others, gas-phase O, O_2, OH, HO_2, H_2O_2, H_2O, CO, and CO_2 species; 70 reversible oxygenation/oxidation elementary reactions were implemented in the newly designed mechanism. Of these reactions, 80% fall into four broad categories: addition/removal of oxygenated groups to/from the target molecule, ether formation/destruction, oxygenated ring closures/openings, and oxidation. The newly created pathways accounted for reactions wherein oxygen atoms can be added to hydrocarbon species on the edge of the molecules as well as those where hydrocarbons can attach to oxyradical sites present on the molecule. Present are pathways that describe the formation of five- and six-member rings containing one oxygen atom due to their favored nature because of relatively lower ring strains. This methodology, as shown in the schematic in Figure 2.2, provides for the development of a mechanism that allows for incorporation of oxygen atoms on the edges of the molecule as well as embedding oxygen atoms in the molecule without favoring molecular growth over molecular reduction in any given stochastic event.

2.1 Developing Oxygenation Pathways

Having established the lack of oxygenation kinetics in current PAH growth and particle formation mechanisms, the first aim was to develop and establish a set of kinetic pathways that more comprehensively describe the PAH growth process. This was accomplished by defining the classes of reactions necessary to explain the interaction of PAH evolution and oxygen chemistry. The main classes of reactions are: (1) addition of oxygen atoms via bimolecular reactions with the set of oxygenated gas-phase species that are most prevalent during combustion, namely molecular oxygen, atomic oxygen radical, hydroxyl radical, water, hydroperoxyl radical , hydrogen peroxide, carbon monoxide, and carbon dioxide; (2) the removal, abstraction, or ejection of oxygenated functional groups, namely oxyradicals, alcohols, enols, peroxyls, hydroperoxyls, carbonyls, etc.; (3) the removal of carbon-oxygen groups like carboxylic acids, aldehydes, ketones, ketenes, ethers, esters, carbon dioxide and carbon monoxide; (4) saturation of oxyradicals and peroxy radical groups with bimolecular addition of hydrogen from the set of hydrogen containing species, i.e. hydrogen radical, molecular hydrogen, water, hydroxyl radical, hydroperoxyl radical, hydrogen peroxide, methyl, methane, ethylene, ethane, etc; (5) the bimolecular or unimolecular rejection or removal of hydrogen atoms from oxygen atoms thereby creating active oxygen sites; (6) the bimolecular addition of carbonated and oxygenated species to oxy radicals, e.g. methyl radical, acetylene, ethylene, ethyl radical, propargyl radical, benzene, phenyl, methylene radical, ethynyl radical, carbon monoxide, hydroxyl, hydroperoxyl radical etc.; (7) hydrogen transfers between two oxygen atoms as well as between an oxygen and carbon atom; (8) isomerizations of oxygenated groups, e.g. keto-enol tautomerization, aldehyde-ketone isomerization; (9) furan (5 membered ring with 4 carbon atoms and 1 oxygen atom) and pyran (6 membered ring with 5 carbon atoms and 1 oxygen atom) formations; (10) generic carbon-oxygen bond fragmentation; (11) pyranic to furanic ring manipulation in the style of ring migration present in the HACA mechanism; and (12) oxidation chemistry, namely the ejection or removal of carbon monoxide, carbon dioxide, molecular oxygen, oxyradicals, hydroxyl groups, and hydroperoxyl groups that result in reducing the size of rings of the particle. Every reaction implemented has an exact reverse reaction to ensure the reversibility of the evolution scheme. Table 2.1 lists the broad types of reaction classes that were implemented in the reaction scheme. The new intricate reaction scheme accounting for the oxygenation of precursors necessitated a term to encompass all structures, regardless of whether or not they are oxygenated, high mass aromatic molecules (HMAMs). In Table 2.2 is a brief example of specific reactions that fall into each class of reactions. The nomenclature of the reaction descriptions are such that $C_{ar}(*)$ is an aromatic carbon radical (an active site) and $C_{ar}(OH)$ represents a site where a hydroxyl group is bonded to an aromatic carbon (forming an enol). The set of newly proposed kinetic reactions forms the set of reaction pathways that will compose the PAH growth scheme. The main reaction pathways consist of adding oxygen atoms to PAHs (creating OPAHs), creation of active oxygen sites similar to active carbon sites, continued growth upon those active oxygen sites, embedding oxygen atoms into the core of the structure via ether formations and the construction of oxygenated rings, ring manipulation to promote growth, and oxidation to promote reduction of the PAH. Figure 2.3 demonstrates a few key oxygenation reaction classes that are significant to the performance of the model. The main reaction classes are exemplified with specific example reactions that represent the oxygen addition utility of active oxygen sites, embedding oxygen into the core of the PAH, creating stable oxygenated groups, and oxidation of the PAH. Figure 2.4 demonstrates the types of oxygenated functional groups that are constructed during the evolution of the particle precursor species in the model.

2.1.1 Reaction Rate Constant Development

After designing the oxygenation and oxidation reaction schemes I proceeded to develop specific reactions that would satisfy the chemical pathways; this also consisted of assigning reaction rate coefficients to each reaction type in the mechanism. Once a type of reaction was identified and included in the model – for example, a bimolecular reaction with gas-phase hydroxyl radical that results in the hydroxyl being added to an aromatic free edge carbon radical, as depicted in Figure 2.5 – a reaction rate coefficient needed to be assigned. Note that the same reaction is applied to a given type of reaction site, in this example any aromatic free edge carbon radical that resides in a 6-membered carbon ring, and thus one rate coefficient is applied when the algorithm executes the event no matter the size of the PAH or the morphologic aspects in other parts of the molecule. This aspect of the model makes it more realistic to describe the interconnected network of growth pathways without needing tens of thousands of reaction parameters in the mechanism, but the drawback is the use of one rate where, in reality, the rates are not identical for all PAHs. For example a single ring aromatic like phenyl has a different rate of hydroxyl addition than a larger aromatic like a pyrene radical. Thus it is important to carefully choose the value of the rate coefficient (i.e. the Arrhenius parameters) in order to best represent the range of reactant structures and corresponding reaction rates associated with each type of reaction site.

For example, for this reaction type I used the rate coefficient calculated with RRKM/ME theory for the naphthyl+O_2→naphthyl-peroxy reaction [250] rather than a rate for the similar phenyl+O_2→phenyl-peroxy reaction because the former will be more realistic for the majority of hydroxyl addition reactions in SNAPS trajectories. That is, the vast majority of the times this reaction will be called by the code the target molecule will have multiple rings, thus the naphthyl+O_2 rate constant is more appropriate in the SNAPS mechanism than the phenyl+O_2 rate. Of course, the rate constant used is not exactly accurate for every hydroxyl addition reaction that can occur in a simulation due to the different structures and sizes of the particles.

There certainly are implications with the approach to use one rate constant for a large number of similar reactions. The cost of a simpler mechanism that does not rely as heavily on chemical intuition and enables the code to explore unconventional chemical structures is paid by sacrificing some accuracy. If each reaction were explicitly described as in deterministic models, rate constants would vary between similar reactions like phenyl+O_2 vs. naphtyl+O_2. It would be difficult to quantify the impact of the approach used here because a corresponding deterministic mechanism to compare to would be impossibly large and complex to build. However, some tests are still possible, such as in this case, the naphthyl+O_2 rate coefficient as calculated by Kislov et al. [250] at 1 atm and 2000 K is 10.1% faster than the phenyl+O_2 rate coefficient – $2.29*10^{23}$ $cm^3mol^{-1}sec^{-1}$ compared to $2.08*10^{23}$ $cm^3mol^{-1}sec^{-1}$, respectively. As the size of the structure gets larger, the rate coefficient for O_2 addition to increases. Thus as target PAHs increase in size, the simulation under-predicts the oxygenation rate. However, this drawback is more than offset by the unique ability of the model to explore limitless configurations and provide insight into the dominant growth pathways and key compositions and conformations of PAHs. For the sake of estimation, let us assume the error in mass growth associated with this approach can be very roughly estimated by assuming all addition reaction rate constants increase 10% for each 64% increase in mass of the PAH (the ratio of rate constant increase and mass increase associated with phenyl and naphthyl reactants mentioned discussed above). Thus, as an example, the O_2 addition reaction rate constant to a PAH with mass 600 amu would be approximately 104% greater than the phenyl + O_2 rate constant, or roughly twice as much. Therefore SNAPS would be using a rate constant roughly half of what is expected for an O_2 addition to a PAH of 600 amu. The impact of this is that SNAPS underestimates the rate of mass growth of large PAHs in flames.

The reversibility of all the elementary reactions implemented in the reaction scheme is a key aspect of the mechanism. For new pathways developed that had applicable forward and reverse reaction rate constants previously reported, those were used in the model. However, for reactions in which a rate constant was reported for one direction only, it was necessary to calculate the rate constant for the opposite direction using the thermochemical information of the reactants and products of the reaction. In these cases CHEMRev software [251] was used to aid in calculating the backward rate constant for a given explicit reaction and forward rate constant. I compiled the thermodynamic NASA polynomials of the reactants and products to calculate the enthalpy and entropy of the reaction, which are then used to ascertain the Gibbs energy of the reaction, which is used to calculate the equilibrium constant; the reverse rate constant is directly proportional to the forward rate constant and inversely proportional to the equilibrium constant. CHEMRev aids in the process by calculating the constants at many temperatures and then fitting modified Arrhenius parameters to the set of reverse rate constants. The set of equations used to calculate the reverse rate constant given the NASA polynomials for each species in a reaction are listed in Table 2.3. Calculating reverse rate constants from the thermodynamic data of the reaction and the forward ensured that the mechanisms maintained thermodynamic consistency. Because the rate constants are general and not specific to each reaction, it was important that paired reactions had rate constants that were in equilibrium. Therefore, there would be no rate imbalance that would prevent an ensemble of simulations from approaching the thermodynamic limit.

The set of reaction types and pathways employed in the kinetic PAH growth model are listed in Table 2.4 and categorized according to class, e.g. hydrogen-abstraction, saturation, fragment addition or removal, isomerizations, oxidation, ring formations, etc. The table is color-organized by class of reaction and within each class the reactions are sorted in descending order of the reaction rate evaluated at 1750K. The reactions are sorted in descending order to easily capture the comparative value of competing reactions. 1750K was chosen to represent a relatively ubiquitous temperature in many combustion scenarios. Table 2.4 provides Arrhenius parameters for the reaction rate coefficients for all oxygenation reactions created in this work. Similarly, Table 2.5 comprises a list of reaction pictorials that visualize the reaction concepts for all new pathways categorized by class of reaction. The pictorials only show the part of the PAH that will undergo changes, the dashed lines signify that the PAH can be much larger and of any composition and overall structure as long as it contains the substructure highlighted in the pictorial. The appendix has corresponding tables that list all the reactions in the new mechanism and shows how the oxygenation and hydrocarbon pathways are interconnected.

One aspect of designing a more comprehensive PAH growth model was to compare the rate coefficients of oxygenation pathways to traditional hydrocarbon pathways. Figure 2.6 compares the rate coefficients of the entire set of bimolecular reactions at 1750K – the blue bars are hydrocarbon and the red oxygenation reactions. 1750K is chosen because temperatures within ±200 K of that temperature often are represented in SNAPS trajectories of premixed flames. Figure 2.7 is the equivalent for the set of unimolecular reactions. It is noteworthy that the magnitudes of the rate constants for oxygenation kinetics are similar to non-oxygenation kinetics. As will be discussed in subsequent chapters, this is an important aspect of the model because it rules out the possibility that inappropriately fast oxygen chemistry could be the cause for the finding that oxygenation pathways are key determinants of the growth pattern of PAHs. That is, the significant amount of oxygenation taking place during PAH growth is not caused by dominating kinetics of the oxygenation pathways.

2.2 Designing a Synergistic Growth Mechanism

It is important to note that the newly implemented oxygenation pathways interact in a synergistic manner with the traditional hydrocarbon pathways. A key to creating a chemical growth mechanism that describes the kinetic evolution of particle precursors was to integrate the oxygenation pathways with the previous hydrocarbon pathways such that the sets of pathways work in parallel; specifically, the oxygenation pathways work in tandem with the previous set rather than independently. This led to a growth scheme where oxygenation reactions compete with but do not dominate or exclude hydrocarbon reactions. When the new reactions compete with pervious reactions it creates a more comprehensive set of pathways that enables the particles to explore a much more vast set of compositions and conformations than any other model. Figure 2.8 displays a representative example of HACA and oxygenation pathways operating in parallel to create a web of pathways that can explore compositions and conformations not considered by the user, thus eliminating much of the chemical intuition necessary to create a deterministic mechanism attempting to describe the evolution of PAHs. In Figure 2.8 it is clear that the growth trajectory of the end PAH could comprise hydrocarbon and oxygenation reactions in several permutations. Additionally, the oxygenation pathways neither stunt nor disrupt the hydrocarbon pathways; they provide added avenues of hydrocarbon growth on top of active oxygen sites. This is a novel aspect of the mechanism; the scheme not incorporates the philosophy of conventional pathways with oxygenation pathways to enable the formation of OPAHs not previously considered in growth models.

The new kinetic growth scheme is a much more comprehensive mechanism to describe PAH growth than others previously proposed. One of the benefits of this is the introduction of so many new pathways, molecular configurations, and compositions that can be explored. For example, consider the growth of a two-ringed PAH to a three-ringed PAH, and let neither structure contain any side chains. Given a hydrocarbon-only model there are two main two-ringed PAH structures, indene and naphthalene. If we say naphthalene is the initial structure, then there are only a couple pathways that would describe the growth to a three-ringed PAH structure with no side-chains (where said structure maintains the two-ringed structure of naphthalene), of which there are six possible given the hydrocarbon-only growth scheme like HACA. Figure 2.9a shows those pathways and structures and is referenced here when discussing the comparison with the oxygenation/hydrocarbon model. In the set of pathways shown in Figure 2.9b the oxygenation scheme works synergistically with hydrocarbon growth scheme and leads to many multiples of potential growth pathways from naphthalene to a three-ringed structure. In the new model these pathways lead to one of the 15 possible configurations in which the original naphthalene backbone structure is not altered and the third ring is oxygenated. That plus the same six possible hydrocarbon configurations possible in the HACA model are 21 potential structures – all assuming the original naphthalene structure is not altered during the process of forming a three-ringed structure. For the purposes of clarification Figure 2.9 has been simplified, only the pathways that are initiated with the addition of carbon or oxygen to the zig-zag carbon are displayed. The oxygenation scheme not only covers all the pathways present in the hydrocarbon-only model but it layers oxygen chemistry on top, weaves oxygen reactions into the hydrocarbon pathways, and yields an intricate interaction of the two sets. The last level of reactions shown in Figure 2.9b is the oxidation step in which furanic and pyranic rings are converted to five-member and six-member aromatic rings which provides a mechanism to eliminate embedded oxygen atoms from the PAH and nanoparticles structures. Not only are there many more pathways, but the species are related by one simple oxidation step in the more comprehensive oxygen/hydrocarbon growth mechanism. In the example in Figure 2.9 there are numerous pathways for each end product (three-ringed, no side-chain structure with a naphthalene backbone), and there are six times as many products. Those multiplicative ratios increase as the scope of the pathways is broadened, such that there are thousands of additional pathways in the mechanism that yield the same hydrocarbon species, as well as the set of oxygenated structures not possible in traditional growth schemes.

The stochastic nature of the code enables an ensemble of trajectories to explore the vast array of pathways and configurations that could not be explored in a deterministic code because of the sheer number of reactions that would be needed as well as the immense chemical intuition required to design a mechanism that would explore all the configurations. The ability of the model to predict species not previously considered is shown in subsequent chapters. The growth pathways and kinetics were in part validated by comparing model predictions to experiments – species detected in experimental flames included key oxygenated and non-oxygenated species that the model predicted would be present.

2.3 Reaction Sites Description

One of the key features of the SNAPS code is the manner in which reactions are defined. Rather than define the entirety of a reactant(s) species and the resulting product(s) species as is traditional in deterministic kinetic mechanisms, the code defines a reaction site on the species. Reaction sites are specified in terms of properties including the atom type (e.g., aromatic carbon, aliphatic carbon, saturated oxygen, oxyradical), the bond type, and molecular connectivity (e.g., membership in ring(s) or a specific functional group). Reactions are defined in terms of these reaction sites and corresponding kinetic rate constants. As a clarifying example let us consider a bimolecular reaction between a phenyl radical (our target molecule) and a gas-phase hydroxyl radical resulting in a single product, phenol. In a traditional deterministic mechanism this exact reaction would be defined as $C_6H_5+OH \rightarrow C_6H_5OH$. Here the exact species are defined for all reactants and products. As a second example consider a bimolecular reaction between a naphthyl radical (our target molecule) and a gas-phase hydroxyl radical resulting in a single product, naphthol. In a traditional deterministic mechanism this exact reaction would be defined as $C_{10}H_7 + OH \rightarrow C_{10}H_7OH$. Again the exact species are defined for all reactants and products; thus for these two reactions there are five explicitly defined species.

In the model created in this work the reaction site definitions are handled differently. For the first example the target phenyl molecule would react with the gas-phase hydroxyl to form phenol, however the methodology doesn't define the reactant species as C_6H_5 but rather just notes the presence of a free edge aromatic carbon radical that is a constituent of a six-member carbon ring and is an active site available to bond with a gas-phase species in a bimolecular reaction. The hydroxyl is then attached to the active site. Using this reaction site definition enables the user to define the reaction in the second aforementioned example with the same reaction site – that is an active carbon site that is a member of an aromatic ring – even though the reactant species are different molecules. Note that many reaction sites are present and defined on a target molecule. The list of available events (reactions) that could possibly occur are those for which there is a reaction site defined that matches the expected reaction site of the reaction. For example in the case of the naphthyl radical, in addition to the hydroxyl addition reaction which occurred, there was a possibility that an oxidation reaction could have occurred. This reaction requires the defined reaction site of a six-member carbon ring with a radical in which gas-phase oxygen can attack and strip off a carbon in the ring leaving a five-member ring. Thus, the hydroxyl addition reaction and oxidation reaction were competing with each other.

Figure 2.5 portrays these two example reactions with blue highlights that are the defined reaction site (a ring of six aromatic carbons where a free edge carbon is unsaturated). The two reactant species have the same reaction site which is available for the same hydroxyl addition reaction. In the figure the dashed lines signal that anything can be bonded to those atoms; thus no matter how large a species is, if there is an aromatic ring on the edge of it the model will identify the radical carbon among the six carbons. A second example is depicted in Figure 2.10 where the reaction type is the closure of a four carbon, one oxygen ring on a zig-zag site. There are two distinct reactant species of different sizes, compositions, and overall structure, but the zig-zag site with an oxygenated side chain is common to both reactants; therefore the same reaction site is defined (in blue) on both reactants. A set of atoms in the highlighted configuration, namely, the three carbons of the zig-zag site and the –OC* chain are the defined reaction site for a furanic ring closure. Thus the reaction is executed the same way with both reactant species and only one reaction site need be defined. Again the structures can be of any size and conformation as long as they have the set of atoms at the edge of the molecule that fit the reaction site defined in blue in the figure. Using this type of site definition means I have to define one type of reaction for an unlimited number of conformations. There is one reaction in the code that can apply to any PAH which eliminates the need to design thousands of similar reactions with different specific reactant conformations. This is why a target molecule can explore a vast number of compositions and conformations and the amount of chemical intuition needed is reduced.

Figure 2.11 provides a target molecule with several types of reaction sites that the algorithm would recognize and use to define the set of potential reactions that are possible given the configuration. The blue circles on saturated carbons indicate those carbons are available for hydrogen abstraction/removal; dark blue are aromatic and light blue are aliphatic. The reaction sites distinguish between aromatic and aliphatic carbons because the rate coefficients for abstraction/removal reactions are significantly different. That is the rate of abstraction via interaction with gas-phase OH is appreciably different for an aromatic and aliphatic carbon and thus the site definitions are distinct. Additionally, the sites distinguish between types of carbon (primary, secondary, tertiary) for similar reasons. The red circles in Figure 2.11 highlight the radicals on the target molecule to which interactions with gas-phase species could result in saturation or other addition. The lower left is an oxyradical and has its set of reactions and accompanying rate coefficients very distinct from a carbon radical like in the top right. Again the reaction scheme distinguishes between aromatic and aliphatic carbons and amongst types of aliphatic carbons. The green circles are sites that are defined as available for ring opening reactions. At the top the reaction site would be a set of five carbons forming a ring at a zig-zag site. The highlighted ring on the bottom of the molecule is a pyran group whose reaction site is defined appropriately to distinguish it from other furan rings and carbon rings. Finally, the purple oval highlights a neighboring set of six carbon atoms that are available for a ring closing reaction. The last atom of the side-chain would form a bond with the ring atom to from a six-member aromatic ring. The molecule in Figure 2.11 represents a possible step in the growth trajectory of a PAH in SNAPS. For any given structure there are several types of reaction sites which are available to undergo a reaction of some type. There are usually several reactions that use the same reaction site, e.g. hydrogen abstraction could be carried out by one of several gas-phase species or one of several species could be absorbed onto a radical site. Thus at each step in the algorithm the molecule will change according to the possibilities given its current conformation.

The exact reaction that is executed in the code algorithm is randomly chosen based on a weighted probability of the reaction rate for the given conditions (temperature, pressure, concentration of gas-phase species in the case of bimolecular reactions.

2.4 SNAPS team

SNAPS is a collaborative code developed under the supervision of principle investigator Prof. Angela Violi at the University of Michigan. Principle authors and developers of the code are Jason Lai (2011-2014), Paolo Elvati (2011-2014), and this author (2014-2017). Table 2.6 lists descriptions of the roles of each author in the process of creating and maintaining the code.

2.5 Summary

The design, implementation, evaluation, validation, and results produced with the current work represent a significant advancement in the understanding of the formation and precursor growth mechanisms of combustion-generated particles. This work produced the first nanoparticles precursor chemical growth mechanism consisting of oxygenation pathways and is both novel and noteworthy because the mechanism includes the potential formation of oxygenated structures. The methodology generated a set of chemical pathways that account for the addition of oxygen onto PAHs structures, the formation of stable oxygenated structures, the embedding of oxygen into the core of the structures, and the oxidation of OPAHs and PAHs. A new set of pathways, listed in Table

2.4 and Table 2.5, created and implemented into a novel PAH reaction mechanism are weaved with conventional hydrocarbon pathways in a manner such that simulations can model particle precursors more comprehensively. The software SNAPS was appreciably modified in order to accommodate the novel reaction scheme developed and to account for the formation of complex structures, including OPAHs. The new code and kinetic scheme was utilized to model the evolution of particle precursors in premixed flames. The impact of the studies upon particle formation kinetics is considerable.

2.5.1 Contributions

- Recognized that oxygen chemistry is a major missing aspect of previous investigations into the production and growth of particle precursors in high temperature combustion environments
- Proposed novel kinetic pathways that might be relevant to PAH production in premixed flames in which oxygen plays a role
- Identified kinetic reactions relevant to PAH-oxygenate interaction as well as OPAH interactions with gas-phase environment typical of flames
- Evaluated kinetic rates known in literature to determine trustworthiness and reliability based on a comparisons where available and repeatability of experiments
- Determined with extensive benchmark testing the need for more accurate and reliable kinetic rates for the adsorption of hydrocarbon molecules onto oxyradical sites

- Used first principle techniques to generate energy surface of oxyradical + acetylene complex
- Use master equation techniques to compute kinetic reaction rates of the oxyradical + acetylene complex using the thermochemical data generated from ab initio calculations
- Designed and developed a novel kinetic mechanism describing detailed evolution pathways of PAHs and OPAHs in flames, and wrote it to be compatible with SNAPs software
- Extended, modified, and re-wrote SNAPS code to enable over 70 new elementary reactions, including those that oxygenate PAHs and form stable OPAHs
- All the work presented in this chapter is the sole work of this author

Tables

Table 2.1: The main classes of reaction pathways that the oxygenation kinetic growth mechanism comprises.

Number	Reaction class
A	Addition of oxygen atoms
B	Removal of oxygenated functional groups
C	Ejection of carbon-oxygen compounds
D	Saturation of active oxygen sties
E	Creation of oxyradicals
F	Addition of carbonated species to active oxygen sites
G	Hydrogen transfers between oxygen-oxygen and oxygen-carbon
H	Isomerization of oxygenated functional groups
I	Furan and pyran formation
J	Generic carbon-oxygen bond fragmentation
K	Oxygenated ring migration
L	Oxidation reactions

Table 2.2: Example reactions from each major class of oxygenation pathways in the SNAPS mechanism. (g) signifies a gas-phase molecule interacting with a HMAM, C_{ar} represents an aromatic carbon on the HMAM, C_{al} represents and aliphatic carbon on the HMAM, C with no subscript represents either type of carbon on the HMAM, X(Y) implies that atom(s) Y is bonded to atom X on the HMAM, $^{+}$ signifies that the rate was calculated from the forward rate using standard thermodynamic properties to calculate the equilibrium constant, and * implies a radical or active site. Units for pre-exponential factor A are s^{-1} for unimolecular reactions and $cm^{3}*s^{-1}*mol^{-1}$ for bimolecular reactions, units for Activation Energy (Ea) are $kcal*mol^{-1}$.

Class	Example reaction	A	N	Ea	Ref.
a	O(g) + $C_{ar} \rightarrow C_{ar}$(O)	7.06×10^{4}	1.03	–6.96	[230]
b	C_{ar}(O) $\rightarrow$ O(g) + C_{ar}	6.09×10^{9}	0.10	72.77	[230]$^{+}$
c	OH(g) + C_{ar}(O*) $\rightarrow$ C_{ar}(*) + HO_2	5.23×10^{16}	-0.66	62.35	[245]$^{+}$
d	OH(g) + C_{ar}(*)$\rightarrow$ C_{ar}(OH)	6.50×10^{14}	-0.85	-2.73	[252]
e	O_2(g) + C(*)$\rightarrow$ C_{ar} (O*) + O(g)	2.60×10^{13}	0.00	6.10	[252]
f	O(g) + C_{ar}(O*) $\rightarrow$ C_{ar}(*) + O_2(g)	2.21×10^{17}	-0.96	15.0	[230]$^{+}$
g	H(g) + C_{ar}(O) $\rightarrow$ C_{ar}(OH)	2.50×10^{14}	0.00	0.00	[252]
h	H(g) + C_{ar}(O) $\rightarrow$ C_{ar}(OH)	3.47×10^{29}	-4.30	102.3	[253]
i	C_{ar}(OH) $\rightarrow$ H(g) + C_{ar}(O)	8.95×10^{31}	-4.71	98.35	[253]$^{+}$
j	CH_3(g) + C_{ar} (O) $\rightarrow$ C_{ar} (OCH3)	1.21×10^{13}	0.0	0.00	[230]
k	C_2H_2(g) + C(O) $\rightarrow$ C(OC_2H_2)	3.20×10^{11}	0.00	0.20	[254]
l	C_{ar} (OCH_3) $\rightarrow$ CH_3(g) + C_{ar} (O)	1.21×10^{13}	0.0	0.00	[230]$^{+}$

m	$C_4O(*) \rightarrow C_4O + H*(g)$	2.65×10^{13}	0.15	17.36	[241]
n	$C_4O(*) \rightarrow C_4O + H*(g)$	2.90×10^{7}	1.70	8.16	[241]
o	$C_5O \rightarrow C_5(*) + CO(g)$	3.15×10^{7}	0.00	0.00	[250]

Table 2.3: The set of equations used to calculate the reverse rate constant given the forward constant, temperature, and NASA polynomials for each species in the reaction. This method was used several times at varying temperatures to calculate several reverse rates and then modified Arrhenius parameters were fit to the rates to derive parameters used in the SNAPS mechanism for reach reverse reaction. Note that coefficients $\{a_1 \ldots a_7\}$ are the appropriate coefficients from the NASA polynomial table for that particular species for the temperature at which the enthalpy and entropy are being evaluated.

$k_r = \frac{k_f}{K_{eq}}$	(1)
$K_{eq} = e^{\frac{-\Delta G_{rxn}}{RT}}$	(2)
$\Delta G_{rxn} = \Delta H_{rxn} - T\Delta S_{rxn}$	(3)
$\Delta H_{rxn} = H_{rxn}(T) - H_{rxn}(298K)$	(4)
$\Delta S_{rxn} = S_{rxn}(T) - S_{rxn}(298K)$	(5)
$H_{rxn}(T) = H_{products}(T) - H_{reactants}(T)$	(6)
$S_{rxn}(T) = S_{products}(T) - S_{reactants}(T)$	(7)
$H_{rxn}(298K) = H_{products}(298K) - H_{reactants}(298K)$	(8)
$S_{rxn}(298K) = S_{products}(298K) - S_{reactants}(298K)$	(9)
$H_{species}(T) = R(\frac{a_1}{1}T^1+\frac{a_2}{2}T^2+\frac{a_3}{3}T^3+\frac{a_4}{4}T^4+\frac{a_5}{5}T^5+a_6)$	(10)
$S_{species}(T) = R(a_1 \ln(T) + \frac{a_2}{1}T^1+\frac{a_3}{2}T^2+\frac{a_4}{3}T^3+\frac{a_5}{4}T^4+a_7)$	(11)

Table 2.4: List of all new oxygenation reactions in the mechanism. A listing of all reactions demonstrating how the oxygenation pathways are weaved into hydrocarbon pathways is give in Table A.6.1. Reactions are organized by class (color). The classes of reactions (in order top to bottom): light red are hydrogen removal/abstraction reactions; dark red are hydrogen addition reactions; dark orange are hydrogen transfer reactions; dark blue are fragment addition reactions; light blue are fragment removal/abstraction reactions; light green are ring closure reactions; dark green are ring opening reactions; tan are isomerization reactions; dark tan are oxidation reactions. Within each class (color) the reactions are ordered in descending reaction rate coefficient as evaluated at 1750 K (1750 K chosen to represent a median combustion temperature for a broad range of flame types/conditions). Notations for the “Reaction Description” column: (g) represents gas-phase molecule interacting with HMAM, C_{ar} represents and aromatic carbon on the HMAM, C_{al} represents and aliphatic carbon on the HMAM, C with no subscript

represents either type of carbon on the HMAM, X(Y) implies that atom(s) Y is bonded to atom X on the HMAM. Units for the pre-exponential factor ("A" column) are s^{-1} for unimolecular reactions and $cm^3*s^{-1}*mol^{-1}$ for bimolecular reactions. Units for the activation energy ("Ea" column) are kcal/mol. PW stands for present work, Eq is used to signify that the rate constant was calculated in this work using thermodynamic properties to obtain the equilibrium constant.

Rxn	**A**	**n**	**Ea**	**Reaction type Description**	**order**	**Source**
HAB1	6.0000E+14	0.000	0.000	C2H3(g) + Car(-O-H) --> Car(-O*) + C2H4(g)	bi	[252]
HAB2	2.9500E+06	2.000	-1.312	OH*(g) + Car(-O-H) --> Car(-O*) + H2O(g)	bi	[230]
HAB3	1.2000E+14	0.000	12.400	H*(g) + Car(-O-H) --> Car(-O*) + H2(g)	bi	[252]
HAB4	2.8100E+13	0.000	7.532	O*(g) + Car(-O-H) --> Car(-O*) + OH(g)	bi	[230]
HAB6	4.9000E+12	0.000	4.400	C6H5(g) + Car(-O-H) --> Car(-O*) + C6H6(g)	bi	[252]
HAB7	1.0000E+12	0.000	1.000	HO2(g) + Car(-O-H) --> Car(*) + H2O2(g)	bi	[252]
HAB10	1.0000E+13	0.000	38.000	O2(g) + Car(-O-H) --> Car(*) + HO2(g)	bi	[252]
HAB12	6.4450E+16	-0.414	88.127	Car(-O-H) --> H*(g) + Car(-O*)	uni	Eq
HAB13	8.9460E+31	-4.717	98.357	Cal(-O-H) --> H*(g) + Cal(-O*)	uni	Eq
HAD1	2.5000E+14	0.000	0.000	H*(g) + Car(-O*) --> Car(-O-H)	bi	[252]
HAD2	3.4700E+29	-4.303	10.230	H*(g) + Cal(-O*) --> Cal(-O-H)	bi	[252]
HT5	1.2200E+04	1.000	8.007	Car(-O*) + Car(-H) --> Car(-O-H) + Car(*)	uni	[255]
HT6	3.2200E+03	0.927	7.384	Car(-O-H) + Car(*) --> Car(-O*) + Car(-H)	uni	Eq
FA2	5.0000E+13	0.000	0.000	OH*(g) + Car(*) --> Car(-O*) + H*(g)	bi	[32]
FA3	3.0000E+13	0.000	0.000	HO2(g) + Car(*) --> Car(-O*) + OH*(g)	bi	[252]
FA4	6.3000E+29	-4.690	11.650	HO2(g) + Cal(*) --> Cal(-O*) + OH*(g)	bi	[252]
FA5	1.2100E+13	0.000	0.000	CH3*(g) + Car(-O*) --> Car(-O-CH3)	bi	[256]
FA6	1.2100E+13	0.000	0.000	C6H6(g) + Car(-O*) --> Car(-O-C6H5) + H*(g)	bi	[256]
FA7	1.2100E+13	0.000	0.000	C6H5*(g) + Car(-O*) --> Car(-O-C6H5)	bi	[256]
FA11	2.6000E+13	0.000	6.100	O2(g) + Car(*) --> Car(-O*) + O*(g)	bi	[257]
FA14	6.5000E+14	-0.850	-2.730	OH*(g) + Cal(*) --> Cal(-O-H)	bi	[252]
FA15	3.4000E+30	-5.100	12.950	O2(g) + Car(*) --> Car(-O*) + O*(g)	bi	[250]
FA19	2.3300E+06	2.174	20.909	C2H2(g) + Cal(-O*) --> Cal(-O-(CH)=(C*H))	bi	pw
FA22	7.3100E+07	0.080	-9.570	Cal(*) + O2(g) --> Cal(-O-O*)	bi	[250]

FA23	7.0600E+04	1.030	-6.960	O*(g) + Car(*) --> Car(-O*)	bi	[230]
FA24	1.8400E+03	1.030	-6.960	O*(g) + Cal(*) --> Cal(-O*)	bi	[230]
FR2	1.2700E+20	-1.331	26.087	H*(g) + Car(-O*) --> Car(*) + OH*(g)	bi	Eq
FR3	2.2060E+17	-0.957	15.045	O*(g) + Car(-O*) --> Car(*) + O2(g)	bi	Eq
FR4	2.8850E+34	-6.058	21.895	O*(g) + Cal(-O*) --> Cal(*) + O2(g)	bi	Eq
FR5	4.0300E+13	0.000	12.260	Cal(-O-O*) --> Cal(*) + O2(g)	uni	[250]
FR6	7.2900E+31	-5.146	24.866	OH*(g) + Cal(-O*) --> Cal(*) + HO2(g)	bi	Eq
FR8	3.7720E+13	0.251	22.552	Cal(-O-(CH)=(C*H)) --> C2H2(g) + Cal(-O*)	uni	pw
FR11	3.6100E+12	0.000	37.300	Cal(-O-O*) --> Cal(=O) + OH*(g)	uni	[245]
FR12	1.8230E+21	-1.671	66.493	Car(-O-CH3) --> CH3*(g) + Car(-O*)	uni	Eq
FR13	3.1390E+16	-0.656	61.355	OH*(g) + Car(-O*) --> Car(*) + HO2(g)	bi	Eq
FR14	2.0500E+19	-0.945	81.964	Car(-O-C6H5) + H*(g) --> C6H6(g) + Car(-O*)	bi	Eq
FR15	2.0500E+19	-0.945	81.964	Car(-O-C6H5) --> C6H5*(g) + Car(-O*)	uni	Eq
FR16	1.0900E+15	0.000	74.120	Cal(-O-H) --> Cal(*) + OH*(g)	uni	Eq
FR20	6.0900E+09	0.101	72.772	Car(-O*) --> Car(*) + O*(g)	uni	Eq
FR21	1.5900E+08	0.101	72.772	Cal(-O*) --> Cal(*) + O*(g)	uni	Eq
RC14	4.728E+09	0.344	7.803	C-C-C-C-O-C[open] --> pyran[closed] + H*(g)	uni	pw
RC15	4.728E+09	0.344	7.803	C-C-C-O-C-C[open] --> pyran[closed] + H*(g)	uni	pw
RC16	4.728E+09	0.344	7.803	C-C-O-C-C-C[open] --> pyran[closed] + H*(g)	uni	pw
RC17	4.728E+09	0.344	7.803	C-C-C-C-O-C[open] -->furan[closed] + H*(g)	uni	pw
RC18	4.728E+09	0.344	7.803	C-C-C-O-C-C[open] -->furan[closed] + H*(g)	uni	pw
RC19	4.728E+09	0.344	7.803	C-C-O-C-C-C[open] --> furan[closed] + H*(g)	uni	pw
RC21	7.0000E+09	0.000	14.5	C-C-C-C-C*[open] --> C-C-C-C-C[closed]-C1*	uni	[152]
RC22	7.0000E+09	0.000	18.7	C-C-C-C-C*[open] --> C2*-C-C-C-C-C[closed]	uni	[152]
RO18	3.1400E+07	1.692	8.184	pyran[closed] + H*(g) --> C-C-C-C-O-C[open]	bi	pw
RO19	3.1400E+07	1.692	8.184	pyran[closed] + H*(g) --> C-C-C-O-C-C[open]	bi	pw
RO20	3.1400E+07	1.692	8.184	pyran[closed] + H*(g) --> C-C-O-C-C-C[open]	bi	pw
RO21	3.1400E+07	1.692	8.184	furan[closed] + H*(g) --> C-C-C-C-O-C[open]	bi	pw
RO22	3.1400E+07	1.692	8.184	furan[closed] + H*(g) --> C-C-C-O-C-C[open]	bi	pw
RO23	3.1400E+07	1.692	8.184	furan[closed] + H*(g) --> C-C-O-C-C-C[open]	bi	pw

RO29	8.9000E+07	0.000	31.200	C-C-C-C-C[closed]-C1* --> C-C-C-C-C*[open]	uni	[152]
RO30	8.9000E+07	0.000	36.300	C2*-C-C-C-C-C[closed] --> C-C-C-C-C*[open]	uni	[152]
ISO3	1.1200E+30	-5.975	-1.444	Cal(=O) + H*(g) --> H-Cal(-O*)	bi	Eq
ISO5	2.9000E+32	-6.500	21.200	H-Cal(-O*) --> Cal(=O) + H*(g)	uni	[252]
OX1	2.8100E+12	0.907	7.068	R-C* + *O-C-R(g) --> R-C-O-C-R	bi	Eq
OX2	4.5700E+04	1.959	-9.364	R-C-C* + *C-C-R(g) --> R-C-C-C-C-R	bi	Eq
OX3	2.3100E+09	0.763	0.000	2-naphthyl[closed] + O2(g) --> indenyl[closed] + CO2(g)	bi	[152]
OX4	4.1800E+12	0.185	14.500	indenyl[closed] + CO(g) --> 2-naphthyl[closed] + O(g)	bi	[136]
OX5	4.3600E+13	0.177	40.000	indenyl[closed] + CO2(g) --> 2-naphthyl[closed] + O2(g)	bi	Eq
OX6	4.7900E+11	0.242	33.700	2-naphthyl[closed] + O(g) --> indenyl[closed] + CO(g)	bi	Eq
OX7	3.1500E+07	0.000	0.000	1-naphthoxy --> 1-indenyl + CO	uni	[250]
OX8	3.1500E+07	0.000	0.000	2-naphthoxy --> 1-indenyl + CO	uni	[250]
OX9	2.5100E+11	0.000	43.900	c1-c-c-c(-O*)-c-c1 --> c1-c-c*-c-c1 + CO(g)	uni	[250]
OX10	2.5100E+11	0.000	43.900	c1-c-c-c(-O*)-c-c1 --> c1-c-c*-c-c1 + CO(g)	uni	[250]
OX11	9.1600E+14	0.110	75.820	R-C-O-C-R --> R-C* + *O-C-R(g)	uni	[258]
OX12	4.0200E+15	-0.180	78.820	R-C-C-C-C-R --> R-C-C* + *C-C-R(g)	uni	[258]

Table 2.5: Pictorials of reaction types. Dashed lines on the molecules off of atoms signify that anything can be attached to those atoms. For example, ---CH signifies that they key group is a saturated carbon atom bonded to any other atom (which in turn may or may not be bonded to other atoms). Where there is an “X” in the pictorial, the “X” can represent any of the species listed underneath the pictorial.

	Classes of reaction types
	Hydrogen abstraction/addition
a	----CH + OH $\rightleftharpoons$ ----C + H_2O
b	---OH + X $\rightleftharpoons$ ---O• + XH X is H, O2, HO2, C2H3, phenyl, O, OH

c	$\text{----OH} \rightleftharpoons \text{----O}^* + \text{H}$
	Hydrogen transfer
d	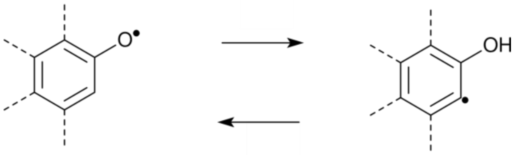
	Fragment addition/removal
e	$\text{---C-O}^* + \text{X} \rightleftharpoons \text{---C-O-X}$ X is CH3, CH2, CH4, benzene, phenyl, C2H2, C2H3, C2H4, C2H5, C2H6, C3H3, C4H2, C4H4, O, OH, HO2
f	$\text{---C}^* + \text{O} \rightleftharpoons \text{---C-O}^*$
g	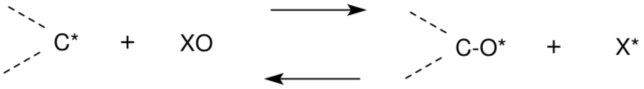 X is H, O, OH, H2O, H2, CO
h	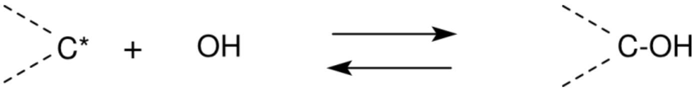
i	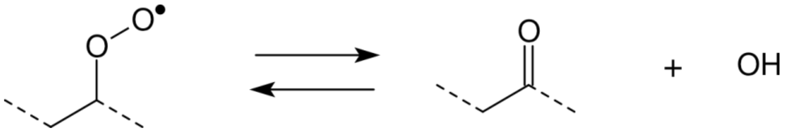
	Ring opening/closure

j	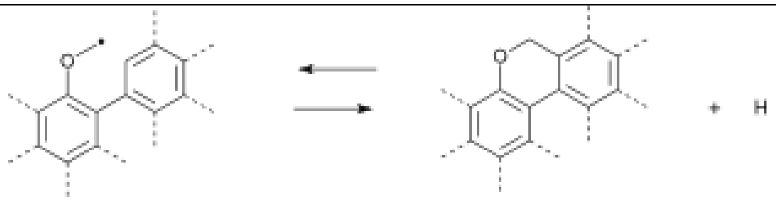
k	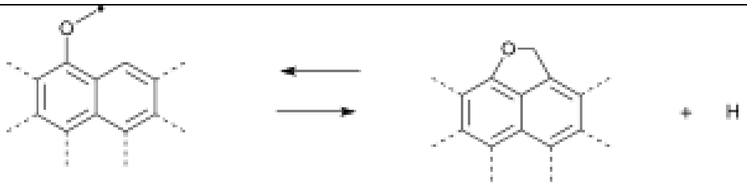
l	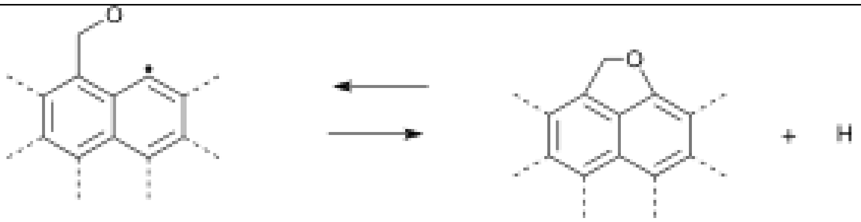
m	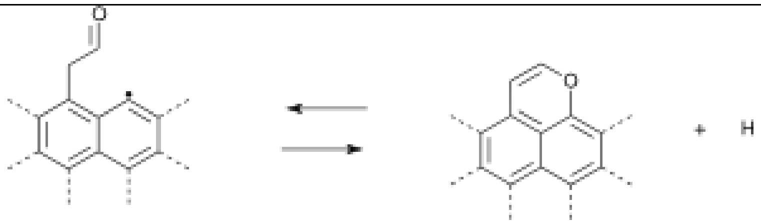
n	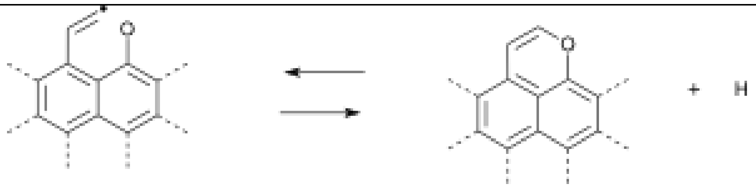
o	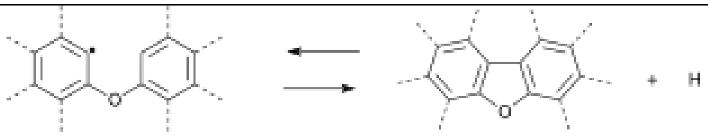
p	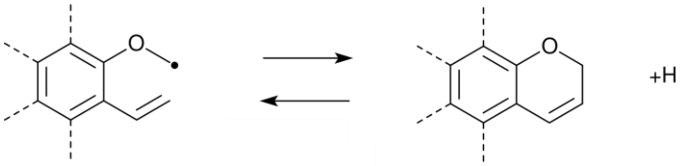

q	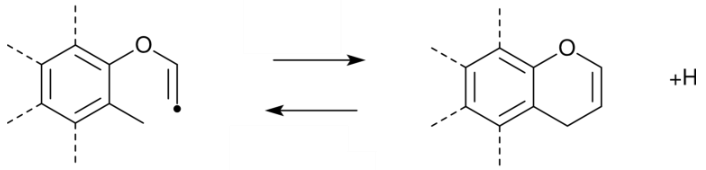
r	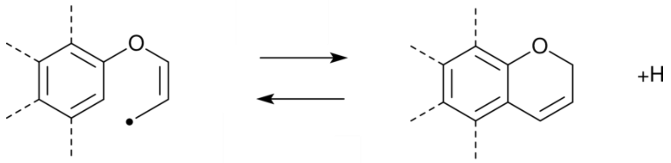
s	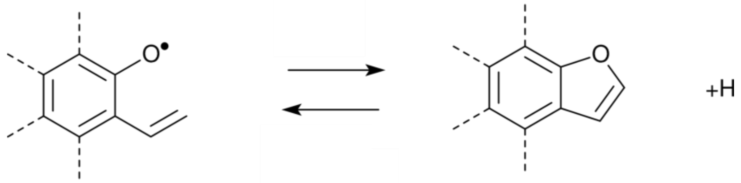
t	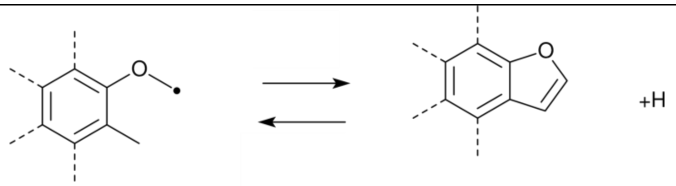
u	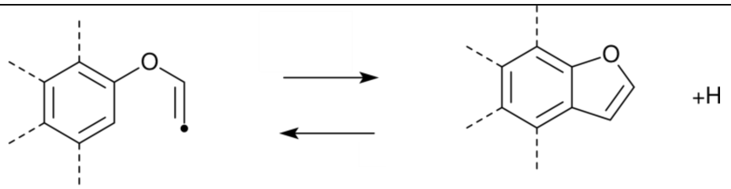
v	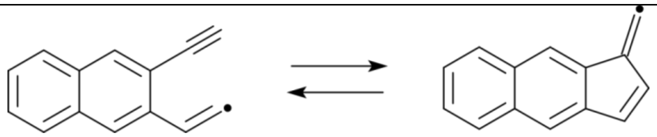
w	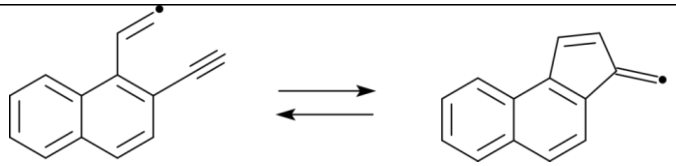
	Isomerizations

x	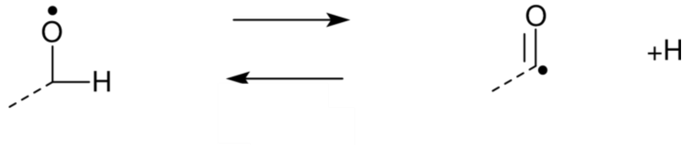
	Oxidation
y	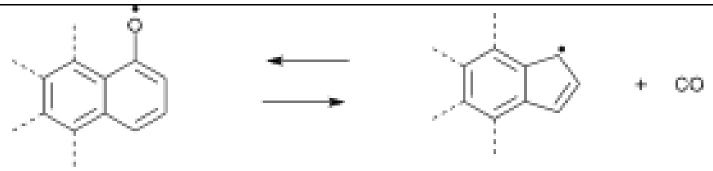
z	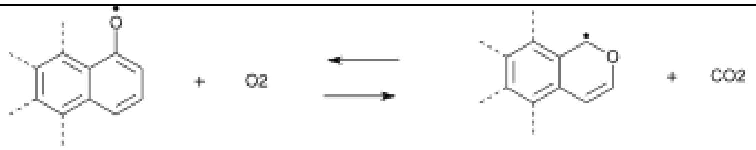
aa	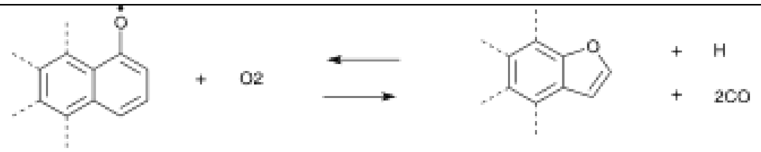
ab	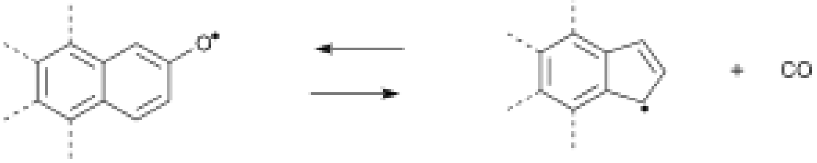
ac	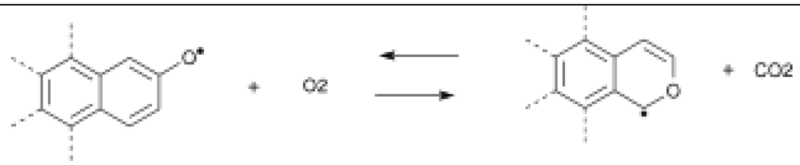
ad	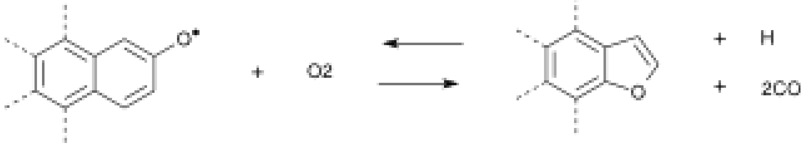

ae	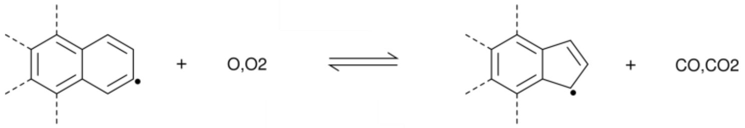
af	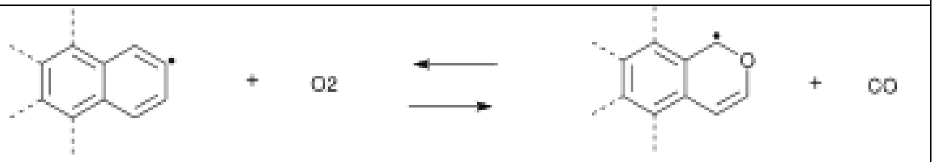
ag	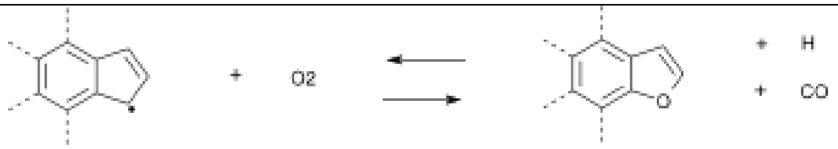
ah	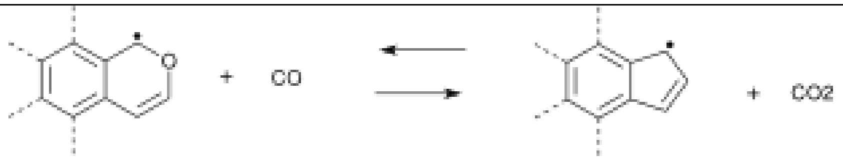
ai	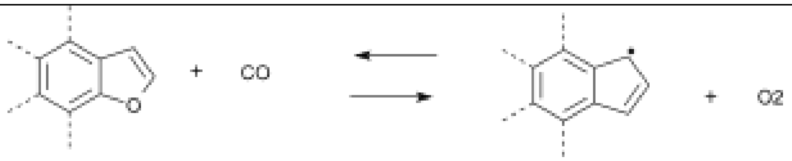
aj	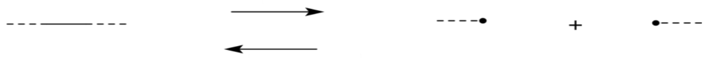

Table 2.6: SNAPS developer descriptions.

Code Development Activity	**Jason Lai**	**Paolo Elvati**	**Tyler Dillstrom**
Implement code base including kMC algorithm and tying in the cheminformatics third party libraries OpenBabel	**X**	**X**	
Developed initial hydrocarbon kinetic mechanism	**X**		
Extend use of SMARTS string for reaction sites containing or involving oxygen and most covalent connections among oxygen, carbon, and hydrogen			**X**

Extended and refined hydrocarbon mechanism			**X**
Identified missing oxygen chemistry in PAH growth models			**X**
Developed and designed oxygenation pathways relevant to high temperature PAH growth			**X**
Implemented oxygen-hydrocarbon mechanism			**X**
Extended code base to enable the new reaction sites and reactions developed in present mechanism			**X**
Validated that extended code and new mechanism continued to produce expected results of benchmark simulations			**X**

Figures

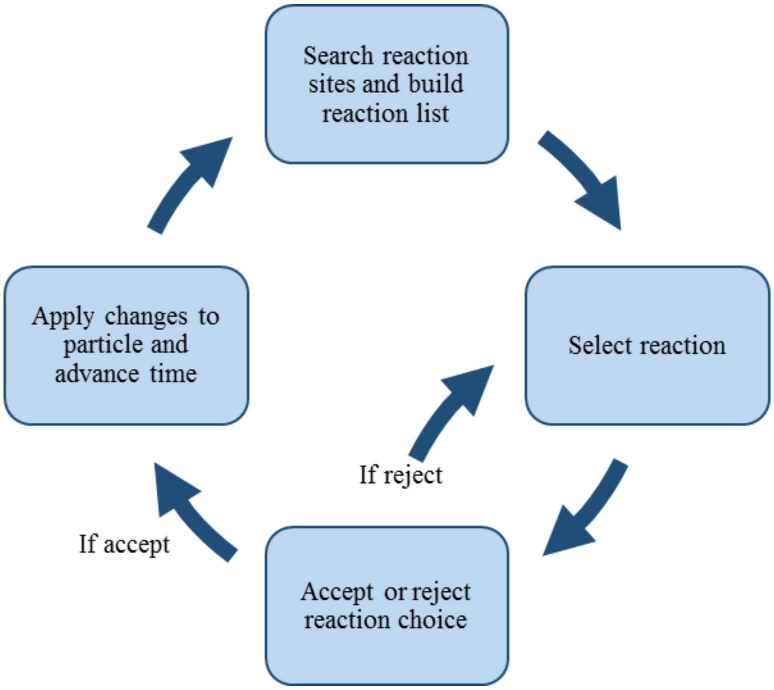
Search reaction sites and build reaction list
Select reaction
Accept or reject reaction choice
If reject
If accept
Apply changes to particle and advance time

Figure 2.1: A schematic of the SNAPS algorithm. If a reaction is rejected, step two is repeated and the cycle continued.

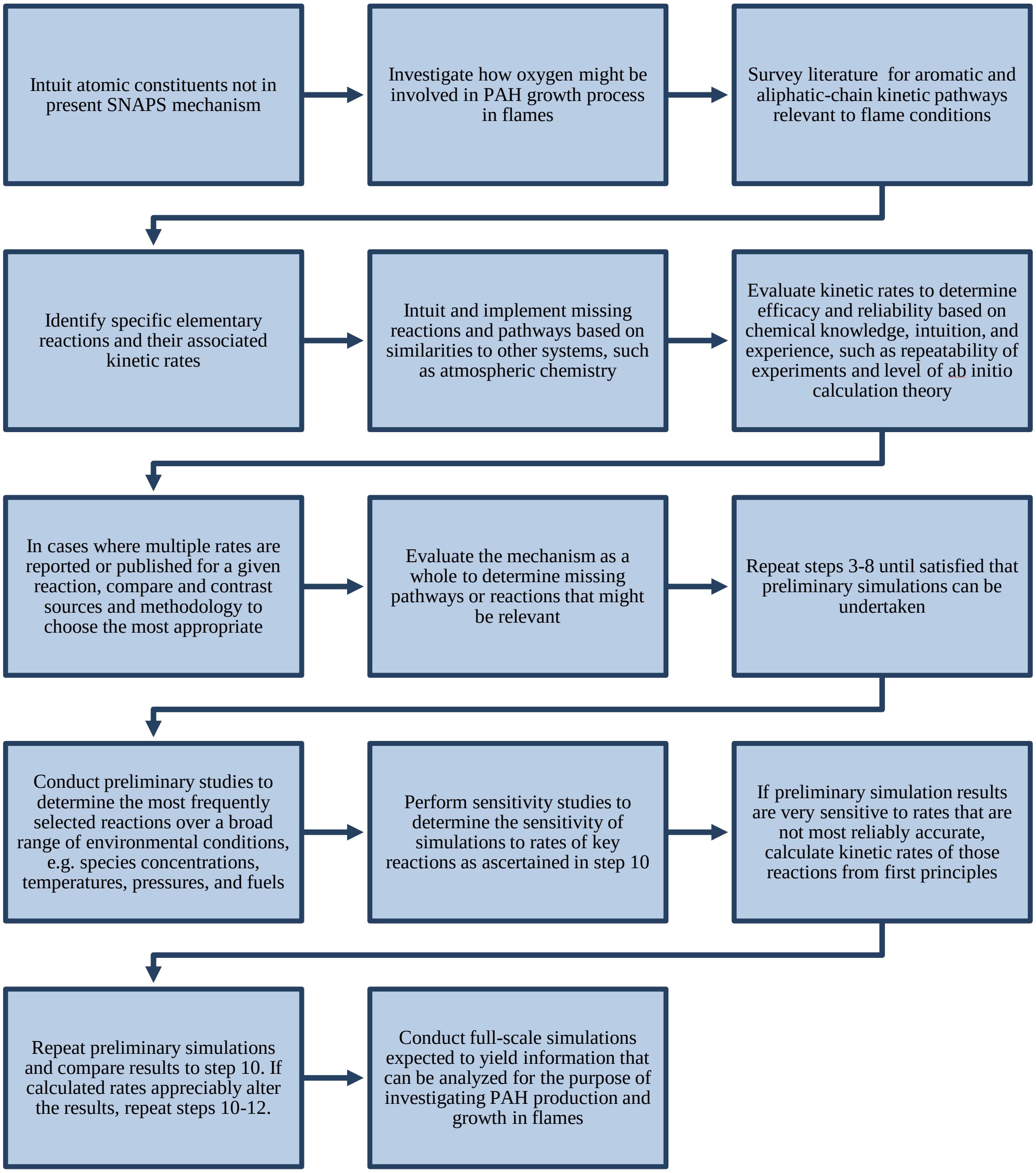
Intuit atomic constituents not in present SNAPS mechanism
Investigate how oxygen might be involved in PAH growth process in flames
Survey literature for aromatic and aliphatic-chain kinetic pathways relevant to flame conditions
Identify specific elementary reactions and their associated kinetic rates
Intuit and implement missing reactions and pathways based on similarities to other systems, such as atmospheric chemistry
Evaluate kinetic rates to determine efficacy and reliability based on chemical knowledge, intuition, and experience, such as repeatability of experiments and level of ab initio calculation theory
In cases where multiple rates are reported or published for a given reaction, compare and contrast sources and methodology to choose the most appropriate
Evaluate the mechanism as a whole to determine missing pathways or reactions that might be relevant
Repeat steps 3-8 until satisfied that preliminary simulations can be undertaken
Conduct preliminary studies to determine the most frequently selected reactions over a broad range of environmental conditions, e.g. species concentrations, temperatures, pressures, and fuels
Perform sensitivity studies to determine the sensitivity of simulations to rates of key reactions as ascertained in step 10
If preliminary simulation results are very sensitive to rates that are not most reliably accurate, calculate kinetic rates of those reactions from first principles
Repeat preliminary simulations and compare results to step 10. If calculated rates appreciably alter the results, repeat steps 10-12.
Conduct full-scale simulations expected to yield information that can be analyzed for the purpose of investigating PAH production and growth in flames

Figure 2.2: Flow chart schematic of the design process of the new oxygenated hydrocarbon kinetic mechanism used in SNAPS modeling of PAH growth in premixed flames for this work.

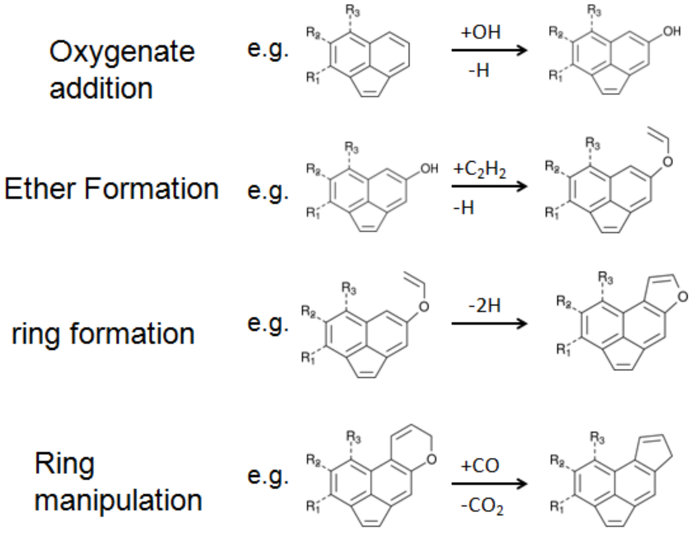
Oxygenate addition
e.g.
+OH
-H
Ether Formation
e.g.
+C2H2
-H
ring formation
e.g.
-2H
Ring manipulation
e.g.
+CO
-CO2
R1
R2
R3
OH
O

Figure 2.3: Examples of key oxygenation reactions in SNAPS mechanism. Specific reactions chosen to represent each type of class of reactions are because they are the most dominant reactions in their respective class.

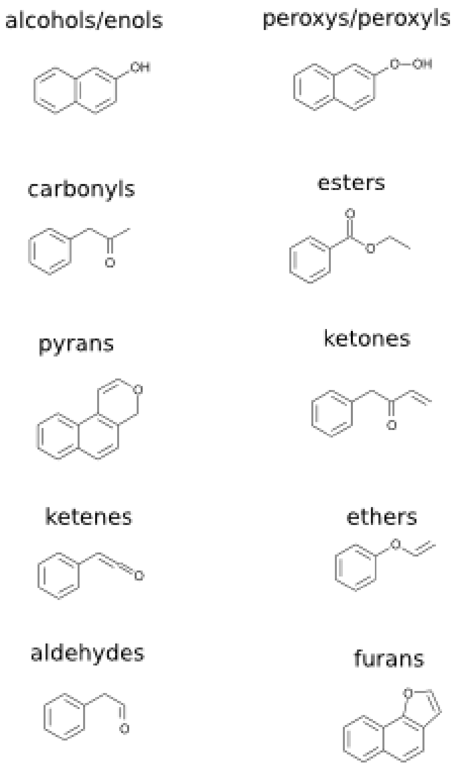
alcohols/enols
OH
peroxys/peroxyls
O—OH
carbonyls
O
esters
O
O
pyrans
O
ketones
O
ketenes
O
ethers
O
aldehydes
O
furans
O

Figure 2.4: Oxygenated functional groups that are generated in SNAPS trajectories via the oxygenation and oxidation pathways.

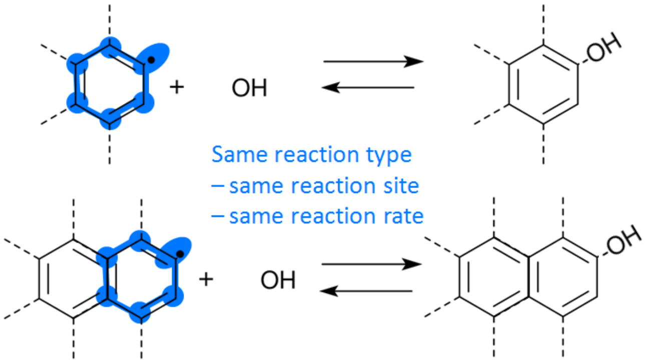
+
OH
OH
Same reaction type
– same reaction site
– same reaction rate
+
OH
OH

Figure 2.5: The blue highlights are the definition of a reaction site for bimolecular hydroxyl addition to a radical aromatic carbon. They reaction site only considers the exact composition and structure of the six highlighted carbon atoms (and their attached hydrogen neighbors), thus the two distinct species on the left undergo the same reaction event. This eliminates the need to specifically define all species – of which there are hundreds of thousands when considering all potential species larger than benzene.

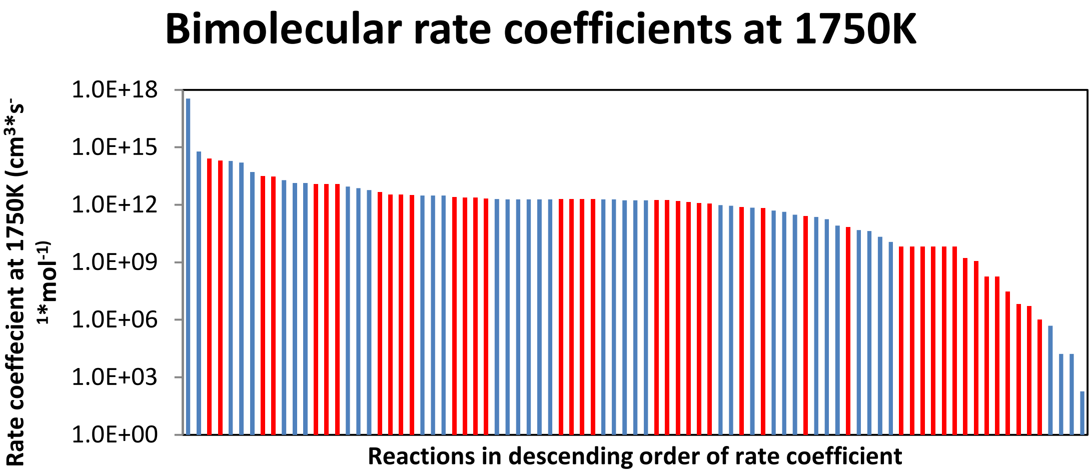

Figure 2.6: 92 bimolecular reaction rate coefficients as evaluated at 1750K sorted in descending order. 80% of the reaction rate coefficients are within 2 orders of magnitude of each other. There is one outlier (far left) on the far side and the slowest 10% of rate coefficients are several orders slower than the median (1.69×10^{12} $cm^3 \cdot s^{-1} \cdot mol^{-1}$) and average ($4.08 \times 10^{15}$ $cm^3 \cdot s^{-1} \cdot mol^{-1}$). Red bars are novel oxygenation pathways. Blue bars are hydrocarbon reactions. The sets of pathways work synergistically to create a more comprehensive chemical evolution mechanism.

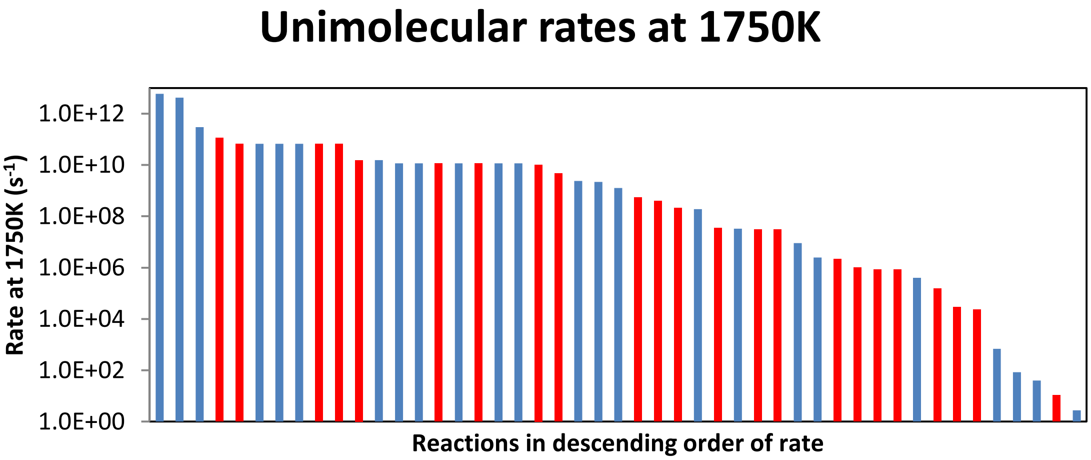

Figure 2.7: 48 Unimolecular reaction rate coefficients as evaluated at 1750K sorted in descending order. Because the rate coefficients of the lower half of the reactions steadily and continuously decrease, the average of the coefficients (2.39×10^{11} s^{-1}) is skewed such that the lower 75% of reactions are slower than the average. The median reaction rate

coefficient is $2.19*10^9$ s^{-1}. Red bars are novel oxygenation pathways. Blue bars are hydrocarbon reactions. The sets of pathways work synergistically to create a more comprehensive chemical evolution mechanism.

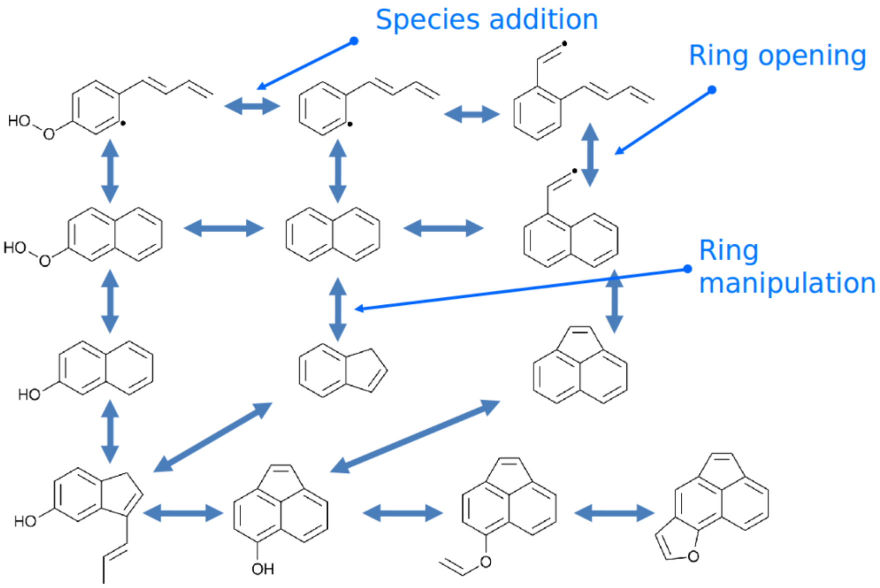
Species addition
Ring opening
Ring manipulation
HO
O
OH

Figure 2.8: Example subset of a potential reaction pathway diagram. A trajectory where indene (center) is the seed molecule could evolve along the given route shown or any number of other routes not depicted. All reactions and pathways are reversible.

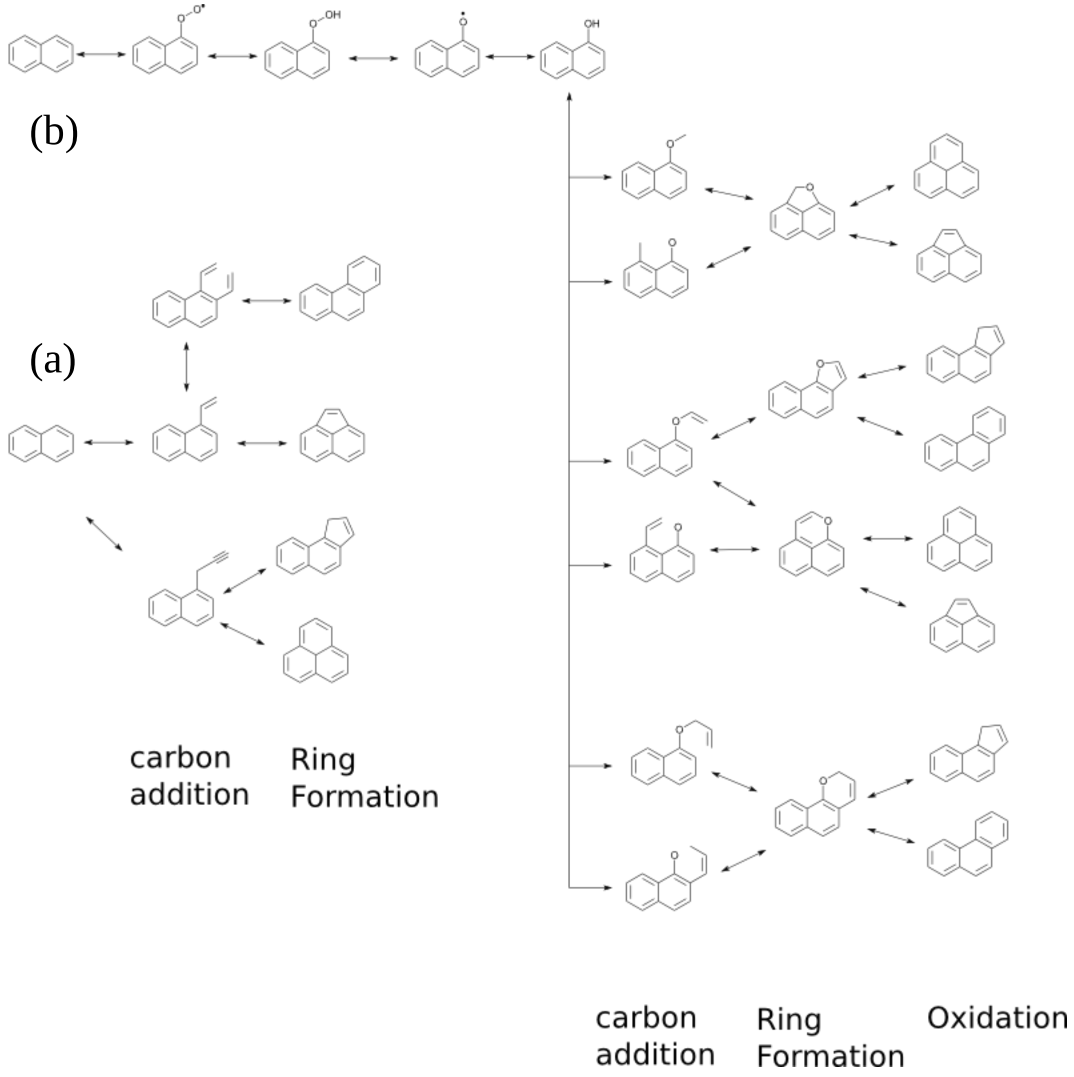

Figure 2.9: Comparing the hydrocarbon-only pathways to the combined oxygenation and hydrocarbon pathways. Here the pathways from naphthalene (2 rings) to a 3 ring structure with no chains. In the set of pathways (b) there are only a small set of pathways that go from naphthalene to a 3 ringed structure, and there are only 4 possible structures that contain 3 rings. In the set of pathways (a) oxygenation pathways that work synergistically with hydrocarbon growth pathways lead to many multiples of potential growth pathways from naphthalene to a 3 ringed structure. Additionally there are 10 conformations of a structure with one oxygenated ring in addition to the same 4 carbon-only 3 ringed structures present in the set of pathways (a). Oxidation pathways present in the oxygen growth mechanism provide quick avenues from oxygenated rings to carbon-only rings. This provides a mechanism to eliminate embedded oxygen atoms from the PAH and nanoparticles structures. Note: not all pathways and bimolecular additions present in the SNAPS mechanism are shown in the diagram for the purpose of clarity. Because oxygenation reactions work in parallel and in coordination with hydrocarbon reactions including all pathways has a multiplier effect on the number of number of pathways when oxygen chemistry is included in the SNAPS mechanism.

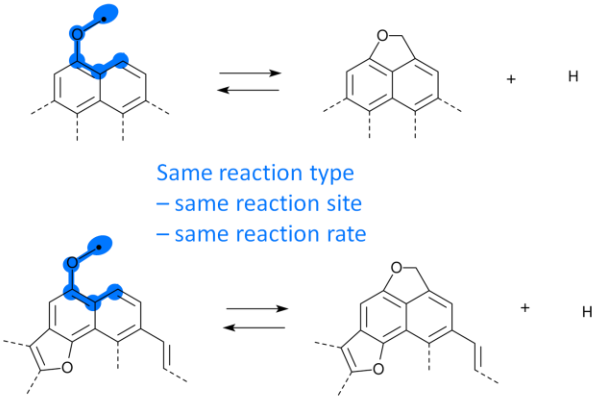
+
H
Same reaction type
– same reaction site
– same reaction rate
+
H

Figure 2.10: The blue highlights are the definition of a reaction site for which a 5 membered ring could form on a zig-zag site. They reaction site only considers the exact composition and structure of the 5 highlighted carbon atoms (and their attached hydrogen neighbors), thus the two distinct species on the left undergo the same reaction event. This eliminates the need to specifically define all species – of which there are hundreds of thousands when considering all potential species larger than benzene.

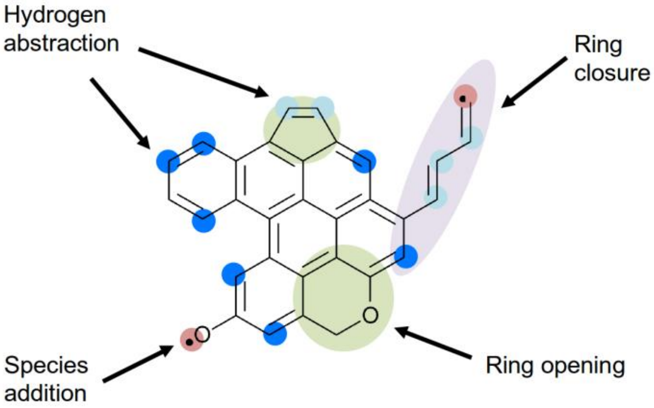
Hydrogen abstraction
Ring closure
Species addition
Ring opening

Figure 2.11: Reaction site definitions for the key reaction types in the mechanism. Dark blue circles are reaction sites for all reactions which lead to hydrogen abstraction from a saturated aromatic carbon. Light blue circles are reaction sites for all reactions which lead to hydrogen abstraction from a saturated aliphatic carbon. The top examples are representative of carbons which are a member of a ring of 5 carbons comprising a zig-zag site. The right examples are representative of generic aliphatic carbons. The light green circles are reaction sites for all reactions which are vulnerable to ring opening reactions.

The top example would be the opening of a five-member carbon ring on a zig-zag site. The bottom example would be the opening of a pyran (5 carbons, 1 oxygen atom) ring. The light red circles are reaction sites for all reactions which lead to the bimolecular addition of a gas-phase species to a radical site on the molecule. The top example would be addition to an aliphatic carbon. The bottom example would be addition to an oxyradical. The light chain highlighted in light maroon on the right is an example of a reaction site that could undergo ring closure. The highlighted six carbons in that structure and composition are able to form a six-member aromatic ring on the edge of the molecule.

Chapter 3

Exploring the Effect of Oxygenation Pathways on PAH Growth in a Benzene-Air Flame

3.1 Simulation Design

The current study as well as the subsequent studies reported in this work, in following the order of events depicted in Figure 3.1, consisted of modeling the gas-phase chemistry using the solver PREMIX in the CHEMKIN software suite [155] and particle precursor growth, using the oxygenation/hydrocarbon model in SNAPS, of a 1 atm fuel-rich benzene–air premixed laminar flame with a C/O ratio of 0.77 (equivalence ratio of 1.925) and cold-gas-flow velocity of 4 cm*s^{-1} [248]. The flame simulation utilized a fixed temperature profile measured in the experiment as input to the PREMIX solver. The height of the burner was set to 20.0 mm with an inlet velocity of 4.0 cm/sec for the flame. The inlet normalized mole fractions for the reactant species (fuel and air) were benzene: 0.051161363, O_2: 0.19932467, and N_2: 0.749513967. The maximum number of grid points allowed was 250 with the number of adaptive grid points equal to 10. The adaptive grid control based on solution gradient and curvature were set to 0.1 and 0.5, respectively. The gas-phase deterministic kinetic mechanism from Appel et al. [95] was used to model the combustion chemistry of the flame. Particle formation simulations in SNAPS consisted of an ensemble of 12,000 trajectories. The experiments [248] provide measured temperature profiles and small PAH profiles, and most importantly, mass spectra in the 200-400 amu range, which are critical size PAHs for particulate formation. Importantly, mass spectra of PAHs in the range 200–400 amu – calculated by sampling all the trajectories of the ensemble at a specific flame height (and time) and assessing their mass – formed in a sooting benzene flame, change dramatically in the presence of the new oxygenation chemistry. The results show that the inclusion of oxygen kinetics is a significant step in crafting a more descriptive particle precursor simulator.

3.2 Results and Discussion

The focus of the present study is four-fold: firstly, validating the novel oxygenation/hydrocarbon mechanism by comparing the production of small PAHs to deterministic models and experiment; secondly, investigating how the user-defined ‘seed’ molecule influenced the evolution of aromatics in the flame region (this acted as a computational experiment to exercise the code and PAH growth model); thirdly, exploring the effects on PAH growth rate when including or excluding the newly developed set of oxygenation pathways in the reaction mechanism; and fourthly, ascertaining how the two reaction mechanisms influence PAH growth compared to experimental mass spectra measurements. The results of these inquires illuminated the nuances and intricacies of the kMC algorithm as well as the SNAPS growth scheme and more importantly demonstrated that the mechanism that includes the novel oxygenation and oxidation pathways more realistically describes the growth of nanoparticle precursor molecules in the sooting laminar benzene-air flame. The development of the oxygenation growth scheme and inclusion of oxygen chemistry in the kinetic mechanism for SNAPS helps elucidate the key growth process of nanoparticle precursors in flames.

3.2.1 PAH Production in Simulations

To validate the PAH growth scheme of the model, PAH growth was evaluated by comparing the predicted time-histories of several PAHs in a benzene flame [248] to the predictions of a sub-model consisting solely of traditional hydrocarbon pathways, deterministic models [95], [247], and ratios of the PAH profiles measured in the experiment [248]. In Figure 3.2 the PAH profile ratios of indene, naphthalene, acenaphthylene, phenanthrene, and anthracene are contrasted with that of a conventional hydrocarbon-only growth scheme, CHEMKIN simulations, and the experiment. The set of PAHs explored have various formation pathways, including five-member ring formation on free edges and zig-zag sites, HACA reactions that lead to pericondensed six-member rings, and oxidation pathways that result in ring reduction reactions. Hydrocarbon structures are evaluated because only the new model is able to simulate oxygenated structures.

Firstly, the comparison between the oxygen/hydrocarbon SNAPS model and the hydrocarbon-only SNAPS model in Figure 3.2 shows that the PAH production of acenaphthylene, indene, naphthalene, phenanthrene, and anthracene are within a factor of five of each other. This supports the notion that the oxygenation pathways do not appreciably alter the formation HACA pathways that generate those species. When using the oxygen/hydrocarbon growth model these structures compose a smaller portion of the entire collection of PAHs than when using the HC-only growth model because in the former ensemble there are a significant portion of oxygenated structures that cannot exist in the latter. However, the ratios of these PAHs remain similar when the new mechanism is used. The most significant difference when using the oxygen/hydrocarbon mechanism in SNAPS is that the oxidation reactions that lead to ring migration and ring shrinking, e.g. converting six-member carbon rings to five-member rings lead to a lesser amount of anthracene in favor of indenonaphthalene.

SNAPS predictions compare favorably with the deterministic simulation from CHEMKIN; both simulations demonstrate concentrations of key two- and three-ring aromatics within a factor of 10 of the CHEMKIN simulation. Moreover, SNAPS simulations using the oxygenation mechanism compare more favorably with the deterministic solution (consistently around one half of CHEMKIN) that the SNAPS simulations with no oxygenation (consistently between one tenth and one fifth of CHEMKIN). Because SNAPS trajectories are influenced by the gas-phase environment, which was attained from the CHEMKIN simulation itself and used as an input to SNAPS, this result demonstrates that the SNAPS pathways and reaction rates are consistent with the PAH growth sub-mechanism of the deterministic mechanism [95] used in the CHEMKIN simulation. Thirdly, the largest discrepancy between modeling (SNAPS and CHEMKIN) and the experiment is with the acenaphthylene and indene profiles. All the models consistently under predict the amount of indene in the flame which is likely a product of under emphasizing the indene formation pathways in the models. It is noteworthy that the SNAPS model with oxidation chemistry predicts more indene than the SNAPS sub-model with only hydrocarbon pathways. More emphasis might need to be placed on the effect these pathways have on PAHs early in their growth trajectory compared to late in the particle phase, where oxidation chemistry is usually considered important.

3.2.2 Effect of Seed on Growth Rate

The SNAPS technique for simulating the possible evolution sequence of precursors in flames requires the user to define the initial seed molecule. Benzene is generally a good choice because of it abundance in fuel rich flames at relatively early timeframes and because the formation of an aromatic ring is widely considered to be the first step in the nanoparticle production process [29]. Using benzene as a seed molecule in this case is particularly relevant because the fuel source is benzene. Additionally, because PAHs can germinate from any aromatic molecule, using toluene, which differs from benzene in a growth perspective because of the odd-carbon number, and pyrene (often considered as the smallest of potentially strong candidates from which particle nucleation can be initiated) as seed molecules enabled an interesting computational experiment that shed light about how seed choice impacts PAH growth pathways. Thus, I performed studies using benzene (78 amu), toluene (92 amu), and pyrene (202 amu) as seed molecules and modeled their growth in a laminar premixed benzene flame with a carbon/oxygen ratio of 0.77 [248]. This choice of compounds makes it possible to discern the importance of size (benzene versus pyrene) but also the effect of the odd and even number of carbons in the initial seed (benzene versus toluene). Figure 3.3 elucidates the differences in rates of growth amongst the seed molecules in the fuel rich flame.

The value on the y axis of Figure 3.3 is an average of the masses of the SNAPS particles sampled at numerous heights of the flame over the entire ensemble of 6000 trajectories. Though the trajectories initiated with a pyrene seed have an initial increased mass at time zero relative to the smaller benzene and toluene, the average rate of growth is faster for the ensemble of pyrene-seed trajectories, thus the size of the mass gap between those and the benzene- and toluene-seed trajectories increases over the flame height. What was an initial mass difference of 110 amu between pyrene and toluene grows to a mass difference of 206 amu by the time the target PAHs reach the end of the flame. This trend demonstrates that a pyrene present in the early stages of a flame grows to become a much larger precursor than a toluene or benzene given the same gas-phase environment because larger molecules have a greater set of potential growth pathways that can be explored due to the increased number of potentially active sites. Therefore, given a larger seed at time zero, the probability of evolving into a high mass aromatic molecule (HMAM) is greater. A note must be made that benzene is much more abundant than toluene in the early portion of the flame because benzene is the fuel source. Similarly, toluene is more abundant than pyrene in the lower regions of the flame because the dominant pyrene formation pathways in the model and in deterministic models are via sequential growth reactions that are initiated from benzene and toluene. Thus, though the probability of growing to larger particles is greater for pyrene, there is a greater probability that any given particle in a flame originated from a benzene molecule. However, because the possibility of a pyrene molecule forming unusually early in the flame due to the stochastic nature of PAH growth is non-negligible, the results of this study are still relevant. This could be particularly true if future investigations about early PAH growth reveal that the assumed kinetic rates should be revised upwards.

One should note that the concentration of PAHs in this flame reaches a peak between six and eight mm and then begins to decline as the production of particulates increases. That is, the majority PAH growth precedes particulate formation which depletes the amount of PAHs as they molecules participant in nucleation. The ensemble mass profiles as predicted by SNAPS, however, peak at about six mm, which matches the expectation from the experiment, but then plateaus because the model considers chemical growth only. The average mass plateaus because chemical growth slows significantly as the radical pool is depleted and temperature decreases higher in the flame; physical nucleation and coagulation affects that consume the PAHs in the same region which would deplete the pool of precursor molecules are not accounted for in the model.

3.2.3 Oxygenation Pathways Increase Precursor Growth

The second phase of the present study was to investigate the effect of oxygen chemistry on the reaction pathways that lead to the formation of PAHs in this premixed laminar flame. The inherent limitation of the traditional hydrocarbon-only growth model is an inability to describe the oxygenation of large gas-phase molecules that are likely produced in flames [77], [78] and possibly participate in the formation of particles. In order to compare the growth rates of SNAPS particles I performed a sensitivity analysis that highlighted the importance of oxygenation chemistry on the chemical growth of particle precursors. Thus, I simulated the same flame with benzene and toluene seeds with the oxygen/hydrocarbon growth model and with the hydrocarbon-only growth model. When using this reduced mechanism, the average HMAMs grow remarkably slower compared to the full mechanism; Figure 3.4 reports the resulting ensemble average of the molecules as a function of flame height. When oxygenation chemistry is included in the growth scheme, the chemical composition, morphology, and reaction pathways of the particles changes somewhat dramatically. Considering the sample size of 6000 trajectories sampled for each of the 4 ensembles, the expected uncertainty is approximately 1.2%. Given that the ensembles with oxygen chemistry accounted for have an average PAH mass roughly 100% greater than the ensembles with no oxygen chemistry, the uncertainty does not alter the conclusions drawn from the results.

The ensemble of simulations that utilized the model including oxygen chemistry experienced much more kinetic growth of nanoparticle precursor species, on average. Without oxygen chemistry the size of the average PAH stagnates at around 200 amu, or roughly the size of pyrene. The presence of oxygenation reactions provides the target molecule with many more potential growth pathways which in turn yield larger HMAMs. It is noteworthy that the choice of seed molecule between benzene and toluene seems to make little difference on the ensemble average mass due to the similar nature of the seeds and that hydrocarbon additions (including methyl radicals) to aromatic rings are a common step in the evolution trajectories of PAHs.

The results demonstrate that, regardless of seed choice, oxygen addition to PAHs occurs predominantly as a consequence of consecutive bimolecular reactions resulting in H-abstraction from an aromatic carbon, followed by addition of gas-phase hydroxyl or oxygen species onto the radical aromatic carbon occupying an edge site of the PAH. The reactions that lead to oxygen incorporation onto the edges of the molecule are also key to embedding oxygen atoms in PAHs and forming furan and pyran rings on the edges of the molecules. The most probable pathway for embedding oxygen atoms in the PAHs is via ethers formed when hydrocarbon gas-phase molecules (predominantly acetylene) are added to radical oxygen atoms when they collide with the target PAH. Most probable pathway is determined by the frequency of ethers being formed via that pathway in the SNAPS ensemble. SNAPS enables one to track backward from a given species or a given type of species, e.g. ethers, and evaluate the kinetic reaction pathways that led to the formation of that structure. Thus, the most frequent (and thus dominant) pathways leading to ether formation in this benzene flame are acetylene addition to oxyradical sites. Furan and pyran rings are formed when the ether formation occurs near an existing ring wherein the oxy-hydrocarbon chain forms a ring with an edge or zig-zag carbon on the existing ring via a unimolecular ring closure reaction. All the individual steps in the scheme are highly reversible, thus the rings and ether groups are able to decompose during the evolution of the target molecule. Additionally the generality of the scheme does not require a predefined set of possible morphologies and thus the PAHs explore all potential configurations and conformations in a non-predefined process.

There are six main types of configurations that are produced when simulating the evolution of PAHs in the flame with the growth mechanism that contains the set of oxygenation pathways, namely alcohols, peroxy acids, ketenes, non-cyclic ethers, pyrans, and furans. Alcohols and peroxy acids form as a result of bimolecular reactions with gas-phase OH and O_2 molecules and are precursor conformations to the other four classes of molecules. The classes that appear most frequently (and are thus the most abundant) in this benzene flame environment are alcohols, non-cyclic ethers, and furans. Alcohols form so frequently due to the simplicity of the formation pathway which only requires two (H-abstraction followed by OH addition) to four reactions (H-abstraction followed by O_2 of HO_2 addition, O-O cleavage, then H addition). Non-cyclic ethers are common because the relatively high concentration of acetylene enables acetylene addition reactions to compete with alcohol formation reactions when oxyradicals are present. These ethers are abundant and a large portion of them eventually form stable furan groups. Pyran groups form less frequently than furan groups because that requires the oxygen addition and subsequent acetylene addition and ring closure to occur on neighboring zig-zag sites which are less abundant than free-edge sites on most PAHs.

Along with the wider variance in PAH conformations that occur when accounting for oxygenation, the difference between the average mass of ensembles of trajectories (Figure 3.4) can be justified by the inclusion of additional reaction pathways due to the oxygen chemistry. The most significant reason for increased growth rates is the ubiquity of gas-phase hydrocarbons attaching to oxyradicals on the edges of the target molecule and thus spurring continued growth via the HACA scheme. However, the increased growth rate does not provide information about the statistical frequency of occurrences within the ensemble of certain sized species, i.e. the equivalent of a mass spectrum.

3.2.4 Effect of Oxygenation Pathways on Mass Spectra

Beginning with a simulation using benzene as the seed molecule and without the oxygen chemistry, I explored the frequency of occurrences of each mass (organized in 1 amu increments) between 200 and 400 amu at a height of 8 mm above the burner because that matches the range of the mass spectra measurements reported in the experiment [248]. Computational mass spectra resulting from SNAPS simulations are produced by sampling each trajectory in the ensemble at a height to match the height reported in the experiment. Because SNAPS simulations are stochastic and reactions (events in kMC parlance) occur in discrete intervals, a height range must be considered rather than an exact height. This range of ± 0.05 mm around the desired height was chosen because over 95% of trajectories have a data point in that 0.1 mm range. This was considered to be a satisfactory number of trajectories for sampling purposes. Additionally, according to literature, the diameter of the sampling probe makes the uncertainty of experimental height sampled greater than 0.1 mm. Computational mass spectra are simply a histogram of each sampled structure where the exact mass recorded in the simulation is rounded to the nearest nominal amu. Figure 3.5a shows a pattern of striking peaks surrounded by masses never occupied. This pattern is a result of the HACA dominated growth pathways in which two carbons are added and a net of one hydrogen is removed or a net of one hydrogen is added, leading to jumps in the mass by 23 or 25 amu. The result is a mass spectrum with large sets of peaks about every 24 ± 1 amu and smaller sets of peaks every 12 ± 1 amu (from odd-carbon chemistry). 400 trajectories sampled were in the mass range 200-400 amu which leads to a sampling error of 5.0%. in Figure 3.5a Including the oxygen chemistry, as shown in Figure 3.5b, leads to a less regimented mass spectrum.

The results suggest that the inclusion of oxygenation pathways leads to many more types of structures and chemical compositions. This is consistent with the conclusion reached previously that the set of oxygen-containing reactions affords many more pathways for the molecule to grow rather than just hydrogen abstraction and acetylene addition. Though the spikes are less dominant in Figure 3.5b, the 4 most prominent masses are separated by 40 amu. This mass corresponds to an addition of two carbons and an oxygen, highlighting the impact that accounting for oxygen chemistry can have on the growth patterns of particle precursors. Additionally, with the oxygenated mechanism a greater number of trajectories fall in the 200-400 amu range and thus the sampling error is much less, approximately 2.2%.

Similarly, the mass spectra of ensembles with and without the oxygen chemistry using toluene as the seed molecule (Figure 3.6a and Figure 3.6b) is consistent with that observed when using benzene as the seed molecule. The ensemble without oxygenation chemistry shows striking peaks at mass 202, 226, 252, 276, and 300 amu as well as the familiar pattern of dominant sets of peaks in 23 and 25 amu increments and smaller sets of peaks 11 and 13 amu from the larger sets of peaks. A fewer number of trajectories are sampled for the toluene seed study than the benzene seed study and thus the sampling errors for the data presented in Figure 3.6a and Figure 3.6b are approximately 6.4% and 3.5%, respectively.

It is interesting to note the similarities and differences among the simulated mass spectra (Figure 3.5 and Figure 3.6) when the seed choice and evolution mechanism is varied. Without accounting for the oxygenation of PAHs the choice of seed makes little difference in determining the most prevalent masses that are sampled at the simulated flame height of eight mm; the dominant peaks occur at 202, 226, 252, 276, and 300 amu given a benzene or toluene seed (Figure 3.5a and Figure 3.6a, respectively). Even though the toluene starts out with an odd number of carbons, for the model without oxygen chemistry the dominant peaks all contain an even number of carbons. Toluene molecules that end up experiencing the growth pattern highlighted previously tend to undergo a methyl addition in the early stages of the flame to become a xylene (or its radical) or a methyl removal reaction, then follow into the HACA pathway of adding two carbons at a time and maintaining an even number of carbons. Because, when neglecting the potential oxygenation of PAHs, there are a limited number of growth pathways for a molecule with a methyl group attached to an aromatic ring (due to a lack of significant growth pathways available to an odd-carbon structure in a HACA-dependent growth scheme), toluene seeds tend to grow in a similar pattern and rate as benzene seeds. However, when we consider the possibility of PAHs becoming oxygenated, the choice of seed appears to have a more significant impact on the growth trajectories of PAHs.

When accounting for the oxygenation of PAHs, the dominant masses sampled at 8 mm differ as a function of the seed molecule (Figure 3.5b and Figure 3.6b). With a benzene seed (Figure 3.5b), the four masses that stand out in the simulated spectrum are 238, 278, 318, and 358 amu. With a toluene seed (Figure 3.6b), there is not a set of a select few masses that dominate the spectrum, rather there are nine masses that appear with a frequency of at least 80% of the masses that are sampled most often (226 and 240 amu). Unlike the benzene-seed spectrum, there is no set of distinct masses that dominate the toluene-seed spectrum because there are a large portion of structures with an odd number of carbon atoms in the toluene-seed ensemble. While only 23% of the structures represented in Figure 3.5b have an odd number of carbons, 48% of the structures represented in Figure 3.6b have an odd number of carbons. As a result, there are fewer toluene-seed growth trajectories that follow the even-numbered-carbon pathways that are more dominant in the benzene-seed trajectories, both before and after oxygenation of the molecule. Thus, the spectrum (Figure 3.6b) is more evenly saturated in the 200–400 amu mass range and there are no dominant peaks.

Figure 3.7 reports the computed mass spectrum of PAHs in the 200-400 amu range at 8 mm height above burner (HAB), together with the experimental spectrum [248]. The dominant peaks are at masses at or about 202, 226, 252, 276, and 300 amu. The simulated mass spectrum matches replicates well the experimental spectrum in both location of spikes as well as relative abundance of less dominant species. 4000 trajectories were sampled yielding a sampling error of Approximately 1.5% for the data reported in Figure 3.7a. The computational spectrum is a combination of the spectra shown is Figure 3.5 and Figure 3.6 that is weighted according to the abundance of gas-phase benzene, pyrene, and toluene present at a height of 1 mm in the flame. It is important to note that the weighted mass spectrum reproduces well the measured mass spectrum in terms of locations of dominant peaks as well as the occurrence of species with masses neighboring the dominant masses but with much less frequency (Figure 3.7). The novel growth scheme, using a combination of hydrocarbon and oxygenation pathways working in parallel, matches experimental mass spectra to great detail while providing a level of atomic detail (compositions, morphologies, etc.) that cannot be observed in an experiment.

3.3 Summary and Conclusions

This chapter reports an implementation of SNAPS to simulate particle growth in a laminar premixed benzene-air flame environment and showed the impact and importance of the incorporated oxygenation chemistry into the PAH kinetic growth mechanism. The development of the novel oxygen/hydrocarbon particle precursor growth scheme was shown to be effective and accurate when compared to experiment and deterministic growth models based on the similar concentrations of key two- and three-ring aromatics and mass spectra for the premixed benzene flame. The model prescribes pathways for incorporation of oxygen atoms onto the edges of and embedded in particle precursors molecules. This implementation resulted in a significant alteration to the chemical composition and morphology of the ensemble of trajectories as compared to a traditional hydrocarbon-only growth model. Hydrogen abstractions and acetylene additions are still the most common events that the HMAMs experience during their evolution trajectory; however, peroxy and hydroxyl additions are also quite frequent. Additionally, hydrocarbon additions to oxyradicals present on the edges of PAHs are considerable, leading to a significant amount of ethers and rings containing oxygen atoms, specifically five-member furan rings. One of the revelations noted when SNAPS was first developed was that five-member rings were much more common than anticipated given that PAHs were thought to be composed mostly of pericondensed six-member rings, the so-called stabilomers proposed by Stein and Fahr, due to their favored thermodynamic stability [259]. In line with that result, the present study finds that common structures in this flame are not only oxygenated species, but also five-member rings, with and without oxygen. SNAPS simulations predict an array of PAHs in the 200–400 amu range that compare very well with experiments and enable the further exploration into the key morphologies present, and potentially to inform future studies into the significance of these structures in particle formation and their biological impact.

3.3.1 Contributions and Collaborations

- Validated the newly designed oxygenation-hydrocarbon kinetic mechanism against previous hydrocarbon-only mechanism and deterministic models
- Wrote several python and bash language post processing programs for parsing, processing, and analyzing the results of SNAPS simulations
- Codified the process for isolating specific species and types of PAH structures as well as locating their positions in the flames to be used in mass spectra and mass profiles reported in this chapter
- Established the importance of incorporating oxygenation pathways into a PAH chemical growth mechanism
- For the first time reported that oxygen chemistry enables PAHs to grow faster and ultimately to larger sizes in a premixed benzene flame
- For the first time demonstrated that a mechanism including oxygen chemistry much more closely represents the measured mass spectra of PAH in the 200-400 amu range of a premixed benzene flame
- All work reported in this chapter utilized the framework established in Chapter 2 and is the sole work of this author

Figures

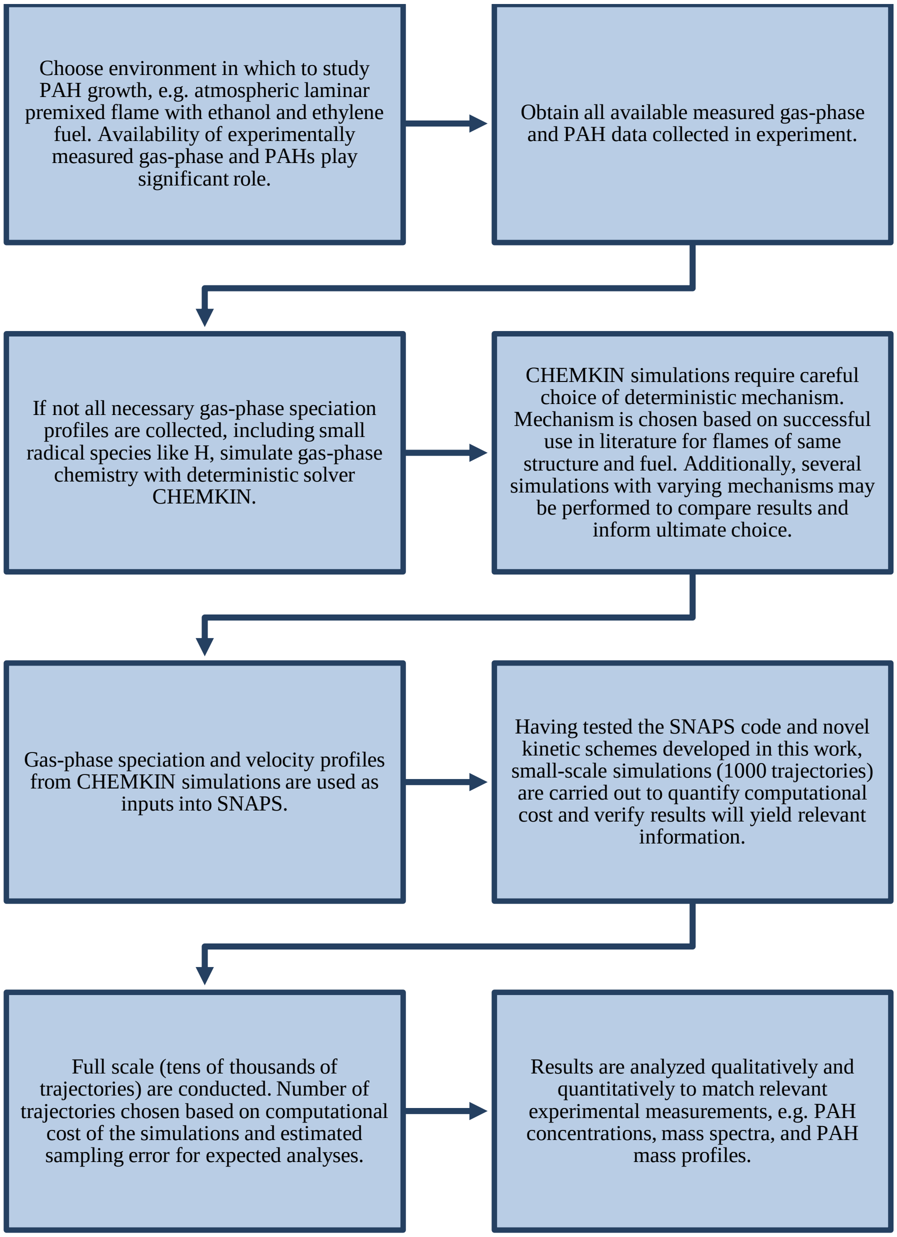
Choose environment in which to study PAH growth, e.g. atmospheric laminar premixed flame with ethanol and ethylene fuel. Availability of experimentally measured gas-phase and PAHs play significant role.
Obtain all available measured gas-phase and PAH data collected in experiment.
If not all necessary gas-phase speciation profiles are collected, including small radical species like H, simulate gas-phase chemistry with deterministic solver CHEMKIN.
CHEMKIN simulations require careful choice of deterministic mechanism. Mechanism is chosen based on successful use in literature for flames of same structure and fuel. Additionally, several simulations with varying mechanisms may be performed to compare results and inform ultimate choice.
Gas-phase speciation and velocity profiles from CHEMKIN simulations are used as inputs into SNAPS.
Having tested the SNAPS code and novel kinetic schemes developed in this work, small-scale simulations (1000 trajectories) are carried out to quantify computational cost and verify results will yield relevant information.
Full scale (tens of thousands of trajectories) are conducted. Number of trajectories chosen based on computational cost of the simulations and estimated sampling error for expected analyses.
Results are analyzed qualitatively and quantitatively to match relevant experimental measurements, e.g. PAH concentrations, mass spectra, and PAH mass profiles.

Figure 3.1: Flow process showing the order and decision points of experimental choice and simulations required in the design of this study, as well as subsequent studies.

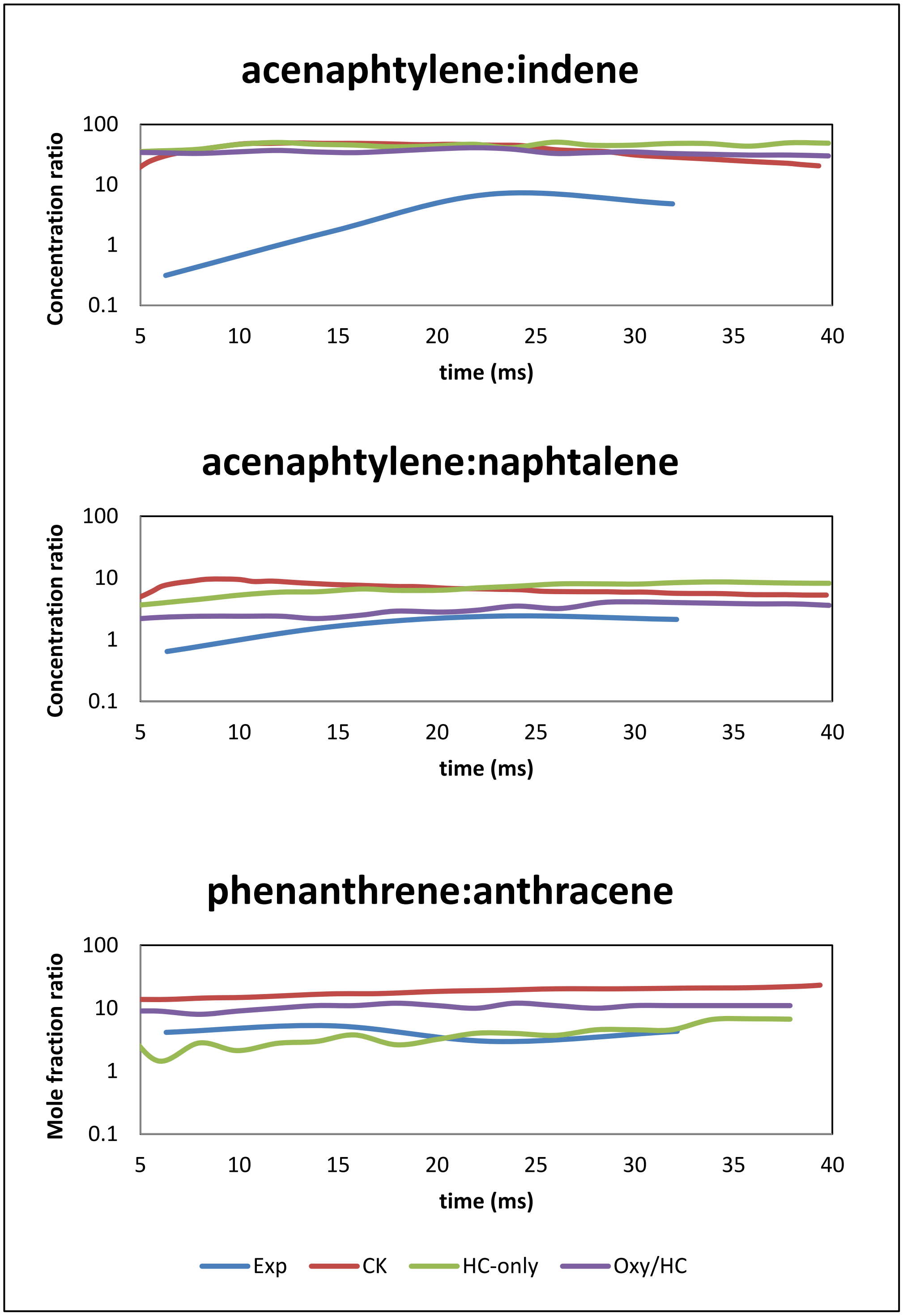

Figure 3.2: Ratios of particular species throughout the height of the flame from [248]. The experiment measured these species; shown here is the ratio of species: (a) acenaphthylene to indene, (b) acenaphthylene to naphthalene, and (c) phenanthrene to

anthracene. Compared are the experiment (blue), a deterministic simulation in CHEMKIN (red), SNAPS while using a mechanism with no oxygen chemistry (green), and SNAPS while using the more comprehensive oxygen/hydrocarbon mechanism (purple).

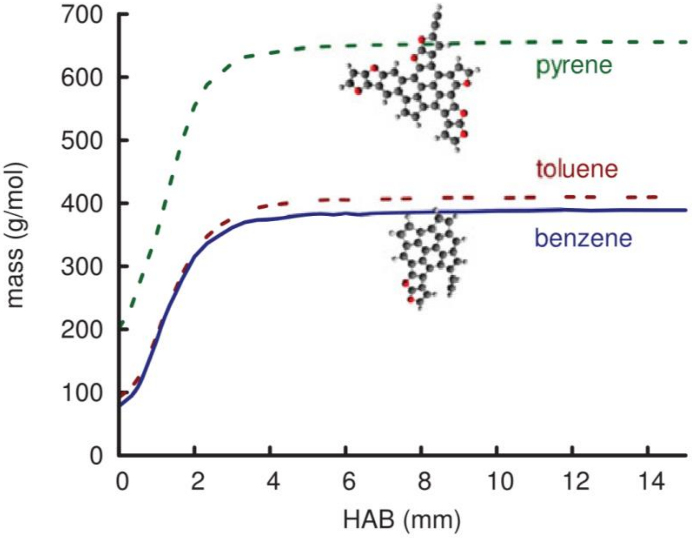

Figure 3.3: Profiles of the average masses of the ensembles of trajectories versus the height of the flame obtained using a mechanism that comprises hydrocarbon and oxygenation pathways. The larger pyrene seed allows for more potential growth pathways early in the flame when the environment is radical-rich and thus the rate of growth is appreciably faster than when using the smaller benzene or toluene seeds. The inset molecules are representative of typical SNAPS-generated PAHs at 8 mm with a mass roughly equivalent to the average mass of the ensemble at 8 mm. The top molecule has a mass of 654 amu (average mass for pyrene-seed trajectories is 655 amu at 8mm). The lower molecule has a mass of 403 amu (average mass for benzene-seed trajectories is 395 amu at 8 mm).

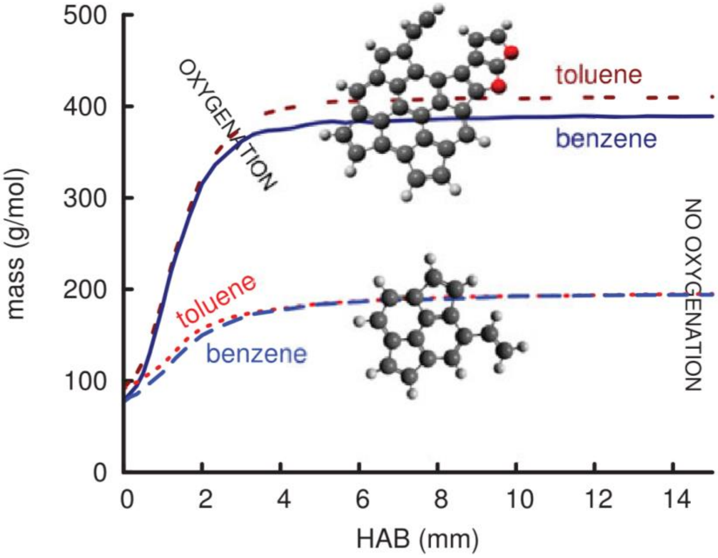

Figure 3.4: Average SNAPS ensemble masses profiles over the height of the flame. The inclusion of oxygenation pathways allows for a greater number of growth options and thus a faster rate of growth, hence the much higher plateau mass (about 400 amu) than when oxygenation is not allowed in the SNAPS mechanism (200 amu plateau). A slight deviation is observed greater than 2 mm when the oxygenation is accounted for; very little difference is observed when the oxygenation is not accounted for because the restricted number of pathways confines toluene and benzene to identical growth pathways after 2 mm. The inset molecules are representative of typical SNAPS-generated PAHs at 8 mm with a mass roughly equivalent to the average mass of the ensemble at 8 mm. The top molecule has a mass of 403 amu (average mass for benzene-seed trajectories with oxygenation pathways is 395 amu at 8mm). The lower molecule has a mass of 202 amu (average mass for benzene and toluene-seed trajectories without oxygenation pathways is 189 amu at 8 mm).

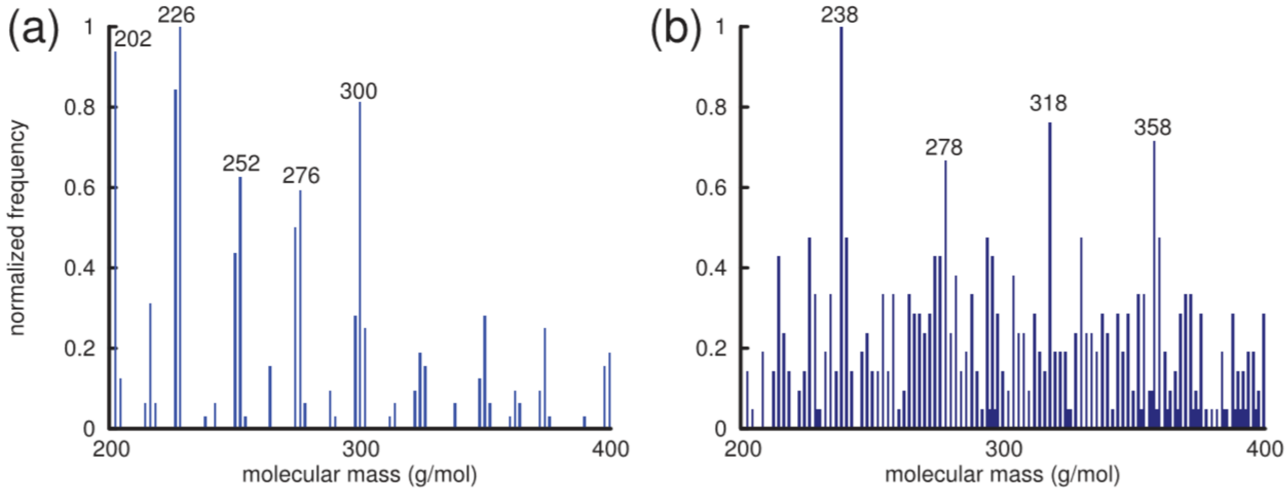

Figure 3.5: Computed mass spectra using a benzene seed with two varying mechanisms: (a) without accounting for the oxygenation of PAHs and (b) while accounting for the oxygenation pathways. SNAPS ensembles consist of 3000 trajectories to achieve statistical significance. The spectrum created with oxygen chemistry included in the SNAPS code shows that the oxygenation pathways work with the HACA pathways to broaden the range of potential species to all masses.

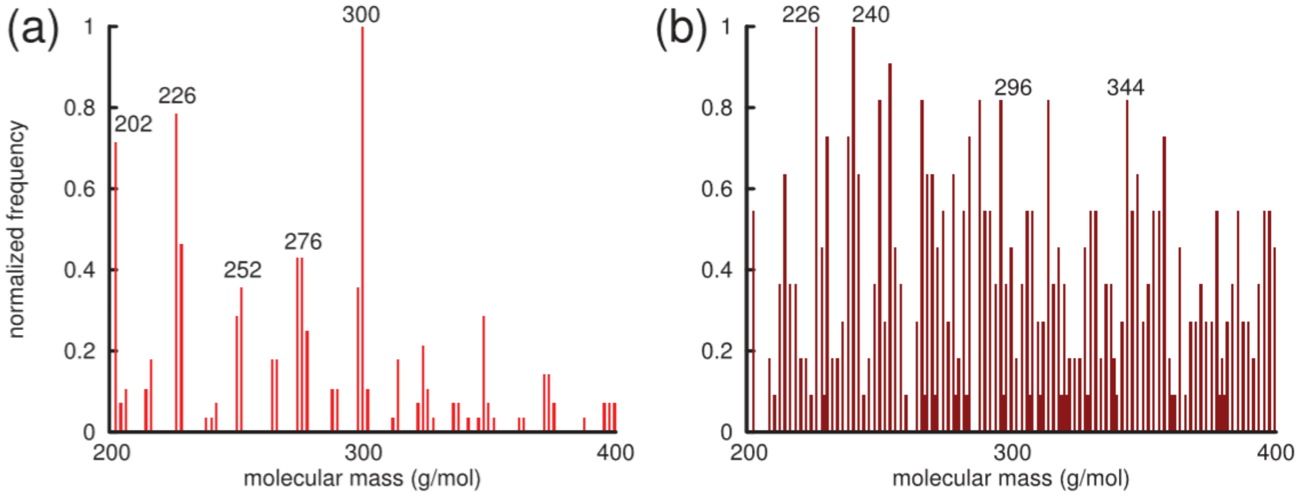

Figure 3.6: Computational mass spectra developed with SNAPS using a toluene seed with two varying mechanisms: (a) without accounting for the oxygenation of PAHs and (b) while accounting for the oxygenation pathways. SNAPS ensembles consist of 3000 trajectories to achieve statistical significance. The spectrum created with oxygen chemistry included in the SNAPS code is much noisier with no dominant peaks because

the oxygenated PAHs do not fall into the ± 12 amu pattern that purely hydrocarbon PAHs do.

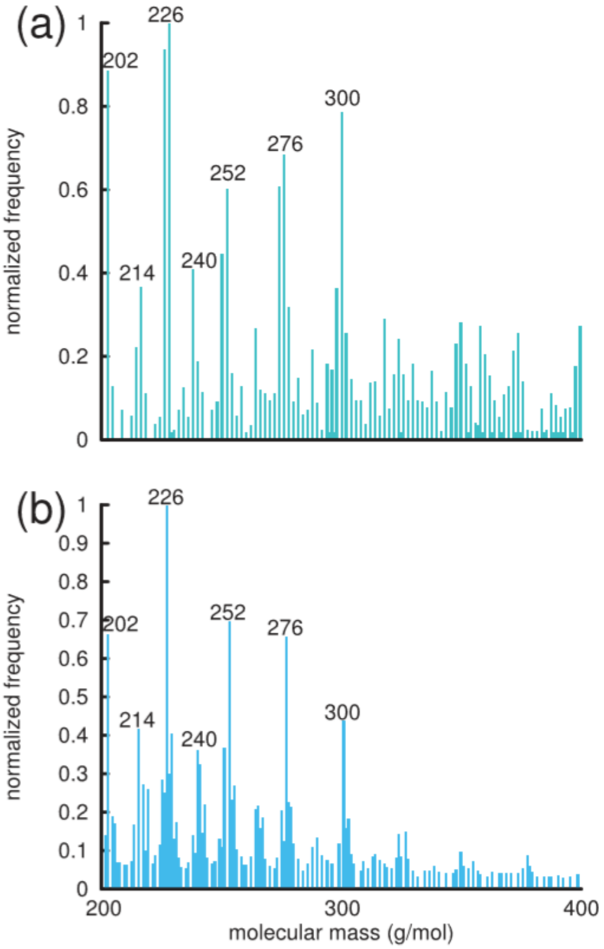

Figure 3.7: (a) Computed mass spectrum using a mixture of initial seed molecules, benzene:toluene:pyrene of 0.945:0.045:0.01. The ratios of the relative mole fraction concentrations of benzene:toluene:pyrene are 0.037:0.0018:0.00039 at the beginning of the flame where SNAPS simulation commence. The computational mass spectra are a combination of 4000 trajectories with oxygenation reactions and 6000 trajectories without oxygenation reactions. (b) Experimental mass spectrum of benzene–air laminar premixed flame [248]. SNAPS correctly predicts the dominant masses (202, 226, 252, 276, 300 amu) as well as predicting the spectrum of less abundant masses that make up the noisy bedding of the spectrum. Both sets of growth pathways work in parallel to yield an ensemble of partially oxygenated PAHs that represent the spectrum in the flame.

Chapter 4

The Formation of Oxygenated Compounds in a Premixed Ethylene-Oxygen Flame

4.1 Simulation Design

The present study involved modeling particle precursor growth in a fuel-rich sooting premixed laminar ethylene-oxygen flame. The temperature and gas-phase species concentrations inputs SNAPS requires were computed by solving the gas-energy equation using the PREMIX program in CHEMKIN [155], [247] with the gas-phase mechanism from Appel et al. [95] because it best represented an average of the speciation profiles generated when using four well validated gas-phase mechanisms (Appel et al. [95], Miller and Melius [32], Richter et al. [260], and Raj et al. [158]). PREMIX is a code first developed by Reaction Design in 2000 for computing temperature and species profiles in steady-state premixed laminar flames; it models finite-rate chemical kinetics and multicomponent molecular transport of the flame. Together with the integration solver of CHEMKIN, the PREMIX module processes the chemical kinetics, and transport properties of the simulated flame in discrete time steps. Because for this study there were no experimental speciation profiles for which to compare CHEMKIN simulations, I gathered these oft-used mechanisms and chose from them. Figure 4.1 displays the concentration profiles of a set of species from four simulations, one for each deterministic mechanism. All the mechanisms actually yielded speciation profiles very similar to each other. Ultimately, the speciation profiles when using the mechanism from Appel et al. best captured the average trends of the four mechanisms. Benzene and toluene were used as seed molecules because formation of the first aromatic ring is considered to be the first step in particle formation [29].

4.1.1 Experimental Setup

For this part of the dissertation work, I collaborated with experimentalists that recorded aerosol mass spectra sampled from the ethylene flame, using synchrotron-generated vacuum-UV (VUV) radiation for ionization, in order to compare with exact masses of the predicted chemical compositions. This enabled them to verify that the mass spectra showed masses of oxygenated species that agreed with the atomic compositions I predicted with the simulations. They also recorded X-ray photoelectron spectroscopy (XPS) spectra of samples extracted from these flames for further validation of the growth mechanisms that I proposed by comparing with functional groups of the predicted oxygenated species. The XPS measurements confirmed formation of furan precursors, hydroxyl groups, early in the particle formation process and evolution of furan signatures, ether groups, as the combustion and particles evolve.

The experimental setup consists of sampling condensed particles ex situ and capturing them on a heated plate. The plate heats up to 500K as particle start to disassociate and decompose into their constituent components. Gas-phase mass spectrometry analysis of the sublimated molecules reveals the constituent molecular details as well as information about the precursor species that participate in particle nucleation. Details of the experimental methods utilized to verify the presence of predicted oxygenated species and conformational structures can be found in reference [241].

4.2 Results and Discussion

The simulations demonstrate that oxygen addition to PAHs occurs mainly through consecutive bimolecular reactions resulting in H-abstraction followed by addition of OH or O_2 onto PAH edge sites. The most probable pathway, i.e. the dominant pathway, for embedding oxygen into the hydrocarbon molecules – that is the most frequently selected set of reactions that lead to the formation of oxygenated structures – is via ethers formed when H is abstracted from hydroxyl groups or OH/O is abstracted from peroxyl and peroxy groups, followed by hydrocarbon addition to the oxyradical and furan-ring closure. Acetylene is the most frequently added hydrocarbon; Figure 4.2 shows the reaction sequence leading to formation of a furan group discussed here. This pathway is important to a wide range of hydrocarbon oxidation processes and virtually any hydrocarbon-combustion system because of high acetylene concentrations and low reaction barriers. Thus, apart from the toxic potential of furanic species, furans may also play a dominant role in determining growth and oxidation sites of the precursors formed during combustion. Experimentalists were able to corroborate that as these oxygenated species evolve in the flame, they can become large enough to condense onto incipient particles, leading to incorporation of oxygen onto the surface. Oxygen embedded in the particle surface might contribute to gaseous oxidation products and affect the further growth and oxidation of the particle [223].

4.2.1 Electronic Structure Calculations

During the present study, SNAPS simulations revealed a significant production of furanic species. The dominant route was through oxygen addition to six-member rings on the edges of PAHs followed by acetylene addition and then unimolecular ring closure. In order to verify the validity of this pathway, I investigated that reaction pathway using first principle computational techniques. I investigated the formation of benzofuran from phenoxy + acetylene because that reaction pathway encapsulated the key reactions identified as important in SNAPS simulations and because the size of the system was reasonable for a relatively high level of theory for the electronic structure calculations. Electronic structure calculations for the relevant kinetic pathways were carried out using the CBS-QB3 method [261], [262] as implemented in Gaussian 09 [263]. The CBS-QB3 method [264] used for the electronic structure calculations involves a sequence of five calculations: (i) geometry optimization at the B3LYP/CBSB7 level of theory (i.e. B3LYP/6-311G(d,p) for the first row atoms and hydrogen) and (ii) frequency calculation followed by single-point energy calculations at (iii) CCSD(T), (iv) MP4SDQ, and (v) MP2 levels. The extrapolation method unique to CBS then gives the final zero-point corrected energies [265]. Singlet, doublet, and triplet spin multiplicities were tested for the reactant, and the lowest energy (doublet) was determined to be the ground state and thus used for all subsequent calculations. Intrinsic reaction-coordinate calculations [266], [267] were carried out at the B3LYP/CBS level to confirm the identities of the reactants and products for each optimized transition state. The potential energy diagram of the benzofuran formation pathway is shown in Figure 4.3. The high pressure limit reaction rate constants were then computed using the master equation code and software suite MultiWell [268]–[270] using canonical transition state theory.

The unimolecular rate constant for phenoxy-acetylene decomposition (backward of TS1 in Figure 4.3) was calculated at many temperatures between 300 and 2500K and modified Arrhenius parameters were fit to obtain a rate constant equation of $k = 3.773*10^{13}*T^{0.2506}*\exp(11333.67/T)\ s^{-1}$. Similarly, the recombination rate constant was defined to be $k = 2.3387*10^{6}*T^{2.1741}*\exp(10522.90/T)\ cm^{3}mol^{-1}s^{-1}$. The rate constants for both steps of the ring closure process were calculated in the same method. However, because the reaction was implemented in a single step in the mechanism, the slower of the rate constants was applied because it was the rate limiter. Interestingly, the first step (TS2) was faster than the second step (TS3) at temperatures lower than 900 K. At greater temperatures, the first step was slower. The rate constant for the first step was applied in the mechanism to represent the ring closure because modeling is conducted in temperature regimes greater than 1000 K. A similar methodology was applied to obtain the ring opening rate constants. The lower rate constant, and thus rate limiting, in the high temperature regime for ring closure was the backward of TS3 in Figure 4.3. The assigned rate constants for ring closure and ring opening were, respectively, $k = 4.728*10^{9}*10^{0.3442}*\exp(3927.03/T)\ s^{-1}$ and $k = 3.140*10^{7}*T^{1.6919}*\exp(4118.77/T)\ cm^{3}mol^{-1}s^{-1}$.

4.2.2 Evolution of OPAHs

Particle growth simulations for the premixed ethylene flame yielded six main classes of oxygenated groups: alcohol/enol, peroxy acid/radical, ketene, pyran, noncyclic ether, and furan. Alcohols/enols and peroxy acids and radicals are formed via reactions of hydrocarbons with small oxygen-containing molecules, mainly OH and O_2, and serve as precursors to the other four oxygenated groups. Section 4.2.3 has more details about enol formation in the flame.

The SNAPS simulations showed that ketenes are formed as the result of oxyradicals present on the terminal carbon of aliphatic chains. Noncyclic ethers are produced when hydrocarbons add to oxyradical sites, following three evolution pathways: (i) decomposition, (ii) continued hydrocarbon addition, or (iii) ring-closure reactions to form furan/pyran groups. Pyran groups are rare, forming when propargyl or methyl and acetylene add to oxyradicals on free-edge sites of aromatic rings, or when acetylene adds to oxyradicals on zigzag sites. Furans are much more common because the abundance of acetylene (relative to methyl and propargyl) in the gas-phase environment promotes the addition of acetylene to oxyradical sites on free-edges of PAHs which then undergo a unimolecular ring closure to form a furan. The second most common furan formation route, though much less frequent, is the addition of methoxy groups to zig-zag sites that close to form furanic groups (section 4.2.4 contains details about furans in the flame). The results also showed potential precursor molecules for formation of dioxins, species with six-member rings including two oxygen atoms. However, the code does not include any elementary reactions that close a ring containing two oxygen atoms because of their relatively unstable nature.

4.2.3 Enol Intermediates

Enols containing 6–14 carbon atoms account for ∼20% of OPAHs close to the burner, where oxygen-containing radicals are present, demonstrating that large enols are important for the chemistry of oxygenated particle precursor species. The importance of larger enols supports the findings of Taatjes et al. [271], which found a significant presence of smaller enols in premixed flames. In addition to the isomerization reactions, removal of enols may proceed via reactions with flame radicals, particularly H and OH, producing oxyradicals. Production of large enols can proceed through radical attacks on the carbon–carbon double bond of enols, followed by alkyl radical addition. Masses identified by SNAPS to contain enol contributions at small heights in the ethylene flame are 94 u (phenol), 108 u (C7H8O), 118 u (C8H6O), 168 u (C12H8O), and 192 u (C14H8O), as displayed in Figure 4.4.

4.2.4 Furanic Structures

Figure 4.5 shows some of the most common structures obtained from SNAPS at 160, 168, 194, and 220 u low in the premixed flame. Many of the ether structures formed are furan precursors. Competing reactions to furan-ring closure in the final step in Figure 4.2 includes addition of a second hydrocarbon species (Figure 4.5a and Figure 4.5b) or

H-addition forming an R–O–CH=CH2 group (Figure 4.5d and Figure 4.5f) or acetylene removal. The most common oxygenated structure at 192 u is the 194-u structure shown in Figure 4.5d with a furan ring instead of the –OCHCH2 chain; the most common structure at 158 u is the furan formed with the oxygen attached to the phenyl ring in Figure 4.5b. The species in Figure 4.5b has a ketene group at the terminal carbon of the aliphatic branch, showing that, if acetylene adds to a radical site and OH or O_2 adds to the acetylene chain, a ketene may form instead of a furan and that aliphatic side chains provide sites for the formation of carbonyl bonds.

Simulations revealed that, between a flame height of 3.5 mm and 8.2 mm, the structures in Figure 4.5a and Figure 4.5b evolved into larger furan compounds; the structure in Figure 4.5d either evolved into furan compounds (70% probability) or became deoxygenated (30%), and the structure in Figure 4.5e maintained its dibenzofuran substructure while following traditional HACA growth pathways on the other sites of the molecule. Although ethers and ketenes are common in Figure 4.5, the majority of the oxygenated compounds predicted by SNAPS at a height of 3.5 mm have furanic groups. The fraction of ethers and furans in particular among the oxygenated structures increased with increasing distance from the burner in the simulations. This result was validated by the XPS measurements which detect a greater abundance of C-O-C bonds at the expense of C-O-H and C=O bonds at lower heights.

The evolution of the structure in Figure 4.5f frequently proceeds via acetylene loss from the oxygen atom or formation of a pyran ring with the zigzag-site carbon, yielding a structure with mass 218u. The majority of the species predicted experienced molecular growth as they evolved in the flame. Furans constituted the largest group of oxygenated species at greater distances from the burner, where the flame temperature was around 1,750 K. An important furan-destruction pathway identified in the simulations is CO reactions: CO can open furan rings and abstract the oxygen atom to form CO_2, leaving the original furan ring as an aliphatic radical side chain. This oxidation mechanism may explain the observed aliphatics on the surface of particles under some conditions [69], [70], [76], [83].

4.2.4.1 Furan Formation Pathway

In Figure 4.2, an H atom is abstracted/eliminated from the aromatic ring before OH addition, because, at high temperatures, the pre-reaction complex formed from direct OH addition to an aromatic ring is unstable; above 350K the equilibrium highly favors decomposition back to the reactants [272]–[274]. In addition, electronic structure calculations have shown that benzene + OH reactions do not lead primarily to oxygen addition to benzene at high temperatures. The potential energy barrier for the benzene + OH → C_6H_5OH + H reaction proceeding via the C_6H_6OH pre-reaction complex is greater than the reaction barrier for benzene + OH → phenyl + H2O by a factor of at least 9 [273], [274], and perhaps as great as a factor of 82 [275]. Hence, H-abstraction reactions by OH are much more favorable than direct OH addition to the benzene ring [162], [273]–[275]. The substitution reaction (PAH + OH → PAH-OH + H) accounts for less than 10% of the H-atom abstraction rate, and the formation of C_6H_6OH is negligible [275]. Electronic structure calculations have also shown that the products following H abstraction (phenyl + H_2O) are 24–40 kJ/mol more stable than the products following oxygenation (phenol + H) [273]–[275]. In addition, the mole fraction of H is roughly 8–15 times higher than the OH mole fraction at the flame height where most of the oxygenation occurs, that is, between 0.5 mm and 2 mm, as shown in Figure 4.6. Hence, PAHs are predominantly activated by H abstraction in the conditions of this flame. An OH molecule can then add to the radical site on the aromatic ring. This OH group then readily and rapidly decomposes to an oxyradical + H at high temperatures [276]. This rapid decomposition leads to an abundance of active oxygen sites attached to aromatic rings, which is why the frequency of acetylene addition to the oxyradical is relatively significant; at lower temperatures, however, the alcohols are more stable.

Furanic compounds are stable at later stages of PAH growth because that time corresponds to a dearth of hydrogen radicals in the gas-phase environment. In H-rich environments, the bimolecular rate of ring opening (directly proportional to the rate constant and the concentration of H radical) is competitive with the unimolecular rate of ring closure. In the H-poor environments that exist at greater heights in the flame, the rate of ring closure is unaffected, but the rate of ring opening decreases severely. Therefore, despite the opening rate constant being four orders of magnitude greater than the closure rate constant at high temperatures, depletion of the hydrogen radical pool renders the former rate much slower and thus opening reactions less probable. Thus, the furan compounds essentially gain stability higher in the flame.

4.2.4.2 Furan Formation Kinetics

In part, this study explored the new reaction pathways for the formation and decomposition of oxygenated species using *ab initio* electronic-structure calculations to elucidate how oxygen becomes incorporated into the carbon framework of nanoparticle precursor species. The investigation revealed a generic furan-formation route with low reaction barriers involving species that are abundant in hydrocarbon flames, such as acetylene (see Figure 4.3). The reaction pathway is likely to end with a unimolecular ring closure, suggesting that there should be a high fraction of furans present among OPAHs formed during combustion. Figure 4.3 illustrates the barriers (TS1, TS2, and TS3) of the unimolecular furan-ring closure by showing the formation of benzofuran from phenoxy radical + acetylene. In SNAPS this pathway is a set of two reactions (and their reverses). The first reaction is the bimolecular addition of acetylene to an oxyradical via TS1. The first intermediate is a species in SNAPS that could undergo many distinct reactions (e.g. hydrogen addition to the terminal carbon in the chain, subsequent bimolecular addition, etc.) in addition to the second step in the pathway shown. The second step in the pathway is one SNAPS reaction that is unimolecular ring closure. This step is implemented as one reaction in SNAPS rather than two because the second intermediate species (between TS2 and TS3) is not sufficiently handled in SNAPS due to the over coordination of the ring carbon atom and the breaking of aromaticity; the only exit pathways from that well would be to the reactant or product. The implementation of this reaction sequence in one step in SNAPS neglects the potential formation of the second intermediate but is necessary because of the code’s inability to properly handle over-coordinated atoms. The energy barriers for this reaction are relatively low compared with the average temperature fluctuations in combustion environments. The low energy barriers support the frequency of these reactions being executed during simulations. Similarly, ring closure rate constants calculated in this work were comparable to, if not relatively slower than, similar reactions in the growth scheme. For example, there are 21 unimolecular ring closure reactions in the model and that which forms a furanic ring on the edge of the particle (RC19) is second slowest at 1750 K (Table 2.4). Similarly, there are 24 bimolecular addition reactions in the model and that which results in the adsorption of ethylene onto an oxyradical site (the dominant preceding reaction to furan ring closure) is the sixth slowest at 1750 K. Thus, the pathways and kinetics of furan formation are valid in a PAH growth scheme and the resulting abundance of oxygenated nanoparticle precursor species appears to have merit.

4.2.5 Impact of SNAPS Predicted Particles

Sampling the ensemble at specific flame heights and categorizing the predicted structures by mass enabled an identification of the spectrum of masses that consist of a majority oxygenated structures. That is, the simulations provided information about which masses are likely predominantly oxygenated. The simulations predicted which masses would be oxygenated if found in the experiment and what their chemical compositions and morphologies would be. Figure 4.7 shows experimental mass spectra of species drawn from three flame heights (that match the heights sampled in the SNAPS ensemble) in the premixed ethylene flame. The experimental results are consistent with the SNAPS simulations and demonstrate that a remarkably large fraction (~50%) of the mass peaks between 140 and 250 amu are associated with oxygenated species. Mass peaks identified as being associated with oxygenated species are highlighted red in Figure 4.7. The masses of these species agree with the masses of OPAHs predicted by simulations; that is, the experimentally observed and predicted species have the same atomic compositions (Table 4.1). Both the particle growth simulations and the experiments revealed that these oxygenated species are present under a very wide range of combustion conditions, suggesting that the generic formation mechanisms proposed in this study are consistent with growth in flames.

The experimental measurements were able to verify the compositions of predicted species because analysis of the simulations provided composition and exact masses of species that would be present at the given height in the flame. The knowledge of the exact mass facilitates experimental analysis in distinguishing pure hydrocarbon species from oxygenated structures because the exact mass of one carbon atom and 4 hydrogen atoms is not equal to the exact mass of one oxygen atom. The experimental techniques utilized the exact mass to distinguish between structures with the same nominal mass to verify that the OPAH structures predicted by SNAPS simulations were present in the flame. Table 4.1 contains a set of the species I predicted to be present (their chemical composition, exact mass, and the type of OPAH) along with the matching measurements from the experiment. The experimental matching verified the validity of the model predictions, the kinetic growth scheme, and the oxygenation pathways present therein.

4.2.6 Structural Predictions of Pyrene and its Isomers

Amongst the SNAPS predicted structures in the flame, of particular noteworthiness is the dearth of pyrene. Pyrene still remains a commonly discussed species because of its use in nucleation models (see section 1.2.1 for a discussion of this). Specifically, SNAPS simulations of PAH growth in the ethylene flame indicate that the mass 202 amu species observed appear to be more closely linked to anthracene than pyrene (Figure 4.8 left column). At a flame height of 3.4 mm, pyrene is only the fifth most likely (12%) isomer of 202 amu species, and 86% of 202 amu species contain at least one five-membered ring and are products of the growth trajectories of acenaphthylene (C12H8). This result can be explained by analyzing the most common growth pathways observed with SNAPS that lead to species with mass 202 amu. Starting from benzene, the initial growth pathways strongly favor the formation of a second six-member ring (naphthalene) rather than a five-member ring (indene) because the former requires the adsorption of two C_2 molecules (e.g., acetylene) on neighboring carbons while the latter requires the adsorption of either one C_3 molecule (e.g., propargyl) or one C_2 molecule and one methyl group. Because of the high concentration of acetylene relative to propargyl or methyl in the gas phase environment of this flame, bimolecular reactions involving acetylene are significantly more frequent: the probability of reactions that involve acetylene during PAH growth is about 11.3%, whereas for propargyl and methyl reactions the probability decreases to 0.008% and 0.04%, respectively. For this reason, the vast majority of nascent PAHs are naphthalene molecules, which then grow to form acenaphthylene rather than anthracene or phenanthrene because the former simply requires the adsorption of one acetylene to one of four zigzag sites of the molecule and a fast unimolecular ring closure, while anthracene or phenanthrene require the addition of two acetylene molecules on neighboring carbons. The result is that formation of acenaphthylene is about five times more likely in the lower portion of the flame than formation of phenanthrene. Hence, the pathways leading to pyrene formation are restricted, explaining the low concentration of pyrene relative to mass 202 amu structures containing at least one five-membered ring.

The precursors of species A.I and A.II (Figure 4.8) have similar concentrations. Phenanthrene, however, has two main pathways to further molecular growth, i.e., addition of one acetylene on the bay site (followed by a ring closure) to form pyrene (compound A.V), or addition of one acetylene on the zigzag sites (followed by a ring closure) to form compound A.II. Hence, the fraction of phenanthrene molecules that grow to 202 amu is divided between compounds A.II and A.V, which ensures a larger abundance of A.I than A.II or A.V.

Although pyrene appears to be insignificant among the species found in incipient particles, structure B.I in Figure 4.8 indicates that it may play a role for the continued mass growth of gas-phase species in the flames. Structure B.I, which is the most commonly predicted structure with mass 226 amu, can be formed through acetylene addition to pyrene followed by ring closure, or via acetylene addition to the bay site of structure A.II followed by ring closure.

4.2.7 Radical-Radical Recombination

During the course of the collaborative investigation, structures with masses 202 amu, 226 amu, 266 amu, and 278 amu were identified as being influential in the experimental measurements at a flame height of 3.4 mm. Simulations revealed a greater abundance of species with masses 202 amu (0.60% of total PAH species) and 226 amu (0.46%) than those with masses 266 amu (0.19%) and 278 amu (0.02%) at 3.4 mm.

However, a significant quantity of smaller (O)PAH radicals (the most common are shown in Figure 4.9) were also predicted, and, if chemically linked (i.e. radical-radical recombination reactions), they could change the amounts of the species at the four masses 202 amu, 226 amu, 266 amu, and 278 amu. A negligible amount of masses 202 amu and 226 amu are formed from PAH radical-radical combination reactions, whereas significant amounts of species with masses 266 amu and 278 amu are formed, increasing the amount of mass 266 amu by 35% and the amount of mass 278 amu by over 133% at 3.4 mm. These computational results indicate that masses 266 amu and 278 amu could have comparable concentrations to some smaller masses, such as 202 amu, at small flame heights if non-sequential growth is a factor. Moreover, in the case of 278 amu, about 93% of the species skip sequential hydrocarbon growth pathways and potentially form via PAH radical-radical combination. For species at 266 amu, about 26% could have undergone PAH radical–radical combination. The importance of the PAH radical–radical reaction pathways depends on the distribution of radical species at a given point in the flame; frequent combinations will be effective at changing the mass frequency distribution. As the concentration of PAH radicals is comparatively small, however, the most relevant effects are observed when the small collision frequency is offset by a substantial increase in mass. For these reasons, non-sequential growth via PAH radical-radical combination grows in importance with increasing height in the flame. The presence of non-sequential growth at small heights shows that fast particle precursor growth pathways could play a role at lower flame heights. Continued growth of PAHs in simulations with flame height also suggests that it is conceivable that these and similar pathways also remain active higher in the flame. The hints at non-sequential growth made possible by recombination of (O)PAH radicals in the flame is a growth scheme that shows promise and is worth exploring further.

4.3 Summary and Conclusions

This study utilized SNAPS and the novel oxygenation/hydrocarbon growth scheme previously validated to investigate the evolution of particle precursors in a premixed laminar ethylene-oxygen flame. The simulations revealed a significant quantity of oxygenated species, including alcohols, enols, ketones, ethers, pyrans, and notably, furanic compounds. The investigation presented support for a generic furan formation pathway that involves the creation of enols, followed by acetylene addition to oxyradical sites forming ethers, and eventually furan ring closure on the edge of PAHs. As PAHs progress up the flame via bulk flow, enols are first produced in great quantity, are chemical precursors to ethers, and eventually furans higher in the flame. First principle energy and rate constant calculations supported the likelihood of the pathways due to low reaction barriers and fast kinetics. The rate constants for the furan forming pathways were slower than comparable pathways leading to pericondensed carbon rings in the mechanism.

With the detailed structural and compositional information presented, I was able to collaborate with experimentalists who validated the significant presence of OPAHs predicted with simulation and verified the presence of enols at low heights and furans at higher heights. Experimental measurements enabled us to match the compositions of specific oxygenated structures I predicted would exist at specific heights in the flame with techniques that deduced the exact masses of species they observed. This also confirmed the prediction that approximately 50% of all masses (nominal) of precursors between 140 and 350 amu in the flame contained some amount of oxygenated content. Given specific conformations predicted by simulations, the collaboration led to confirmation of those species in the flames. This is a very significant finding for the community. The presence of oxygenated structures in quantities equal to or slightly greater than pure hydrocarbon PAHs suggests that future studies of nanoparticle formation and growth during combustion should consider how oxygenated structures form, behave, and how their presence may influence particle formation processes.

4.3.1 Contributions and Collaborations

- Demonstrated for the first time the presence of specific OPAHs in a premixed ethylene flame

- Showed likely dominant pathway leading to the formation of ethers and furanic compounds ranging from 100 to 500 amu, highlighting the significance and importance of kinetic pathways leading to the formation of oxygenated rings
- Reported the stability of furanic compounds in high temperature flame based on thermodynamic properties and kinetics
- Showed for the first time that smaller enols may be key precursors of larger ethers and furans in premixed ethylene flame
- Predicted morphologies of dominant structures at specific oxygenated enols, ethers, and furans in the flame
- Conducted ab initio quantum calculations leading to a report of the only electronic structure energy landscape of phenoxy + acetylene complex
- Utilized Master Equation methodologies to calculate and report the only kinetic reaction rates of phenoxy + acetylene complex
- The radical-radical combination material discussed in section 4.2.7 is generated by SNAPS simulations and is the sole work of this author
- In this chapter, experimental work reported was conducted by collaborators Olof Johansson and Hope Michelsen at the Combustion Research Facility of Sandia National Laboratories
- Columns 2-4 of Table 4.1 were the result of work from experimentalists in attempt to match the simulation predictions generated by this author reported in columns 5 and 6 of Table 4.1
- Distinguishing between oxygenated and non-oxygenated PAHs in the flame was the result of the simulation predictions of structures, produced by this author

Tables

Table 4.1: Analysis of mass peaks. Columns 5 and 6 are my predictions based on analysis of SNAPS simulations. The first four columns are the verifications as measured by the XPS experiment.

Mass, amu	Constituents based on mass	Residual*, amu	Fit accuracy^	SNAPS prediction	Predicted structure
Mass peaks related to oxygenated species					
144.0658	C10H8O	0.0082	0.0054	C10H8O	Furan
146.0699	C10H10O	0.0033	0.0077	C10H10O	Ether
160.0478	C10H8O2	0.0046	0.0049	C10H8O2	Ether, ketene, furan
182.0737	C13H10O	0.0006	0.0033	C13H10O	Furan
184.0602	C12H8O2	0.0078	0.0075	C12H8O2	Furan
194.0738	C14H10O	0.0007	0.0035	C14H10O	Ether, furan
196.0820	C14H12O	0.0068	0.0039	C14H12O	Ether
198.0587	C13H10O2	0.0094	0.0041	C13H10O2	Furan
208.0841	C15H12O	0.0047	0.0046	C15H12O	Furan
218.0942	C13H14O3^{+}	0.0001	0.0021	C16H10O	Furan
220.0851	C16H12O	0.0037	0.0041	C16H12O	Ether
234.0843	C13H14O4^{+}	0.0050	0.0062	C16H10O2	Furan
Mass peaks related to pure hydrocarbon species					
102.0528	C8H6	0.0058	0.0028	C8H6	Phenylacetylene
141.0705	C11H9	0.0000	0.0027	C11H9	Aromatic with aliphatic chain
152.0568	C12H8	0.0058	0.0016	C12H8	Acenaphthylene
178.0748	C14H10	0.0035	0.0023	C14H10	Aromatic with aliphatic chain
190.0736	C15H10	0.0047	0.0020	C15H10	Aromatic with methyl chain
216.0866	C17H12	0.0073	0.0015	C17H12	Aromatic with aliphatic chain
226.0814	C18H10	0.0069	0.0012	C18H10	Aromatic

*The residual is the absolute difference between the peak location of the Gaussian fit to the mass peak and the mass derived from the sum of the atomic masses.

^The fit accuracies are 95% confidence intervals of the center position of the fitted Gaussian functions (i.e., the measured species mass).

$^{+}$These formulas are highly hydrogenated and have few carbon atoms compared with those of similar masses. It is likely that the real structures, as the SNAPS simulations predict, have higher carbon contents and fewer hydrogen and oxygen atoms. The actual mass peaks may, however, contain signal from species with different atomic compositions. If none of these species completely dominates the signal, the mass suggested by the Gaussian fit might not precisely match any of the signal-contributing atomic combination.

Figures

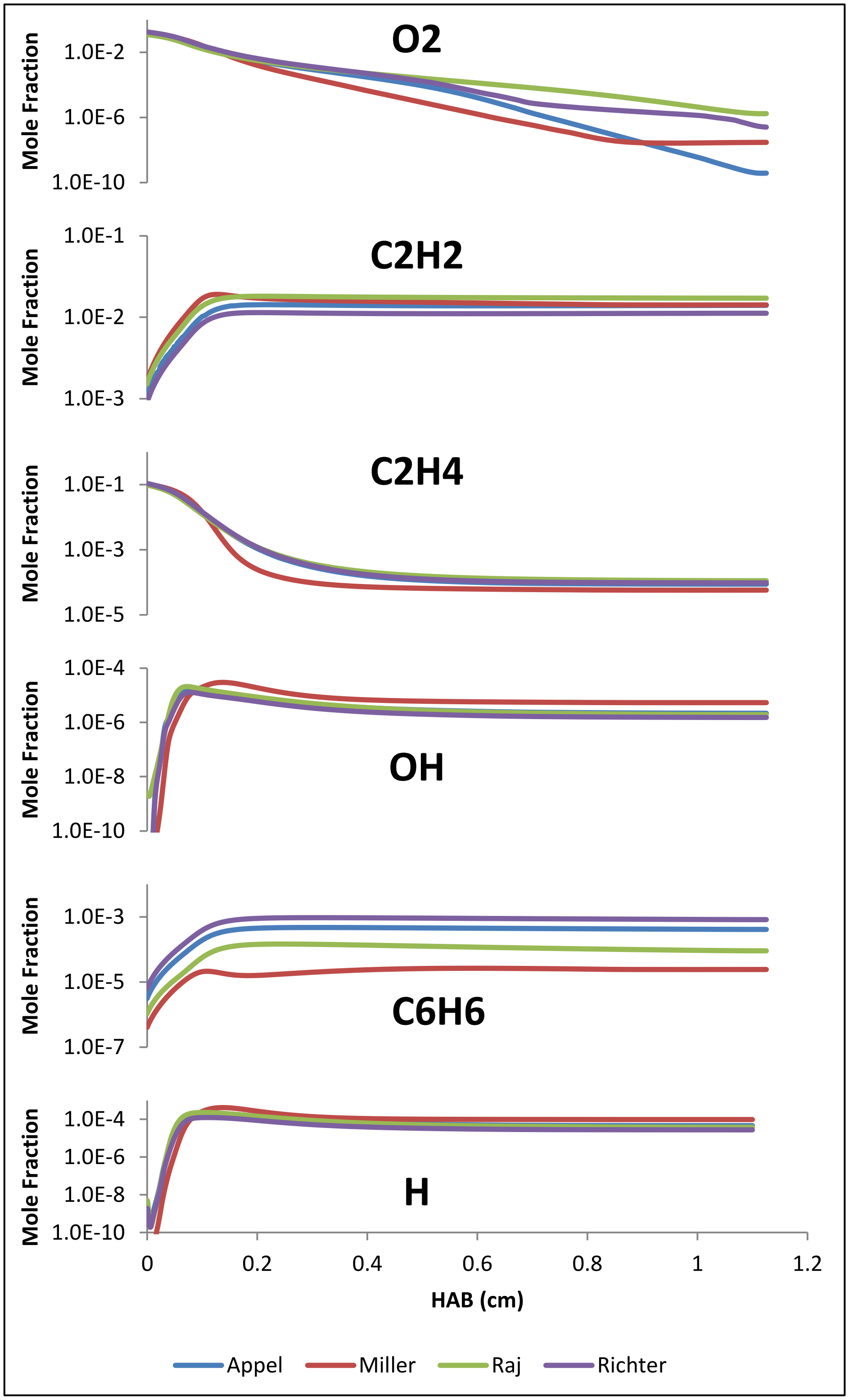

Figure 4.1: Simulated concentration profiles of key species from the premixed laminar ethylene flame. Four distinct deterministic mechanisms were utilized in identical

simulations using CHEMKIN [155]: Appel et al. [95], Miller et al. [32], Raj et al. [158], and Richter et al. [260]. Of the four, all were relatively similar for the entire set of species. Miller et al. is the least like the other three. Of the set, the mechanism from Appel et al. most closely captured the average of the species concentrations and profiles.

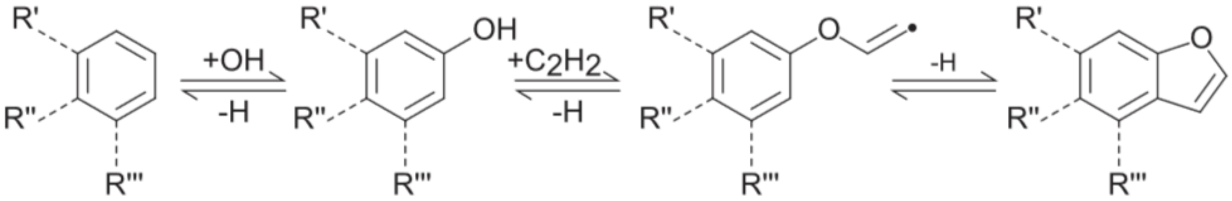

Figure 4.2: Most probable reaction sequence leading to formation of a furan group. (Left to Right) H-abstraction followed by OH addition to the radical free edge site on an aromatic ring; H-abstraction from the OH group, followed by acetylene addition, forming an ether group; H-elimination during ring closure to form a furan group. The left side of the molecule has been left attached to an indeterminate PAH backbone to illustrate an arbitrary molecular size.

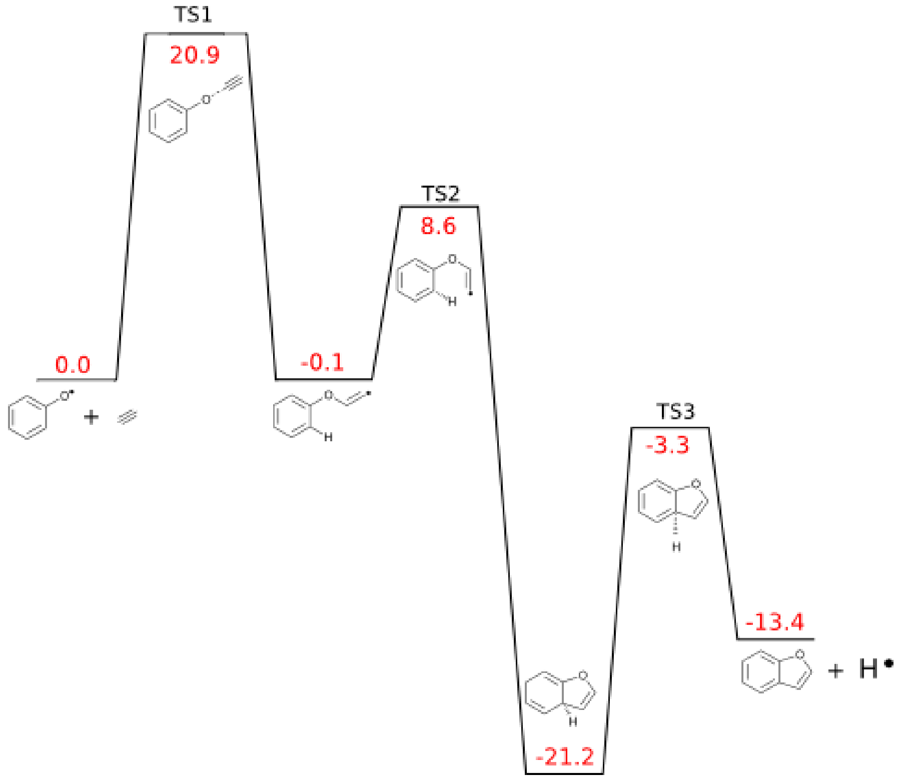

Figure 4.3: Potential-energy diagram for the formation of benzofuran. The energies are in kilocalories per mole and are referenced to the reactant species. The ring-closing reaction is exothermic, and the closed-ring structure is thus favored over the phenoxy + acetylene reactants as well as the open-ring structure (first intermediate). In SNAPS the first reaction (TS1) is distinct from the second reaction (TS2 and TS3). The first reaction is a unimolecular acetylene addition to an oxyradical and the second reaction is a unimolecular ring closure to form a furan ring (steps TS2 and TS3 are treated as one reaction in SNAPS because the second intermediate structure would only go to the product or the first intermediate due to the unique nature of the over coordination and loss of aromaticity of the structure). The energy barriers of the ring closure reaction steps are low compared with the average temperature fluctuations in flames. For example, at 1,500 K, TS2 is $3k_BT$ and TS3 is$-1k_BT$ with respect to the first intermediate species.

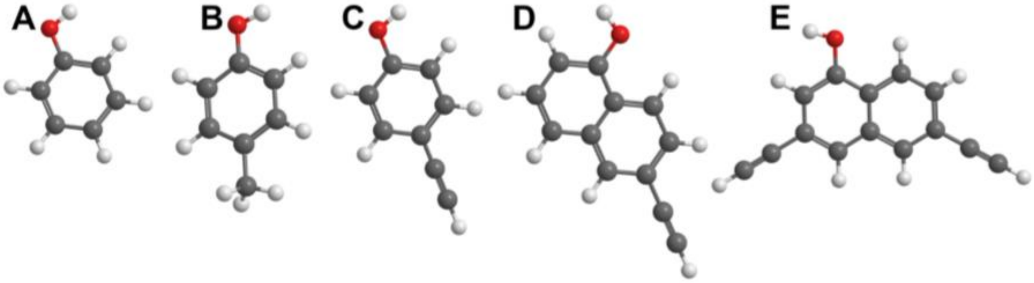

Figure 4.4: Enols predicted by the SNAPS simulations. Enols predicted to be important to the OC chemistry at small DFFOs in premixed combustion are (A) 94 u (phenol), (B) 108 u (C_7H_8O), (C) 118 u (C_8H_6O), (D) 168 u ($C_{12}H_8O$), and (E) 192 u ($C_{14}H_8O$).

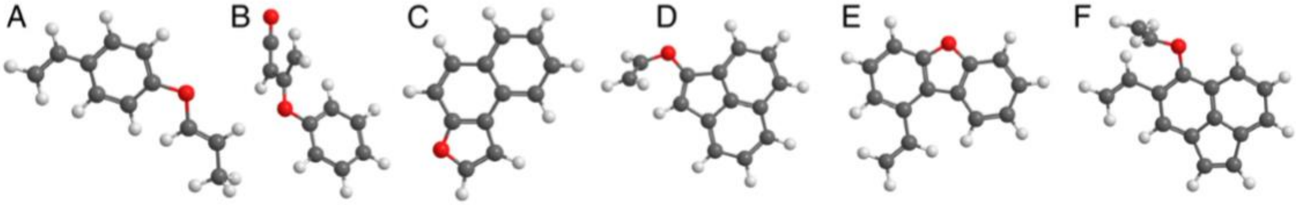

Figure 4.5: Frequently predicted oxygen-containing structures of selected masses low in a premixed flame. Red atoms, oxygen; gray, carbon; white, hydrogen. (A and B) Ether and ether/ketene, 160 u. (C) Furan, 168 u. (D and E) Ether and furan, 194 u. (F) Ether, 220 u.

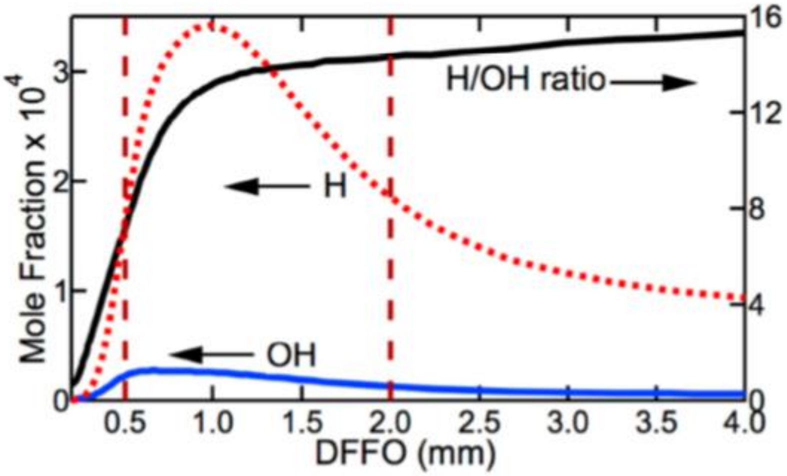

Figure 4.6: Predicted H and OH mole fractions at low flame heights in the Ar-diluted premixed flame using the Appel–Bockhorn–Frenklach deterministic mechanism [95]. The ratio between the H and OH mole fractions is also shown. The vertical dashed lines are the edges of the region where the majority of the oxygenation occurs, according to the SNAPS simulations.

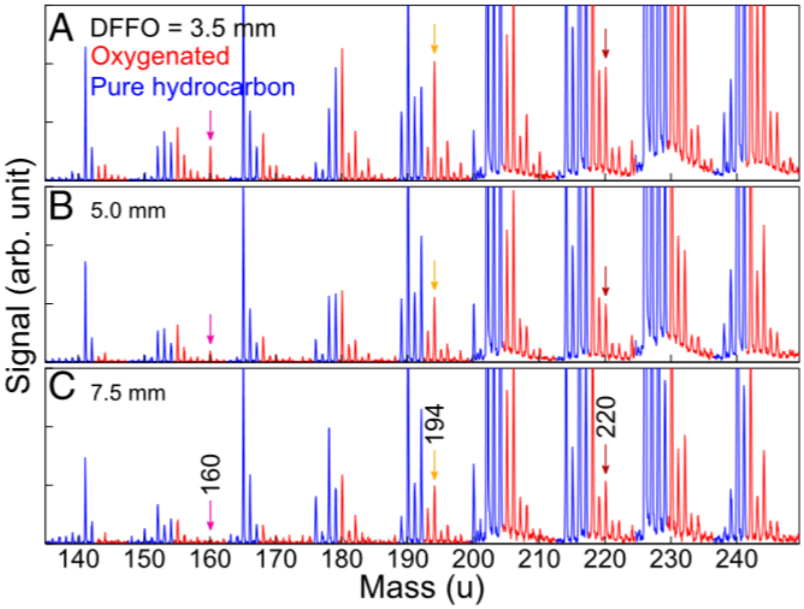

Figure 4.7: Experimental AMS spectra from a premixed flame as measured by Michelsen and coworkers [241]. Mass spectra are shown for particles extracted from selected heights in the flame; that is, DFFOs of (A) 3.5, (B) 5.0, and (C) 7.5 mm. Red peaks contain signal from oxygenated species. The arrows indicate the peaks at 160, 194, and 220 u for comparison with Figure 4.5 where one can see the main predicted structures at a DFFO of ~3.5 mm.

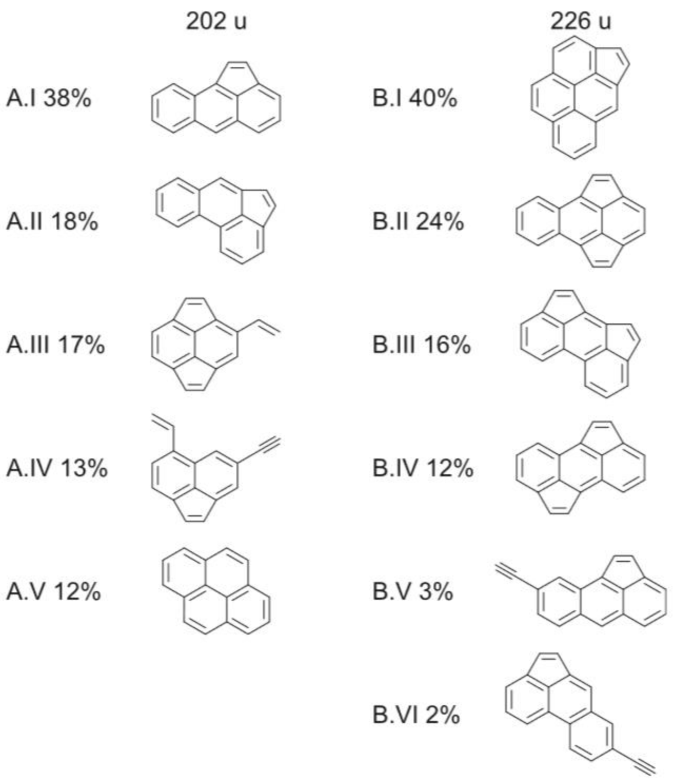
202 u
226 u
A.I 38%
B.I 40%
A.II 18%
B.II 24%
A.III 17%
B.III 16%
A.IV 13%
B.IV 12%
A.V 12%
B.V 3%
B.VI 2%

Figure 4.8: Relative concentrations of the most abundant species with mass 202 u (left) and 226 u (right) at a DFFO of 3.4 mm computed by SNAPS. These species account for 98% of all 202-u species and 97% of all 226-u species at 3.4 mm.

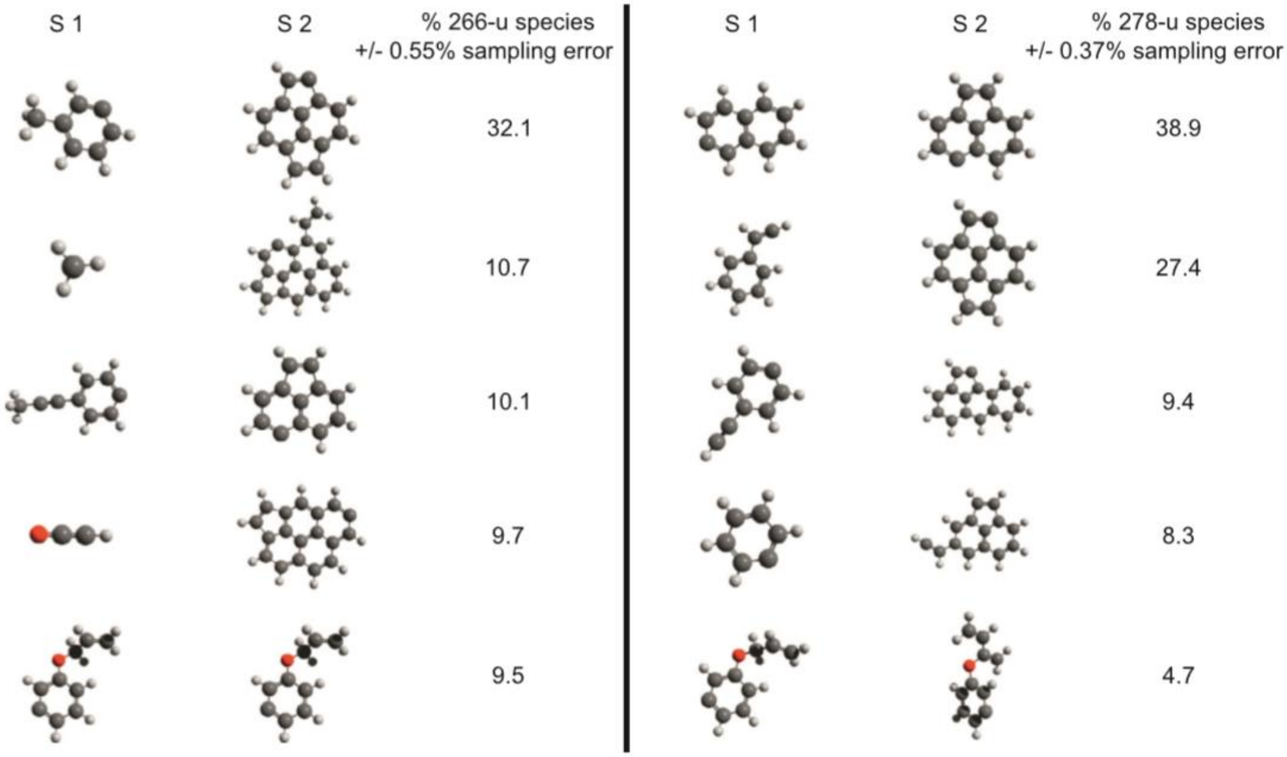
S 1
S 2
% 266-u species
+/- 0.55% sampling error
32.1
10.7
10.1
9.7
9.5
S 1
S 2
% 278-u species
+/- 0.37% sampling error
38.9
27.4
9.4
8.3
4.7

Figure 4.9: SNAPS results showing the five most common pairs of radicals that combine to make structures at 266 u and 278 u at a DFFO of 3.4 mm in the premixed flame. These reactions account for 72% of all combined structures at 266 u and 89% of all combined structures at 278 u.

Chapter 5

Effect of Oxygenated Fuels on PAH Growth and Particle Formation in Ethylene Flames

In order to investigate the impact of oxygenated fuel chemistry on the growth pathways of particle precursor molecules, this study details analysis of ethylene–air and ethylene/ethanol–air premixed laminar flames [234]. Recent work has suggested the addition of ethanol alters the particle size distributions in flames, yet provides no information about the effect on particle precursor species [78], [239]. The chosen flames make for an interesting case study to investigate the mechanisms leading to the formation of nanoparticles because they present similar measured temperature profiles as well as the same equivalence ratio and carbon flow rate, thus ensuring a similar gas-phase environment between the flames. The measured particle size distributions (PSDF), however, differ dramatically [234]: ethanol doped ethylene flames showed less total particulate volume fraction and smaller mean size of particles when compared with the pure ethylene flame. Additionally, the appearance of bimodal distribution in the PSDF of the pure ethylene flame disappears altogether when the fuel is doped with 30% ethanol. These systems enable isolation of the effect of an oxygenated dopant and oxygen concentration on the evolution of PAHs and the formation of nanoparticles.

To study these systems, the study utilized a combination of tools to investigate the differences in the gas phase growth chemistry of particle precursors and their aggregation propensity. Surprisingly, the study revealed that in the flame systems [234], the addition of ethanol as a dopant increases the concentration of species that are generally thought to lead to conventional particle precursors, but particle growth was instead hampered by lower rates of oxygenation of the larger precursors. The study identified several oxygenation pathways that significantly accelerate the rate of growth of PAHs by embedding oxygen atoms into the molecular structures, which in turn can affect their nucleation propensity. Increased oxygenation spurs increased generation of actives sites on the surface of PAHs which enables faster rate of growth and consequently increases particle formation. Specifically, deviation from stabilomer structures introduced by oxygenation, the formation of five-member rings, and aliphatic chains greatly reduces the stabilization of non-chemically bonded aggregates, even for fairly large precursor structures (greater than 650 amu). We propose, however, a different mechanism by which molecules can reach remarkable size (higher than 1500 amu) quite early in the flame.

5.1 Simulation Design

The gas-phase chemistries of the atmospheric premixed laminar flames studied by Salamanca et al. [234] and Wu et al. [235] were modeled using CHEMKIN-PRO [155] and a reaction mechanism developed by D’Anna and Kent [277] amended with the ethanol oxidation reaction scheme from Marinov [278]. The ethylene-air (pure) and ethanol/ethylene-air (doped) flames from [234] have identical carbon flow rates, equivalence ratios of 2.01, gas velocities of 10.0 cm/sec, and very similar measured temperature profiles (see Figure 5.1a). The ethylene-air and ethanol/ethylene-air flames from [235] both have the same equivalence ratio of 2.34, carbon flow rates, and similar measured temperature profiles. For both systems the measured temperature profiles was used as input to CHEMKIN. The primary flame system [234] is that in which SNAPS was employed modeled the PAH growth using the novel oxygenation-hydrocarbon mechanism. The primary experimental flame system was more interesting to model PAH evolution because the pure ethylene flame generated more particles (as expected) despite the decrease in “traditional” particle precursor species, e.g. acetylene and benzene, as shown in Figure 5.2 and Figure 5.3. The secondary flame [235] system was involved in the study to justify the choice of deterministic mechanism and the validity of the CHEMKIN flame simulation that was used to collect gas-phase information used as SNAPS input data.

5.1.1 Primary Flame System

The primary flame system [234] consisted of two ethylene flames, one pure and the second doped with ethanol. In the doped flame the amount of ethanol added was equal to 30% of the total carbon feed. The equivalence ratio was constant at 2.01. A fixed temperature profile from the experimental data was inputted for each respective flame with a pressure of 1.0 atm. The height of the burner was set to 15.0 mm with an inlet velocity of 10.0 cm/sec for both flames. For the pure ethylene flame (EF), the normalized reactant mole fractions were 0.692 N_2, 0.184 O_2, and 0.123 C_2H_4. For the ethylene flame doped with 30% ethanol, the normalized reactant mole fractions were 0.692 N_2, 0.184 O_2, 0.086 C_2H_4, and 0.037 ethanol. For both flames, the maximum number of grid points allowed was 250 with the number of adaptive grid points equal to 10. The adaptive grid control based on solution gradient and curvature were set to 0.1 and 0.5, respectively.

The gas-phase solver PREMIX in the CHEMKIN [155] software suite was used to model the gas-phase environment of all the flames in the current work. The gas-phase kinetic mechanism is a merger of the small PAH mechanism by D'Anna and Kent [277] and the ethanol sub-mechanism by Marinov [278]. The average measured temperature of the flames is 1687K and 1705K for the pure ethylene and ethanol doped flames, respectively. The doped flame has a consistently higher simulated axial velocity, which leads to a shorter residence time for the gases flowing up through the flame as shown in Figure 5.1a and Figure 5.1b, respectively.

5.1.2 Secondary Flame System

The secondary flame system [235] consisted of two ethylene flames, one pure and the second doped with ethanol. In the ethanol doped flame the ethanol was added in an amount such that 10% of the total weight of oxygen atoms was bound to ethanol fuel molecules. Both flames had identical cold flow temperatures and flow rate and an equivalence ratio of 2.34. A fixed temperature profile from the experimental data was used in CHEMKIN simulations for each respective flame with a pressure of 1.0 atm and the burner height was set to 20 mm. For the pure ethylene flame, the normalized reactant mole fractions were 0.679 N_2, 0.181 O_2, and 0.141 C_2H_4. For the ethylene flame doped with 28.8% ethanol by weight, the normalized reactant mole fractions were 0.679 N_2, 0.181 O_2, 0.113 C_2H_4, and 0.028 C_2H_5OH. For both flames, the maximum number of grid points allowed was 250 with the number of adaptive grid points equal to 10. The adaptive grid control based on solution gradient and curvature were set to 0.1 and 0.5, respectively. The pure ethylene and ethanol doped flames of the secondary flame system [235] were modeled in the same manner and with the same gas-phase mechanism [277], [278] as the flames in the primary flame system [234].

5.2 Results and Discussion

5.2.1 Gas-phase Modeling

The first step in this study was to compute the gas-phase environments of the two flames (pure and doped) studied by Salamanca et al. [234] (primary flame system). Since there are no experimental data available for the gas-phase species in this flame, I analyzed a second set of ethylene and ethylene/ethanol premixed flames reported by Wu et al. [235] (secondary flame system) to assess the validity of the gas-phase kinetic mechanism selected for this study.

5.2.1.1 Primary Flame System

An interesting result of the experiment conducted in the primary flames [234] is that a smaller particulate volume fraction and particle sizes were observed in the doped flame, despite the fact that the gas-phase modeling for the same system shows consistently higher concentrations of all the conventional aromatic precursors, single-ring aromatics, and small multiple-ring aromatics (see Figure 5.2 and Figure 5.3). This result suggests that the link between small aromatics and large particles is not straightforward and the presence of more benzene and acetylene in the gas-phase does not necessarily lead to formation of more particles.

For example, the pure ethylene flame has a consistently higher O_2 concentration (between 0.5-4 orders of magnitude, see Figure 5.2a and Figure 5.2g) and a consistently lower C_2H_2 concentration (about 0.5 orders of magnitude, see Figure 5.2b). Rates of production analyses showed that the higher level of C_2H_2 in the ethanol doped flame is initially due to a greater concentration of O_2, OH, H, and O species which interact with C_2 species to form acetylene. It is consistent in both flames, however, that at greater heights acetylene reaches equilibrium with other small carbon species, accounting for the relatively constant concentrations of acetylene with height in each flame.

The pure etheylene flame also has less benzene, toluene, naphthalene, acenaphthylene, and indene (about a half order to one order of magnitude, see Figure 5.3) that is a direct result of the flame having a lower concentration of acetylene and propargyl species. In the deterministic gas-phase mechanism [277] acetylene and propargyl are the precursors to benzene and benzene is the precursor to toluene, naphthalene, acenaphthylene, indene, phenanthrene, and pyrene. Rates of production analyses demonstrated that the relative rates and pathways are the same for producing the aromatics and PAHs; therefore a reduced production of conventional aromatic precursors, e.g. acetylene and propargyl, leads directly to fewer aromatics. Additionally, similar trends are evident in the SNAPS simulations wherein evaluation reveals a greater number of small PAHs in the ethanol doped flame and larger HMAMs (and thus a higher overall average aromatic mass) in the pure ethylene flame.

5.2.1.2 Secondary Flame System

The secondary flame system served to validate the choice of deterministic mechanism because I observed the opposite trends of small aromatics and acetylene as those observed in the flames of [234], and match those of the experiment in [235]. The gas-phase mechanism thus adequately captures the trends of the key species and small aromatics. Figure 5.4 shows the trends of the secondary flame system. In particular, the trends of the gas-phase simulation of the flames from the secondary system [235] match those of the experiment. Specifically, there is a slightly higher relative concentration of acetylene, benzene, toluene, indene, naphthalene, and acenaphthylene over the height of the flame.

Furthermore, the gas-phase mechanism reproduces well the relative concentrations of small and large PAHs as measured in the experiment. Figure 5.5 displays comparisons of experiments and predicted concentrations. As defined by the experimentalists [235], small PAHs are the sum of benzene and naphthalene because they are the expected dominant one- and two-ring aromatics, and large PAHs are the sum of the three- and four-ring aromatics, namely acenaphthylene, phenanthrene, and pyrene. For both sets of PAHs, they measure a greater concentration in the pure flame consistently throughout all heights of the flame. Similarly, the gas-phase model predicts a greater concentration of small and large PAHs in the pure flame. The model even captures the slight concavity of the profile in the small PAHs and the near linearity of the large PAH profiles. The comparisons highlight the ability of the oxygenation/hydrocarbon mechanism developed in this dissertation to capture the main trends of small and large aromatic compounds, as well as the effect of ethanol doping in the fuel on the evolution of PAHs.

The D'Anna and Kent mechanism [277] captured the trends for the key species in both the flames in the primary system as well as both the flames in the secondary system. Thus, though the gas-phase trends are counter-intuitive in the primary set of flames, the ability of the gas-phase mechanism to capture the opposing trends in the secondary flames demonstrates the validity of the gas-phase CHEMKIN modeling to be used as input into SNAPS simulations.

5.2.2 Fuel Effects on Growth Rate of Particle Precursors

I used the computed gas-phase species concentrations and experimental temperature profile along the centerline of the pure and doped flames studied by Salamanca et al. [234] as inputs for SNAPS. The results of SNAPS simulations, in particular the average mass (shown in Figure 5.6, filled symbols) are in agreement with the experimental observations, as the particles in the doped flame grow markedly less compared to the ones in the pure flame. The plot also highlights that the crucial region for the chemical growth of the HMAMs – species produced by SNAPS with mass greater than the original seed (benzene and toluene in this study) – is clearly in the first two millimeters above the burner. The analysis of the most common reactions in this region shows that SNAPS predicts faster growth in the pure flame because of the higher concentrations of gas-phase O_2, OH, and O as compared to the doped flame. Figure 5.2a, Figure 5.2e, and Figure 5.2f display the concentration profiles of those species.

To confirm that the oxygen chemistry has a significant impact on the chemical growth, I repeated the SNAPS simulations without including the oxygenation pathways developed in this dissertation work (open symbols, labeled as HC-only in Figure 5.6). When using this reduced mechanism containing only the hydrocarbon pathways of the PAH mechanism, the average growth of HMAMs is remarkably slower as compared to the full oxygenation/hydrocarbon mechanism. By the end of the flame (15 mm from the burner), when accounting for oxygenation pathways, the average mass of HMAMs in the pure flame is 430 u greater than the case without oxygen chemistry. For the doped flame the difference is 166 u. These results show not only the importance of the oxygenation reactions, but also the extraordinary sensitivity of particle precursor formation to the oxygen species present in the gas phase. The fast growth observed in the first two millimeters above the burner is due to an environment rich in oxygen and radicals (e.g., H, OH, O) that promotes formation of active sites and chemical reactivity [25], [122]. When oxygen chemistry is neglected, acetylene addition dominates the growth, but, when oxygen chemistry is accounted for in a PAH growth mechanism, addition of O_2 and OH are competitive with acetylene addition.

The lower gas-phase O_2 and OH concentrations in the first two mm of the doped flame compared to the pure flame partially leads to the difference in HMAMs growth in these flames. Analysis of the reactions occurring during SNAPS simulations shows that, in the first mm of the flames, HMAMs in the pure flame undergo gas-phase oxygen addition reactions 2.6 times more frequently than in the doped flame, and undergo hydrocarbon addition to active oxygen sites 3.5 times more frequently.

Moreover, the portion of hydrocarbon-to-active-carbon addition reactions is only slightly higher in the pure flame. The temperature of the flames is relatively equal (Figure 5.1a). Thus, the key factor driving the faster rate of mass growth in the pure flame is the higher (roughly three times) number of mass-growing reactions that occur in the same time interval due to the higher concentration of gas-phase O_2, O, OH, and H in the pure flame below two mm. For further details about comparisons of reactions between flames see section 5.2.3, Figure 5.7 and Figure 5.8.

The rate of growth of HMAMs slows down considerably above two mm. Analysis of the most frequent reactions from two to 15 mm reveals that HACA [122] pathways dominate the growth of HMAMs for both flames in this region. Since the doped flame has a consistently higher concentration of acetylene (Figure 5.2b), there are 1.7 times more acetylene additions per HMAM in the former flame, which accounts for the faster rate of growth. However, the rate of growth above two mm, is dwarfed by the rate of growth below two mm due to the much smaller radical pool which spurs the creation of active sites and thus continued growth on HMAMs.

It is worth noting that there is a sensitivity of the SNAPS results to the variations in the gas-phase concentrations. This is true for bimolecular reactions that are linearly dependent on gas-phase concentrations. However, since the probability of selecting the top 10 most frequent reactions with SNAPS spans three orders of magnitudes, a change in species concentration of even one order of magnitude will affect the relative importance of the associated reaction, but it will still be among the fastest. At the same time, a reasonable variance in temperature of ± 60K due to experimental uncertainty would lead to a fluctuation of 30% or less in the rates of the fastest reactions in the reaction network. This latter value is in turn much less than the variance in the rates amount the set of reactions (several orders of magnitude) and thus the dominant growth pathways are not significantly affected by a potential temperature uncertainty associated with the experiments.

The key insight is that only when accounting for the potential oxygenation of the particles, as done in the growth scheme developed in this work, can models begin to fully capture the growth mechanisms of particle precursors in flames. The oxygenation pathways present in the growth model are what differentiate the growth and molecular characteristics of PAHs in the two flames. Without the insight of the oxygenation pathways a model is unable to capture the distinguishing aspects of the sets of HMAMs and one would be unable to hypothesize about why there is greater particle production in the pure ethylene flame.

5.2.3 Characteristics of Precursors in the Flames

The HMAMs in the pure ethylene flame are larger on average than in the ethanol doped flame because the growth pathways amongst particle precursors differ slightly between the flames. In particular, the distinctions between the sets of OPAHs in the two flames are highlighted by the stark differences in molecular structure and composition. For example, note the ratios of carbons to hydrogens (C/H ratios) and carbons to oxygens

(C/O ratios) on each HMAM at several heights in the flames. Figure 5.7 portrays the average C/H and C/O ratios for the set of trajectories in the SNAPS ensembles for each flame. Given the collection of HMAMs in each flame, those in the pure flame show an appreciably higher C/H and appreciably lower C/O ratio over the entire length of the flames. This measurement demonstrates that HMAMs in the pure flame tend to evolve by adding fewer hydrogen atoms and more oxygen atoms (in net, accounting for the difference between addition and removal/abstraction reactions) than HMAMs in the ethanol doped flame. This is due to the greater preponderance of hydrogen abstractions below 2mm in the pure ethylene flame which is due to the slightly higher concentration of H and OH radicals in that range. The higher preponderance of active sites on the HMAMs in the pure ethylene flame creates more opportunity for oxygenation of those molecules (mainly OH, O, and O_2 additions) and thus there is a lower measured ensemble averaged C/O ratio amongst the HMAMs in the pure ethylene flame. Additionally, the higher relative concentration of acetylene in the ethanol doped flame ensures the rate of acetylene additions is slightly faster in that flame than the pure ethylene flame and subsequently partially responsible for the higher C/O ratio amongst HMAMs in the ethanol doped flame.

One additional characteristic worth noting is the ratio of oxygenation to carbonation reactions that the HMAMs experience. Oxygenation is defined as the net gain (or loss) of oxygen atoms to the HMAM via a kinetic reaction. Carbonation is defined as the net gain (or loss) of oxygen atoms to the HMAM via a kinetic reaction. That is, a reaction can result is the addition or subtraction of an atom from the HMAM. The net is the difference between addition and loss of the specific atom types. Analyses can track these throughout the duration of each trajectory and compile an average for the entire ensemble (for each flame). A reaction where a carbon and an oxygen atom are ejected from the HMAM will account for a net loss for both the oxygenation and carbonation values. I tracked both the non-cumulative values for net oxygenation and carbonation as well as the cumulative values. The ratios are presented in Figure 5.8. Non-cumulative values are isolated to 1 mm height windows (e.g. 0.5-1.5 mm HAB, 1.5-2.5 mm HAB etc.). Cumulative net oxygenation and net carbonation values are tracked during the duration of the flame such that the value at HAB 14 mm is biased by the sum of the values up to that point.

The higher net oxygenation to net carbonation ratios of the HMAMs in the pure flame shown in Figure 5.8a and Figure 5.8b are a result of the higher rate of net oxygen addition reactions in said flame. Specifically, the greater relative concentration of O_2 and OH in the pure ethylene flame leads to a higher ratio as seen in Figure 5.8b. The trends of the non-cumulative net oxygenation to net carbonation ratios are directly correlated to the O_2 profiles in each flame. Because the ethanol doped flame has a relative O_2 concentration one to three orders of magnitude lower than pure ethylene flame the ratio of oxygen addition to oxygen removal reactions in much lower in the former flame resulting in ratio that approaches zero four mm before that in the pure ethylene flame (long dashed pale blue line vs. solid dark red line in Figure 5.8b). The lower net oxygenation to net carbonation ratio of the HMAMs in the ethanol doped flame results in the higher C/O ratio seen in Figure 5.7b and the lower ensemble averaged mass (Figure 5.6) of the HMAMs in that flame.

The increased rate of growth of particle precursor molecules in the pure ethylene flame as compared to the doped flame is directly correlated with the increased concentration of O_2 and OH in the flame environment which leads to a higher oxygenation rate of the molecules in the pure flame. The higher rate of oxygenation leads to more active sites and more reactive species (and lower C/O ratios) and subsequently faster growth and growth to much larger sizes. These molecular trends are consistent with the experimental measurements of greater particle production in the pure ethylene flame compared to the doped flame. This is all true despite the higher concentration of conventional particle precursor species like acetylene and benzene in the gas-phase environment of the doped flame. This computational modeling of (O)PAH growth in laminar premixed flames suggests that the kinetic growth pathways are much more complex than the traditional hydrocarbon pathways and that oxygenation pathways are an important defining characteristic of the evolution of particle precursors.

5.3 Summary and Conclusions

The present study investigated the impact of oxygenated fuel chemistry on the growth pathways of particle precursor molecules in ethylene–air and ethylene/ethanol–air premixed laminar flames [234]. Experimental analysis of the two flames revealed that the addition of ethanol reduced the particle sizes and particle numbers but provided no information about the effect on particle precursors. The ethanol doped ethylene flame showed less total particulate volume fraction and smaller mean size of particles than the pure ethylene flame. Additionally, the appearance of bimodal distribution in the PSDF of the pure ethylene flame disappears altogether when the fuel is doped with 30% ethanol. The chosen flames were an interesting case study to investigate the mechanisms of PAH growth leading to the formation of nanoparticles because they present similar measured temperature profiles as well as the same equivalence ratio and carbon flow rate, thus ensuring a similar gas-phase environment between the flames. Simulations using the oxygenation/hydrocarbon mechanism developed in this work enables one to isolate of the effect of an oxygenated dopant on the evolution of HMAMs and the formation of nanoparticles.

Surprisingly, gas-phase CHEMKIN modeling revealed that the addition of ethanol as a dopant increased the concentration of species that are generally thought to lead to conventional particle precursors, e.g. benzene and acetylene. However, PAH modeling using SNAPS and the new oxygenation/hydrocarbon mechanism revealed that particle formation was likely hampered by lower rates of oxygenation of PAHs. The lower PAH oxygenation rates were more significant than the reduced abundance of gas-phase acetylene and benzene in the doped flame. The study identified several oxygenation pathways that significantly accelerate the rate of growth of particle precursors by embedding oxygen atoms into the molecular structures, which in turn affect their nucleation propensity. Increased oxygenation spurred increased generation of actives sites on the surface of PAHs which enabled faster rate of growth and consequently likely leads to increased particle formation.

5.3.1 Contributions and Collaborations

- Using deterministic CHEMKIN models, demonstrated that very similar ethanol doped ethylene flames can yield different speciation profiles
- Demonstrated that measured differences in particle yield between pure ethylene flame and ethylene-ethanol flame can only be captured if considering oxygenated PAH growth pathways
- Used newly developed kinetic growth mechanism to show that PAHs grow quicker and to much larger sizes because of the oxygen chemistry
- Used the simulations to highlight the importance of oxygen chemistry in the first two mm above the burner in both ethylene and ethylene-ethanol flames
- Reported that, contrary to conventional thought, the most crucial species affecting PAH growth in premixed flames are O, OH, and O2, not acetylene and propargyl
- For the first time showed that C/O ratio of PAHs is directly correlated with average mass and rate of growth in premixed ethylene and ethylene-ethanol flames
- All the material presented in this chapter is the sole work of this author

Figures

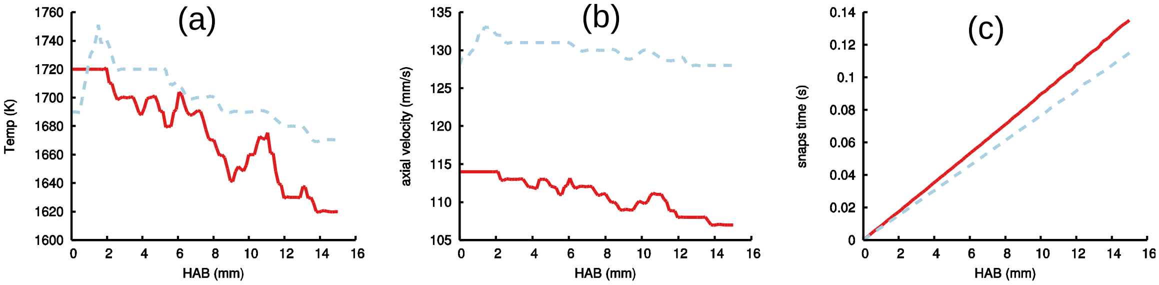

Figure 5.1: Red solid lines represent the pure ethylene flame and blue dashed lines represent the ethanol doped flames. (a) Temperature profile obtained from the Salamanca et al. [234] (b) Axial velocity of the flames as modeled in with the CHEMKIN PREMIX [155], [247] software. (c) Residence time of the gases in the flames. The residence time is shown to highlight that particles have almost equal residence times in the flames to grow, thus differences in SNAPS simulations is not due to residence time.

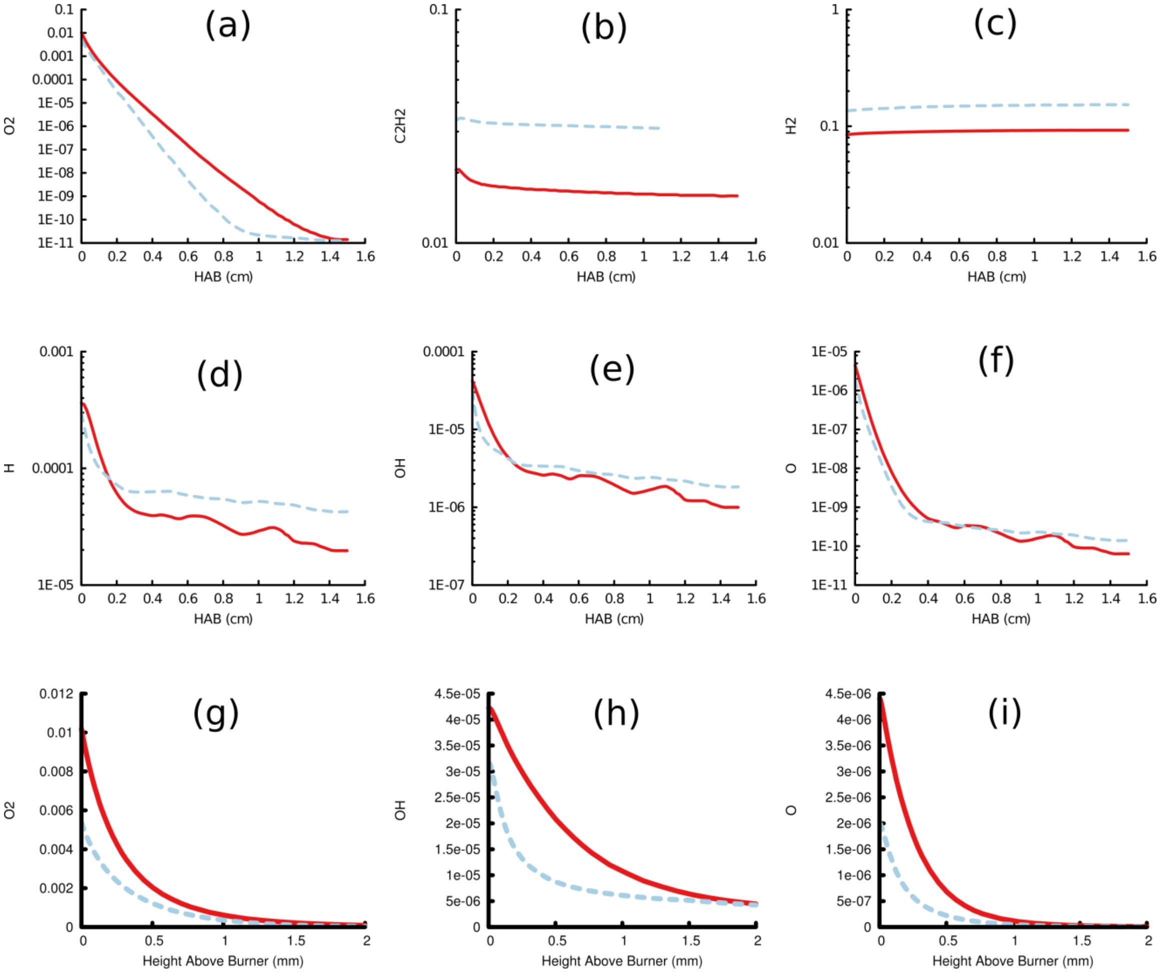

Figure 5.2: Species profiles of the pure ethylene (solid red lines) and ethanol doped (dashed blue lines) flames from [234] simulated in CHEMKIN [155], [247]. (a) O_2, (b) C_2H_2, (c) H_2, (d) H, (e) OH, (f) O, (g) O_2 0-2mm only, (h) OH 0-2mm only, (i) O 0-2mm only. The latter three are presented for qualitative clarity at HAB less than 2 mm.

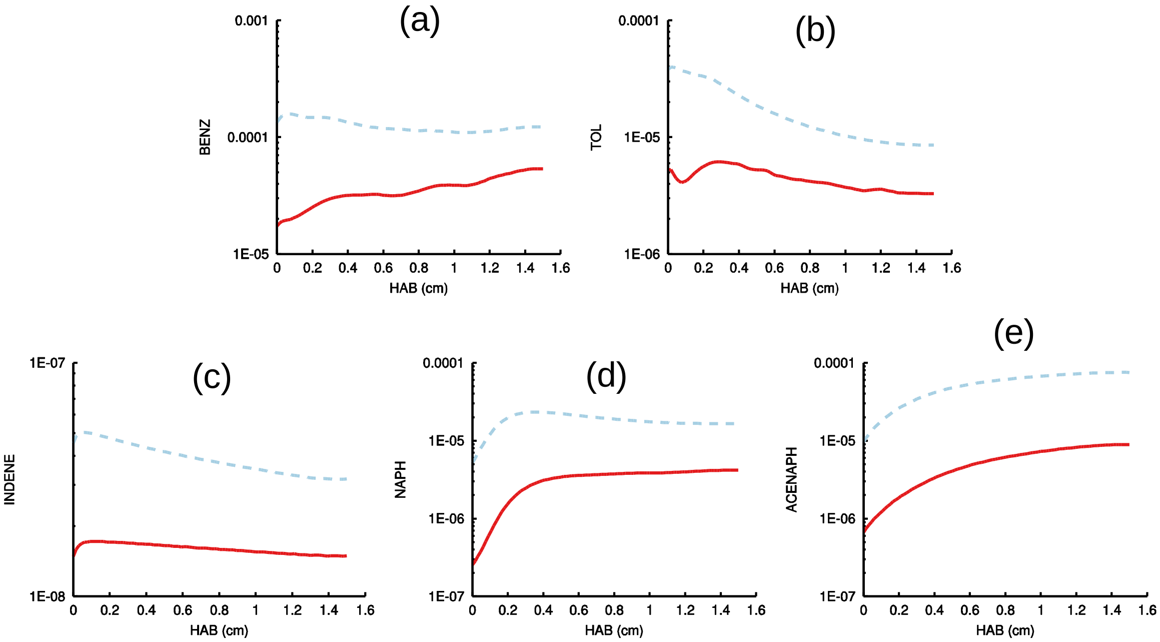

Figure 5.3: Species profiles of the pure ethylene (solid red lines) and ethanol doped (dashed blue lines) flames from [234] simulated in CHEMKIN [155], [247]. (a) benzene, (b) toluene, (c) indene, (d) naphthalene, (e) acenaphthylene. The ethanol doped flame has consistently higher concentrations of small aromatics than the pure ethylene flame.

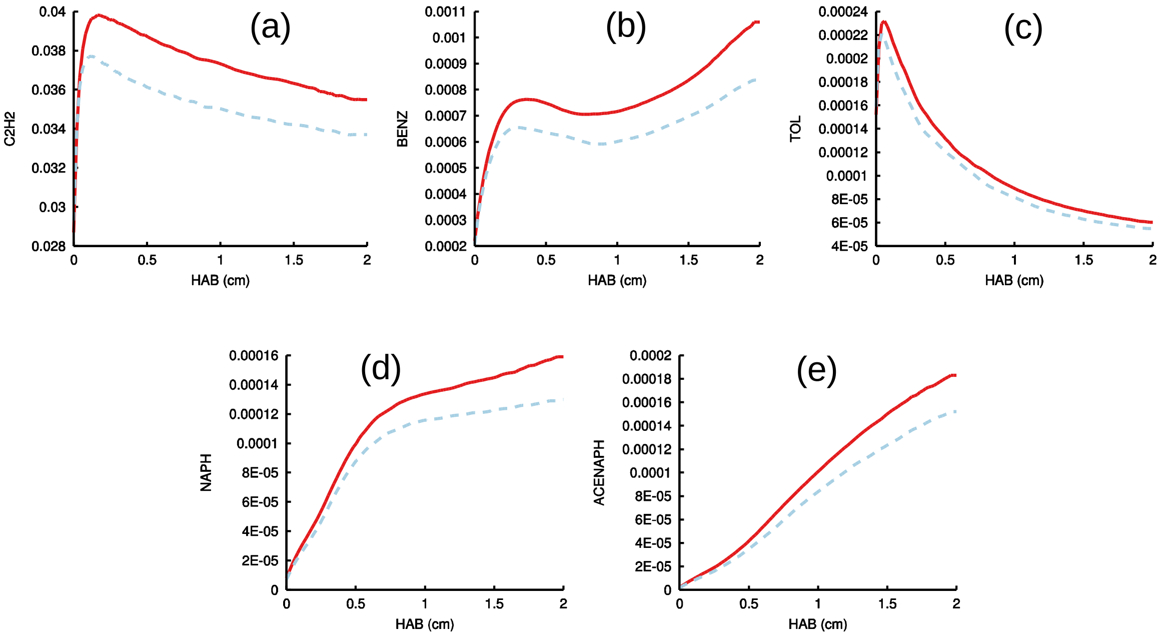

Figure 5.4: Species profiles of the pure ethylene (solid red lines) and ethanol doped (dashed blue lines) flames from Wu et al. [235] simulated in CHEMKIN [155], [247]. (a) C_2H_2, (b) benzene, (c) toluene, (d) naphthalene, (e) acenaphthylene. The pure ethylene flame has consistently higher concentrations of acetylene and small aromatics than the ethanol doped flame.

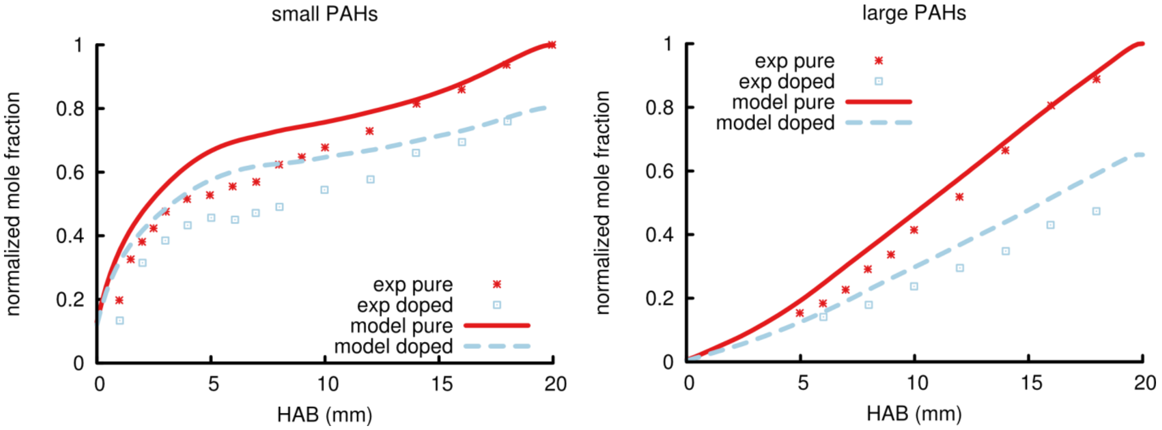

Figure 5.5: Small (left) and large (right) PAH profiles of the pure ethylene (experiment: red star symbols, gas-phase model: solid red lines) and ethanol doped (experiment: blue square symbols, gas-phase model: dashed blue lines) flames from Wu et al. [235] and simulated in CHEMKIN. The pure ethylene flame has consistently higher concentrations of small and large PAHs. The model captures that as well as the general shape of the profiles (slight concavity around five mm in the small PAH profiles and near linearity in the large PAH profiles). As defined in reference [235], the profiles are normalized by the final concentration of the pure flame. That is, the models are normalized by the concentration at 20 mm in the pure flame, and the sets of experimental data are normalized by the concentration at 20 mm in the pure flame.

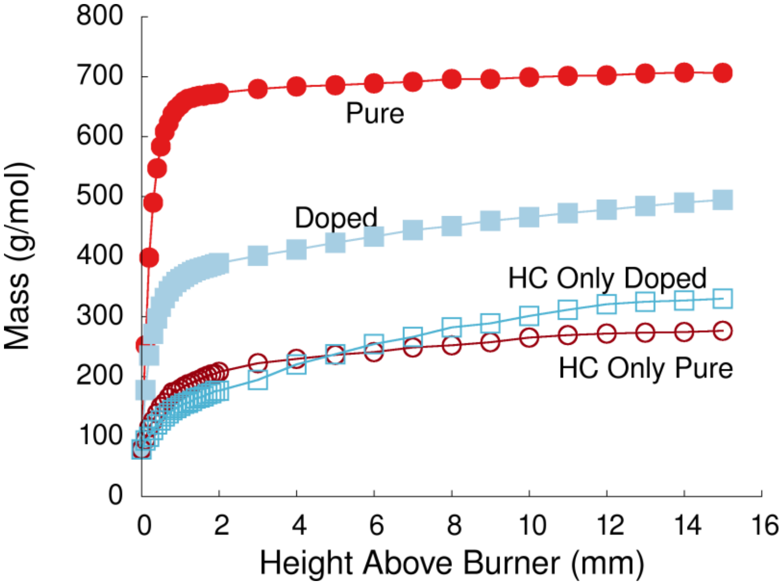

Figure 5.6: Average mass of an ensemble of HMAMs generated using SNAPS in the pure flame (circles) and doped flame (squares). Closed and open symbols represent simulations with the oxygen/hydrocarbon and the reduced (hydrocarbon only, no oxygenation pathways) growth mechanism, respectively. Each line is obtained by

averaging 11000 trajectories (oxygen/hydrocarbon mechanism) or 1000 trajectories (HC only). The 99% confidence interval for the ensemble mean was calculated for all data points. The largest range for each ensemble is: ±6.1 u (pure flame with full mechanism), ±3.9 u (doped flame with full mechanism), ±12.9 u (pure flame with partial mechanism), and ±16.6 u (doped flame with partial mechanism).

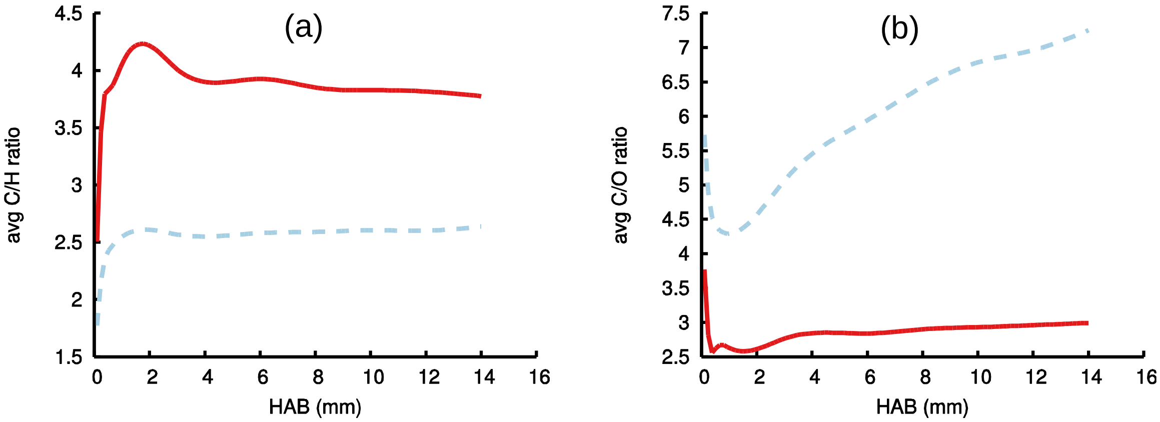

Figure 5.7: Ensemble average C/H (a) and C/O (b) ratios of the HMAMs predicted by SNAPS for the pure ethylene (solid red lines) and ethanol doped (dashed blue lines) flames from [234]. At each height every HMAM trajectory is sampled and a molecule-specific C/H and C/O ratio is calculated; the ratios are then averaged to create the plotted profiles. The sampled heights for both methods were 0.1, 0.2, 0.5, 1, 3, 6, 8, 10, 12, and 14 mm HAB.

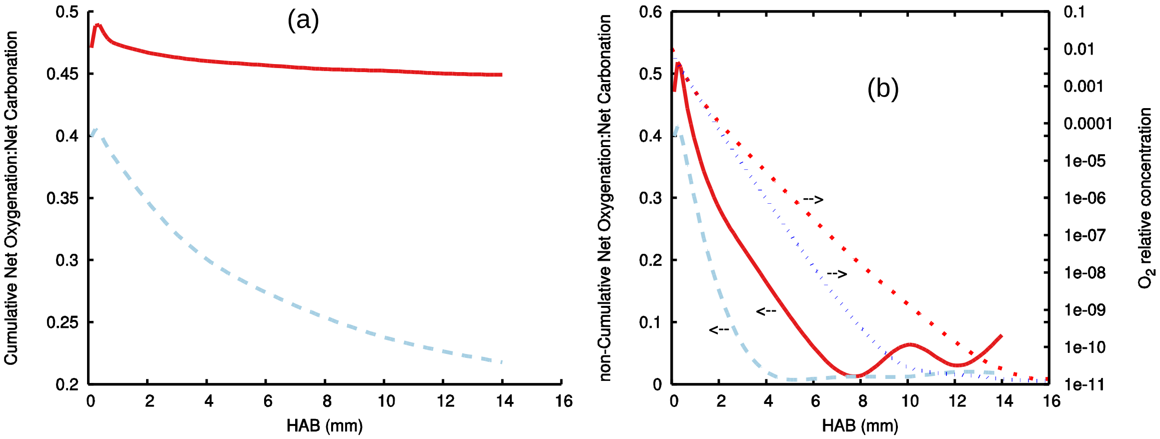

Figure 5.8: Ensemble average ratios of net oxygenation to net carbonation in the pure ethylene (solid red lines) and ethanol doped (dashed blue lines) flames of [234]. Reported are both the cumulative ratios (a) as well as the non-cumulative ratios (b left y-axis) overlaid with the relative O_2 concentrations of the flames (b right y-axis). The medium dashed bright red line represents the O_2 profile of the pure ethylene flame and the dotted

bright blue line represents the O_2 profile of the ethanol doped flame. Net oxygenation accounts for the difference in reactions that add oxygen atoms to the HMAM and those that remove or abstract oxygen atoms (including the number of oxygen atoms involved in the reaction). Similarly, for net carbonation, but with carbon atoms. The cumulative ratios (a) involve accounting for all reactions in all SNAPS trajectories up to that height in the flame. The non-cumulative ratios involve accounting for all reactions in all SNAPS trajectories only in the range of the sampled height, i.e. from midway between the previously sampled height and the current sample height to midway between the currently sampled height and the next height to be sampled. The sampled heights for both methods were 0.1, 0.2, 0.5, 1, 3, 6, 8, 10, 12, and 14 mm HAB. The calculation heights are intentionally more compacted from 0 to 2 mm because the HMAMs were shown to undergo a much faster rate of growth in that region. It is noteworthy that both flames show their highest oxygen addition to carbon addition ratios at 0.2 mm (second height represented) and the ratios quickly become smaller with flame height. This parallels the rate of growth of HMAMs as functions of height of the flame; in particular that the fastest rate of growth was between 0.1 and 0.5 mm.

Chapter 6

Conclusions and Recommendations for Future Work

With the goal of illuminating the chemical growth process preceding the formation of carbonaceous nanoparticles during flame synthesis, this dissertation work explored the formation and growth of oxygenated aromatic precursor species. This study investigated chemical growth pathways of particle precursors and provided considerable evidence outlining the integral role that oxygen chemistry plays in the evolution of PAHs and the formation of particles in premixed flames. This dissertation work utilizes stochastic computational modeling techniques to characterize the formation, chemical growth, and composition of OPAHs for the first time. Detailing the importance of oxygen chemistry in premixed flames represents an important step toward elucidating the morphologies and kinetic growth pathways of OPAHs in addition to ascertaining the effects oxygenated fuels have on particle precursors and particle formation.

The hypothesis that particle precursor species could be oxygenated rather than purely hydrocarbons was to be tested in this work. The first step was the creation of a set of kinetic pathways for particle precursor molecules that accounted for oxygen chemistry and to design a growth mechanism for particle precursors that included the oxygen chemistry as well as conventional hydrocarbon chemistry. The mechanism comprised an intricate set of pathways incorporating previously proposed reaction schemes as well as those proposed in this work. The mechanism was designed to be used in a previously developed stochastic simulator such that reactions not be limited to specific reactant species, but rather act on sub-structures within a reactant species. The mechanism comprised 70 new reversible elementary reaction types that involved oxygenation or oxidation. Where appropriate, reaction rate constants from analogous reactions were assigned to newly proposed oxygenation reactions. However, six reaction rate constants for two key oxygenation pathways were calculated using first principle quantum methodologies. Rate constants for forward and reverse reactions were assigned independently, and care was taken to ensure thermodynamic consistency for paired reactions.

The existing code was modified significantly in order to accommodate the newly designed mechanism. The model was validated against deterministic models and experiments. The simulations conducted matched experimental data, e.g. mass spectra and chemical composition as determined from mass spectrometry, as well as deterministic simulations of small PAH profiles in premixed flames. Validation in a sooting benzene flame revealed that the newly designed oxygenation pathways are integral to the formation of large particle precursors and capturing complex mass spectra profiles. Similarly, oxygenation pathways work synergistically with traditional hydrocarbon pathways; the set of pathways are intertwined and work in parallel.

The new simulator and growth mechanism was utilized to model kinetic evolution of PAHs in premixed ethylene flames in an effort to predict the oxygenated compounds in the flame and help ascertain if they are present in particulates captured and analyzed *ex* *situ*. Simulations predict, for the first time, an abundance of PAHs with oxygen embedded in the molecules and reveal their dominant kinetic formation pathways. Several oxygenated functional groups, including enols and ethers, are identified as being abundant in smaller molecules ranging from approximately 100 amu to 300 amu and serving as stepping stones to larger OPAHs up to 1000 amu that can contribute to particle formation. Simulations predicted specific morphologies of PAHs present at particular heights in the flame. XPS techniques conducted by collaborators were able to validate the presence of specific structures for the first time.

Simulations elucidated the effects of oxygenated fuels on particle production in premixed flames. Oxygenation pathways prove to be the key to differentiating between PAH growth in ethylene flames with and without ethanol dopant. Thus, only with the reaction mechanism developed in this work can simulations capture variance in rates of particle precursor formation which lead to variance in particle formation rate and particle sizes produced in the flames. Additionally, simulations revealed that PAHs grow in specific regions of the flame. In premixed flames where the temperatures rise quickly near the burner surface, there are an abundance of radicals generated by fuel oxidation that aid in PAH growth. Hydrogen radicals play a significant role in generating active sites on the edge of small aromatics that are then available for interaction with oxygen, hydroxyl, and acetylene. As the pool of radicals is reduced, PAH growth slows significantly. Importantly, this study revealed that the reduction of oxygen and OH is the most significant factor in reducing the rate of PAH growth in premixed ethylene. This suggests that the concentration of small carbon species, though a factor, is not the sole driving force behind PAH growth.

In general, the major species predicted by simulations of premixed flames contrast with the commonly held assumptions of PAH growth; across aliphatic and aromatic flames and a broad range of C/O ratios, there is a significant presence of oxygenated compounds. Furthermore, the present work supports a prominent role of the HACA growth scheme while demonstrating the breadth of additional pathways involved in PAH growth and highlighting the importance of oxygen chemistry on the evolution of particle precursors and impact on particle formation. This dissertation reveals previously unexplored chemistry of PAHs and further informs the understanding of their growth and influence on particles in premixed flames. In particular, the set of particle precursor species is much more broad and complex than previously considered and the expansive set of (O)PAHs has diverse effect on particle nucleation. This work synthesized theoretical, computational, and experimental methods to motivate future investigations concerning the evolution of key molecular precursors and nanoparticle formation in combustion.

Further studies using the methodology established in this work could explore the effects of oxygen-rich environments on the evolution of large PAHs, in the vein of experiments wherein mature particles are exposed to oxygen-rich environments in order to facilitate size reduction caused by oxidation chemistry. Oxidation chemistry abstracts carbon from particle surfaces resulting in less total particle mass. Results presented in this dissertation hint that these types of reactions are applicable to large PAHs as well. However, in the set of premixed flames simulated, the environments quickly became oxygen deficient due to the fuel-rich nature of the flames. Thus a study where large PAHs and oxygen are abundant in large quantities in the same spatial region might provide useful information. If PAHs are reduced in size prior to particle nucleation, the effects on particle sizes might be significant. Similarly, oxygenation of PAHs may have a significant influence on particle nucleation.

The presence of OPAHs hints that traditional concepts of particle nucleation, namely physical bonding of pericondensed PAHs, are not a full description of the mechanism. Oxygenated structures likely affect physical bonding because of their polarity compared to pericondensed structures. Recent work that has investigated the dimerization stability of PAHs could be extended to include oxygenated structures to ascertain the effect of oxygenated functional groups on the process. The presence of OPAHs may also affect alternative particle formation mechanisms dependent on chemical reactivity.

The radical-radical combination method for non-sequential PAH growth presented in this dissertation can be extended to model particle nucleation. A future study could utilize the methodology to test the hypothesis that particles are likely to form through chemical reactions alone rather than a combination of chemical and physical bonding. The probability of bonding between PAH radicals is greater than the probability of physical sticking occurring for equivalent molecules, which suggests that particle nucleation may be feasible with relying on physical sticking.

Though the work presented here constitutes advancement towards elucidating the mechanisms of particle precursor growth in flames, there is much room for improvement to the modeling methodologies and approaches. Because information about the gas-phase environment is required as an input to the PAH modeling code, there are limited combustion scenarios applicable to model PAH growth. For example, the code has not been utilized to predict PAH growth and inform particle production during operation of internal combustion engines because detailed temporal and spatial gas-phase data is difficult to obtain. Reactive computational fluid dynamic (CFD) simulations that couple the flow-field with gas-phase data promise to expand the capabilities of PAH modeling. Large deterministic mechanisms are not plausible to combine with CFD simulations because of the computational expense. Therefore, the stochastic code, if coupled with detailed data of the environment during internal engine combustion, could yield valuable information about the process of precursor growth and particle formation.

Additionally, the kinetics in the mechanism could be extended to include low temperature chemistry. Currently, low temperature environments result in very little molecular evolution because the slow kinetics result in large time steps and few reaction events. Low temperature chemistry would greatly benefit the software because it would extend the applicable set of combustion scenarios in which PAH modeling would be applicable. Similarly, the kinetics could be extended to include sulfuric and metallic chemistry towards the goal of modeling a wider variety of nanoparticles produced during combustion and manufacturing processes. Additionally, the most computationally expensive aspect of the code is geometrical optimization of molecular configurations. Great efficiency could be gained by isolating the component of the target molecule that was affected by a reaction event and limiting the geometrical optimization to that component such that computational time isn't wasted re-optimizing unaltered geometry.

In total, the work presented in this investigation represents and advancement towards elucidating the mechanisms of particle precursor growth in flames and their impact on particle formation. The novel insight into the chemical pathways of PAH growth in laboratory-scale flames contributes significantly to understanding the mechanisms of formation and composition of particle precursor species. This atomistic modeling provides detailed information about the particle formation process that greatly benefits the community and provides a level of detail difficult for experiments to capture. This work therefore has a considerable impact on efforts to curtail emissions of harmful aromatic content and nanoparticles generated during combustion.

Appendix

Table A.6.1: List of all reactions in the new SNAPS mechanism corresponding to Table 2.4. All reactions are listed in descending order of rate coefficient evaluated at 1750 K within each class. Oxygenation reactions and hydrocarbon reactions are highly interconnected. Units for the pre-exponential factor (“A” column) are s^{-1} for unimolecular reactions and $cm^{3}*s^{-1}*mol^{-1}$ for bimolecular reactions. Units for the activation energy (“Ea” column) are kcal/mol.

Reaction name in SNAPS	Abr.	A	n	Ea	Reaction Description	order	Source
Habs_fromO_byC2H3	HAB1	6.0000E+14	0.000	0.000	C2H3(g) + Car(-O-H) = Car(-O*) + C2H4(g)	bi	[252]
Habs_fromO_byOH	HAB2	2.9500E+06	2.000	-1.312	OH*(g) + Car(-O-H) = Car(-O*) + H2O(g)	bi	[230]
Habs_fromO_byH	HAB3	1.2000E+14	0.000	12.400	H*(g) + Car(-O-H) = Car(-O*) + H2(g)	bi	[252]
Habs_fromO_byO	HAB4	2.8100E+13	0.000	7.532	O*(g) + Car(-O-H) = Car(-O*) + OH(g)	bi	[230]
Habs_byOH	HAB5	8.6517E+02	3.040	3.675	Car(-H) + OH(g) = Car(*) + H2O(g)	bi	[136]
Habs_fromO_byphenyl	HAB6	4.9000E+12	0.000	4.400	C6H5(g) + Car(-O-H) = Car(-O*) + C6H6(g)	bi	[252]
Habs_fromO_byHO2	HAB7	1.0000E+12	0.000	1.000	HO2(g) + Car(-O-H) = Car(*) + H2O2(g)	bi	[252]
Habs_byH	HAB8	6.4600E+07	1.860	15.976	Car(-H) + H(g) = Car(*) + H2(g)	bi	[279]
Habs_byCH3	HAB9	8.9000E+02	2.890	15.992	Car(-H) + CH3(g) = Car(*) + CH4(g)	bi	[136]
Habs_fromO_byO2	HAB10	1.0000E+13	0.000	38.000	O2(g) + Car(-O-H) = Car(*) + HO2(g)	bi	[252]
Hremoval_zigzagR5_anyltoene	HAB11	1.0000E+10	0.219	25.540	Cal*-CH = Cal=Cal + H*(g)	uni	[132]
remove_H_from_Oar	HAB12	6.4450E+16	-0.414	88.127	Car(-O-H) = H*(g) + Car(-O*)	uni	Eq
remove_H_from_Oal	HAB13	8.9460E+31	-4.717	98.357	Cal(-O-H) = H*(g) + Cal(-O*)	uni	Eq
add_H_to_Oar	HAD1	2.5000E+14	0.000	0.000	H*(g) + Car(-O*) = Car(-O-H)	bi	[252]
add_H_to_Oal	HAD2	3.4700E+29	-4.303	10.230	H*(g) + Cal(-O*) = Cal(-O-H)	bi	[252]
addH_fromH2	HAD3	9.2300E+04	2.386	5.815	Car(*) + H2(g) = Car(-H) + H(g)	bi	[136]
addH_fromH2O	HAD4	5.5900E+00	3.573	8.659	Car(*) + H2O(g) = C(-H) + OH(g)	bi	[136]

addH_fromCH4	HAD5	2.1600E+01	3.218	6.921	Car(*) + CH4(g) = Car(-H) + CH3(g)	bi	[136]
addH_zigzagR5_enetoanyl	HAD6	2.7000E+09	0.454	1.820	Cal=Cal + H*(g) = Cal*-CalH	bi	[132]
Htransfer_rev_ethenylbenz	HT1	2.3200E+10	0.693	25.934	Car(*) + Cal(-H) = Car(-H) + Cal(*)	uni	[136]
Htransfer_ethenylbenz	HT2	5.9000E+10	0.547	27.566	Car(-H) + Cal(*) = Car(*) + Cal(-H)	uni	[136]
Htransfer_rev_zigzagrad_ethenyl	HT3	3.2200E+06	0.927	7.384	Car(*) + Cal(-H) = Car(-H) + Cal(*)	uni	[132]
Htransfer_zigzagrad_ethenyl	HT4	1.2200E+06	1.000	8.007	Car(-H) + Cal(*) = Car(*) + Cal(-H)	uni	[132]
Htransfer_fromC_toO	HT5	1.2200E+04	1.000	8.007	Car(-O*) + Car(-H) = Car(-O-H) + Car(*)	uni	[255]
Htransfer_fromO_toC	HT6	3.2200E+03	0.927	7.384	Car(-O-H) + Car(*) = Car(-O*) + Car(-H)	uni	Eq
phenanthrene_to_indenyl	FA1	1.0000E+19	-1.050	-15.560	phenanthrene[closed] = indenyl[closed] + C5H5(g)	bi	Eq
addO_fromOH	FA2	5.0000E+13	0.000	0.000	OH*(g) + Car(*) = Car(-O*) + H*(g)	bi	[32]
addO_fromHO2_Car	FA3	3.0000E+13	0.000	0.000	HO2(g) + Car(*) = Car(-O*) + OH*(g)	bi	[252]
addO_fromHO2_Cal	FA4	6.3000E+29	-4.690	11.650	HO2(g) + Cal(*) = Cal(-O*) + OH*(g)	bi	[252]
add_CH3_to_O	FA5	1.2100E+13	0.000	0.000	CH3*(g) + Car(-O*) = Car(-O-CH3)	bi	[256]
add_benzene_to_O	FA6	1.2100E+13	0.000	0.000	C6H6(g) + Car(-O*) = Car(-O-C6H5) + H*(g)	bi	[256]
add_phenyl_to_O	FA7	1.2100E+13	0.000	0.000	C6H5*(g) + Car(-O*) = Car(-O-C6H5)	bi	[256]
add_c2h3	FA8	1.5000E+22	-2.601	6.280	Car(*) + C2H3(g) = Car(-(CH)=(CH2))	bi	[253]
add_phenyl	FA9	2.0000E+26	-3.900	6.320	Car(*) + C6H5(g) = Car(-C6H5)	bi	[253]
add_c2h2ethenyl	FA10	3.2900E+06	2.048	3.162	Car(*) + C2H2(g) = Car(-(CH)=(C*H))	bi	[253]
addO_fromO2	FA11	2.6000E+13	0.000	6.100	O2(g) + Car(*) = Car(-O*) + O*(g)	bi	[257]
add_propargyl_cnacetyl	FA12	3.0000E+12	0.000	0.000	Car(*) + C3H3(g) = Car(-C#C-(C*H2)) + H*(g)	bi	[171]
add_propargyl_tobiphenylrad	FA13	3.0000E+12	0.000	0.000	phenyl[closed](-C#C-(C*H2)) + H2C*CCH(g) = C12H10(biphenyl)[closed]	bi	[171]
add_OH	FA14	6.5000E+14	-0.850	-2.730	OH*(g) + Cal(*) = Cal(-O-H)	bi	[252]
addO2	FA15	3.4000E+30	-5.100	12.950	O2(g) + Car(*) = Car(-O*) + O*(g)	bi	[250]
add_ch3	FA16	2.8200E+44	-9.360	14.310	Car(*) + CH3(g) = Car(-CH3)	bi	[260]
indenyl_to_phenanthrene	FA17	5.0000E+12	0.000	8.000	indenyl[closed] + C5H5(g) = phenanthrene[closed]	bi	[280]
add_c2h4	FA18	2.5100E+12	0.000	6.200	Car(*) + C2H4(g) = Car(-(CH)=(CH2)) + H*(g)	bi	[260]

add_c2h2_ethenyl_to_O	FA19	2.3300E+06	2.174	20.909	C2H2(g) + Cal(-O*) = Cal(-O-(CH)=(C*H))	bi	pw
add_c2h2ethenyl_tomethyl	FA20	3.2000E+11	0.000	7.000	Cal(*) + C2H2(g) = Cal(-(CH)=(C*H))	bi	[280]
add_benzene	FA21	2.2200E+83	-20.790	46.890	Car(*) + C6H6(g) = Car(-C6H5) + H*(g)	bi	[260]
add_peroxy	FA22	7.3100E+07	0.080	-9.570	Cal(*) + O2(g) = Cal(-O-O*)	bi	[250]
add_Oar	FA23	7.0600E+04	1.030	-6.960	O*(g) + Car(*) = Car(-O*)	bi	[230]
add_Oal	FA24	1.8400E+03	1.030	-6.960	O*(g) + Cal(*) = Cal(-O*)	bi	[230]
remove_propargyl_cnacetyl	FR1	3.3900E+17	-1.060	-0.937	Car(-C#C-(C*H2)) + H*(g) = Car(*) + C3H3(g)	bi	Eq
Oabs_byH	FR2	1.2700E+20	-1.331	26.087	H*(g) + Car(-O*) = Car(*) + OH*(g)	bi	Eq
Oabs_byOar	FR3	2.2060E+17	-0.957	15.045	O*(g) + Car(-O*) = Car(*) + O2(g)	bi	Eq
Oabs_byOal	FR4	2.8850E+34	-6.058	21.895	O*(g) + Cal(-O*) = Cal(*) + O2(g)	bi	Eq
remove_peroxy	FR5	4.0300E+13	0.000	12.260	Cal(-O-O*) = Cal(*) + O2(g)	uni	[250]
Oabs_byOH_Cal	FR6	7.2900E+31	-5.146	24.866	OH*(g) + Cal(-O*) = Cal(*) + HO2(g)	bi	Eq
remove_c2h4	FR7	4.8400E+20	-2.170	13.660	Car(-(CH)=(CH2)) + H*(g) = Car(*) + C2H4(g)	bi	Eq
remove_ethenyl_from_O	FR8	3.7720E+13	0.251	22.552	Cal(-O-(CH)=(C*H)) = C2H2(g) + Cal(-O*)	uni	pw
remove_benzene	FR9	1.7900E+22	-2.450	23.589	Car(-C6H5) + H*(g)= Car(*) + C6H6(g)	bi	Eq
remove_ethenyl	FR10	2.4800E+15	0.011	46.064	Car(-(CH)=(C*H)) = Car(*) + C2H2(g)	uni	[136]
ejectOH_formC=O	FR11	3.6100E+12	0.000	37.300	Cal(-O-O*) = Cal(=O) + OH*(g)	uni	[245]
remove_CH3_from_O	FR12	1.8230E+21	-1.671	66.493	Car(-O-CH3) = CH3*(g) + Car(-O*)	uni	Eq
Oabs_byOH_Car	FR13	3.1390E+16	-0.656	61.355	OH*(g) + Car(-O*) = Car(*) + HO2(g)	bi	Eq
rem_benzene_from_O	FR14	2.0500E+19	-0.945	81.964	Car(-O-C6H5) + H*(g) = C6H6(g) + Car(-O*)	bi	Eq
rem_phenyl_from_O	FR15	2.0500E+19	-0.945	81.964	Car(-O-C6H5) = C6H5*(g) + Car(-O*)	uni	Eq
remove_OH	FR16	1.0900E+15	0.000	74.120	Cal(-O-H) = Cal(*) + OH*(g)	uni	Eq
remove_ch3	FR17	1.0300E+22	-1.800	106.815	Car(-CH3) = Car(*) + CH3(g)	uni	Eq
remove_phenyl	FR18	7.0600E+21	-1.560	119.007	Car(-C6H5) = Car(*) + C6H5(g)	uni	Eq
remove_c2h3	FR19	7.1000E+21	-1.671	118.726	Car(-(CH)=(CH2)) = Car(*) + C2H3(g)	uni	Eq
remove_Oar	FR20	6.0900E+09	0.101	72.772	Car(-O*) = Car(*) + O*(g)	uni	Eq
remove_Oal	FR21	1.5900E+08	0.101	72.772	Cal(-O*) = Cal(*) + O*(g)	uni	Eq

closearmchair6_6&6	RC1	1.9100E+09	1.138	1.629	biphenyl-C2H2[open] = phenanthrene[closed] + H	uni	[158]
close6ring_HACA_ethenyl_ethenylrad	RC2	5.1400E+12	0.056	2.127	benzene-1C2H3,-2C2H2[open] = naphthalene[closed]	uni	[136]
close6ring_HACA_acetyl_ethenylrad	RC3	9.9500E+11	0.045	5.395	benzene-1C2H,-2C2H2[open] = naphthyl[closed]	uni	[136]
close6ring_HACA_butadienyl	RC4	3.6100E+09	0.601	3.635	benzene-C-C-C-C[open] = naphthalene[closed] + H	uni	[136]
closebay6	RC5	1.1100E+11	0.658	23.990	C-C-C-C-C-C*[open] = C-C-C-C-C-C[closed] + H	uni	[158]
close6ring_armchair_benz	RC6	1.1100E+11	0.658	23.990	C-C-C-C-C-C*[open] = C-C-C-C-C-C[closed] + H	uni	[158]
close5ring1propenyl	RC7	2.8800E+11	0.225	17.027	C2H2-naphthyl[open] = acenaphtylene[closed] + H	uni	[136]
close5ring2propenyl	RC8	2.8800E+11	0.225	17.027	C2H2-naphthyl[open] = acenaphtylene[closed] + H	uni	[136]
closezigzag5	RC9	2.8800E+11	0.225	17.027	C2H2-naphthyl[open] = acenaphtylene[closed] + H	uni	[136]
closebay5	RC10	3.8600E+11	0.210	17.700	C-C-C-C-C*[open] = C-C-C-C-C[closed] + H	uni	[158]
close5ring_zigzag_benz	RC11	3.8600E+11	0.210	17.700	C-C-C-C-C*[open] = C-C-C-C-C[closed] + H	uni	[158]
close5ring_zigzag_benz_ringrad	RC12	3.8600E+11	0.210	17.700	C-C-C-C-C*[open] = C-C-C-C-C[closed] + H	uni	[158]
close5ring_edge_methylbenz	RC13	3.8600E+11	0.210	17.700	C-C-C-C-C*[open] = C-C-C-C-C[closed] + H	uni	[158]
close6ring_OC	RC14	4.728E+09	0.344	7.803	C-C-C-C-O-C[open] = pyran[closed] + H*(g)	uni	pw
close6ring_OCC	RC15	4.728E+09	0.344	7.803	C-C-C-O-C-C[open] = pyran[closed] + H*(g)	uni	pw
close6ring_OCCC	RC16	4.728E+09	0.344	7.803	C-C-O-C-C-C[open] = pyran[closed] + H*(g)	uni	pw
close5ring_O	RC17	4.728E+09	0.344	7.803	C-C-C-C-O-C[open] =furan[closed] + H*(g)	uni	pw
close5ring_OC	RC18	4.728E+09	0.344	7.803	C-C-C-O-C-C[open] =furan[closed] + H*(g)	uni	pw
close5ring_OCC	RC19	4.728E+09	0.344	7.803	C-C-O-C-C-C[open] = furan[closed] + H*(g)	uni	pw
closezigzag5_toanyl	RC20	5.0400E+06	0.740	6.566	C-C-C-C-C*[open] = C-C-C-C-C[closed]	uni	[132]
closeanth_to1benzyl	RC21	7.0000E+09	0.000	14.5	C-C-C-C-C*[open] = C-C-C-C-C[closed]-C1*	uni	[152]

closephen_to2benzyl	RC22	7.0000E+09	0.000	18.7	C-C-C-C-C*[open] = C2*-C-C-C-C-C[closed]	uni	[152]
open6ring_biphenylrad_topropargyl	RO1	2.6700E+21	-0.689	39.250	C12H10(biphenyl)[closed] = phenyl[closed](-C#C-(C*H2)) + H2C*CCH(g)	bi	Eq
open_5ring_zigzag	RO2	6.6700E+12	0.430	15.539	acenaphthylene[closed] + H = C2H2-naphthyl[open]	bi	Eq
open_5ring_zigzag_ringrad	RO3	6.6700E+12	0.430	15.539	acenaphthylene[closed] + H = C2H2-naphthyl[open]	bi	Eq
openbay5	RO4	6.6700E+12	0.430	15.539	acenaphthylene[closed] + H = C2H2-naphthyl[open]	bi	Eq
open5ring_1propenyl	RO5	6.6700E+12	0.430	15.539	acenaphthylene[closed] + H = C2H2-naphthyl[open]	bi	Eq
open5ring_2propenyl	RO6	6.6700E+12	0.430	15.539	acenaphthylene[closed] + H = C2H2-naphthyl[open]	bi	Eq
open_5ring_1propenyl_ringrad	RO7	6.6700E+12	0.430	15.539	acenaphthylene[closed] + H = C2H2-naphthyl[open]	bi	Eq
open_5ring_2propenyl_ringrad	RO8	6.6700E+12	0.430	15.539	acenaphthylene[closed] + H = C2H2-naphthyl[open]	bi	Eq
open5ring_zigzagbenz	RO9	6.6700E+12	0.430	15.539	acenaphthylene[closed] + H = C2H2-naphthyl[open]	bi	Eq
open5ring_zigzagbenz_ringrad	RO10	6.6700E+12	0.430	15.539	acenaphthylene[closed] + H = C2H2-naphthyl[open]	bi	Eq
open5ring_edge_methylbenz	RO11	6.6700E+12	0.430	15.539	acenaphthylene[closed] + H = C2H2-naphthyl[open]	bi	Eq
open5ring_edge_methylbenz_ringrad	RO12	6.6700E+12	0.430	15.539	acenaphthylene[closed] + H = C2H2-naphthyl[open]	bi	Eq
openbay6	RO13	3.2900E+11	1.237	26.430	phenanthrene[closed] + H = biphenyl-C2H2[open]	bi	Eq
open_6ring_armchair	RO14	3.2900E+11	1.237	26.430	phenanthrene[closed] + H = biphenyl-C2H2[open]	bi	Eq
open_6ring_armchair_ringrad	RO15	3.2900E+11	1.237	26.430	phenanthrene[closed] + H = biphenyl-C2H2[open]	bi	Eq
open6ring_armchair_benz	RO16	3.2900E+11	1.237	26.430	phenanthrene[closed] + H = biphenyl-C2H2[open]	bi	Eq
open6ring_armchair_benz_ringrad	RO17	3.2900E+11	1.237	26.430	phenanthrene[closed] + H = biphenyl-C2H2[open]	bi	Eq
open6ring_OC	RO18	3.1400E+07	1.692	8.184	pyran[closed] + H*(g) = C-C-C-C-O-C[open]	bi	pw
open6ring_OCC	RO19	3.1400E+07	1.692	8.184	pyran[closed] + H*(g) = C-C-C-O-C-C[open]	bi	pw
open6ring_OCCC	RO20	3.1400E+07	1.692	8.184	pyran[closed] + H*(g) = C-C-O-C-C-C[open]	bi	pw
open5ring_O	RO21	3.1400E+07	1.692	8.184	furan[closed] + H*(g) = C-C-C-C-O-C[open]	bi	pw

open5ring_OC	RO22	3.1400E+07	1.692	8.184	furan[closed] + H*(g) = C-C-C-O-C-C[open]	bi	pw
open5ring_OCC	RO23	3.1400E+07	1.692	8.184	furan[closed] + H*(g) = C-C-O-C-C-C[open]	bi	pw
open6ring_acetyl_ethenylrad	RO24	2.2200E+12	0.740	62.399	naphthyl[closed] = benzene-1C2H,-2C2H2[open]	uni	[136]
openzigzagR5rad	RO25	1.0000E+10	-0.219	23.220	C-C-C-C-C*[open] = C-C-C-C-C[closed]	uni	[132]
open6ring_ethenyl_ethenylrad	RO26	4.1600E+20	-2.050	66.350	naphthalene[closed] + H= benzene-1C2H3,-2C2H2[open]	bi	Eq
open6ring_butadienyl	RO27	3.9100E+17	-1.510	67.910	naphthalene[closed] + H = benzene-C-C-C-C[open]	bi	Eq
open6ring_butadienyl_ringrad	RO28	3.9100E+17	-1.510	67.910	naphthalene[closed] + H = benzene-C-C-C-C[open]	bi	Eq
open1benzyl_anth	RO29	8.9000E+07	0.000	31.200	C-C-C-C-C[closed]-C1* = C-C-C-C-C*[open]	uni	[152]
open2benzyl_phen	RO30	8.9000E+07	0.000	36.300	C2*-C-C-C-C-C[closed] = C-C-C-C-C*[open]	uni	[152]
acetyl_to_ethenyl_byH	ISO1	1.0600E+09	1.531	5.630	Car(-C#C-H) + H*(g) = Car(-(CH)=(C*H))	bi	[136]
ethenyl_to_acetyl_byH	ISO2	1.6500E+11	0.490	10.630	Car(-(CH)=(C*H)) + H*(g)= Car(-C#C-H) + H2(g)	bi	[136]
O=C_to_O-C	ISO3	1.1200E+30	-5.975	-1.444	Cal(=O) + H*(g) = H-Cal(-O*)	bi	Eq
ethenyl_to_acetyl	ISO4	7.1800E+10	1.020	38.674	Car(-(CH)=(C*H)) = Car(-C#C-H)	uni	[136]
O-C_to_O=C	ISO5	2.9000E+32	-6.500	21.200	H-Cal(-O*) = Cal(=O) + H*(g)	uni	[252]
acetyl_to_ethenyl_byH2	ISO6	6.9900E+08	1.320	86.997	Car(-C#C-H) + H2(g) = Car(-(CH)=(C*H)) + H*(g)	bi	[136]
C-O_cleavage_rev	OX1	2.8100E+12	0.907	7.068	R-C* + *O-C-R(g) = R-C-O-C-R	bi	Eq
C-C_cleavage_rev	OX2	4.5700E+04	1.959	-9.364	R-C-C* + *C-C-R(g) = R-C-C-C-C-R	bi	Eq
remove_freeedgeC2	OX3	2.3100E+09	0.763	0.000	2-naphthyl[closed] + O2(g) = indenyl[closed] + CO2(g)	bi	[152]
rev_remove_freeedgeC1	OX4	4.1800E+12	0.185	14.500	indenyl[closed] + CO(g) = 2-naphthyl[closed] + O(g)	bi	[136]
rev_remove_freeedgeC2	OX5	4.3600E+13	0.177	40.000	indenyl[closed] + CO2(g) = 2-naphthyl[closed] + O2(g)	bi	Eq
remove_freeedgeC1	OX6	4.7900E+11	0.242	33.700	2-naphthyl[closed] + O(g) = indenyl[closed] + CO(g)	bi	Eq
remove_CO1_form5Cring	OX7	3.1500E+07	0.000	0.000	1-naphthoxy = 1-indenyl + CO	uni	[250]

remove_CO2_form5Cring	OX8	3.1500E+07	0.000	0.000	2-naphthoxy = 1-indenyl + CO	uni	[250]
rev_remove_CO1_form5Cring	OX9	2.5100E+11	0.000	43.900	c1-c-c(-O*)-c-c1 = c1-c-c*-c-c1 + CO(g)	uni	[250]
rev_remove_CO2_form5Cring	OX10	2.5100E+11	0.000	43.900	c1-c-c(-O*)-c-c1 = c1-c-c*-c-c1 + CO(g)	uni	[250]
C-O_cleavage	OX11	9.1600E+14	0.110	75.820	R-C-O-C-R = R-C* + *O-C-R(g)	uni	[258]
C-C_cleavage	OX12	4.0200E+15	-0.180	78.820	R-C-C-C-C-R = R-C-C* + *C-C-R(g)	uni	[258]

Table A.6.2: Pictorials of al reaction types in the new SNAPS mechanism corresponding to Table 2.5. Dashed lines on the molecules off of atoms signify that anything can be attached to those atoms. For example, ---CH signifies that they key group is a saturated carbon atom bonded to any other atom (which in turn may or may not be bonded to other atoms). Where there is an "X" in the pictorial, the "X" can represent any of the species listed underneath the pictorial.

Classes of reaction types
Hydrogen abstraction/addition
----CH + H $\rightleftharpoons$ ----C + H2
----CH + OH $\rightleftharpoons$ ----C + H2O
----CH + CH3 $\rightleftharpoons$ ----C + CH4
---OH + X $\rightleftharpoons$ ---O• + XH X is H, O2, HO2, C2H3, phenyl, O, OH
----OH $\rightleftharpoons$ ----O* + H
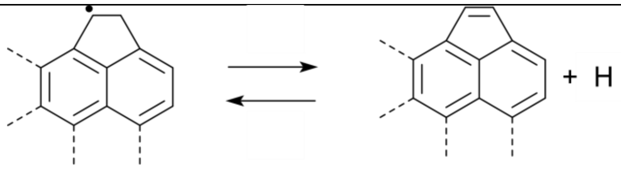
Hydrogen transfer

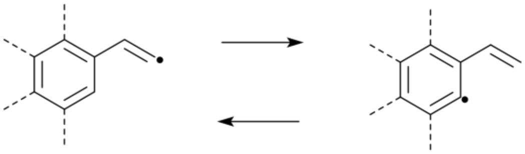
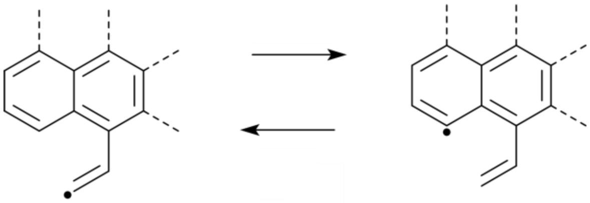
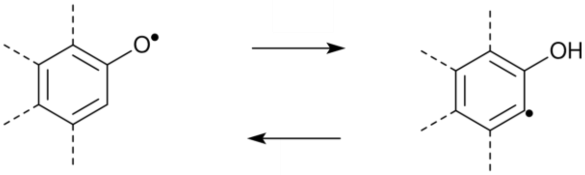
Fragment addition/removal
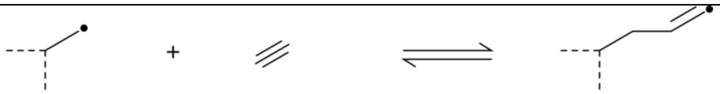
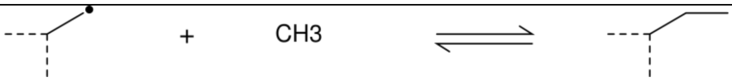
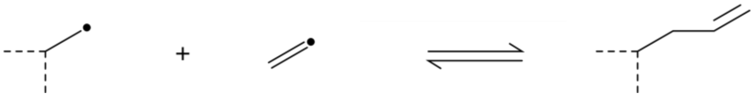
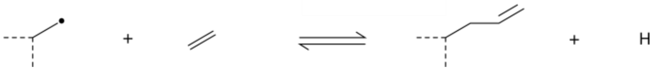

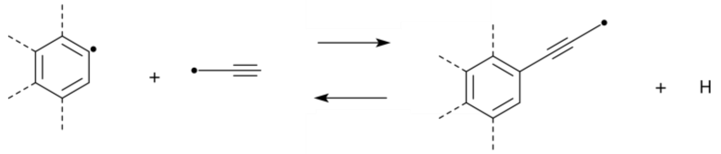
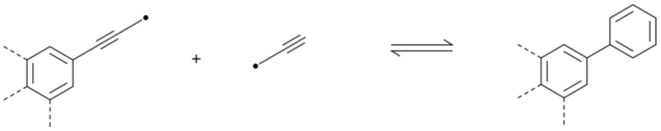
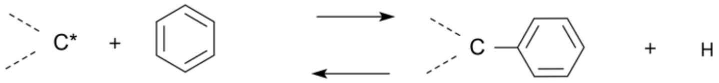
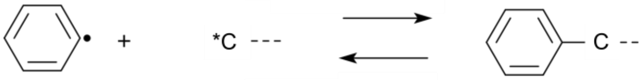
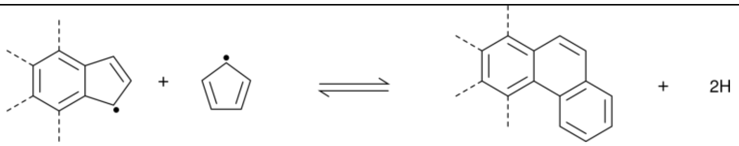
$---C-O^* + X \rightleftharpoons ---C-O-X$ X is CH3, CH2, CH4, benzene, phenyl, C2H2, C2H3, C2H4, C2H5, C2H6, C3H3, C4H2, C4H4, O, OH, HO2
$---C^* + O \rightleftharpoons ---C-O^*$
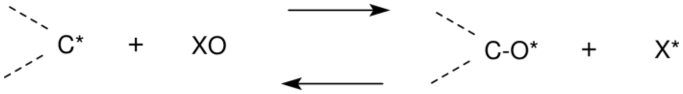

X is H, O, OH, H2O, H2, CO
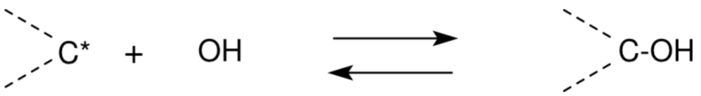
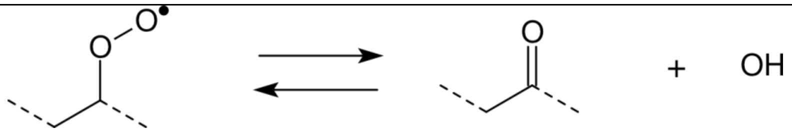
Ring opening/closure
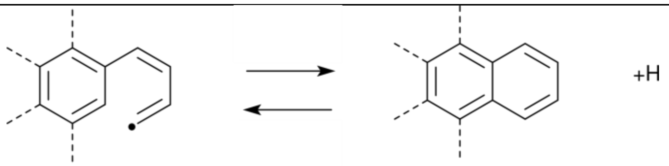
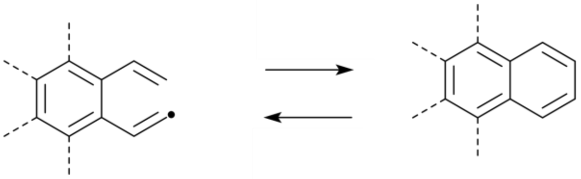
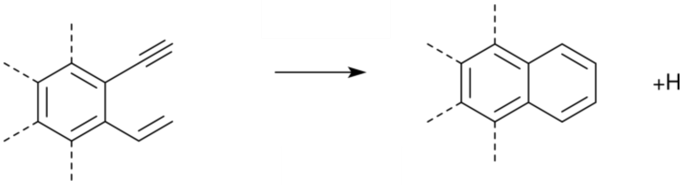
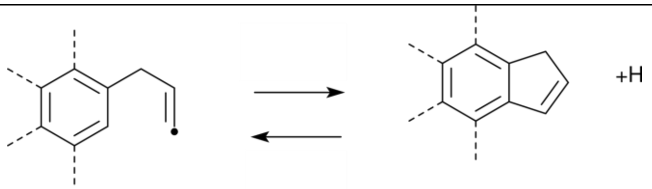

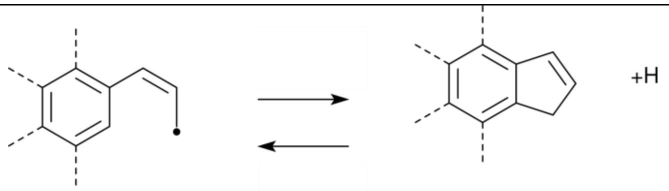
+H

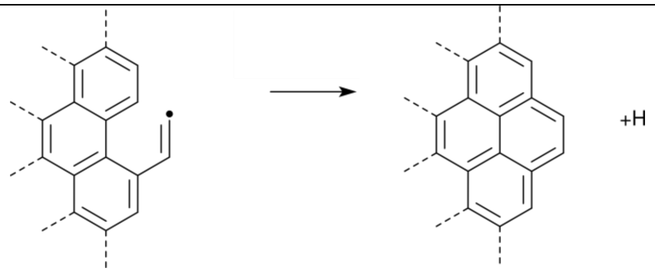
+H

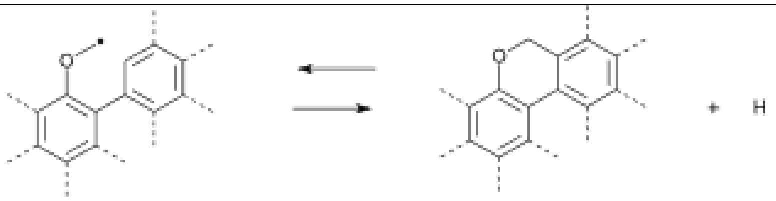
O
O
+ H

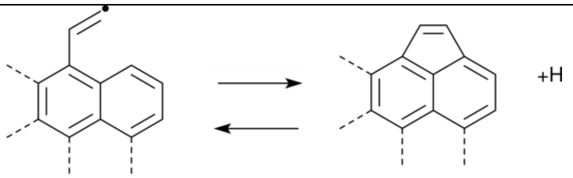
+H

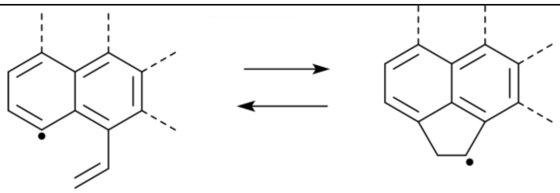

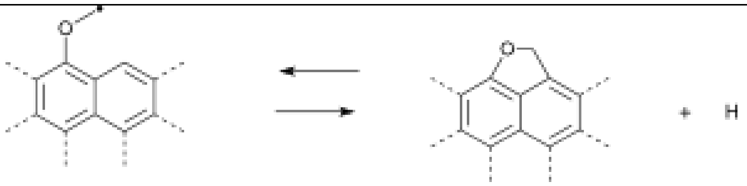
O
O
+ H

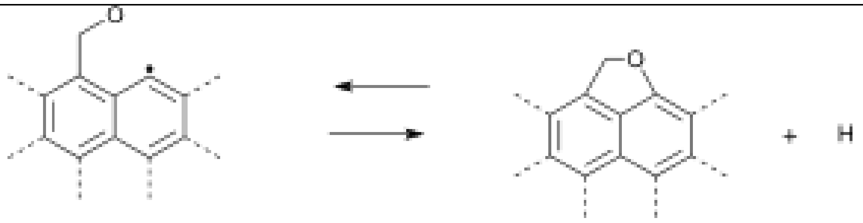
O
O
+ H

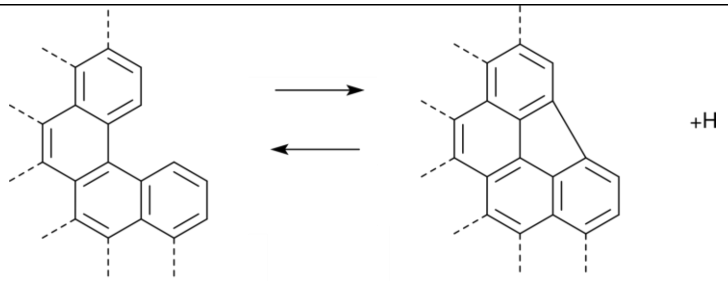
+H

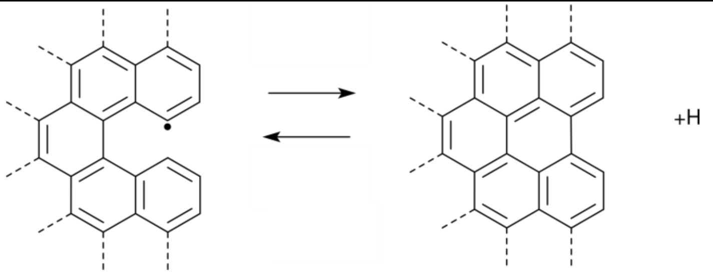
+H

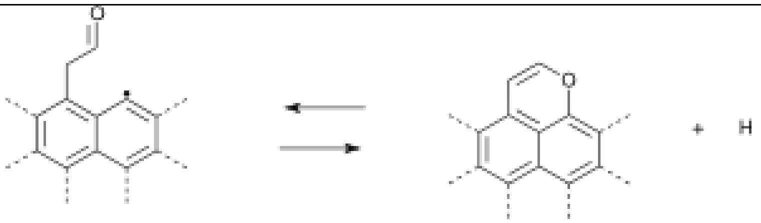
O
O
+ H

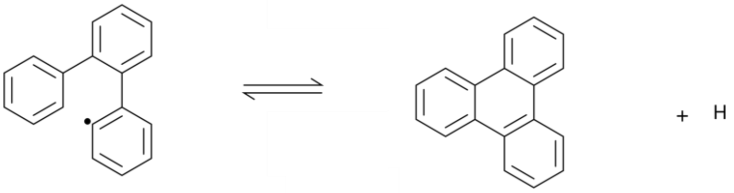
+ H

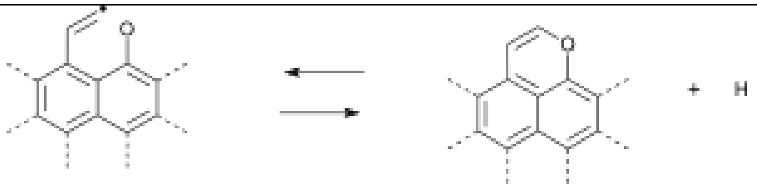
O
O
+ H

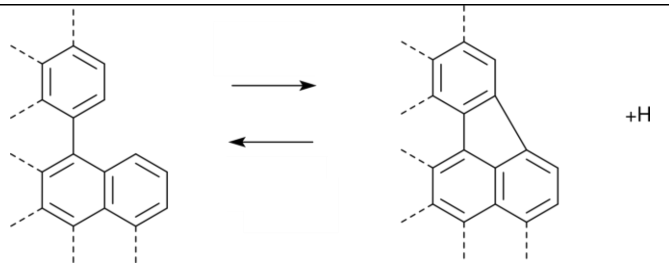
+H

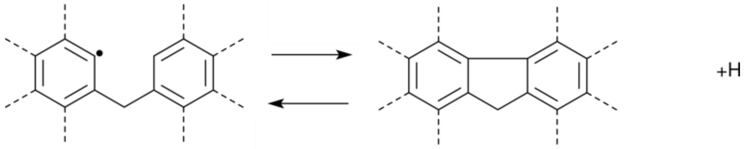
+H

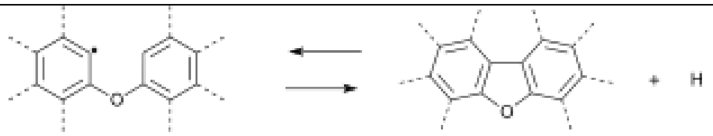
+ H

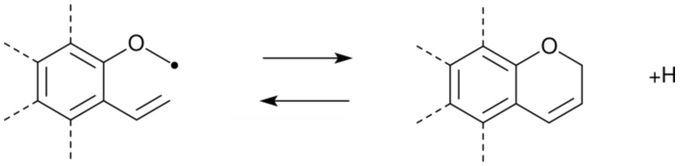
+H

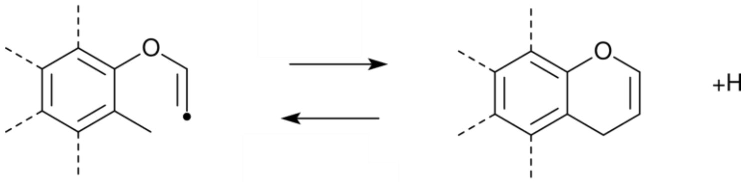
+H

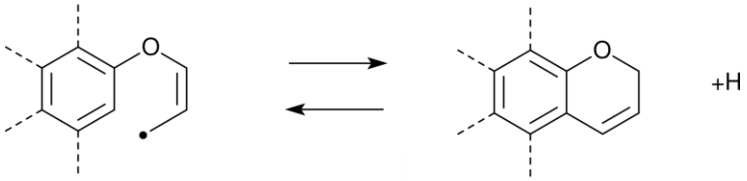
+H

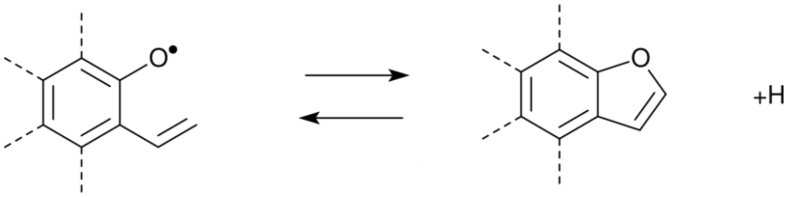
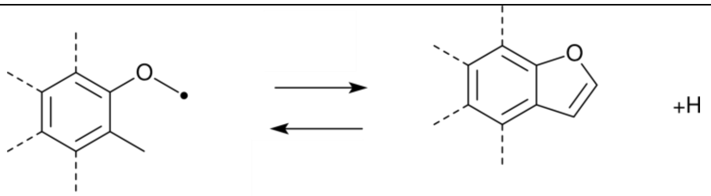
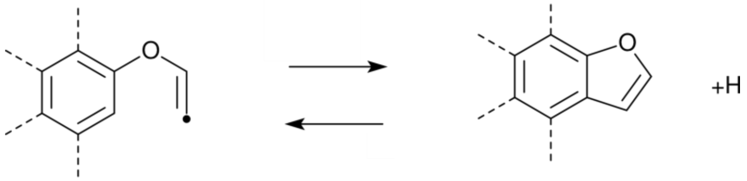
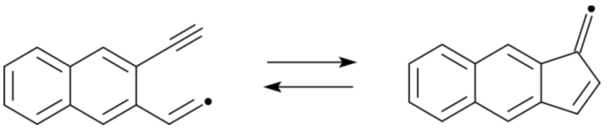
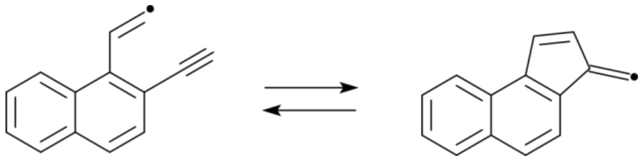
Isomerizations
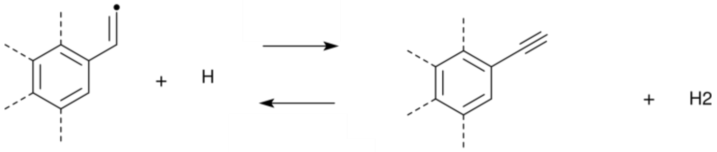

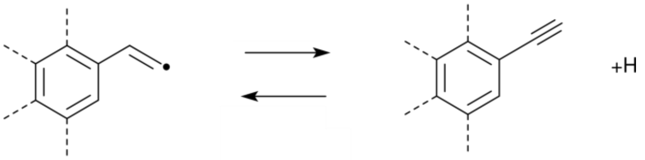
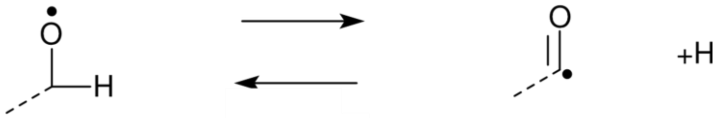
Oxidation
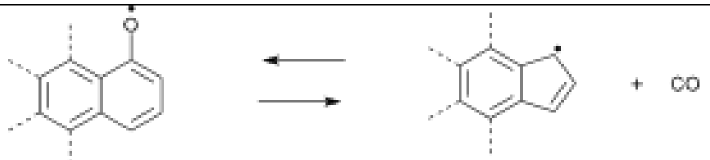
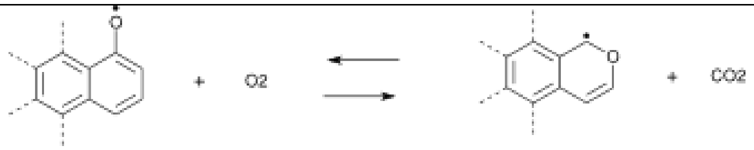
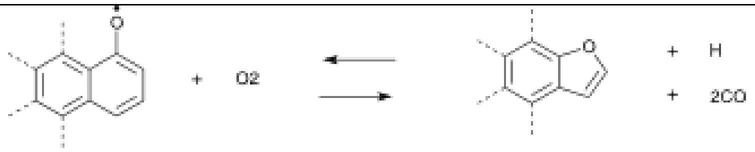
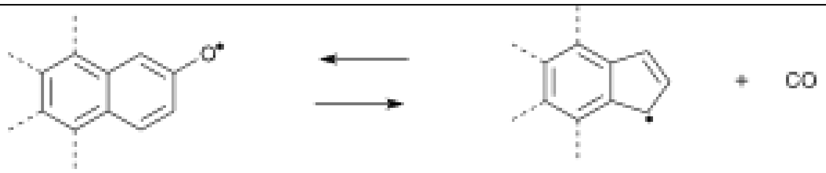
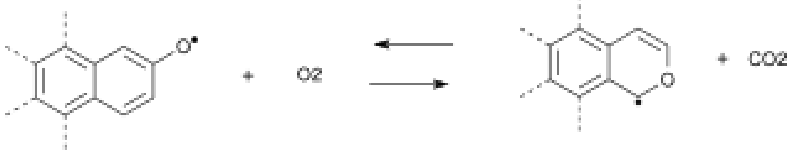

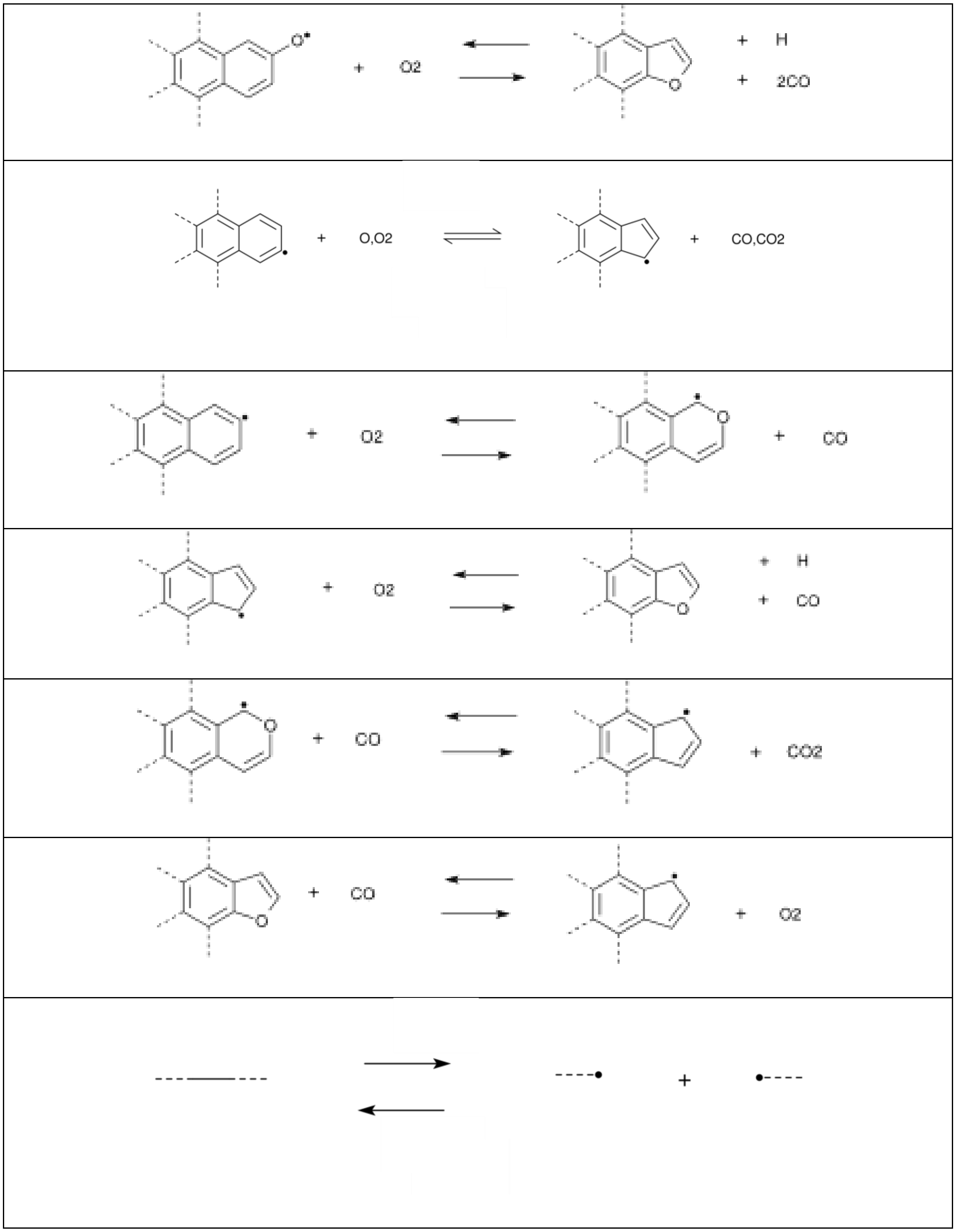

+ O2
+ H
+ 2CO
+ O,O2
+ CO,CO2
+ O2
+ CO
+ O2
+ H
+ CO
+ CO
+ CO2
+ CO
+ O2
+

Bibliography

[1] S. K. Friedlander and D. Y. H. Pui, “Emerging Issues in Nanoparticle Aerosol Science and Technology Experimental Methods and Instrumentation,” *J. Nanoparticle Res.*, vol. 6, no. 4, pp. 313–320, 2004.

[2] A. Kay and M. Gratzel, “Low cost photovoltaic modules based on dye sensitized nanocrystalline titanium dioxide and carbon powder,” *Sol. Energy Mater. Sol. Cells*, vol. 44, pp. 99–117, 1996.

[3] H. K. Kammler, L. Mädler, and S. E. Pratsinis, “Flame Synthesis of Nanoparticles,” *Chem. Eng. Technol.*, vol. 24, no. 6, pp. 583–596, Jun. 2001.

[4] K. A. Russ *et al.*, “C60 fullerene localization and membrane interactions in RAW 264.7 immortalized mouse macrophages,” *Nanoscale*, 2016.

[5] A. Valavanidis, T. Vlachogianni, K. Fiotakis, and S. Loridas, “Pulmonary Oxidative Stress, Inflammation and Cancer: Respirable Particulate Matter, Fibrous Dusts and Ozone as Major Causes of Lung Carcinogenesis through Reactive Oxygen Species Mechanisms,” *Int. J. Environ. Res. Public Health*, vol. 10, no. 9, pp. 3886–3907, Sep. 2013.

[6] A. Violi, “Effects of Combustion-Generated Nanoparticles on Cellular Membranes,” *Combust. Sci. Technol.*, vol. 188, no. 4–5 ed., pp. 769–775, 2016.

[7] “IARC monographs on the evaluation of the carcinogenic risk of chemicals to humans, v. 35: Polynuclear aromatic compounds, pt.4: Bitumens, coal-tars and derived products, shale-oils and soots,” 1985.

[8] K.-H. Kim, S. A. Jahan, E. Kabir, and R. J. C. Brown, “A review of airborne polycyclic aromatic hydrocarbons (PAHs) and their human health effects,” *Environ. Int.*, vol. 60, pp. 71–80, 2013.

[9] N. Nel, A., Xia, T. Li, “Toxic Potential of Materials at the Nanolevel,” *Sci. Rev.*, no. February 2006, pp. 622–628, 2006.

[10] A. E. Nel *et al.*, “Understanding biophysicochemical interactions at the nano-bio interface.,” *Nat. Mater.*, vol. 8, no. 7, pp. 543–557, Jul. 2009.

[11] B. Fubini, M. Ghiazza, and I. Fenoglio, “Chemical features of engineered nanoparticles relevant to their toxicity,” *Nanotoxicology*, vol. 4, no. 4, pp. 347–363, 2010.

[12] R. Chang and A. Violi, “Insights into the Effect of Combustion-Generated Carbon Nanoparticles on Biological Membranes : A Computer Simulation Study,” *J. Phys.*

Chem. B, vol. 110, pp. 5073–5083, 2006.

[13] S. L. Fiedler and A. Violi, “Simulation of nanoparticle permeation through a lipid membrane.,” *Biophys. J.*, vol. 99, no. 1, pp. 144–152, Jul. 2010.

[14] S. Choe, R. Chang, J. Jeon, and A. Violi, “Molecular Dynamics Simulation Study of a Pulmonary Surfactant Film Interacting with a Carbonaceous Nanoparticle,” *Biophys. J.*, vol. 95, no. 9, pp. 4102–4114, 2008.

[15] P. Elvati and A. Violi, “Free Energy Calculation of Permeant-Membrane Interactions Using Molecular Dynamics Simulations,” in *Nanotoxicity*, vol. 926, J. Reineke, Ed. Totowa, NJ: Humana Press, 2012, pp. 189–202.

[16] R. A. Kerr, “Soot Is Warming the World Even More Than Thought,” *Science (80-.).*, vol. 339, no. 6118, 2013.

[17] S. Menon, J. Hansen, L. Nazarenko, and Y. Luo, “Climate Effects of Black Carbon Aerosols in China and India,” *Science (80-.).*, vol. 297, no. 5590, pp. 2250–2253, 2002.

[18] J. H. Seinfeld and S. N. Pandis, “Atmospheric Chemistry and Physics: From Air Pollution to Climate Change,” *Am. Insitute Phys.*, vol. 51, no. 10, pp. 88–90, 1998.

[19] T. C. Bond *et al.*, “Bounding the role of black carbon in the climate system: A scientific assessment,” *J. Geophys. Res. Atmos.*, vol. 118, no. 11, pp. 5380–5552, 2013.

[20] M. Ni, J. Huang, S. Lu, X. Li, J. Yan, and K. Cen, “A review on black carbon emissions, worldwide and in China,” *Chemosphere*, vol. 107, pp. 83–93, Jul. 2014.

[21] D. E. Jensen, “Prediction of Soot Formation Rates: a new Approach,” *Proc. R. Soc. A Math. Phys. Eng. Sci.*, vol. 338, pp. 375–396, 1974.

[22] H. G. Wagner, “Soot formation in combustion,” *Symp. Combust.*, vol. 17, no. 1, pp. 3–19, 1979.

[23] B. S. Haynes and H. G. Wagner, “Soot Formation,” *Prog. Energy Combust. Sci.*, vol. 7, pp. 229–273, 1981.

[24] H. F. Calcote, “Mechanisms of soot nucleation in flames—A critical review,” *Combust. Flame*, vol. 42, pp. 215–242, Jan. 1981.

[25] M. Frenklach, “Reaction mechanism of soot formation in flames,” *Phys. Chem. Chem. Phys.*, vol. 4, no. 11, pp. 2028–2037, 2002.

[26] H. Wang, “Formation of nascent soot and other condensed-phase materials in flames,” *Proc. Combust. Inst.*, vol. 33, no. 1, pp. 41–67, 2011.

[27] M. Kraft, “Modelling of particulate processes,” *KONA Powder Part. J.*, vol. 23, no. March, pp. 18–35, 2005.

[28] A. D’Anna, “Combustion-formed nanoparticles,” *Proc. Combust. Inst.*, vol. 32, no. 1, pp. 593–613, Jan. 2009.

[29] H. Richter and J. B. Howard, “Formation of polycyclic aromatic hydrocarbons and their growth to soot — a review of chemical reaction pathways,” *Prog. Energy Combust. Sci.*, vol. 26, pp. 565–608, 2000.

[30] K. Saito, A. S. Gordon, F. A. Williams, and W. F. Stickle, “A Study of the Early History of Soot Formation in Various Hydrocarbon Diffusion Flames,” *Combust. Sci. Technol.*, vol. 80, no. 1–3, pp. 103–119, 1991.

[31] A. Fahr and S. E. Stein, “Reactions of vinyl and phenyl radicals with ethyne, ethene and benzene,” *Symp. Combust.*, vol. 22, no. 1, pp. 1023–1029, 1988.

[32] J. A. Miller and C. F. Melius, “Kinetic and thermodynamic issues in the formation

of aromatic compounds in flames of aliphatic fuels," *Combust. Flame*, vol. 91, no. 1, pp. 21–39, Oct. 1992.

[33] J. A. Miller and S. J. Klippenstein, "The Recombination of Propargyl Radicals: Solving the Master Equation," *J. Phys. Chem. A*, vol. 105, no. 30, pp. 7254–7266, 2001.

[34] J. A. Miller and S. J. Klippenstein, "The Recombination of Propargyl Radicals and Other Reactions on a C6H6 Potential," *J. Phys. Chem. A*, vol. 107, pp. 7783–7799, 2003.

[35] Y. Georgievskii, J. A. Miller, and S. J. Klippenstein, "Association rate constants for reactions between resonance-stabilized radicals: C3H3 + C3H3, C3H3 + C3H5, and C3H5 + C3H5," *Phys. Chem. Chem. Phys.*, vol. 9, pp. 4529–4268, 2007.

[36] H. Richter and J. B. Howard, "Formation and consumption of single-ring aromatic hydrocarbons and their precursors in premixed acetylene, ethylene and benzene flamesElectronic supplementary information (ESI) available: Thermodynamic and kinetic property data. See http://www.rsc.org/sup," *Phys. Chem. Chem. Phys.*, vol. 4, no. 11, pp. 2038–2055, 2002.

[37] C. J. Pope and J. A. Miller, "Exploring old and new benzene formation pathways in low-pressure premixed flames of aliphatic fuels," *Proc. Combust. Inst.*, vol. 28, no. 2, pp. 1519–1527, Jan. 2000.

[38] K. H. Homann and H. G. Wagner, "Some new aspects of the mechanism of carbon formation in premixed flames," *Symp. Combust.*, vol. 11, no. 1, pp. 371–379, Jan. 1967.

[39] H. A. Michelsen, "Probing soot formation, chemical and physical evolution, and oxidation: A review of in situ diagnostic techniques and needs," *Proc. Combust. Inst.*, vol. 36, no. 1, pp. 717–735, 2017.

[40] M. Frenklach and H. Wang, "Detailed Mechanism and Modeling of Soot Particle Formation," in *Soot Formation in Combustion*, P. D. H. Bockhorn, Ed. Springer Berlin Heidelberg, 1994, pp. 165–192.

[41] I. Glassman, "Soot formation in combustion processes," *Twenty-Second Symp. Combust.*, vol. 22, no. 1, pp. 295–311, Jan. 1989.

[42] K. H. Homann, "Formation of large molecules, particulates and ions in premixed hydrocarbon flames; Progress and unresolved questions," *Proc. Combust. Inst.*, vol. 20, no. 1, pp. 857–870, 1985.

[43] J. B. Howard, "Carbon addition and oxidation reactions in heterogeneous combustion and soot formation," *Symp. Combust.*, vol. 23, no. 1, pp. 1107–1127, 1991.

[44] H. Bockhorn, Ed., *Soot Formation in Combustion: Mechanisms and Models*. Berlin: Springer-Verlag, 1994.

[45] I. Glassman, *Combustion*, 3rd ed. San Diego, CA: Academic Press, 1996.

[46] J. Singh, R. I. A. Patterson, M. Kraft, and H. Wang, "Numerical simulation and sensitivity analysis of detailed soot particle size distribution in laminar premixed ethylene flames," *Combust. Flame*, vol. 145, no. 1, pp. 117–127, 2006.

[47] H.-H. Grotheer, K. Wolf, and K. Hoffmann, "Photoionization mass spectrometry for the investigation of combustion generated nascent nanoparticles and their relation to laser induced incandescence," *Appl. Phys. B*, vol. 104, no. 2, pp. 367–383, Aug. 2011.

[48] B. Zhao, K. Uchikawa, and H. Wang, "A comparative study of nanoparticles in premixed flames by scanning mobility particle sizer, small angle neutron scattering, and transmission electron microscopy," *Proc. Combust. Inst.*, vol. 31, no. 1, pp. 851–860, 2007.

[49] K. Siegmann, K. Sattler, and H. . Siegmann, "Clustering at high temperatures: carbon formation in combustion," *J. Electron Spectros. Relat. Phenomena*, vol. 126, no. 1, pp. 191–202, 2002.

[50] B. L. Wersborg, J. B. Howard, and G. C. Williams, "Physical mechanisms in carbon formation in flames," *Symp. Combust.*, vol. 14, no. 1, pp. 929–940, Jan. 1973.

[51] A. D'Alessio, A. D'Anna, A. D'Orsi, P. Minutolo, R. Barbella, and A. Ciajolo, "Precursor formation and soot inception in premixed ethylene flames," *Symp. Combust.*, vol. 24, no. 1, pp. 973–980, Jan. 1992.

[52] B. Zhao, Z. Yang, J. Wang, M. V. Johnston, and H. Wang, "Analysis of Soot Nanoparticles in a Laminar Premixed Ethylene Flame by Scanning Mobility Particle Sizer," *Aerosol Sci. Technol.*, vol. 37, no. 8, pp. 611–620, Aug. 2003.

[53] H.-H. Grotheer, H. Pokorny, K.-L. Barth, M. Thierley, and M. Aigner, "Mass spectrometry up to 1 million mass units for the simultaneous detection of primary soot and of soot precursors (nanoparticles) in flames," *Chemosphere*, vol. 57, no. 10, pp. 1335–1342, 2004.

[54] L. A. Sgro, A. De Filippo, G. Lanzuolo, and A. D'Alessio, "Characterization of nanoparticles of organic carbon (NOC) produced in rich premixed flames by differential mobility analysis," *Proc. Combust. Inst.*, vol. 31, no. 1, pp. 631–638, 2007.

[55] H.-H. Grotheer *et al.*, "On Combustion Generated Nanoparticles and their Biological Effects. Part I:Measurement of Nanoparticles and their Detection in and Behind Flames," *Curr. Nanosci.*, vol. 3, no. 3, pp. 199–205, 2007.

[56] R. A. Dobbins, R. A. Fletcher, and H. C. Chang, "The evolution of soot precursor particles in a diffusion flame," *Combust. Flame*, vol. 115, no. 3, pp. 285–298, Nov. 1998.

[57] B. Zhao *et al.*, "Measurement and numerical simulation of soot particle size distribution functions in a laminar premixed ethylene-oxygen-argon flame," *Combust. Flame*, vol. 133, no. 1–2, pp. 173–188, Apr. 2003.

[58] R. A. Dobbins, R. A. Fletcher, and W. Lu, "Laser Microprobe Analysis of Soot Precursor Particles and Carbonaceous Soot," *Combusion and Flame*, vol. 100, no. 1–2, pp. 301–309, 1995.

[59] B. Zhao, Z. Yang, Z. Li, M. V. Johnston, and H. Wang, "Particle size distribution function of incipient soot in laminar premixed ethylene flames: effect of flame temperature," *Proc. Combust. Inst.*, vol. 30, no. 1, pp. 1441–1448, Jan. 2005.

[60] M. Commodo, L. A. Sgro, P. Minutolo, and A. D'Anna, "Characterization of Combustion-Generated Carbonaceous Nanoparticles by Size-Dependent Ultraviolet Laser Photoionization," *J. Phys. Chem. A*, vol. 117, no. 19, pp. 3980–3989, May 2013.

[61] M. Commodo, G. Tessitore, G. De Falco, A. Bruno, P. Minutolo, and A. D'Anna, "Further details on particle inception and growth in premixed flames," *Proc. Combust. Inst.*, vol. 35, no. 2, pp. 1795–1802, 2015.

[62] A. Bruno, C. de Lisio, P. Minutolo, and A. D’Alessio, “Evidence of fluorescent carbon nanoparticles produced in premixed flames by time-resolved fluorescence polarization anisotropy,” *Combust. Flame*, vol. 151, no. 3, pp. 472–481, 2007.
[63] A. Bruno, C. de Lisio, P. Minutolo, and A. D’Alessio, “Characterization of ultrafast fluorescence from nanometric carbon particles,” *J. Opt. A Pure Appl. Opt.*, vol. 8, no. 7, pp. S578–S584, Jul. 2006.
[64] T. G. Baquet, H. H. Grotheer, and M. Aigner, “Simultaneous detection of two types of soot precursor particles using photoionization mass spectrometry,” *Rapid Commun. Mass Spectrom.*, vol. 21, no. 24, pp. 4060–4064, 2007.
[65] M. Commodo, G. De Falco, A. Bruno, C. Borriello, P. Minutolo, and A. D’Anna, “Physicochemical evolution of nascent soot particles in a laminar premixed flame: from nucleation to early growth,” *Combust. Flame*, vol. 162, no. 10, pp. 3854–3863, 2015.
[66] H.-H. Grotheer, K. Hoffmann, K. Wolf, S. Kanjarkar, C. Wahl, and M. Aigner, “Study of carbonaceous nanoparticles in premixed C2H4–air flames and behind a spark ignition engine,” *Combust. Flame*, vol. 156, no. 4, pp. 791–800, 2009.
[67] M. Sirignano, A. Collina, M. Commodo, P. Minutolo, and A. D’Anna, “Detection of aromatic hydrocarbons and incipient particles in an opposed-flow flame of ethylene by spectral and time-resolved laser induced emission spectroscopy,” *Combust. Flame*, vol. 159, no. 4, pp. 1663–1669, 2012.
[68] J. Cain, A. Laskin, M. R. Kholghy, M. J. Thomson, and H. Wang, “Molecular characterization of organic content of soot along the centerline of a coflow diffusion flame,” *Phys. Chem. Chem. Phys.*, vol. 16, no. 47, pp. 25862–25875, Oct. 2014.
[69] J. T. Mckinnon, E. Meyer, and J. B. Howard, “Infrared analysis of flame-generated PAH samples,” *Combust. Flame*, vol. 105, no. 1, pp. 161–166, 1996.
[70] B. Öktem, M. P. Tolocka, B. Zhao, H. Wang, and M. V. Johnston, “Chemical species associated with the early stage of soot growth in a laminar premixed ethylene–oxygen–argon flame,” *Combust. Flame*, vol. 142, no. 4, pp. 364–373, Sep. 2005.
[71] C. Russo, A. Tregrossi, and A. Ciajolo, “Dehydrogenation and growth of soot in premixed flames,” *Proc. Combust. Inst.*, vol. 35, no. 2, pp. 1803–1809, 2015.
[72] M. Commodo, A. D’Anna, G. De Falco, R. Larciprete, and P. Minutolo, “Illuminating the earliest stages of the soot formation by photoemission and Raman spectroscopy,” *Combust. Flame*, vol. 181, pp. 188–197, 2017.
[73] G. Rusciano, A. C. De Luca, A. D’Alessio, P. Minutolo, G. Pesce, and A. Sasso, “Surface-enhanced Raman scattering study of nano-sized organic carbon particles produced in combustion processes,” *Carbon N. Y.*, vol. 46, no. 2, pp. 335–341, 2008.
[74] M. Schenk *et al.*, “Morphology of nascent soot in ethylene flames,” *Proc. Combust. Inst.*, vol. 35, pp. 1879–1886, 2014.
[75] S. A. Skeen, H. A. Michelsen, K. R. Wilson, D. M. Popolan, A. Violi, and N. Hansen, “Near-threshold photoionization mass spectra of combustion-generated high-molecular-weight soot precursors,” *J. Aerosol Sci.*, vol. 58, pp. 86–102, Apr. 2013.
[76] J. P. Cain, P. L. Gassman, H. Wang, and A. Laskin, “Micro-FTIR study of soot

chemical composition—evidence of aliphatic hydrocarbons on nascent soot surfaces," *Phys. Chem. Chem. Phys.*, vol. 12, no. 20, pp. 5206–5218, 2010.

[77] M. Commodo, G. De Falco, R. Larciprete, and P. Minutolo, "On the hydrophilic/hydrophobic character of carbonaceous nanoparticles formed in laminar premixed flames," *Exp. Therm. Fluid Sci.*, vol. 73, pp. 56–63, 2016.

[78] M. Commodo, G. De Falco, R. Larciprete, A. D'Anna, and P. Minutolo, "On the hydrophilic / hydrophobic character of carbonaceous nanoparticles formed in laminar premixed flames," in *9th annual Mediterranean Combusion Symposium*, 2015.

[79] C. K. Gaddam and R. L. Vander Wal, "Physical and chemical characterization of SIDI engine particulates," *Combust. Flame*, vol. 160, no. 11, pp. 2517–2528, 2013.

[80] J.-O. Müller, D. S. Su, U. Wild, and R. Schlögl, "Bulk and surface structural investigations of diesel engine soot and carbon black," *Phys. Chem. Chem. Phys.*, vol. 9, no. 30, pp. 4018–4025, 2007.

[81] N. N. Mustafi, R. R. Raine, and B. James, "Characterization of Exhaust Particulates from a Dual Fuel Engine by TGA, XPS, and Raman Techniques," *Aerosol Sci. Technol.*, vol. 44, no. 11, pp. 954–963, Sep. 2010.

[82] A. Santamaría, F. Mondragón, A. Molina, N. D. Marsh, E. G. Eddings, and A. F. Sarofim, "FT-IR and 1H NMR characterization of the products of an ethylene inverse diffusion flame," *Combust. Flame*, vol. 146, no. 1, pp. 52–62, 2006.

[83] S. di Stasio and A. Braun, "Comparative NEXAFS Study on Soot Obtained from an Ethylene/Air Flame, a Diesel Engine, and Graphite," *Energy & Fuels*, vol. 20, pp. 187–194, 2006.

[84] A. D. Abid, N. Heinz, E. D. Tolmachoff, D. J. Phares, C. S. Campbell, and H. Wang, "On evolution of particle size distribution functions of incipient soot in premixed ethylene–oxygen–argon flames," *Combust. Flame*, vol. 154, no. 4, pp. 775–788, 2008.

[85] L. A. Sgro *et al.*, "Measurement of nanoparticles of organic carbon in non-sooting flame conditions," *Proc. Combust. Inst.*, vol. 32, no. 1, pp. 689–696, 2009.

[86] M. M. Maricq, "An examination of soot composition in premixed hydrocarbon flames via laser ablation particle mass spectrometry," *J. Aerosol Sci.*, vol. 40, no. 10, pp. 844–857, 2009.

[87] R. A. Dobbins and C. M. Megaridis, "Morphology of flame-generated soot as determined by thermophoretic sampling," *Langmuir*, vol. 3, no. 2, pp. 254–259, Mar. 1987.

[88] R. A. Dobbins, "Hydrocarbon Nanoparticles Formed in Flames and Diesel Engines," *Aerosol Sci. Technol.*, vol. 41, no. 5, pp. 485–496, Apr. 2007.

[89] L. G. Blevins, R. A. Fletcher, B. A. Benner, E. B. Steel, and G. W. Mulholland, "The existence of young soot in the exhaust of inverse diffusion flames," *Proc. Combust. Inst.*, vol. 29, no. 2, pp. 2325–2333, Jan. 2002.

[90] H. X. Chen and R. A. Dobbins, "Crystallogenesis of Particles Formed in Hydrocarbon Combustion," *Combust. Sci. Technol.*, vol. 159, no. 1, pp. 109–128, Oct. 2000.

[91] A. Bhargava and P. R. Westmoreland, "MBMS analysis of a fuel-lean ethylene flame," *Combust. Flame*, vol. 115, no. 4, pp. 456–467, 1998.

[92] P. F. Jessen and A. G. Gaydon, "Estimation of carbon radical concentrations in

fuel-rich acetylene-oxygen flames by absorption spectroscopy," *Symp. Combust.*, vol. 12, no. 1, pp. 481–489, Jan. 1969.

[93] C. S. McEnally, L. D. Pfefferle, B. Atakan, and K. Kohse-Höinghaus, "Studies of aromatic hydrocarbon formation mechanisms in flames: Progress towards closing the fuel gap," *Prog. Energy Combust. Sci.*, vol. 32, no. 3, pp. 247–294, 2006.

[94] K. H. Homann, "Fullerenes and Soot Formation— New Pathways to Large Particles in Flames," *Angew. Chemie Int. Ed.*, vol. 37, no. 18, pp. 2434–2451, Oct. 1998.

[95] J. Appel, H. Bockhorn, and M. Frenklach, "Kinetic modeling of soot formation with detailed chemistry and physics: laminar premixed flames of C2 hydrocarbons," *Combust. Flame*, vol. 121, no. 1–2, pp. 122–136, Apr. 2000.

[96] X. S. Bai, M. Balthasar, F. Mauss, and L. Fuchs, "Detailed soot modeling in turbulent jet diffusion flames," *Symp. Combust.*, vol. 27, no. 1, pp. 1623–1630, 1998.

[97] N. A. Eaves, A. Veshkini, C. Riese, Q. Zhang, S. B. Dworkin, and M. J. Thomson, "A numerical study of high pressure, laminar, sooting, ethane–air coflow diffusion flames," *Combust. Flame*, vol. 159, no. 10, pp. 3179–3190, 2012.

[98] A. Raj, M. Sander, V. Janardhanan, and M. Kraft, "A study on the coagulation of polycyclic aromatic hydrocarbon clusters to determine their collision efficiency," *Combust. Flame*, vol. 157, no. 3, pp. 523–534, Mar. 2010.

[99] P. Elvati and A. Violi, "Thermodynamics of poly-aromatic hydrocarbon clustering and the effects of substituted aliphatic chains," *Proc. Combust. Inst.*, vol. 34, no. 1, pp. 1837–1843, Jan. 2013.

[100] J. S. Lowe, J. Y. W. Lai, P. Elvati, and A. Violi, "Towards a predictive model for polycyclic aromatic hydrocarbon dimerization propensity," *Proc. Combust. Inst.*, vol. 35, no. 2, pp. 1827–1832, 2015.

[101] J. H. Miller, "The kinetics of polynuclear aromatic hydrocarbon agglomeration in flames," *Twenty-Third Symp. Combust.*, vol. 23, no. 1, pp. 91–98, Jan. 1991.

[102] H. Sabbah, L. Biennier, S. J. Klippenstein, I. R. Sims, and B. R. Rowe, "Exploring the Role of PAHs in the Formation of Soot: Pyrene Dimerization," *J. Phys. Chem. Lett.*, vol. 1, no. 19, pp. 2962–2967, Oct. 2010.

[103] T. S. Totton, A. J. Misquitta, and M. Kraft, "A quantitative study of the clustering of polycyclic aromatic hydrocarbons at high temperatures.," *Phys. Chem. Chem. Phys.*, vol. 14, no. 12, pp. 4081–94, Mar. 2012.

[104] C. A. Schuetz and M. Frenklach, "Nucleation of soot: Molecular dynamics simulations of pyrene dimerization," *Proc. Combust. Inst.*, vol. 29, no. 2, pp. 2307–2314, Jan. 2002.

[105] J. D. Herdman and J. H. Miller, "Intermolecular potential calculations for polynuclear aromatic hydrocarbon clusters.," *J. Phys. Chem. A*, vol. 112, no. 28, pp. 6249–56, Jul. 2008.

[106] A. D'Anna, M. Sirignano, and J. Kent, "A model of particle nucleation in premixed ethylene flames," *Combust. Flame*, vol. 157, no. 11, pp. 2106–2115, Nov. 2010.

[107] M. Balthasar and M. Kraft, "A stochastic approach to calculate the particle size distribution function of soot particles in laminar premixed flames," *Combust. Flame*, vol. 133, no. 3, pp. 289–298, May 2003.

[108] R. I. A. Patterson and M. Kraft, “Models for the aggregate structure of soot particles,” *Combust. Flame*, vol. 151, no. 1, pp. 160–172, 2007.

[109] D. Chen, Z. Zainuddin, E. Yapp, J. Akroyd, S. Mosbach, and M. Kraft, “A fully coupled simulation of PAH and soot growth with a population balance model,” *Proc. Combust. Inst.*, vol. 34, no. 1, pp. 1827–1835, Jan. 2013.

[110] M. Sander, R. I. A. Patterson, A. Braumann, A. Raj, and M. Kraft, “Developing the PAH-PP soot particle model using process informatics and uncertainty propagation,” *Proc. Combust. Inst.*, vol. 33, no. 1, pp. 675–683, 2011.

[111] N. A. Eaves, S. B. Dworkin, and M. J. Thomson, “The importance of reversibility in modeling soot nucleation and condensation processes,” *Proc. Combust. Inst.*, vol. 35, no. 2, pp. 1787–1794, 2015.

[112] N. A. Eaves, S. B. Dworkin, and M. J. Thomson, “Assessing relative contributions of PAHs to soot mass by reversible heterogeneous nucleation and condensation,” *Proc. Combust. Inst.*, vol. 36, no. 1, pp. 935–945, 2017.

[113] S.-H. Chung and A. Violi, “Peri-condensed aromatics with aliphatic chains as key intermediates for the nucleation of aromatic hydrocarbons,” *Proc. Combust. Inst.*, vol. 33, no. 1, pp. 693–700, 2011.

[114] W. G. Mallard, F. Westley, J. T. Herron, R. F. Hampson, and D. H. Frizzell, *NIST Chemical Kinetics Database*. 1998.

[115] J. D. Bittner and J. B. Howard, “Composition profiles and reaction mechanisms in a near-sooting premixed benzene/oxygen/argon flame,” *Symp. Combust.*, vol. 18, no. 1, pp. 1105–1116, 1981.

[116] M. Frenklach, D. W. Clary, W. C. Gardiner Jr., and S. E. Stein, “Detailed kinetic modeling of soot formation in shock-tube pyrolysis of acetylene,” *Symp. Combust.*, vol. 20, no. 1, pp. 887–901, 1985.

[117] M. Frenklach, D. W. Clary, W. C. Gardiner, and S. E. Stein, “Effect of fuel structure on pathways to soot,” *Symp. Combust.*, vol. 21, no. 1, pp. 1067–1076, 1986.

[118] M. Frenklach, T. Yuan, and M. K. Ramachandra, “Soot formation in binary hydrocarbon mixtures,” *Energy and fuels*, vol. 2, no. 25, pp. 462–480, 1988.

[119] M. Frenklach, W. C. Gardiner, S. E. Stein, D. W. Clary, and T. Yuan, “Mechanism of Soot Formation in Acetylene-Oxygen Mixtures,” *Combust. Sci. Technol.*, vol. 50, no. 1–3, pp. 79–115, 1986.

[120] H. Bockhorn, F. Fetting, and H. W. Wenz, “Investigation of the Formation of High Molecular Hydrocarbons and Soot in Premixed Hydrocarbon-Oxygen Flames,” *Ber. Bunsenges. Phys. Chem*, vol. 87, pp. 1067–1073, 1983.

[121] M. Frenklach and J. Warnatz, “Detailed Modeling of PAH Profiles in a Sooting Low-Pressure Acetylene Flame,” *Combust. Sci. Technol.*, vol. 51, no. 4–6, pp. 265–283, 1987.

[122] M. Frenklach and H. Wang, “Detailed modeling of soot particle nucleation and growth,” *Proc. Combust. Inst.*, vol. 23, no. 1, pp. 1559–1566, 1990.

[123] M. Frenklach, “Production of Polycyclic Aromatic Hydrocarbons in Chlorine Containing Environments,” *Combust. Sci. Technol.*, vol. 74, no. 1–6, pp. 283–296, 1990.

[124] M. Frenklach, J. P. Hsu, D. L. Miller, and R. A. Matula, “Shock-tube pyrolysis of chlorinated hydrocarbons: Formation of soot,” *Combust. Flame*, vol. 64, no. 2, pp.

141–155, 1986.

[125] M. Frenklach, “On the driving force of PAH production,” *Symp. Combust.*, vol. 22, no. 1, pp. 1075–1082, Jan. 1988.

[126] H. Wang and M. Frenklach, “Calculations of Rate Coefficients for the Chemically Activated Reactions of Acetylene with Vinylic and Aromatic Radicals,” *J. Phys. Chem.*, vol. 98, no. 44, pp. 11465–11489, 1994.

[127] H. Wang and M. Frenklach, “A detailed kinetic modeling study of aromatics formation in laminar premixed acetylene and ethylene flames,” *Combust. Flame*, vol. 110, no. 1–2, pp. 173–221, Jul. 1997.

[128] M. Frenklach, “Computer modeling of infinite reaction sequences: A chemical lumping,” *Chem. Eng. Sci.*, vol. 40, no. 10, pp. 1843–1849, 1985.

[129] A. M. Dean, “Detailed Kinetic Modeling,” *J. Phys. Chem.*, vol. 94, no. 7, pp. 1432–1439, 1990.

[130] M. Frenklach, N. W. Moriarty, and N. J. Brown, “Hydrogen migration in polyaromatic growth,” *Symp. Combust.*, vol. 27, no. 2, pp. 1655–1661, 1998.

[131] M. Frenklach, “On surface growth mechanism of soot particles,” *Symp. Combust.*, vol. 26, no. 2, pp. 2285–2293, 1996.

[132] M. Frenklach, C. A. Schuetz, and J. Ping, “Migration mechanism of aromatic-edge growth,” *Proc. Combust. Inst.*, vol. 30, no. 1, pp. 1389–1396, 2005.

[133] R. Whitesides, A. C. Kollias, D. Domin, W. A. Lester, and M. Frenklach, “Graphene layer growth: Collision of migrating five-member rings,” *Proc. Combust. Inst.*, vol. 31, pp. 539–546, 2007.

[134] R. Whitesides and M. Frenklach, “Detailed Kinetic Monte Carlo Simulations of Graphene-Edge Growth,” *J. Phys. Chem. A*, vol. 114, no. 2, pp. 689–703, Jan. 2010.

[135] K. Siegmann and K. Sattler, “Formation mechanism for polycyclic aromatic hydrocarbons in methane flames,” *J. Chem. Phys.*, vol. 112, no. 2, pp. 698–709, 2000.

[136] V. V Kislov, N. I. Islamova, A. M. Kolker, S. H. Lin, and A. M. Mebel, “Hydrogen Abstraction Acetylene Addition and Diels - Alder Mechanisms of PAH Formation : A Detailed Study Using First Principles Calculations,” *J. Chem. Theory Comput.*, vol. 1, no. 5, pp. 908–924, 2005.

[137] M. B. Colket and D. J. Seery, “Reaction mechanisms for toluene pyrolysis,” *Symp. Combust.*, vol. 25, no. 1, pp. 883–891, 1994.

[138] M. J. Castaldi *et al.*, “Experimental and modeling investigation of aromatic and polycyclic aromatic hydrocarbon formation in a premixed ethylene flame,” *Symp. Combust.*, vol. 26, no. 1, pp. 693–702, Jan. 1996.

[139] N. M. Marinov, W. J. Pitz, C. K. Westbrook, M. J. Castaldi, and S. M. Senkan, *Modeling of Aromatic and Polycyclic Aromatic Hydrocarbon Formation in Premixed Methane and Ethane Flames*, vol. 116–117, no. 1–6. 1996.

[140] N. M. Marinov, W. J. Pitz, and C. K. Westbrook, “Aromatic and Polycyclic Aromatic Hydrocarbon Formation in a Laminar Premixed n-Butane Flame,” *Combusion and Flame*, vol. 213, pp. 192–213, 1998.

[141] C. F. Melius, M. E. Colvin, N. M. Marinov, W. J. Pit, and S. M. Senkan, “Reaction mechanisms in aromatic hydrocarbon formation involving the C5H5 cyclopentadienyl moiety,” *Symp. Combust.*, vol. 26, no. 1, pp. 685–692, 1996.

[142] A. M. Mebel, A. Landera, and R. I. Kaiser, “Formation Mechanisms of Naphthalene and Indene: From the Interstellar Medium to Combustion Flames,” *J. Phys. Chem. A*, vol. 121, no. 5, pp. 901–926, Feb. 2017.

[143] V. V. Kislov, A. M. Mebel, J. Aguilera-Iparraguirre, and W. H. Green, “Reaction of Phenyl Radical with Propylene as a Possible Source of Indene and Other Polycyclic Aromatic Hydrocarbons: An Ab Initio/RRKM-ME Study,” *J. Phys. Chem. A*, vol. 116, no. 16, pp. 4176–4191, Apr. 2012.

[144] A. M. Mebel and V. V. Kislov, “Can the C5H5 + C5H5 → C10H8 +H2 Reaction Produce Naphthalene? An Ab Initio/RRKM Study,” *J. Phys. Chem. A*, vol. 113, no. 36, pp. 9825–9833, Sep. 2009.

[145] V. V. Kislov, A. M. Mebel, and S. H. Lin, “Ab Initio and DFT Study of the Formation Mechanisms of Polycyclic Aromatic Hydrocarbons: The Phenanthrene Synthesis from Biphenyl and Naphthalene,” *J. Phys. Chem. A*, vol. 106, no. 25, pp. 6171–6182, 2002.

[146] V. D. Knyazev and K. V. Popov, “Kinetics of the Self Reaction of Cyclopentadienyl Radicals,” *J. Phys. Chem. A*, vol. 119, no. 28, pp. 7418–7429, Jul. 2015.

[147] C. Cavallotti, D. Polino, A. Frassoldati, and E. Ranzi, “Analysis of Some Reaction Pathways Active during Cyclopentadiene Pyrolysis,” *J. Phys. Chem. A*, vol. 116, no. 13, pp. 3313–3324, Apr. 2012.

[148] M. R. Djokic, K. M. Van Geem, C. Cavallotti, A. Frassoldati, E. Ranzi, and G. B. Marin, “An experimental and kinetic modeling study of cyclopentadiene pyrolysis: First growth of polycyclic aromatic hydrocarbons,” *Combust. Flame*, vol. 161, no. 11, pp. 2739–2751, 2014.

[149] C. Cavallotti and D. Polino, “On the kinetics of the C5H5+C5H5 reaction,” *Proc. Combust. Inst.*, vol. 34, no. 1, pp. 557–564, 2013.

[150] F. Zhang, R. I. Kaiser, V. V. Kislov, A. M. Mebel, A. Golan, and M. Ahmed, “A VUV Photoionization Study of the Formation of the Indene Molecule and Its Isomers,” *J. Phys. Chem. Lett.*, vol. 2, no. 14, pp. 1731–1735, Jul. 2011.

[151] A. M. Mebel, Y. Georgievskii, A. W. Jasper, and S. J. Klippenstein, “Pressure-dependent rate constants for PAH growth: formation of indene and its conversion to naphthalene,” *Faraday Discuss. Faraday Discuss*, vol. 195, no. 195, pp. 637–670, 2016.

[152] V. V. Kislov, A. I. Sadovnikov, and A. M. Mebel, “Formation Mechanism of Polycyclic Aromatic Hydrocarbons beyond the Second Aromatic Ring,” *J. Phys. Chem. A*, vol. 117, no. 23, pp. 4794–4816, 2013.

[153] A. M. Mebel, Y. Georgievskii, A. W. Jasper, and S. J. Klippenstein, “Temperature- and pressure-dependent rate coefficients for the HACA pathways from benzene to naphthalene,” *Proc. Combust. Inst.*, vol. 36, no. 1, pp. 919–926, 2017.

[154] S. J. Klippenstein, “From theoretical reaction dynamics to chemical modeling of combustion,” *Proc. Combust. Inst.*, vol. 36, no. 1, pp. 77–111, 2017.

[155] R. Design, “CHEMKIN-PRO 15131.” San Diego, CA, 2013.

[156] P. R. Westmoreland, A. M. Dean, J. B. Howard, and J. P. Longwellt, “Forming Benzene in Flames by Chemically Activated Isomerization,” *J. Phys. Chem*, vol. 93, pp. 8171–8180, 1989.

[157] S. J. Harris, A. M. Weiner, and R. J. Blint, “Formation of small aromatic molecules in a sooting ethylene flame,” *Combust. Flame,* vol. 72, no. 1, pp. 91–109, Apr. 1988.

[158] A. Raj, I. D. C. Prada, A. A. Amer, and S. H. Chung, “A reaction mechanism for gasoline surrogate fuels for large polycyclic aromatic hydrocarbons,” *Combust. Flame*, vol. 159, no. 2, pp. 500–515, 2012.

[159] P. Selvaraj *et al.*, “A computational study of ethylene-air sooting flames: Effects of large polycyclic aromatic hydrocarbons,” *Combust. Flame*, vol. 163, pp. 427–436, 2016.

[160] Y. Wang, A. Raj, and S. H. Chung, “A PAH growth mechanism and synergistic effect on PAH formation in counterflow diffusion flames,” *Combust. Flame*, vol. 160, no. 9, pp. 1667–1676, 2013.

[161] Y. Wang, A. Raj, and S. H. Chung, “Soot modeling of counterflow diffusion flames of ethylene-based binary mixture fuels,” *Combust. Flame*, vol. 162, no. 3, pp. 586–596, 2015.

[162] G. Blanquart, P. Pepiot-Desjardins, and H. Pitsch, “Chemical mechanism for high temperature combustion of engine relevant fuels with emphasis on soot precursors,” *Combust. Flame*, vol. 156, no. 3, pp. 588–607, 2009.

[163] N. W. Moriarty and M. Frenklach, “Ab initio study of naphthalene formation by addition of vinylacetylene to phenyl,” *Proc. Combust. Inst.*, vol. 28, no. Pt. 2, pp. 2563–2568, 2000.

[164] A. D’Anna and J. H. Kent, “Aromatic formation pathways in non-premixed methane flames,” *Combust. Flame*, vol. 132, no. 4, pp. 715–722, 2003.

[165] N. a. Slavinskaya and P. Frank, “A modelling study of aromatic soot precursors formation in laminar methane and ethene flames,” *Combust. Flame*, vol. 156, no. 9, pp. 1705–1722, Sep. 2009.

[166] V. Chernov, M. J. Thomson, S. B. Dworkin, N. A. Slavinskaya, and U. Riedel, “Soot formation with C1 and C2 fuels using an improved chemical mechanism for PAH growth,” *Combust. Flame*, vol. 161, no. 2, pp. 592–601, Feb. 2014.

[167] N. A. Slavinskaya, U. Riedel, S. B. Dworkin, and M. J. Thomson, “Detailed numerical modeling of PAH formation and growth in non-premixed ethylene and ethane flames,” *Combust. Flame*, vol. 159, no. 3, pp. 979–995, 2012.

[168] N. Olten and S. Senkan, “Formation of polycyclic aromatic hydrocarbons in an atmospheric pressure ethylene diffusion flame,” *Combust. Flame*, vol. 118, no. 3, pp. 500–507, 1999.

[169] A. M. Vincitore and S. M. Senkan, “Polycyclic Aromatic Hydrocarbon Formation in Opposed Flow Diffusion Flames of Ethane,” *Combust. Flame*, vol. 114, no. 1, pp. 259–266, 1998.

[170] A. D’Anna and A. Violi, “A kinetic model for the formation of aromatic hydrocarbons in premixed laminar flames,” *Proc. Combust. Inst.*, vol. 27, pp. 425–433, 1998.

[171] A. D’Anna, A. Violi, and A. D’Alessio, “Modeling the rich combustion of aliphatic hydrocarbons,” *Combust. Flame*, vol. 121, no. 3, pp. 418–429, 2000.

[172] A. Violi, A. . Sarofim, and T. . Truong, “Quantum mechanical study of molecular weight growth process by combination of aromatic molecules,” *Combust. Flame*, vol. 126, no. 1, pp. 1506–1515, 2001.

[173] A. Violi, A. D'Anna, and A. D'Alessio, "Modeling of particulate formation in combustion and pyrolysis," *Chem. Eng. Sci.*, vol. 54, no. 15–16, pp. 3433–3442, 1999.

[174] A. D'Anna, A. Violi, A. D'Alessio, and A. F. Sarofim, "A reaction pathway for nanoparticle formation in rich premixed flames," *Combust. Flame*, vol. 127, no. 1–2, pp. 1995–2003, 2001.

[175] A. Violi, A. Kubota, T. N. Truong, W. J. Pitz, C. K. Westbrook, and A. F. Sarofim, "A fully integrated kinetic monte carlo/molecular dynamics approach for the simulation of soot precursor growth," *Proc. Combust. Inst.*, vol. 29, no. 2, pp. 2343–2349, Jan. 2002.

[176] A. Violi, A. F. Sarofim, and G. A. Voth, "Kinetic Monte Carlo–Molecular Dynamics Approach To Model Soot Inception," *Combust. Sci. Technol.*, vol. 176, no. 5–6, pp. 991–1005, 2004.

[177] A. Violi, "Modeling of soot particle inception in aromatic and aliphatic premixed flames," *Combust. Flame*, vol. 139, pp. 279–287, 2004.

[178] A. Violi, G. A. Voth, and A. F. Sarofim, "The relative roles of acetylene and aromatic precursors during soot particle inception," *Proc. Combust. Inst.*, vol. 30, no. 1, pp. 1343–1351, 2005.

[179] A. Violi and A. Venkatnathan, "Combustion-generated nanoparticles produced in a benzene flame: a multiscale approach.," *J. Chem. Phys.*, vol. 125, no. 5, p. 54302, Aug. 2006.

[180] D. T. Gillespie, "A General Method for Numerically Simulating the Stochastic Time Evolution of Coupled Chemical Reactions," *J. Comput. Phys.*, vol. 434, pp. 403–434, 1976.

[181] D. T. Gillespie, "Exact Stochastic Simulation of Coupled Chemical Reactions," *J. Phys. Chem.*, vol. 81, no. 25, pp. 2340–2361, 1977.

[182] J. Y. W. Lai, P. Elvati, and A. Violi, "Stochastic atomistic simulation of polycyclic aromatic hydrocarbon growth in combustion.," *Phys. Chem. Chem. Phys.*, vol. 16, no. 17, pp. 7969–7979, 2014.

[183] N. M. O'Boyle, M. Banck, C. A. James, C. Morley, T. Vandermeersch, and G. R. Hutchison, "Open Babel: An open chemical toolbox," *J. Cheminform.*, vol. 3, no. 1, p. 33, 2011.

[184] A. B. Bortz, M. H. Kalos, and J. L. Lebowitz, "A New Algorithm for Monte Carlo king Spin Systems," *J. Comp. Phys.*, vol. 18, pp. 10–18, 1975.

[185] A. F. Voter, "Introduction to the kinetic Monte Carlo method," in *Radiation Effects in Solids*, 2007, pp. 1–23.

[186] J. Y. W. Lai, "Stochastic Simulation of Carbonaceous Nanoparticle Precursor Formation in Combustion," 2014.

[187] M. Celnik, A. Raj, R. West, R. Patterson, and M. Kraft, "Aromatic site description of soot particles," *Combust. Flame*, vol. 155, no. 1–2, pp. 161–180, 2008.

[188] A. Raj *et al.*, "A statistical approach to develop a detailed soot growth model using PAH characteristics," *Combust. Flame*, vol. 156, no. 4, pp. 896–913, 2009.

[189] E. K. Y. Yapp, C. G. Wells, J. Akroyd, S. Mosbach, R. Xu, and M. Kraft, "Modelling PAH curvature in laminar premixed flames using a detailed population balance model," *Combust. Flame*, vol. 176, pp. 172–180, 2017.

[190] P. Weilmunster, A. Keller, and K. Homann, "Large Molecules, Radicals, Ions, and

Small Soot Particles in Fuel-Rich Hydrocarbon Flames Part I: Positive Ions of Polycyclic Aromatic Hydrocarbons (PAH) in Low-Pressure Premixed Flames of Acetylene and Oxygen," *Combust. Flame*, vol. 116, no. 1–2, pp. 62–83, 1999.

[191] C. Russo, M. Alfè, J.-N. Rouzaud, F. Stanzione, A. Tregrossi, and A. Ciajolo, "Probing structures of soot formed in premixed flames of methane, ethylene and benzene," *Proc. Combust. Inst.*, vol. 34, no. 1, pp. 1885–1892, 2013.

[192] A. Keller, R. Kovacs, and K. Homann, "Large molecules, ions, radicals and small soot particles in fuel-rich hydrocarbon flames Part IV. Large polycyclic aromatic hydrocarbons and their radicals in a fuel-rich benzene-oxygen flame," *Phys. Chem. Chem. Phys.*, vol. 2, pp. 1667–1675, 2000.

[193] A. B. Fialkov and K.-H. Homann, "Large molecules, ions, radicals, and small soot particles in fuel-rich hydrocarbon flames: Part VI: positive ions of aliphatic and aromatic hydrocarbons in a low-pressure premixed flame of n-butane and oxygen," *Combust. Flame*, vol. 127, no. 3, pp. 2076–2090, 2001.

[194] A. . Fialkov, J. Dennebaum, and K.-H. Homann, "Large molecules, ions, radicals, and small soot particles in fuel-rich hydrocarbon flames part V: Positive ions of polycyclic aromatic hydrocarbons (PAH) in low-pressure premixed flames of benzene and oxygen," *Combust. Flame*, vol. 125, no. 1, pp. 763–777, 2001.

[195] J. P. Cain, J. Camacho, D. J. Phares, H. Wang, and A. Laskin, "Evidence of aliphatics in nascent soot particles in premixed ethylene flames," *Proc. Combust. Inst.*, vol. 33, no. 1, pp. 533–540, 2011.

[196] K. O. Johansson *et al.*, "Soot precursor formation and limitations of the stabilomer grid," *Proc. Combust. Inst.*, vol. 35, pp. 1819–1826, Jun. 2015.

[197] S. A. Skeen, B. Yang, H. A. Michelsen, J. A. Miller, A. Violi, and N. Hansen, "Studies of laminar opposed-flow diffusion flames of acetylene at low-pressures with photoionization mass spectrometry," *Proc. Combust. Inst.*, vol. 34, no. 1, pp. 1067–1075, 2013.

[198] J. Griesheimer and K.-H. Homann, "Large molecules, radicals ions, and small soot particles in fuel-rich hydrocarbon flames: Part II. Aromatic radicals and intermediate PAHs in a premixed low-pressure naphthalene/oxygen/argon flame," *Symp. Combust.*, vol. 27, no. 2, pp. 1753–1759, 1998.

[199] A. Albinet, E. Leoz-Garziandia, H. Budzinski, and E. Villenave, "Polycyclic aromatic hydrocarbons (PAHs), nitrated PAHs and oxygenated PAHs in ambient air of the Marseilles area (South of France): Concentrations and sources," *Sci. Total Environ.*, vol. 384, no. 1–3, pp. 280–292, 2007.

[200] A. C. Lewis, R. E. Robinson, K. D. Bartle, and M. J. Pilling, "On-Line Coupled LC-GC-ITD/MS for the Identification of Alkylated, Oxygentaed, and Nitrated Polycyclic Aromatic Compounds in Urban Air Particulate Extracts," *Environ. Sci. Technol.*, vol. 29, no. 8, pp. 1977–1981, 1995.

[201] N. K. Wilson, T. R. McCurdy, and J. C. Chuang, "Concentrations and phase distributions of nitrated and oxygenated polycyclic aromatic hydrocarbons in ambient air," *Atmos. Environ.*, vol. 29, no. 19, pp. 2575–2584, 1995.

[202] M. M. Del Rosario Sienra, "Oxygenated polycyclic aromatic hydrocarbons in urban air particulate matter," *Atmos. Environ.*, vol. 40, no. 13, pp. 2374–2384, 2006.

[203] K. Cautreels, W.; Van Cauwenbergue, "Determination of Organic Compounds in

Airborne Particulate Matter By Gas Chromatography-Mass Spectrometry," *Atmos. Environ.*, vol. 10, no. Cautreels, W.; Van Cauwenbergue, K., pp. 447–457, 1976.

[204] J. Konig, E. Balfanz, W. Funcke, and T. Romanowskl, "Determination of Oxygenated Polycyclic Aromatic Hydrocarbons in Airborne Particulate Matter by Capillary Gas Chromatography and Gas Chromatography/Mass Spectrometry," *Anal. Chem.*, vol. 55, no. 4, pp. 599–603, 1983.

[205] J. O. Allen, N. M. Dookeran, K. Taghizadeh, A. L. Lafleur, K. A. Smith, and A. F. Sarofim, "Measurement of Oxygenated Polycyclic Aromatic Hydrocarbons Associated with a Size-Segregated Urban Aerosol," *Environ. Sci. Technol.*, vol. 31, no. 7, pp. 2064–2070, 1997.

[206] G. Shen *et al.*, "Emission of oxygenated polycyclic aromatic hydrocarbons from indoor solid fuel combustion," *Environ. Sci. Technol.*, vol. 45, no. 8, pp. 3459–3465, 2011.

[207] S. Lundstedt *et al.*, "Sources, Fate, and Toxic Hazards of Oxygenated Polycyclic Aromatic Hydrocarbons (PAHs) at PAH-contaminated Sites," *Source AMBIO A J. Hum. Environ.*, vol. 36, no. 6, pp. 475–485, 2007.

[208] M. Machala, M. Ciganek, L. Bláha, K. Minksová, and J. Vondráck, "Aryl hydrocarbon receptor-mediated and estrogenic activities of oxygenated polycyclic aromatic hydrocarbons and azaarenes originally identified in extracts of river sediments.," *Environ. Toxicol. Chem.*, vol. 20, no. 12, pp. 2736–43, 2001.

[209] "Toxicology and carcinogenesis studies of furan (CAS No. 110-00-9) in F344/N rats and B6C3F1 mice (gavage studies). sl: NTP Technical Report No. 402, US Department of Health and Human Services," Research Triangle Park, NC, 1993.

[210] B. H. Monien, K. Herrmann, S. Florian, and H. Glatt, "Metabolic activation of furfuryl alcohol: formation of 2-methylfuranyl DNA adducts in Salmonella typhimurium strains expressing human sulfotransferase 1A1 and in FVB/N mice," *Carcinogenesis*, vol. 32, no. 10, pp. 1533–1539, Oct. 2011.

[211] V. Ravindranath, L. Burka, and M. Boyd, "Reactive metabolites from the bioactivation of toxic methylfurans," *Science (80-.).*, vol. 224, no. 4651, 1984.

[212] L. a Peterson, "Electrophilic intermediates produced by bioactivation of furan.," *Drug Metab. Rev.*, vol. 38, no. 4, pp. 615–626, 2006.

[213] J. L. Durant, W. F. Busby, A. L. Lafleur, B. W. Penman, and C. L. Crespi, "Human cell mutagenicity of oxygenated, nitrated and unsubstituted polycyclic aromatic hydrocarbons associated with urban aerosols," *Mutat. Res. - Genet. Toxicol.*, vol. 371, no. 3–4, pp. 123–157, 1996.

[214] C. Walgraeve, K. Demeestere, J. Dewulf, R. Zimmermann, and H. Van Langenhove, "Oxygenated polycyclic aromatic hydrocarbons in atmospheric particulate matter: Molecular characterization and occurrence," *Atmos. Environ.*, vol. 44, no. 15, pp. 1831–1846, 2010.

[215] World Health Organization International Agency for Research On Cancer, "IARC Monographs on the Evaluation of Carcinogenic Risks to Humans World Health Organization (2014) IARC monographs on the evaluation of carcinogenic risks to humans, Internal report 14/002 (World Health Organization, Lyon, France).," Lyon, France, 2014.

[216] J. M. Czuczwa, B. D. McVeety, and R. A. Hites, "Polychlorinated dibenzo-p-dioxins and dibenzofurans in sediments from Siskiwit Lake, Isle Royale," *Science*

(80-.)., vol. 226, pp. 568–570, 1984.

[217] E. D. Lavric, A. A. Konnov, and J. De Ruyck, “Dioxin levels in wood combustion—a review,” *Biomass and Bioenergy*, vol. 26, no. 2, pp. 115–145, 2004.

[218] N. W. Tame, B. Z. Dlugogorski, and E. M. Kennedy, “Formation of dioxins and furans during combustion of treated wood,” *Prog. Energy Combust. Sci.*, vol. 33, no. 4, pp. 384–408, 2007.

[219] A. A. Meharg and K. Killham, “Environment: A pre-industrial source of dioxins and furans,” *Nature*, vol. 421, no. 6926, pp. 909–910, Feb. 2003.

[220] J. Schubert, J. Bewersdorff, A. Luch, and T. G. Schulz, “Waterpipe smoke: A considerable source of human exposure against furanic compounds,” *Anal. Chim. Acta*, vol. 709, pp. 105–112, 2012.

[221] E. B. Sanders, A. I. Goldsmith, and J. I. Seeman, “A model that distinguishes the pyrolysis of d-glucose, d-fructose, and sucrose from that of cellulose. Application to the understanding of cigarette smoke formation,” *J. Anal. Appl. Pyrolysis*, vol. 66, no. 1, pp. 29–50, 2003.

[222] F. Iino, T. Imagawa, M. Takeuchi, and M. Sadakata, “De Novo Synthesis Mechanism of Polychlorinated Dibenzofurans from Polycyclic Aromatic Hydrocarbons and the Characteristic Isomers of Polychlorinated Naphthalenes,” *Environ. Sci. Technol.*, vol. 33, no. 7, pp. 1038–1043, 1999.

[223] J. Wilhelm, L. Stieglitz, E. Dinjus, and R. Will, “Mechanistic studies on the role of PAHs and related compounds in PCDD/F formation on model fly ashes,” *Chemosphere*, vol. 42, no. 5, pp. 797–802, 2001.

[224] R. Atkinson, J. Arey, and S. M. Aschmann, “Atmospheric chemistry of alkanes: Review and recent developments,” *Atmos. Environ.*, vol. 42, no. 23, pp. 5859–5871, 2008.

[225] K. A. Schilling Fahnestock *et al.*, “Secondary Organic Aerosol Composition from C_{12} Alkanes,” *J. Phys. Chem. A*, vol. 119, no. 19, pp. 4281–4297, May 2015.

[226] R. Zhang, A. F. Khalizov, J. Pagels, D. Zhang, H. Xue, and P. H. McMurry, “Variability in morphology, hygroscopicity, and optical properties of soot aerosols during atmospheric processing.,” *Proc. Natl. Acad. Sci. U. S. A.*, vol. 105, no. 30, pp. 10291–6, Jul. 2008.

[227] V. Ramanathan *et al.*, “Atmospheric brown clouds: impacts on South Asian climate and hydrological cycle.,” *Proc. Natl. Acad. Sci. U. S. A.*, vol. 102, no. 15, pp. 5326–33, Apr. 2005.

[228] Y. J. Kaufman, I. Koren, L. A. Remer, D. Rosenfeld, and Y. Rudich, “The effect of smoke, dust, and pollution aerosol on shallow cloud development over the Atlantic Ocean.,” *Proc. Natl. Acad. Sci. U. S. A.*, vol. 102, no. 32, pp. 11207–12, Aug. 2005.

[229] A. Violi and G. A. Voth, “A Multi-scale Computational Approach for Nanoparticle Growth in Combustion Environments,” in *High Performance Computing and Communications*, J. D. L.T. Yang, O.F. Rana, B.D. Martino, Ed. Springer, Berlin, Heidelberg, 2005, pp. 938–947.

[230] S. H. Chung and A. Violi, “Insights on the nanoparticle formation process in counterflow diffusion flames,” *Carbon N. Y.*, vol. 45, pp. 2400–2410, 2007.

[231] C. S. McEnally and L. D. Pfefferle, “The effects of dimethyl ether and ethanol on benzene and soot formation in ethylene nonpremixed flames,” *Proc. Combust.*

Inst., vol. 31, no. 1, pp. 603–610, Jan. 2007.

[232] F. Inal and S. M. Senkan, “Effects of oxygenate additives on polycyclic aromatic hydrocarbons(pahs) and soot formation,” *Combust. Sci. Technol.*, vol. 174, no. 9, pp. 1–19, 2002.

[233] R. J. Therrien, A. Ergut, Y. a. Levendis, H. Richter, J. B. Howard, and J. B. Carlson, “Investigation of critical equivalence ratio and chemical speciation in flames of ethylbenzene–ethanol blends,” *Combust. Flame*, vol. 157, no. 2, pp. 296–312, Feb. 2010.

[234] M. Salamanca, M. Sirignano, M. Commodo, P. Minutolo, and A. D’Anna, “The effect of ethanol on the particle size distributions in ethylene premixed flames,” *Exp. Therm. Fluid Sci.*, vol. 43, pp. 71–75, Nov. 2012.

[235] J. Wu *et al.*, “Reduction of PAH and soot in premixed ethylene–air flames by addition of ethanol,” *Combust. Flame*, vol. 144, no. 4, pp. 675–687, Mar. 2006.

[236] C. S. Mcenally and L. D. Pfefferle, “Species and soot concentration measurements in a methane/air nonpremixed flame doped with C4 hydrocarbons,” *Combust. Flame*, vol. 115, no. 1–2, pp. 81–92, 1998.

[237] W. Merchan-Merchan, S. McCollam, and J. F. C. Pugliese, “Soot formation in diffusion oxygen-enhanced biodiesel flames,” *Fuel*, vol. 156, pp. 129–141, 2015.

[238] J. Camacho, S. Lieb, and H. Wang, “Evolution of size distribution of nascent soot in n- and i-butanol flames,” *Proc. Combust. Inst.*, vol. 34, no. 1, pp. 1853–1860, 2013.

[239] M. Commodo, G. Tessitore, G. De Falco, P. Minutolo, and A. D’Anna, “Photoionization Study of Soot Precursor Nanoparticles in Laminar Premixed Ethylene/Ethanol Flames,” *Combust. Sci. Technol.*, vol. 186, no. January 2015, pp. 37–41, 2014.

[240] T. Dillstrom and A. Violi, “The effect of reaction mechanisms on the formation of soot precursors in flames,” *Combust. Theory Model.*, vol. 21, no. 1, pp. 23–34, Aug. 2017.

[241] K. O. Johansson *et al.*, “Formation and emission of large furans and oxygenated hydrocarbons from flames.,” *Proc. Natl. Acad. Sci. U. S. A.*, vol. 113, no. 30, pp. 8374–8379, Jul. 2016.

[242] V. T. Dillstrom, P. Elvati, and A. Violi, “Oxygen driven soot formation,” *Proc. Combust. Inst.*, 2016.

[243] K. O. Johansson *et al.*, “Radical–radical reactions, pyrene nucleation, and incipient soot formation in combustion,” *Proc. Combust. Inst.*, vol. 36, no. 1, pp. 799–806, 2017.

[244] D. X. Du, R. L. Axelbaum, and C. K. Law, “The influence of carbon dioxide and oxygen as additives on soot formation in diffusion flames,” *Symp. Combust.*, vol. 23, no. 1, pp. 1501–1507, 1991.

[245] K. M. Leung, R. P. Lindstedt, and W. P. Jones, “A simplified reaction mechanism for soot formation in nonpremixed flames,” *Combust. Flame*, vol. 87, no. 3–4, pp. 289–305, Dec. 1991.

[246] J. Y. Hwang, S. H. Chung, and W. Lee, “Effects of oxygen and propane addition on soot formation in counterflow ethylene flames and the role of C3 chemistry,” *Symp. Combust.*, vol. 27, pp. 1531–1538, 1998.

[247] R. Kee, “CHEMKIN.” San Diego, CA, 2006.

[248] A. Tregrossi, A. Ciajolo, and R. Barbella, “The combustion of benzene in rich premixed flames at atmospheric pressure,” *Combust. Flame*, vol. 117, no. 3, pp. 553–561, May 1999.

[249] B. Apicella *et al.*, “Mass spectrometric analysis of large PAH in a fuel-rich ethylene flame,” *Proc. Combust. Inst.*, vol. 31, no. 1, pp. 547–553, Jan. 2007.

[250] V. V. Kislov, R. I. Singh, D. E. Edwards, A. M. Mebel, and M. Frenklach, “Rate coefficients and product branching ratios for the oxidation of phenyl and naphthyl radicals: A theoretical RRKM-ME study,” *Proc. Combust. Inst.*, vol. 35, no. 2, pp. 1861–1869, 2015.

[251] S. Rolland and J. M. Simmie, “The comparison of detailed chemical kinetic mechanisms; forward versus reverse rates with CHEMRev,” *Int. J. Chem. Kinet.*, vol. 37, no. 3, pp. 119–125, Mar. 2005.

[252] M. U. Alzueta, P. Glarborg, and K. I. M. Dam-johansen, “Experimental and Kinetic Modeling Study of the Oxidation of Benzene,” *Int. J. Chem. Kinet.*, vol. 32, no. 8, pp. 498–522, 2000.

[253] H. Richter, S. Granata, W. H. Green, J. B. Howard, and V. D. Knyazev, “Detailed modeling of PAH and soot formation in a laminar premixed benzene/oxygen/argon low-pressure flame,” *Proc. Combust. Inst.*, vol. 30 I, no. 1, pp. 1397–1405, 2005.

[254] J. A. Miller, R. E. Mitchell, M. D. Smooke, and R. J. Kee, “Toward a comprehensive chemical kinetic mechanism for the oxidation of acetylene: Comparison of model predictions with results from flame and shock tube experiments,” *Symp. Combust.*, vol. 19, no. 1, pp. 181–196, Jan. 1982.

[255] H. Richter, W. J. Grieco, J. B. Howard, A. P, S. Chrysen, and P. Benznap, “Formation Mechanism of Polycyclic Aromatic Hydrocarbons and Fullerenes in Premixed Benzene Flames,” *Combust. Flame*, vol. 119, pp. 1–22, 1999.

[256] W. Tsang and R. F. Hampson, “Chemical Kinetic Data Base for Combustion Chemistry. Part I. Methane and Related Compounds,” *J. Phys. Chem. Ref. Data*, vol. 15, no. 3, pp. 1087–1279, Jul. 1986.

[257] K. M. Leung and R. P. Lindstedt, “Detailed kinetic modeling of C1 — C3 alkane diffusion flames,” *Combust. Flame*, vol. 102, no. 1–2, pp. 129–160, Jul. 1995.

[258] M. A. Ali, V. T. Dillstrom, J. Y. W. Lai, and A. Violi, “Ab initio investigation of the thermal decomposition of n-butylcyclohexane.,” *J. Phys. Chem. A*, vol. 118, no. 6, pp. 1067–76, Feb. 2014.

[259] S. Stein and A. Fahr, “High-Temperature Stabilities of Hydrocarbons,” *J. Phys. Chem.*, vol. 89, no. 17, pp. 3714–3725, 1985.

[260] H. Richter, T. G. Benish, O. A. Mazyar, W. H. Green, and J. B. Howard, “Formation of polycyclic aromatic hydrocarbons and their radicals in a nearly sooting premixed benzene flame,” *Proc. Combust. Inst.*, vol. 28, no. 2, pp. 2609–2618, 2000.

[261] J. A. Montgomery, M. J. Frisch, J. W. Ochterski, and G. a. Petersson, “A complete basis set model chemistry. VII. Use of the minimum population localization method,” *J. Chem. Phys.*, vol. 112, no. 15, pp. 6532–6542, 2000.

[262] J. A. Montgomery, M. J. Frisch, J. W. Ochterski, and G. A. Petersson, “A complete basis set model chemistry. VI. Use of density functional geometries and frequencies,” *J. Chem. Phys.*, vol. 110, no. 6, pp. 2822–2827, 1999.

[263] M. Frisch et al., “Gaussian 09, Revision A.02.” Gaussian, Inc., Wallingford, CT,

2009.
[264] B. Sirjean *et al.*, “The autoignition of cyclopentane and cyclohexane in a shock tube,” *Proc. Combust. Inst.*, vol. 31, no. 1, pp. 277–284, Jan. 2007.
[265] V. Guner, K. Khuong, A. Leach, P. Lee, M. Bartberger, and K. Houk, “reactions of hydrocarbons for the benchmarking of computational methods: the performance of ab initio, density functional, CASSCF, CASPT2, and CBS-QB3 methods,” *J. Phys. Chem. A*, vol. 107, pp. 11445–11459, 2003.
[266] H. P. Hratchian and H. B. Schlegel, “Finding minima, transition states, and following reaction pathways on ab initio potential energy surfaces,” in *Theory and Applications of Computational Chemistry*, C. E. Dykstra, G. Frenking, K. S. Kim, and G. E. Scuseria, Eds. Amsterdam: Elsevier, 2005, pp. 195–249.
[267] K. Fukui, “The Path of Chemical Reactions - The IRC Approach,” *Acc. Chem. Res.*, vol. 14, no. 12, pp. 363–375, 1981.
[268] J. R. Barker, “Multiple-Well, Multiple Path Unimolecular Reaction Sytems. I. MultiWell Computer Program Suite,” *Int. J. Chem. Kinet.*, vol. 33, pp. 232–245, 2001.
[269]J. R. Barker, “Energy Transfer in Master Equation Simulations: A New Approach,” *Int. J. Chem. Kinet.*, vol. 41, pp. 748–763, 2009.
[270] J. R. Barker *et al.*, “MultiWell-2017 Software Suite.” University of Michigan, 2017.
[271] C. A. Taatjes *et al.*, “Enols are common intermediates in hydrocarbon oxidation.,” *Science*, vol. 308, no. 5730, pp. 1887–1889, 2005.
[272] B. Bohn and C. Zetzsch, “Gas-phase reaction of the OH–benzene adduct with O2: reversibility and secondary formation of HO2,” *Phys. Chem. Chem. Phys.*, vol. 1, no. 22, pp. 5097–5107, 1999.
[273] I. V. Tokmakov and M. C. Lin, “Kinetics and Mechanism of the OH + C6H6 Reaction: A Detailed Analysis with First-Principles Calculations,” *J. Phys. Chem. A*, vol. 106, no. 46, pp. 11309–11326, 2002.
[274] I. V. Tokmakov, G. S. Kim, V. V. Kislov, A. M. Mebel, and M. C. Lin, “The reaction of phenyl radical with molecular oxygen: A G2M study of the potential energy surface,” *J. Phys. Chem. A*, vol. 109, no. 27, pp. 6114–6127, 2005.
[275] T. Seta, M. Nakajima, and A. Miyoshi, “High-Temperature Reactions of OH Radicals with Benzene and Toluene,” *J. Phys. Chem. A*, vol. 110, no. 15, pp. 5081–5090, 2006.
[276] Z. F. Xu and M. C. Lin, “Ab Initio Kinetics for the Unimolecular Reaction C6H5OH → CO + C5H6,” *J. Phys. Chem. A*, vol. 110, no. 4, pp. 1672–1677, 2005.
[277] A. D’Anna and J. H. Kent, “A model of particulate and species formation applied to laminar, nonpremixed flames for three aliphatic-hydrocarbon fuels,” *Combust. Flame*, vol. 152, no. 4, pp. 573–587, 2008.
[278] N. Marinov, “A detailed chemical kinetic model for high temperature ethanol oxidation,” *Int. J. Chem. Kinet.*, vol. 31, no. 3, pp. 183–220, 1999.
[279] X. Zhong and J. W. Bozzelli, “Thermochemical and Kinetic Analysis of the H , OH , HO2 , O , and O2 Association Reactions with Cyclopentadienyl Radical,” *J. Phys. Chem. A*, vol. 5, no. 98, pp. 3537–3555, 1998.
[280] N. M. MARINOV, M. J. CASTALDI, C. F. MELIUS, and W. TSANG, “Aromatic and Polycyclic Aromatic Hydrocarbon Formation in a Premixed Propane Flame,”

Combust. Sci. Technol., vol. 128, no. 1–6, pp. 295–342, Oct. 1997.